SOURCE MECHANISMS OF VOLCANIC INDUCED SEISMICITY – MIYAKEJIMA, JAPAN, 2000

by

Sarah Minson

University of California, Berkeley

Spring, 2003

Advisor: Professor Douglas S. Dreger

UNIVERSITY OF CALIFORNIA, BERKELEY

ABSTRACT

SOURCE MECHANISMS OF VOLCANIC INDUCED SEISMICITY – MIYAKEJIMA, JAPAN, 2000

by Sarah Minson

Advisor: Professor Douglas S. Dreger
Department of Earth and Planetary Science

During a period of volcanic unrest and eruption on Miyakejima, Japan, a significant number of earthquakes with anomalous non-double-couple mechanisms were observed. In this study, linear moment tensor inversions in two passbands are used to establish the mechanism of eighteen of these earthquakes. For each event, mechanisms from deviatoric moment tensor inversions and full moment tensor inversions are compared to the best mechanisms comprised of isotropic and double-couple components (ISO+DC), which are determined by a grid search over faulting parameters.

The results show that although the full moment tensor inversions produce mechanisms which fit the data best, the isotropic components of most, if not all, of the events are not statistically significant. The dominant faulting mechanism is a positive horizontal CLVD mechanism which appears to indicate tensile faulting related to the intrusion of a dike. A few earthquakes have double-couple mechanisms, and one earthquake might have an ISO+DC mechanism.

GPS data are independently inverted to determine the slip mechanism of the two largest earthquakes in the sequence: a vertical strike-slip earthquake and a non-double-couple event. For both earthquakes, the two data sets independently converge to consistent mechanisms. The GPS data confirms the simple mechanism of the tectonic earthquake, and strongly indicates that the anomalous earthquake is caused by an opening fault.

TABLE OF CONTENTS

LIST OF TABLES

LIST OF FIGURES

ACKNOWLEDGMENTS

The author wishes to acknowledge Professor Douglas Dreger, without whom this thesis would not have been possible. He did the original research on the Long Valley Caldera earthquakes on which this thesis is based, he wrote the inversion program, arranged to get the data from Japan, and helped apply for grants to fund the project. Most importantly, he was always available to answer questions, no matter how inane, and to fix problems, even frighteningly large problems.

Professor Roland Burgmann provided the programs to invert the geodetic data and instruction on how to use them. Eiichi Fukuyama provided supplemental data from the F-net Broadband Seismograph Network, and Fumiko Tajima obtained the earthquake hypocenter catalog from the Japan Meteorological Agency. Dr. Mark Jellinek provided useful discussions on the mechanics of fluid filled cracks, and Professor James Kirchner was consulted about the statistical analyses. Mark Murray helped to acquire the geodetic data from the Geographical Survey Institute of Japan. Margie Winn provided support and encouragement. Nearly everyone in the Berkeley Seismological Laboratory helped to resolve problems. They include Wu-Cheng Chi, Junkee Rhie, Yuan-Cheng Gung, Charley Paffenbarger, Doug Neuhauser, Peggy Hellweg, Sébastien Rousset, Gilead Wurman, Aimin Cao, Dennise Templeton, and Akiko To.

Chapter 1

INTRODUCTION

Miyakejima is a member of the Izu Islands, a volcanic chain located south of the island of Honshu, Japan. Mount Oyama on Miyakejima erupts approximately every twenty years, with previous eruptions in 1940, 1962, and 1983 (Ukawa et al., 2000). Its most recent eruption began on June 26, 2000, Japanese standard time, and was accompanied by the largest earthquake swarm ever recorded in Japan (Japan Meteorological Agency (JMA), 2000). The seismic activity showed complex variations in space and time (JMA, 2000), but its most notable feature is that it migrated northwest with an offshore dike intrusion. Moment tensor solutions from the F-net Broadband Seismograph Network show that the double-couple components for many of these events are consistent with strike-slip faulting, with normal faulting events occurring between Miyakejima and Kozushima (Fukuyama et al., 2001). However, many of these earthquakes have large non-double-couple components which might be indicative of fluid involvement in the seismic source process.

To investigate the processes involved in this sequence of earthquakes, this study used linear moment tensor inversions to determine the focal mechanisms for a number of significant earthquakes. Different types of inversions were used to resolve whether the non-double-couple components of these earthquakes are best modeled as compensated linear vector dipoles, isotropic components, or both. The stability of these focal mechanisms was examined, and the statistical significance of the non-double-couple components was analyzed.

TECTONIC SETTING

The Izu-Bonin island arc was created by the subduction of the Pacific plate beneath the Philippine Sea plate, which is, in turn, moving to the northwest at approximately 4 cm/yr (Seno et al., 1993) and is subducting beneath the Eurasian plate (Figure 1). The interaction of these plates leads to extensional stress in the northeast-southwest direction due to the bending of the Philippine Sea plate from subduction, and compression in the northwest-southeast direction from its collision with the Eurasian and North American plates (Hashimoto and Tada, 1990). Ito and Yoshioka (2002) discuss the theory proposed in Nakamura (1980) that the northeast-southwest oriented extensional stresses are caused by the bending of the Philippine Sea plate as it subducts along the Sagami trough. This bending forces magma formed by the Pacific plate subducting under the Philippine Sea plate to travel upwards through tensile cracks in the Philippine Sea plate. This theory is confirmed by the 1986 eruption of the nearby Izu-Oshima volcano, which was marked by the opening of northwest striking fissures (Hashimoto and Tada, 1990).

Chapter 2

METHODOLOGY

This study employed the methods of Dreger et al. (2000) and Dreger and Woods (2002) to investigate the mechanisms of eighteen events which occurred from 29 June to 18 July, 2000 (UT). These eighteen events are comprised of the twelve events which the F-net network determined to have moment magnitudes of 5.5 or larger, plus six smaller events (Table 1). The smaller events were chosen because the F-net moment tensors had anomalous characteristics such as large non-double-couple components or solutions with large variances.

Linear moment tensor inversions, as described in Dreger and Helmberger (1993), are used to invert complete, three-component, broadband velocity seismograms recorded by the F-net network. The instrument response is deconvolved from the seismograms, and they are integrated to displacement and bandpass filtered with a four-pole, two-pass, acausal Butterworth filter. In this study, all of the events were separately inverted in two frequency ranges: 0.01 to 0.033 Hz, and 0.02 to 0.05 Hz. Event hypocenters determined by JMA were used. Green's functions for the inversions are calculated using frequency wave number integration (Saikia, 1994) and the velocity model of Fukuyama and Dreger (2000) (Table 2), which is the same velocity model employed by F-net in their moment tensor inversions (Table 3). It is a one-dimensional flat layer model which is probably much simpler than the true velocity structure of this region, given that there are three plates interacting in a complex fashion. But because of the low frequencies that are used in the inversions, the effects of complex three-dimensional structure are expected to be negligible. This was confirmed for the Long Valley Caldera in California by Panning et al. (2001), for data that were bandpass filtered between 0.02 and 0.05 Hz. The inversions with data filtered between 0.01 0.033 Hz are expected to be less affected by complex structure, although some depth resolution is lost by using lower frequencies.

The seismic moment tensor, M_{ij}, is a nine element symmetric tensor, and thus contains only six independent elements. The diagonalized moment tensor

$$\mathbf{M} = \begin{bmatrix} M_1 & 0 & 0 \\ 0 & M_2 & 0 \\ 0 & 0 & M_3 \end{bmatrix}$$

can be decomposed into isotropic and deviatoric tensors

$$\mathbf{M} = \frac{1}{3} \cdot \begin{bmatrix} tr(\mathbf{M}) & 0 & 0 \\ 0 & tr(\mathbf{M}) & 0 \\ 0 & 0 & tr(\mathbf{M}) \end{bmatrix} + \begin{bmatrix} M_1^1 & 0 & 0 \\ 0 & M_2^1 & 0 \\ 0 & 0 & M_3^1 \end{bmatrix}$$

where M_i^1 are the deviatoric eigenvalues (Lay and Wallace, 1995). The deviatoric part of the moment tensor can be further decomposed into separate double-couple and CLVD tensors

$$\mathbf{M} = \frac{1}{3}\cdot\begin{bmatrix} tr(\mathbf{M}) & 0 & 0 \\ 0 & tr(\mathbf{M}) & 0 \\ 0 & 0 & tr(\mathbf{M}) \end{bmatrix} + (1-2\cdot\varepsilon)\cdot\begin{bmatrix} 0 & 0 & 0 \\ 0 & -M_3 & 0 \\ 0 & 0 & M_3 \end{bmatrix} + \varepsilon\cdot\begin{bmatrix} -M_3 & 0 & 0 \\ 0 & -M_3 & 0 \\ 0 & 0 & 2M_3 \end{bmatrix}$$

where $\varepsilon = \dfrac{-M_2^1}{M_3^1}$ for $\left|M_1^1\right| \geq \left|M_2^1\right| \geq \left|M_3^1\right|$ (Figure 2).

In deviatoric moment tensors, the further simplifying assumption is made that there is no volume change. This implies that the trace of the seismic moment tensor is zero, or that

$$M_1 + M_2 = -M_3$$

For the moment tensor inversions, it is also necessary to determine the location of the earthquake in three dimensions. The latitude and longitude of the hypocenters for these events were determined by JMA, and the depth of each event can be established by performing independent moment tensor inversions at a range of depths to find which one produces the best fit to the data. The ability of the synthetics to fit the data is assessed by the variance reduction (VR), where

$$VR = \left[1.0 - \frac{\int (data - synthetic)^2\, dt}{\int (data)^2\, dt}\right]\cdot 100\%$$

and a variance reduction of 100% implies a perfect fit between the synthetic and the data. Depths from 2 km to 16 km were tested in increments of 2 km.

Since the depth of the hypocenter is not assumed, it is also a variable in the inversion. Therefore, the deviatoric inversions have six independent variables: five elements of the seismic moment tensor and the depth of the event. These six variables could also be interpreted as the strike, dip, and rake of the mechanism, moment, depth, and the percentage of the moment which is comprised of the compensated linear vector dipole (CLVD) component.

For each event, full moment tensor inversions were performed and compared to the deviatoric inversions. In the full moment tensor inversions, all six elements of the seismic moment tensor are inverted for, and the trace does not have to be zero. Thus, there can be a net volume change at the source which is represented by the isotropic component of the moment tensor, but there is also an additional model parameter which must be solved for. It then follows that there are seven model parameters in the full moment tensor inversions: the six parameters from the deviatoric inversions plus the sixth moment tensor element or the percentage of the moment which the isotropic component comprises. The stability of both the full moment tensor

inversions and the deviatoric moment tensor inversions is examined by use of the jackknife test, in which data from every subset of the stations used in the original inversion are used to invert for the mechanism.

The third type of mechanism investigated is the set mechanisms comprised only of isotropic and double-couple components (ISO+DC). Since the CLVD component is assumed to be zero, these mechanisms are equivalent to the deviatoric moment tensor inversions in terms of the number of model parameters. Moment tensors without CLVD components have intermediate eigenvalues equal to zero, or $\varepsilon = 0$. The seismic moment tensor decomposition then simplifies to

$$\mathbf{M} = \frac{1}{3} \cdot \begin{bmatrix} tr(\mathbf{M}) & 0 & 0 \\ 0 & tr(\mathbf{M}) & 0 \\ 0 & 0 & tr(\mathbf{M}) \end{bmatrix} + \begin{bmatrix} 0 & 0 & 0 \\ 0 & -M_3 & 0 \\ 0 & 0 & M_3 \end{bmatrix}$$

However, a limitation on the intermediate eigenvalue is not as simple a constraint on the moment tensor as is the zero trace constraint of deviatoric moment tensor inversions. Therefore, these mechanisms are determined by a grid search over six parameters: double-couple moment; isotropic moment; and strike, rake, and dip of the double-couple.

The best ISO+DC mechanism for each event was determined by first performing a coarse grid search of strike, rake, and dip in ten-degree increments; twenty double-couple moments, from one third of the moment determined by the deviatoric inversions to three times the deviatoric moment; and twenty isotropic moments, from zero to the deviatoric moment. This was followed by a three-degree increment search of ten each double-couple and isotropic moments, from half of their respective moments determined in the coarse grid search to two times those moments. In cases where the initial coarse grid search found that an isotropic moment of zero fit best, the fine grid search tested ten isotropic moments from zero to one twentieth of the double-couple moment.

Since the full moment tensor inversions have an additional model parameter relative to the deviatoric inversions, the statistical significance of the isotropic components of the complete moment tensors is determined by the F-test. If C is a complicated model with m model parameters and S is a simpler model with k parameters, where $m > k$, then the F statistic tests whether model C fits the data significantly better than S. The statistic depends on the degrees of freedom, df_S and df_C, for each model, which are defined as $df_S = N - k - 1$ and $df_C = N - m - 1$ for S and C, respectively, where N is the number of observations. In this study, three-component seismograms were used and 120 points in each seismogram were sampled and inverted for. However, the data are correlated and the correlation length is assumed to be the high corner frequency of the passband filter used. Therefore,

$$N = \frac{3 \cdot 120 \cdot (Number\ of\ stations)}{T}$$

where T is the period of the high corner of the passband filter, and in this study is either 30 sec or 20 sec.

Two types of F-tests are used. The first is the F-test which Menke (1984) advocated:

$$F = \frac{\frac{SSE_S}{df_S}}{\frac{SSE_C}{df_C}}$$

where SSE is the error sum of squares. This tests whether the variance of the more complex model is significantly smaller than the variance of the simpler model. The second F-test used is the nested F-test proposed by Helsel and Hirsch (1992):

$$F = \frac{\left(SSE_S - SSE_C\right)}{\left(df_S - df_C\right)} \Big/ \left(SSE_C / df_C\right)$$

The nested F-test statistic tests whether the decreased variance of the more complex model is significant, relative to the decrease in the degrees of freedom due to adding additional model parameters, in the special case that all of the model parameters in the simpler model are also included in the complex model. In this study, full moment tensor inversions will be compared to deviatoric inversions, and deviatoric inversions will be compared to double-couple inversions. In each case, the difference in the number of model parameters is one (seven model parameters in full moment tensor inversions versus six in deviatoric inversions, and six parameters versus five in double-couple inversions). These models correspond to an even more specific case of the F-test where $m = k + 1$ and the nested F-test becomes the partial F-test:

$$F = \frac{\left(SSE_S - SSE_C\right)}{\left(SSE_C / df_C\right)}$$

In this formulation, the F-test analyzes whether the specific parameter which was added to the model yields significant explanatory power in the presence of the other variables in the model (Helsel and Hirsch, 1992).

Chapter 3

MOMENT TENSOR INVERSIONS

The location of the nine F-net stations used in the study and the hypocenters determined by JMA are plotted in Figure 3. Data from YMZ were not available for EVT11 and EVT12. The TYM record for EVT15 is clipped and was excluded from all inversions. And although TYM also went off-scale during EVT3, an inspection of the waveform shows that any nonlinearity in the instrument response is negligible, and those data were included.

The results of the deviatoric and full moment tensor inversions in the 0.01 to 0.033 Hz passband are shown in Figures 4 and 5, respectively, and Figures 6 and Figure 7 show the same for the 0.02 to 0.05 Hz passband. Comparing these results to the Harvard CMT solutions (Figure 8), it is apparent that most of these events have large positive horizontal CLVD components with T-axes oriented in the northeast-southwest direction, which is consistent with the regional stress field (Hashimoto and Tada, 1990). However, since these events occurred during a volcanic eruption, there is no reason to assume that they are tectonic in origin.

Plotting variance reduction as a function of depth for the deviatoric inversions shows that many of these earthquakes are quite shallow, and none appear to be deeper than 12 km (Figures 9-44). These plots also show the depth dependence of the ratio of the variance of the solution to the percentage of the solution comprised by the double-couple component (Var/Pdc). It is desirable that the depth with the best variance reduction also has a low value of Var/Pdc, since it should be assumed that the mechanism is simple unless the data absolutely require more complex slip. For a simple mechanism, the variance should be small and the percent double-couple large, which means that Var/Pdc is small. For many events, the depth with the highest variance reduction is also at least a local minimum in Var/Pdc. Comparison of the synthetic and observed waveforms and focal mechanisms for all of the events are presented in Figures 45-116.

Since the grid search inversions for ISO+DC mechanisms have the same number of model parameters as deviatoric inversions, these two types of inversions should be compared to determine which better represents the mechanisms of the events studied. For every event except EVT7, the ISO+DC SSE was larger than the deviatoric SSE (Table 7). Therefore, it appears that the majority of these mechanisms are better modeled with a deviatoric moment tensor than with a combination of isotropic and double-couple components, and the grid search inversions will not be discussed further except in reference to EVT7.

The results of the jackknife tests show that the relative contribution of the double-couple, CLVD, and isotropic components of the moment tensor are robust features of the inversions (Figures 117-134). Also, the preferred orientation of the T-axes of the mechanisms is very stable for every event inverted with the 20 sec corner passband except for EVT7 (Figures 135-152) and for all of the 30 sec corner passband inversions (Figures 153-170). The instability of

the higher frequency inversion for the mechanism of EVT7 is just one of several things that make that event anomalous.

Since most of the events have non-double-couple mechanisms, it is important to consider whether the CLVD components are statistically significant. Table 6 compares the SSE for EVT3 from the deviatoric moment tensor inversion to the SSE for a three-degree grid search inversion with zero isotropic moment. Clearly the decrease in variance with the addition of a CLVD component is significant regardless of the type of F-test employed. However, the F-test results comparing the full moment tensor inversions to the deviatoric inversions are less clear. Menke's F-test shows that only one of the events has an isotropic component which is statistically significant with at least 90% confidence. That event is EVT7, which is an unusual event, and the inversions may not be reliable. Contrariwise, Helsel and Hirsch's method suggests that many of the events have isotropic components which are statistically significant with high levels of confidence.

EVT1

The deviatoric inversions in both frequency ranges yield majority double-couple mechanisms, and the jackknife tests show that both the deviatoric and full moment tensor inversions are very stable. However, the F-test values comparing the full moment tensor solution to the deviatoric mechanism are rather small, and the scalar seismic moment of the full moment tensor inversion filtered with a 20 sec period corner is more than twice the moment from the deviatoric mechanism, which could mean that components of the moment tensor are trading off (Dreger and Woods, 2002). So it is quite likely that this event does not have a significant isotropic component.

EVT2

The deviatoric mechanisms from this event are denominated by a positive horizontal CLVD component, and the full moment tensor mechanisms have fairly large isotropic components. Again the jackknife tests show that these mechanisms are stable. But the isotropic component may not be statistically significant.

EVT3

EVT3 is another event which is dominated by a horizontal positive CLVD. The deviatoric inversions in the two frequency domains have similar orientations of the T-axes. But because of the large CLVD component, the orientation of the P-axis and the double-couple component are not as well resolved. For the 30 sec corner filter, most of the CLVD component becomes an

isotropic component in the full moment tensor inversion; however, the 20 sec full moment tensor mechanism is still partly controlled by the CLVD component. The moments of the different inversions are similar and the mechanism is very stable. This is a large event (Mw 6.1-6.2) which produced noticeable displacements in GPS time series recorded in the region. These geodetic data can be used to independently verify the CLVD mechanism of this event.

EVT4

This is another CLVD event and the CLVD orientation is consistent with the other earthquakes studied. For this event, the 20 sec corner full moment tensor inversion favors an isotropic component, while the 30 sec corner inversion retains much of the CLVD component of the deviatoric inversion. The mechanism of this event is also stable. Another discrepancy between the two frequency ranges is that the best depth from the 30 sec corner inversions is 2 km, while the depth from the 20 sec corner inversions is 4 km. This discrepancy may be caused by errors in the Green's functions (D. Dreger, written communication, 2003).

EVT5

EVT5 is another positive horizontal CLVD event. Full moment tensor inversions with both bandpass filters have larger CLVD components than isotropic components, and the F-values are quite low in the 20 sec corner passband. The jackknife tests show that this mechanism is also stable.

EVT6

Similar to EVT5, this event has large CLVD components in both frequency passbands for the deviatoric and full moment tensor inversions, and the F-value is low in the 30 sec corner passband. In the 20 sec corner inversion, the CLVD component in the full moment tensor inversion is larger than it is in the deviatoric inversion. The inversions in the different frequency ranges disagree as to the depth of the event. But in both frequency ranges, the jackknife results indicate that the solution is stable.

EVT7

For this event, there is a large discrepancy between the inversions in the different frequency ranges both in the depth of the event and in its mechanism. The 20 sec corner passband produces a simple double-couple vertical dip-slip mechanism at a depth of 12 km. However,

the 30 sec corner inversion prefers a negative vertical CLVD mechanism at 8 km depth. This is also the only event for which the ISO+DC inversion fit better than the deviatoric inversion, but only in the 30 sec corner passband. The ISO+DC synthetics for this frequency range are compared to the data in Figure 171. Although this inversion produces an unusual mechanism, it is the same mechanism which the deviatoric and full moment tensor inversions generated (Figure 172). Furthermore, the CLVD mechanism is very stable, while a jackknife test of the dip-slip mechanism from the higher frequency inversion shows that there is significant variation in the orientation of the T-axis of that mechanism.

The difference in the mechanisms produced by the inversions in the different frequency ranges leads to differing statistical significance for the isotropic components. The isotropic component of the full moment tensor inversion in the lower frequency passband is the only isotropic component that appears to be statistically significant. Conversely, the isotropic component of the higher frequency full moment tensor inversion is the only component that is definitely not statistically significant when evaluated by both the Menke (1984) and the Helsel and Hirsch (1992) methods of analysis.

While many other events in this study have large CLVD components, the orientation of those components is consistent with the opening of a vertical crack. None of the other deviatoric or full moment tensor inversions yielded this type of mechanism. However, the deviatoric part of the full moment tensor mechanism for EVT1 is somewhat similar (Figures 5 and 7).

These discrepant mechanisms could be due to some mistake in the inversions. For instance, the different inversions could simply be fitting different parts of the record rather than illustrating a real variation in the data in these two passbands. The displacement seismograms filtered in the two frequency ranges are compared in Figure 173. For the purpose of contrast, the data for EVT3 are filtered and plotted in Figure 174. The EVT3 record is dominated by a two-sided pulse in the lower frequency range, and that pulse is a prominent feature of the higher frequency passband as well. But for EVT7, there does seem to be a larger change in the waveforms between the two frequency ranges.

EVT7 is located to the east of every other event in the study. So it is possible that part of the cause of the irregularities in the moment tensor inversions for this event could be some bias introduced by the event location and station geometry. However, the distance between this event and the others in the study is small; for example, EVT7 is 22.2 km from EVT2. The jackknife tests for the lower frequency inversion show that that mechanism is stable.

EVT8

The deviatoric mechanism of this event is majority double-couple. However, the F-value for the lower frequency inversion is fairly high, making this event one of the most likely to have a statistically significant isotropic component. The mechanism is quite stable.

EVT9

This is another event where inversions in the two frequency ranges prefer different depths. Every inversion for this event generated a mechanism that was majority double-couple, but there is a large non-double-couple component. Jackknife tests show that the mechanism is stable.

EVT10

There are two unusual features of the moment tensor inversions for the mechanism of this event. First, the 30 sec corner passband inversion picked a depth of 8 km, while the higher frequency inversion preferred a depth of 4 km. Second, the lower frequency deviatoric inversion generated a mechanism that was overwhelmingly double-couple, while the other inversions have large non-double-couple components. Again, the mechanism of this event is stable.

EVT11

The mechanism of this event has a large non-double-couple component. However, while the F-value in the 30 sec corner passband is fairly large, the statistic is significantly smaller for the 20 sec corner inversion. The jackknife tests show that the inversion is stable. There is also a disagreement between the two frequency passbands as to the depth of the event.

EVT12

The various moment tensor inversions for EVT12 do show some trade off between the components of the moment tensor, but the mechanism itself is stable. Its stability is confirmed by jackknife tests. The F-values for this event are rather low, and again there is a discrepancy between the different passbands as to the depth of the event.

EVT13

This event has a majority double-couple mechanism, and jackknife tests show that the mechanism is stable. Like EVT12, the F-values are fairly low.

EVT14

For this event, there are two discrepancies between the inversions in the two passbands. First, there is a disagreement as to the depth of the event. Second, the deviatoric focal mechanism in the 20 sec corner passband is majority CLVD, while the lower frequency inversion yields a simple double-couple mechanism. The jackknife tests show that both mechanisms are stable.

EVT15

EVT15 has a simple vertical strike-slip mechanism. It is the largest event that occurred in this sequence of earthquakes and has a moment magnitude of 6.4. Because of its large magnitude, this event produced significant displacements in the GPS time series at the GPS stations in the region, and these data can be used to independently confirm the mechanism of the event. Also the event was located south of the dike in the region that Fukuyama et al. (2001) identified as only having strike-slip earthquakes. The 30 sec corner passband inversions picked a depth of 12 km, while the higher frequency inversions prefer a depth of 10 km, but jackknife tests show that the mechanism is stable.

EVT16

This is a majority CLVD event and the full moment tensor inversions yield mechanisms with large isotropic components. However, the F-value is fairly low. The jackknife tests indicate that the inversion is stable.

EVT17

This event has a double-couple mechanism. As is expected, the F-value is low. Jackknife tests show that the mechanism is stable.

EVT18

EVT18 is another double-couple event. The mechanism is somewhat similar to the mechanism of EVT17 and, as with EVT17, the F-value is low. Once again, the jackknife tests indicate that the mechanism is stable.

Chapter 4

GEODETIC OBSERVATIONS

EVT15 and EVT3 are the two largest events in the earthquake sequence. EVT15, the largest event, has a moment magnitude of 6.4 and a simple vertical strike-slip mechanism, while the mechanism of EVT3 is approximately 83% CLVD. Both events produced displacements which were recorded by nearby GPS stations (Kaidzu et al., 2000). However, the GPS time series also reflect the continuing deformation due to the dike intrusions and deflation of the magma chamber beneath Miyakejima (Ito and Yoshioka, 2002).

Ito and Yoshioka (2002) used Monte Carlo inversions to determine the geometry, location, and volume change of the dike and magma chamber for ten time periods from June 15 to August 27, 2000. Toda et al. (2002) also proposed a model for the dike and magma chamber in their paper. Using these models, it is possible to invert the GPS data for the slip mechanism of EVT3 and EVT15.

Chapter 5

METHODOLOGY OF GEODETIC INVERSIONS

Data from ten GPS stations operated by the Geographical Survey Institute of Japan (GSI) were used to invert for the slip and rupture geometry of both EVT3 and EVT15 (Figure 175). Displacements due to each event were determined by differencing the daily coordinates from the day before and after each earthquake. These displacements were modeled relative to the position of station 93086, the GSI station located on the Izu Peninsula. Data from station 960599 were not available for EVT15.

The nonlinear inversion methods of Burgmann et al. (1997) were used to determine the slip and rupture geometry of each earthquake as well as the deformation due to the dike intrusion and magma chamber deflation. The locations of aftershocks in the F-net catalog for the 24 hours following each earthquake were used to identify which of the two nodal planes of the focal mechanism is the fault plane along which slip occurred, which helps to constrain the geometry of the fault. However, for each earthquake, the data were inverted for both nodal planes to confirm that the fault plane indicated by the aftershock locations does fit the data best. The strike and dip of the fault plane are constrained to be within 15° of the values determined from the moment tensor inversions, and the fault itself is required to be located within 5 km of the JMA hypocenter. The depth of the top of the fault is allowed to vary from the surface to a depth of 16 km, which is the same range of depths tested in the moment tensor inversions. To constrain the dimensions of the rupture, the empirical scaling relationships between magnitude and rupture length and width reported in Wells and Coppersmith (1994) were used. Since these are only approximate relationships, the widest range of possible rupture dimensions was allowed for by setting the bounds on the minimum rupture length and width to those given in the Wells and Coppersmith (1994) study, minus the standard error they reported, and rounded down to the nearest one-half-kilometer. Likewise, the maximum dimensions are those from the study, plus the standard error, and rounded up to the nearest half-kilometer.

The magma chamber is modeled as a horizontal volume source with no slip, and length and width from 1 km to 5 km, and the bounds on the dike geometry are the maximum and minimum values determined by the Ito and Yoshioka (2002) paper. However, the depth of the top of the dike in that study was very shallow, and significantly less than the depth of 8 km in the dike model of Toda et al. (2002). Because of this, the maximum dike depth tested was chosen to be 8 km.

In addition to the earthquake, the dike and magma chamber also contribute to the displacements recorded in the GPS time series. Inversions without one or both of these other deformation sources were performed. But they are not discussed since the dike and magma chamber are known to have caused substantial deformation, and it is not realistic to use a deformation model that does not include them.

Chapter 6

RESULTS OF GEODETIC INVERSIONS

MODEL FOR EVT15

Separate inversions along each nodal plane show that the data are fit significantly better when the north-south trending plane is chosen, which is consistent with the aftershock locations. Two models were used to invert for the slip on the fault. In Model 1, the fault is allowed to slip with both strike-slip and dip-slip motion (Figure 176), and there are two additional deformation sources: the offshore dike and the magma chamber beneath Miyakejima. Although the inversion was allowed to choose either type of motion, it converged to a solution that was mostly strike-slip, which independently confirms the focal mechanism determined from the moment tensor inversions (Tables 8 and 9). The data fit very well with a small weighted residual sum of squares (WRSS) (Table 8). For Model 2 (Figure 177, Table 10)), the fault is allowed to open as well as to slip. Even though this model has an additional parameter, the data actually fit slightly worse, showing that there was no volume change associated with this earthquake. This is also consistent with the results of the moment tensor inversions.

MODEL FOR EVT3

For EVT3, three different slip models were tested. In Model 1 (Figure 178, Table 11), simple strike-slip and dip-slip motion occurs along a fault defined by the nodal planes of the focal mechanism, and there is deformation due to the dike and the magma chamber. Model 2 (Figure 179, Table 12) is the same as the first model, but the fault is allowed to open as well as to slip. In Model 3 (Figure 180, Table 13), no slip is allowed to result from the earthquake, but the fault is allowed to open. For this model the geometry of the fault is derived from the orientation of the CLVD component of the focal mechanism rather than the orientation of the nodal planes. As can be seen from Table 8, the WRSS values for all of these models are significantly higher than those for EVT15. The model with both slip and opening does fit better than the model with only slip along the fault. But most importantly, the CLVD-based model with only opening fits better than either model with slip.

It should be noted that for the two models that allow for opening on the fault, the predicted volume change for the dike is negative. No other studies have reported dike deflation. However, studies such as Ito and Yoshioka (2002) are modeling deformation over longer periods of time than are considered in this study.

Since EVT3 is located near the dike intrusion, and both the moment tensor inversions and the geodetic inversions align the strike of the fault with the dike, it is important to consider how

much of the proposed opening along the fault might be opening along the dike which the inversion is falsely attributing to the earthquake fault. To investigate this possibility, the geometry inversion for the EVT3 was repeated with only the magma chamber and the dike as possible sources of deformation (Figure 181, Table 14). This model cannot fit the observed data, which confirms the significance of opening along the earthquake fault.

Chapter 7

DISCUSSION OF FAULTING MECHANISMS

Some of the earthquakes in this study have double-couple mechanisms, but most have large CLVD components and might have isotropic components as well. There is always concern that large non-double-couple components may result from an error in the inversion method and are not truly a part of the source process. However, the non-double-couple mechanisms in this study fit the data very well, and the solutions are extremely stable. Furthermore, in the case of EVT3, the addition of a CLVD component to the inversion greatly decreases the variance, and the increase in fit is definitely statistically significant. These earthquakes occurred during a period of volcanic unrest, and CLVD mechanisms are commonly observed in volcanic and geothermal areas. Therefore, there is no reason to suspect that the CLVD components are nonphysical.

Since all of the events in the study are shallow, another possible source of error is free surface effects. There is zero traction at a free surface, so the M_{xz} and M_{yz} terms of the Green's functions go to zero. This, in turn, allows the corresponding terms of the moment tensor to become large. However, most of the CLVD components in this study have horizontal major dipoles, which implies that the M_{xz} and M_{yz} elements of the moment tensor are small (D. Dreger, written communication, 2003). The only mechanism with large values of M_{xz} and M_{yz} is the vertical dip-slip mechanism from the higher frequency moment tensor inversion for EVT7. But the preferred depth from this inversion is 12 km, so free surface effects may not be an issue.

COMPLEX FAULTING

The CLVD component of moment tensor can be decomposed into two double-couple moment tensors. Therefore, CLVD components of earthquakes can be generated by double-couple slip on two suitably oriented fault planes. Most of the earthquakes in this study have the type of CLVD mechanism which can be made by the combination of normal faulting and strike-slip faulting (Frohlich, 1994), the two types of mechanisms identified by Fukuyama et al. (2001) in their study of earthquakes related to the eruption in 2000. Strike-slip and normal faulting is also consistent with the findings of Toda et al. (2002) that supported the Hill mesh hypothesis, in which extension from the opening dike is partially accommodated by conjugate strike-slip faults.

But this is not the best explanation for the observed faulting. Some of the earthquakes which Toda et al. (2002) identified as having strike-slip mechanisms were found in this study to have CLVD mechanisms. There is no clear spatial pattern of CLVD mechanisms and strike-slip mechanisms. Furthermore, a CLVD mechanism generated by a combination of normal faulting

and strike-slip faulting might be expected to be oriented at an angle to the direction of opening (Frohlich, 1994). However, the CLVD components are so well aligned with the strike of the dike (Ito and Yoshioka, 2002, Toda et al., 2002) and the observed seismicity that they may be more consistent with tensile faulting due to opening along the dike. Tensile faulting is also supported by the geodetic data.

While CLVD components could be the result of two double-couples, isotropic components cannot be formed from double-couples (Julian et al., 1998). It is unfortunate that the isotropic components are not necessarily statistically significant. If they were, complex shear faulting as the source of the CLVD mechanisms could definitely be eliminated.

CLVD components can also result from faulting along a complex surface. Here, the CLVD mechanisms are consistent with tensile faulting related to the dike intrusion, and there is no evidence for complex fault surfaces. But this explanation cannot be ruled out.

TENSILE FAULTING

The orientation of all of the CLVD mechanisms except for EVT7 is consistent with the opening of a vertical crack. Such extensional CLVD mechanisms have repeatedly been observed in volcanic areas and have been theorized to be the result of fluid injection (for example, Kanamori et al., 1993, Julian and Sipkin, 1985). The main requirement for tensile faulting due to high pore pressures is that the depth of the event cannot be more than a few kilometers, or else the lithostatic pressure will exceed the hydrostatic pressure (Frohlich, 1994). Most of the CLVD events occur at depths of 2 to 4 km, which is consistent with this requirement.

The double-couple events located nearby to the CLVD events in no way argue against a tensile faulting regime. The strike-slip faults could be helping to accommodate stress from the opening of the dike, as suggested by Toda et al. (2002). However, an important case study may be the 1997 earthquake swarm in a geothermal area of northwest Bohemia. Both non-double-couple events with mechanisms indicative of tensile faulting and double-couple events were found within a volume of 700 x 700 x 1000 m at a depth of 8.5 to 9.5 km (Horalek et al. 2002). Vavrycuk (2002) examined the double-couple percentage of these events as a function of the orientation of faulting relative to the stress field. The results show that the double-couple earthquakes occurred on faults with high values of shear traction, while the non-double-couple events were located on faults that were not optimally aligned with the stress field. This misalignment, combined with the effects of high pore pressure, allowed tensile faulting to occur.

Chapter 8

CONCLUSIONS

Moment tensor inversions for deviatoric, full moment tensor, and ISO+DC mechanisms in two frequency passbands were performed for eighteen earthquakes related to the eruption on Miyakejima, Japan in 2000. The majority of these events have large CLVD components which are consistent with the opening of a vertical crack. The orientation of these mechanisms relative to the dike intrusion and the observed seismicity indicate that these mechanisms might reflect tensile faulting related to inflation along the dike. These observations are confirmed by inversions of GPS data.

All of the mechanisms except for the higher frequency passband inversion of EVT7 are very stable. In some ways, the extreme stability of the orientation of the T-axes is supportive of the conclusion that the physical process at work is tensile faulting. For a positive horizontal CLVD, the major dipole of the CLVD is the T-axis, and thus it is expected to be a robust feature of the inversion.

EVT7 is an unusual event with a vertical CLVD mechanism which is best modeled by an ISO+DC in the lower frequency passband inversion, but it has a vertical dip-slip mechanism when higher frequencies are used. The vertical dip-slip mechanism is not stable, and there is a difference of 4 km in the preferred depths from these inversions. The moment tensor inversions for this event simply may not be reliable.

Although most of these events are non-double-couple, they do not necessarily have statistically significant isotropic components. The F-test suggested by Menke (1984) indicates that only the isotropic component for the long period inversion of EVT7 is significant, although it may not be physical for other reasons, while the method of Helsel and Hirsch (1992) indicates that most of the isotropic components are significant. It is probably best to rely on the statistics from Menke (1984) and conclude that isotropic components are not necessary to explain the observed data when CLVD mechanisms fit so well.

Inversions of GPS data for the two largest events, EVT15 and EVT3, find slip mechanisms that support the linear moment tensor inversions. EVT15 appears to be a simple vertical strike-slip earthquake without any volume change while EVT3 is best modeled as an opening fault with an orientation determined by the CLVD component of the focal mechanism. The latter finding is significant because the model which fit best had only opening and no slip on the fault, which means that it had the fewest number of model parameters, and suggests that there is a net volume change associated with this event.

While most of the events studied have CLVD mechanisms, several have double-couple mechanisms. These earthquakes could occur on conjugate faults which act to relieve the stress from the dike intrusion (Toda et al., 2002), or they could occur on faults with higher values of shear traction than the fault where the CLVD events are located (Vavrycuk, 2002). To discriminate between these two theories, a more thorough study of earthquake locations and faulting parameters would have to be conducted.

BIBLIOGRAPHY

Burgmann, R., P. Segall, M. Lisowski, and J. Svarc, Postseismic strain following the 1989 Loma Prieta earthquake from GPS and leveling measurements, *J. Geophys. Res., 102*(3B), .4933-4955, 1997.

Dreger, D. S., and D. V. Helmberger, Determination of source parameters at regional distances with three-component sparse network data, *J. Geophys. Res., 98*(B5), 8107-8125, 1993.

Dreger, D., and B. Woods, Regional distance seismic moment tensors of nuclear explosions, *Tectonophysics, 356*, 139.156, 2002.

Dreger, D. S., H. Tkalcic, and M. Johnston, Dilational processes accompanying earthquakes in the Long Valley Caldera, *Science, 288*, 122-125, 2000.

Frohlich, C., Earthquakes with non-double-couple mechanisms, *Science, 264*, 804-809, 1994.

Fukuyama, E., and D. S. Dreger, Performance test of an automated moment tensor determination system for the future "Tokai" earthquake, *Earth Planets Space, 52*, 383-392, 2000.

Fukuyama, E., A. Kubo, H. Kawai, and K. Nonomura, Seismic remote monitoring of stress field, *Earth Planets Space, 53*(10), 1021-1026, 2001.

Hashimoto, M., and T. Tada, Crustal deformations associated with the 1986 fissure eruption of the Izu-Oshima volcano, Japan, and their tectonic significance, *Phys. Earth Plan. Inter., 60*, 324-338, 1990.

Helsel, D. R., and R. M. Hirsch, *Statistical Methods in Water Resources, Studies in Environmental Science, 49*, pp. 296-299, Elsevier Science Publishers, Amsterdam, 1992.

Horalek, J., J. Sileny, and T. Fischer, Moment tensors of the January 1997 earthquake swarm in NW Bohemia (Czech Republic): double-couple vs. non-double-couple events, *Tectonophysics, 356*, 65-85, 2002.

Ito, T., and S, Yoshioka, A dike intrusion model in and around Miyakejima, Niijima and Kozushima in 2000, *Tectonophysics*, *359*, 171-187, 2002.

Japan Meteorological Agency, Recent seismic activity in the Miyakejima and Niijima-Kozushima region, Japan – the largest earthquake swarm ever recorded, *Earth Planets Space, 52*(8), i-vii, 2000.

Julian, B. R., and S. A. Sipkin, Earthquake processes in the Long Valley Caldera area, California, *J. Geophys. Res., 90*(B13), 11,155-11,169, 1985.

Julian, B. R., A. D. Miller, and G. R. Foulger, Non-double-couple earthquakes, 1: Theory, *Rev. Geophys., 36*(4), 525-549, 1998.

Kanamori, H., G. Ekstrom, A. Dziewonski, J. S. Barker, and S. A. Sipkin, Seismic radiation by magma injection: An anomalous seismic event near Tori Shima, Japan, *J. Geophys. Res., 98*(B4), 6511-6522, 1993.

Lay, T, and T. C. Wallace, The Seismic Moment Tensor, in *Modern Global Seismology, International Geophysics Series, 58*, edited by R. Dmowska and J. R. Holton, pp. 344-346, Academic Press, San Diego, 1995.

Menke, W., *Geophysical Data Analysis: Discrete Inverse Theory,* pp. 96-97, Academic Press, San Diego, 1984.

Nakamura, K., Tectonic in the Izu Peninsula and plate bending, *Mon. Earth, 2*, 94-102, 1980 (in Japanese).

Panning, M., D. Dreger, and H. Tkalcic, Near-source velocity structure and isotropic moment tensors: a case study of the Long Valley Caldera, *Geophys. Res. Lett., 28*(9), 1815-1818, 2001.

Saikia, C. K., Modified frequency-wavenumber algorithm for regional seismograms using Filon's quadrature: model Lg waves in eastern North America, *Geophys. J. Int.*, *118*, 142-158, 1994.

Seno, T., S. Stein, and A. Gripp, A model for the motion of the Philippine Sea plate consistent with NUVEL-1 and geological data, *J. Geophys. Res., 98*(B10), 17,941-17,948, 1993.

Toda, S., R. Stein, and T. Sagiya, Evidence from the AD 2000 Izu islands earthquake swarm that stressing rate governs seismicity, *Nature, 419*, 58-61, 2002.

Ukawa, M., E. Fujita, E. Yamamoto, Y. Okada, and M. Kikuchi, The 2000 Miyakejima eruption: Crustal deformation and earthquakes observed by the NIED Miyakejima observation network, *Earth Planets Space, 52*(8), xix-xxvi, 2000.

Vavrycuk, V., Non-double-couple earthquakes of 1997 January in West Bohemia, Czech Republic: evidence of tensile faulting, *Geophys. J. Int.*, *149*, 364-373, 2002.

Wells, D. L., and K. J. Coppersmith, New empirical relationships among magnitude, rupture length, rupture width, rupture area, and surface displacement, *Bull. Seismol. Soc. Am.*, 84, 974-1002, 1994.

TABLES

Table 1. JMA earthquake information for the events in this study.

Event ID	Date	Origin Time (UT)	Latitude	Longitude	Depth (km)	Magnitude (M_W)
EVT1	6/29/2000	03:11:52.50	34.23367	139.16500	11.94	5.2
EVT2	6/29/2000	06:30:23:20	34.12983	139.36383	19.04	5.6
EVT3	7/1/2000	07:01:56.30	34.18717	139.19700	16.07	6.4
EVT4	7/2/2000	20:03:36.60	34.17200	139.34683	16.16	5.4
EVT5	7/6/2000	18:59:37.50	34.20600	139.23383	17.31	4.9
EVT6	7/7/2000	02:45:28.20	34.20717	139.24517	16.57	5.0
EVT7	7/8/2000	09:41:46.40	34.12983	139.60500	5.00	5.1
EVT8	7/8/2000	18:57:44.90	34.20883	139.23367	15.39	6.1
EVT9	7/14/2000	18:28:24.20	34.16450	139.33100	14.66	5.2
EVT10	7/15/2000	01:30:32.00	34.42050	139.24533	9.56	6.3
EVT11	7/20/2000	03:10:26.20	34.19867	139.25117	15.35	5.1
EVT12	7/23/2000	21:52:45.80	34.18583	139.22817	11.67	5.5
EVT13	7/27/2000	01:49:53.30	34.18750	139.29550	12.73	5.6
EVT14	7/30/2000	00:18:02.20	34.02733	139.40533	11.17	5.8
EVT15	7/30/2000	12:25:46.60	33.96800	139.41433	17.10	6.5
EVT16	7/30/2000	12:48:57.10	34.01750	139.40733	16.81	5.7
EVT17	8/2/2000	21:42:27.60	34.21867	139.28883	15.47	5.1
EVT18	8/18/2000	01:52:22.60	34.19900	139.24433	12.38	6.0

Table 2. Velocity model used to calculate Green's functions.

Thickness (km)	P-wave velocity (km/s)	S-wave velocity (km/s)	Density (kg/m^3)	Q_α	Q_β
3.0	5.50	3.14	2300	600	300
15.0	6.00	3.55	2400	600	300
15.0	6.70	3.83	2800	600	300
67.0	7.80	4.46	3200	600	300
—	8.00	4.57	3300	600	300

Table 3. F-net focal mechanisms for events in this study.

Event ID	Strike	Dip	Rake	Mo (Nm)	Depth	Mw	VR	% DC	% CLVD
EVT1	13 ; 152	56 ; 42	-64 ; -123	7.27e+16	5 km	5.2	70.82	99	1
EVT2	6 ; 97	85 ; 78	-12 ; -175	2.38e+17	14 km	5.6	88.96	66	34
EVT3	352 ; 100	75 ; 41	-52 ; -156	2.28e+18	5 km	6.2	90.67	88	12
EVT4	336 ; 91	62 ; 52	-44 ; -143	3.30e+17	5 km	5.6	88.20	50	50
EVT5	342 ; 75	82 ; 69	-21 ; -171	2.72e+16	5 km	4.9	94.23	39	61
EVT6	165 ; 264	76 ; 58	-33 ; -163	8.55e+16	5 km	5.3	90.71	34	66
EVT7	255 ; 58	78 ; 13	-86 ; -107	7.63e+16	23 km	5.2	73.70	95	5
EVT8	346 ; 95	70 ; 48	-45 ; -152	7.79e+17	5 km	5.9	93.69	97	3
EVT9	151 ; 285	59 ; 41	-62 ; -127	1.68e+17	5 km	5.5	90.50	97	3
EVT10	107 ; 16	82 ; 78	-167 ; -8	1.24e+18	8 km	6.0	92.76	68	32
EVT11	344 ; 80	80 ; 56	-34 ; -168	6.00e+16	5 km	5.2	95.62	57	43
EVT12	316 ; 159	46 ; 46	-106 ; -73	3.31e+17	5 km	5.6	84.02	85	15
EVT13	170 ; 272	68 ; 63	-30 ; -156	2.18e+17	5 km	5.5	87.61	30	70
EVT14	351 ; 89	79 ; 54	-36 ; -167	4.28e+17	5 km	5.7	91.00	56	44
EVT15	11 ; 103	85 ; 77	-13 ; -174	5.02e+18	11 km	6.4	90.42	95	5
EVT16	352 ; 86	82 ; 64	-26 ; -171	3.07e+17	5 km	5.6	93.19	69	31
EVT17	170 ; 283	60 ; 57	-40 ; -143	6.00e+16	5 km	5.2	82.48	39	61
EVT18	181 ; 90	87 ; 74	16 ; 177	4.65e+17	17 km	5.7	82.77	72	28

Table 4. Results of moment tensor inversions in 0.01 to 0.033 Hz passband.

Table 5. Results of moment tensor inversions in 0.02 to 0.05 Hz passband.
(deviatoric inversion/full moment tensor inversion)

Event ID	Number of stations	Depth (km)	Mw	DC (%)	CLVD (%)	ISO (%)	VR
EVT1	9	2	5.2/5.4	64/30	36/29	0/41	64.1/66.5
EVT2	9	4	5.5/5.6	23/40	77/27	0/32	84.4/85.6
EVT3	9	4	6.1/6.2	25/38	75/37	0/25	86.9/87.5
EVT4	9	4	5.6/5.6	36/32	64/45	0/22	88.4/88.4
EVT5	9	6	4.9/4.9	47/27	53/55	0/18	82.6/83.0
EVT6	9	4	5.2/5.2	33/5	67/71	0/24	85.1/86.0
EVT7	9	12	5.1/5.1	90/90	10/10	0/0	59.2/59.2
EVT8	9	4	5.8/5.9	20/41	80/29	0/30	87.7/55.6
EVT9	9	4	5.4/5.4	55/58	45/29	0/12	88.4/88.5
EVT10	9	4	6.0/6.1	45/36	55/32	0/32	88.9/90.1
EVT11	8	2	5.1/5.2	45/34	55/34	0/32	90.0/90.3
EVT12	8	4	5.7/5.7	90/67	10/18	0/16	80.7/81.2
EVT13	9	2	5.6/5.6	69/62	31/15	0/23	87.4/87.6
EVT14	9	2	5.7/5.8	21/52	79/9	0/39	86.4/87.2
EVT15	8	10	6.4/6.4	95/56	5/30	0/13	85.2/86.0
EVT16	9	4	5.6/5.6	24/18	76/47	0/35	86.0/87.0
EVT17	9	2	5.2/5.2	100/76	0/2	0/22	85.6/85.7
EVT18	9	2	5.8/5.8	99/69	1/7	0/24	85.4/85.5

Table 6. Statistical significance of CLVD components.
Error sum of square (SSE) values are normalized by the number of stations used in the inversion (Tables 4 and 5). F-test values are calculated using two methods, and the values for each method are given along with the percent confidence to which each is significant.

Event	Double-couple SSE	Deviatoric SSE	F (after Menke)	Significance (%)	F (after Helsel and Hirsch)	Significance (%)
EVT3	1.236E-03	2.84E-06	431.089	≈100	4.387E+04	≈100

Table 7. F-test results.

Error sum of square values (SSE) are normalized by the number of stations used in the inversion (Tables 4 and 5). F-test values are calculated using two methods, and the values for each method are given along with the percent confidence to which each is significant.

Event	Deviatoric SSE	Full SSE	ISO+DC SSE	F (after Menke)	Significance (%)	F (after Helsel and Hirsch)	Significance (%)
0.01 to 0.033 Hz passband							
EVT1	2.84E-06	2.48E-06	3.42E-05	1.136466	73.859	14.78304	99.979
EVT2	1.32E-05	1.09E-05	1.23E-04	1.201049	81.987	21.30592	99.999
EVT3	1.05E-03	8.86E-04	9.73E-03	1.173197	78.751	18.49292	99.996
EVT4	2.14E-05	2.01E-05	2.62E-04	1.050247	59.668	6.074945	98.458
EVT5	2.37E-07	1.95E-07	8.73E-07	1.200993	81.981	21.30027	99.999
EVT6	2.53E-06	2.49E-06	4.70E-06	1.006177	51.215	1.623924	79.45
EVT7[a]	1.94E-05	4.02E-06	7.48E-06	1.842274	99.878	86.93035	≈100
EVT8	1.07E-04	8.41E-05	8.08E-04	1.258024	87.408	27.06038	≈100
EVT9	4.40E-06	4.31E-06	5.92E-06	1.008824	51.739	1.891249	82.787
EVT10	7.33E-04	6.87E-04	8.04E-04	1.056329	60.782	6.689188	98.886
EVT11	6.99E-07	5.66E-07	4.01E-06	1.22104	82.519	20.67252	99.998
EVT12	2.06E-05	1.95E-05	1.47E-04	1.047433	58.587	5.221537	97.529
EVT13	1.42E-05	1.38E-05	8.70E-05	1.024483	54.800	3.472752	93.468
EVT14	2.95E-05	2.59E-05	2.93E-04	1.127941	72.621	13.92204	99.968
EVT15	3.12E-03	3.09E-03	3.35E-03	0.998105	49.629	0.831327	63.562
EVT16	1.82E-05	1.57E-05	2.18E-04	1.148164	75.495	15.96461	99.988
EVT17	1.38E-06	1.35E-06	5.61E-06	1.015582	53.068	2.573776	88.820
EVT18	6.04E-05	5.75E-05	3.17E-04	1.03958	57.681	4.997595	97.239
0.02 to 0.05 Hz passband							
EVT1	2.76E-05	2.56E-05	2.09E-04	1.070655	66.399	11.95156	99.929
EVT2	9.29E-05	8.46E-05	3.09E-04	1.090981	70.541	15.10213	99.985
EVT3	4.42E-03	4.20E-03	1.86E-02	1.044349	60.606	7.874149	99.434
EVT4	1.27E-04	1.17E-04	3.85E-04	1.074652	67.238	12.57105	99.948
EVT5	1.57E-06	1.51E-06	2.43E-06	1.031533	57.631	5.887578	98.36
EVT6	1.33E-05	1.24E-05	3.39E-05	1.059452	63.988	10.21501	99.831
EVT7	1.62E-05	1.62E-05	1.62E-05	0.993577	48.398	0.004424	5.294
EVT8	5.77E-04	5.27E-04	2.59E-03	1.087956	69.944	14.63325	99.981
EVT9	2.20E-05	2.16E-05	1.44E-04	1.01096	52.689	2.698795	89.754
EVT10	2.49E-03	2.21E-03	9.99E-03	1.120273	75.937	19.6423	99.998
EVT11	4.24E-06	4.07E-06	4.18E-05	1.034311	57.789	5.700641	98.167
EVT12	1.42E-04	1.39E-04	3.10E-04	1.017955	54.124	3.459794	93.496
EVT13	7.19E-05	7.06E-05	2.35E-04	1.011708	52.872	2.814807	90.457
EVT14	2.11E-04	1.97E-04	1.99E-03	1.061331	64.398	10.50629	99.854
EVT15	2.46E-02	2.37E-02	2.52E-02	1.032345	57.354	5.431305	97.875
EVT16	1.52E-04	1.39E-04	4.82E-04	1.083591	69.071	13.95659	99.974
EVT17	6.87E-06	6.78E-06	6.92E-06	1.006793	51.668	2.052906	84.606
EVT18	3.78E-04	3.72E-04	8.43E-04	1.010981	52.694	2.702086	89.774

[a] The F-test values for EVT7 in the 0.01 to 0.033 Hz passband are comparing the full moment tensor inversion to the ISO+DC inversion since the latter inversion had a smaller SSE than the deviatoric inversion. Comparing the full moment tensor to the deviatoric inversion F=4.781084 for Menke's equation and F=382.8895 for the Helsel and Hirsch method. Both F-test values are statistically significant with ≈100% confidence.

Table 8. WRSS values and estimated slip from geodetic inversions.

Model	WRSS	Earthquake Fault (m)			Magma Chamber	Dike
		Strike-slip	Dip-slip	Opening	Opening (m)	Opening (m)
EVT15 Model 1	2.18226	-2.2935	0.7422	—	-3.0073	0.3857
EVT15 Model 2	2.24932	-2.8680	-1.1778	-0.1392	-2.3630	0.2126
EVT3 Model 1	91.7422	-0.3233	-0.3437	—	-1.6963	0.6869
EVT3 Model 2	76.9254	-0.3916	-0.3543	0.1723	-1.6606	-0.2335
EVT3 Model 3	68.7184	—	—	0.3251	-1.6910	-1.7128
EVT3 Model 4	695.76					

Table 9. Fault geometry determined by geodetic inversions for EVT15 Model 1.

	Length (km)	Width (km)	Depth (km)	Dip (degrees)	Strike (degrees)	Volume Change (km^3)
Fault	12.5	8.1401	0.01	63	16.4227	—
Magma Chamber	4.9425	4.8458	0.53749	3	340.8435	-0.072
Dike	18	5.0533	2.5343	88.7367	129.5	0.0351

Table 10. Fault geometry determined by geodetic inversions for EVT15 Model 2.

	Length (km)	Width (km)	Depth (km)	Dip (degrees)	Strike (degrees)	Volume Change (km^3)
Fault	14.4044	6.0184	1.4511	81.8697	14.7418	-0.0121
Magma Chamber	4.6164	5	0	2.3539	340.1717	-0.0545
Dike	15.2801	15	2.3325	81.7	309.5	0.0487

Table 11. Fault geometry determined by geodetic inversions for EVT3 Model 1.

	Length (km)	Width (km)	Depth (km)	Dip (degrees)	Strike (degrees)	Volume Change (km^3)
Fault	15.0836	5.7191	0.010326	89.9557	187.2374	—
Magma Chamber	5	1	2.0001	3	337.5242	-0.0085
Dike	15	5	3.9827	83.6	124.1	0.0515

Table 12. Fault geometry determined by geodetic inversions for EVT3 Model 2.

	Length (km)	Width (km)	Depth (km)	Dip (degrees)	Strike (degrees)	Volume Change (km^3)
Fault	15.5588	5.0002	0.010119	89.9984	180.9472	0.0134
Magma Chamber	5	1	1.8734	3	341.9287	-0.0083
Dike	18	5	0.01	83.6	129.5	-0.021

Table 13. Fault geometry determined by geodetic inversions for EVT3 Model 3.

	Length (km)	Width (km)	Depth (km)	Dip (degrees)	Strike (degrees)	Volume Change (km^3)
Fault	25	15	0.52915	89.37	131.0913	0.1219
Magma Chamber	5	1	1.8053	3	337.4732	-0.0085
Dike	16.4497	5	4.1879	84.1645	124.1	-0.1409

Table 14. Fault geometry determined by geodetic inversions for EVT3 Model 4.

	Length (km)	Width (km)	Depth (km)	Dip (degrees)	Strike (degrees)	Volume Change (km^3)
Magma Chamber	2.5163	1	0	3	345	3.9327
Dike	15	15	8	83.6	129.5	-2.0204

FIGURES

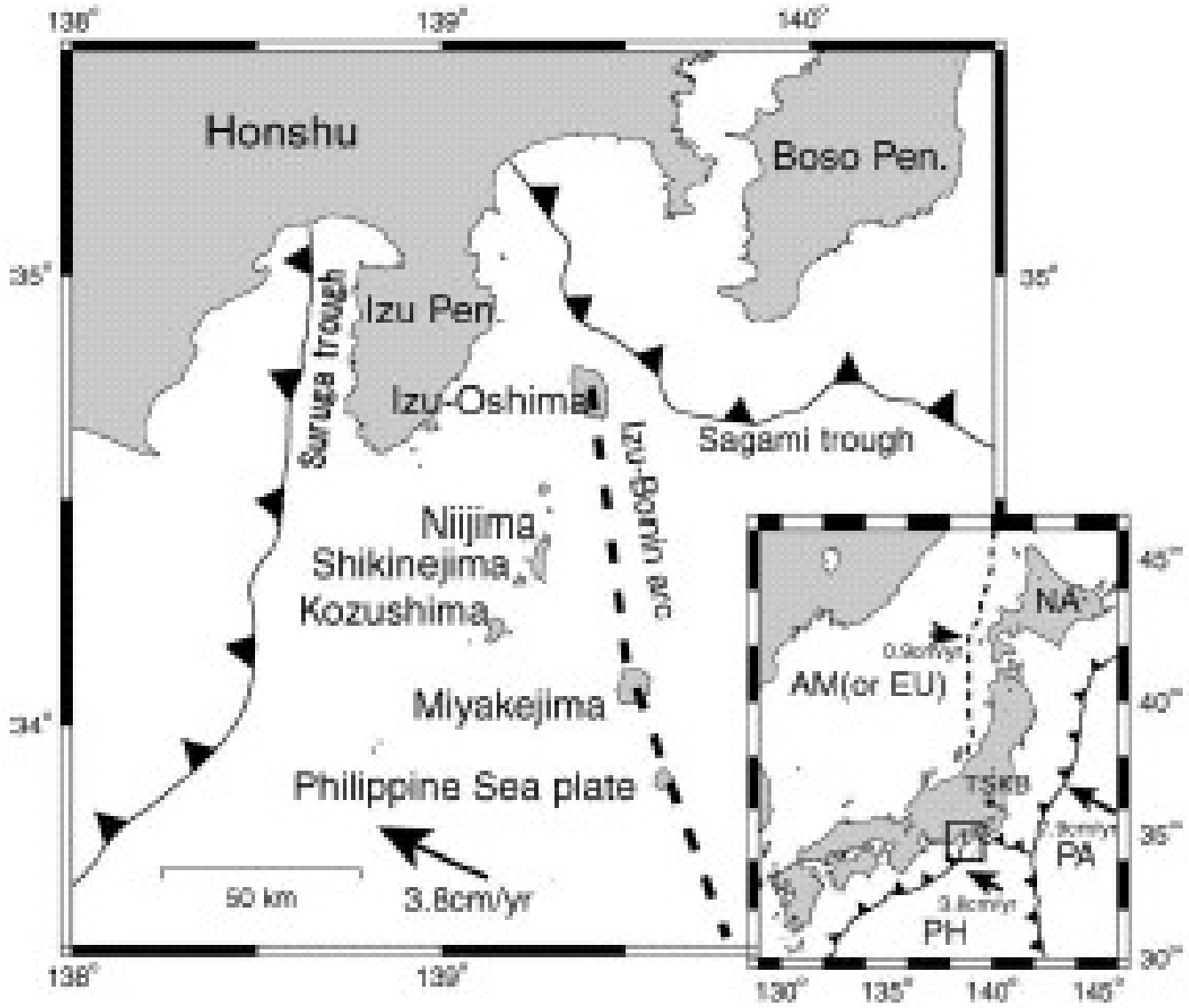

Figure from Ito and Yoshioka (2002).

Figure 1

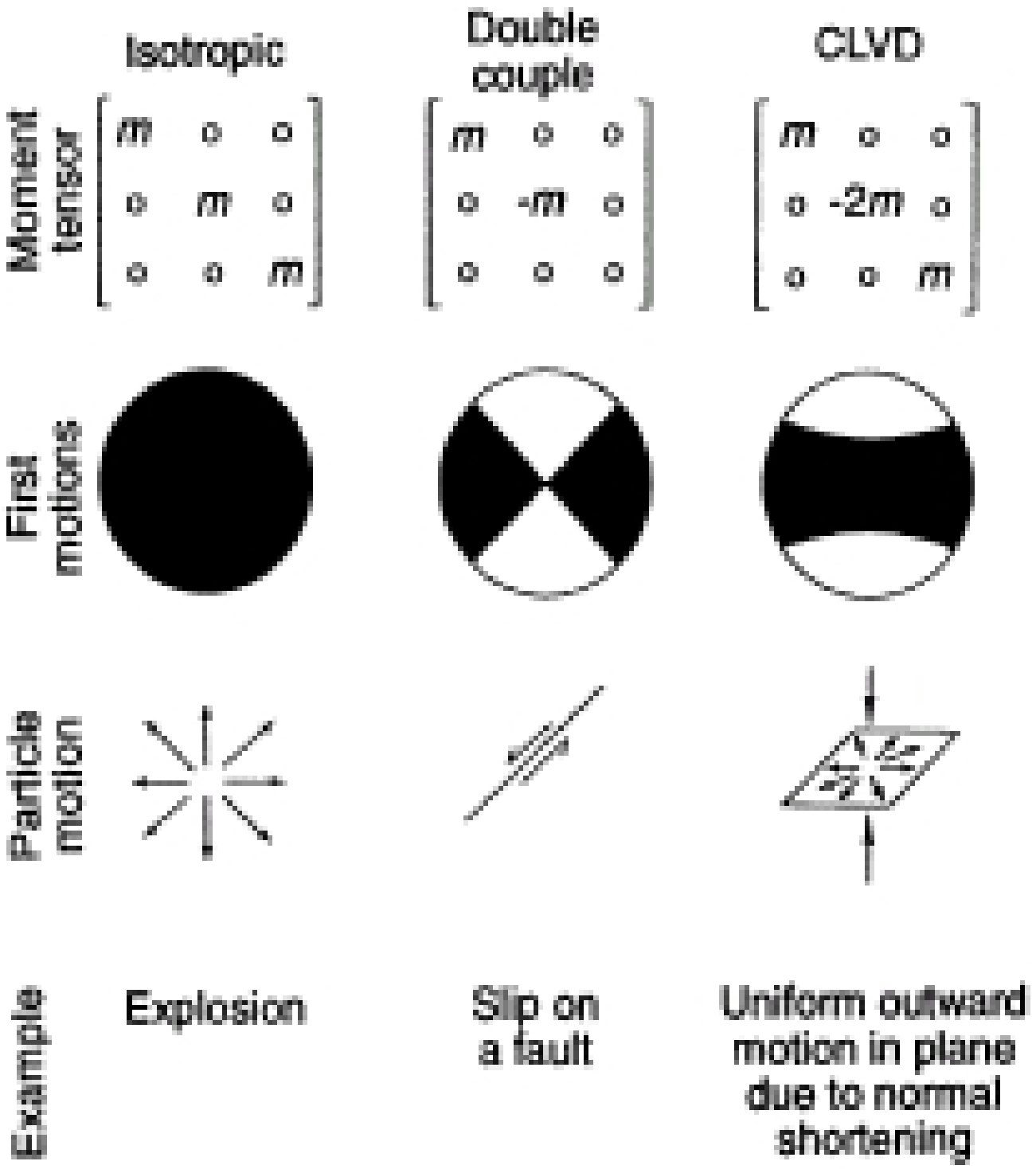

Figure from Frohlich (1994).

Figure 2

Map showing locations of events studied and F-net stations. Event depths are based on the results of deviatoric moment tensor inversions with data bandpass filtered between 0.01 and 0.033 Hz.

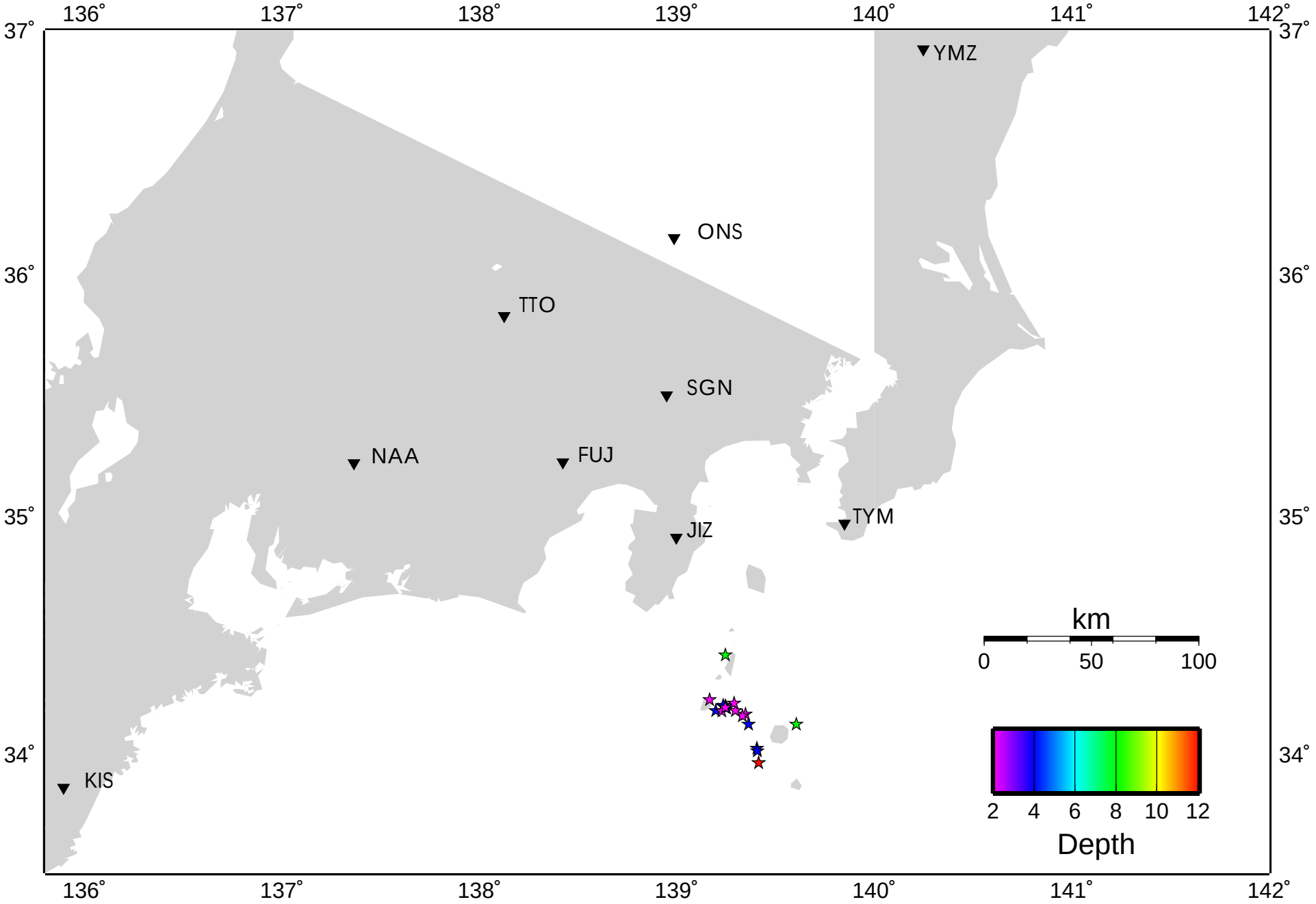

Figure 3

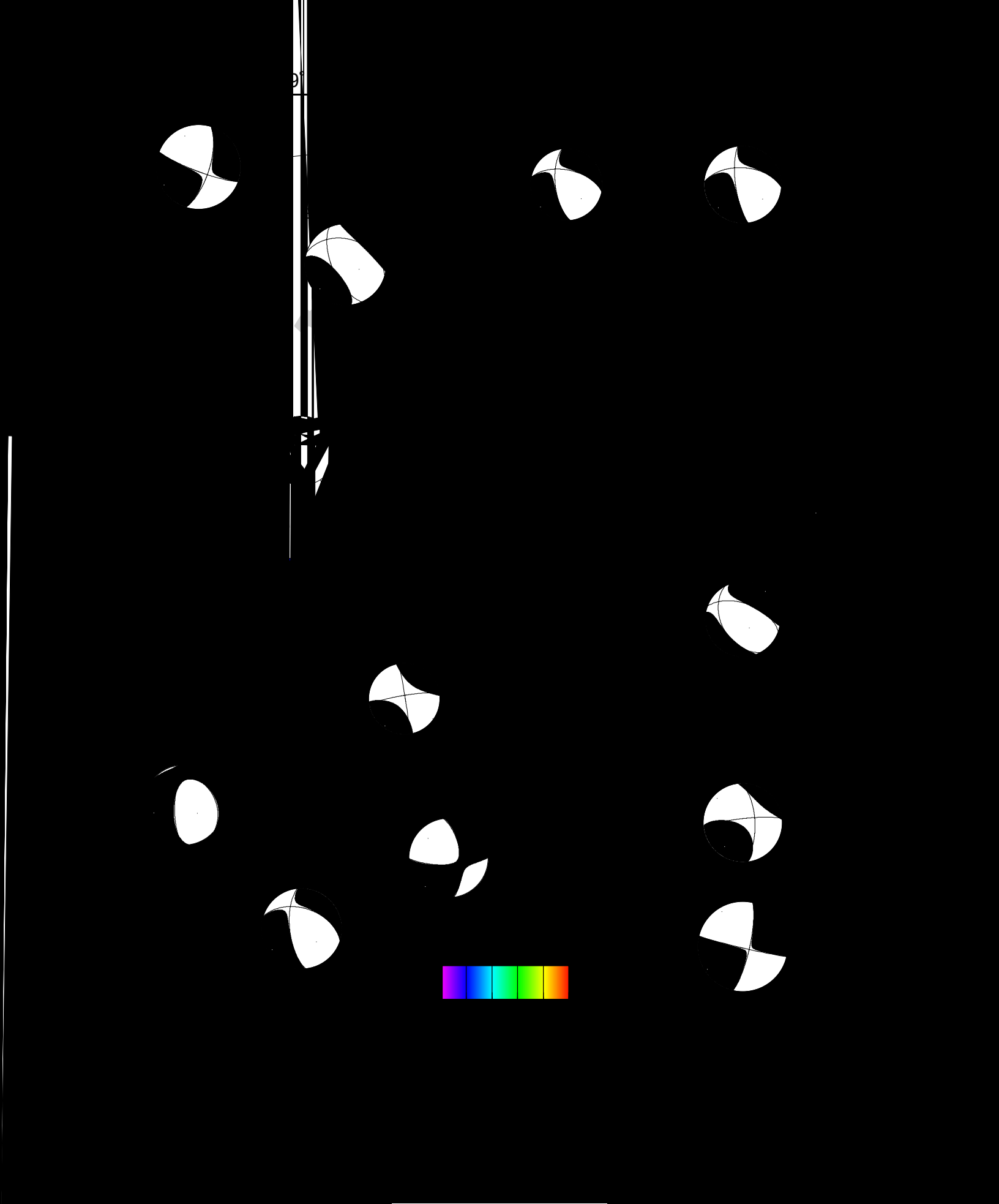

Figure 4

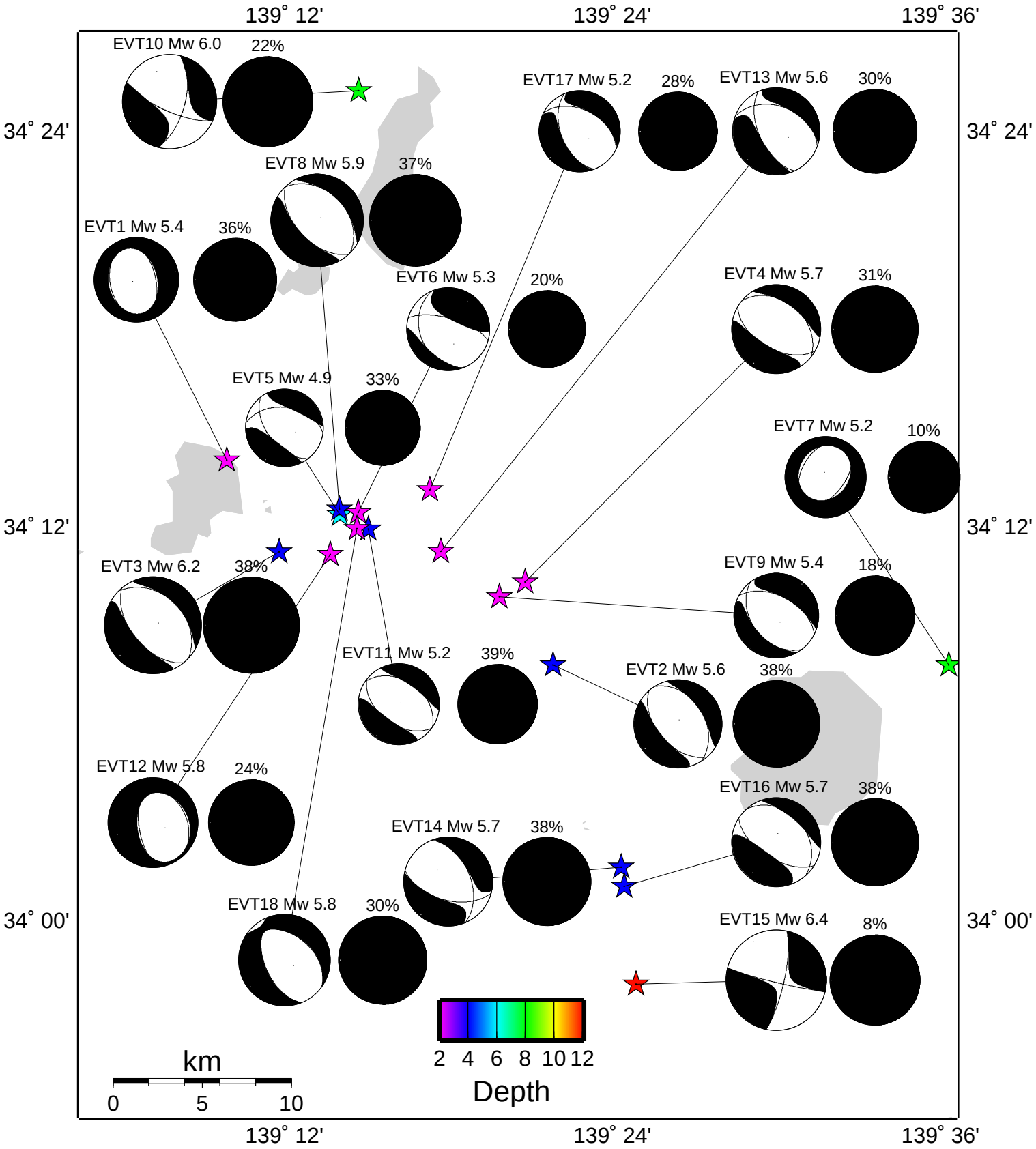

Full moment tensor mechanisms (data are bandpass filtered between 0.01 and 0.033 Hz)

Figure 5

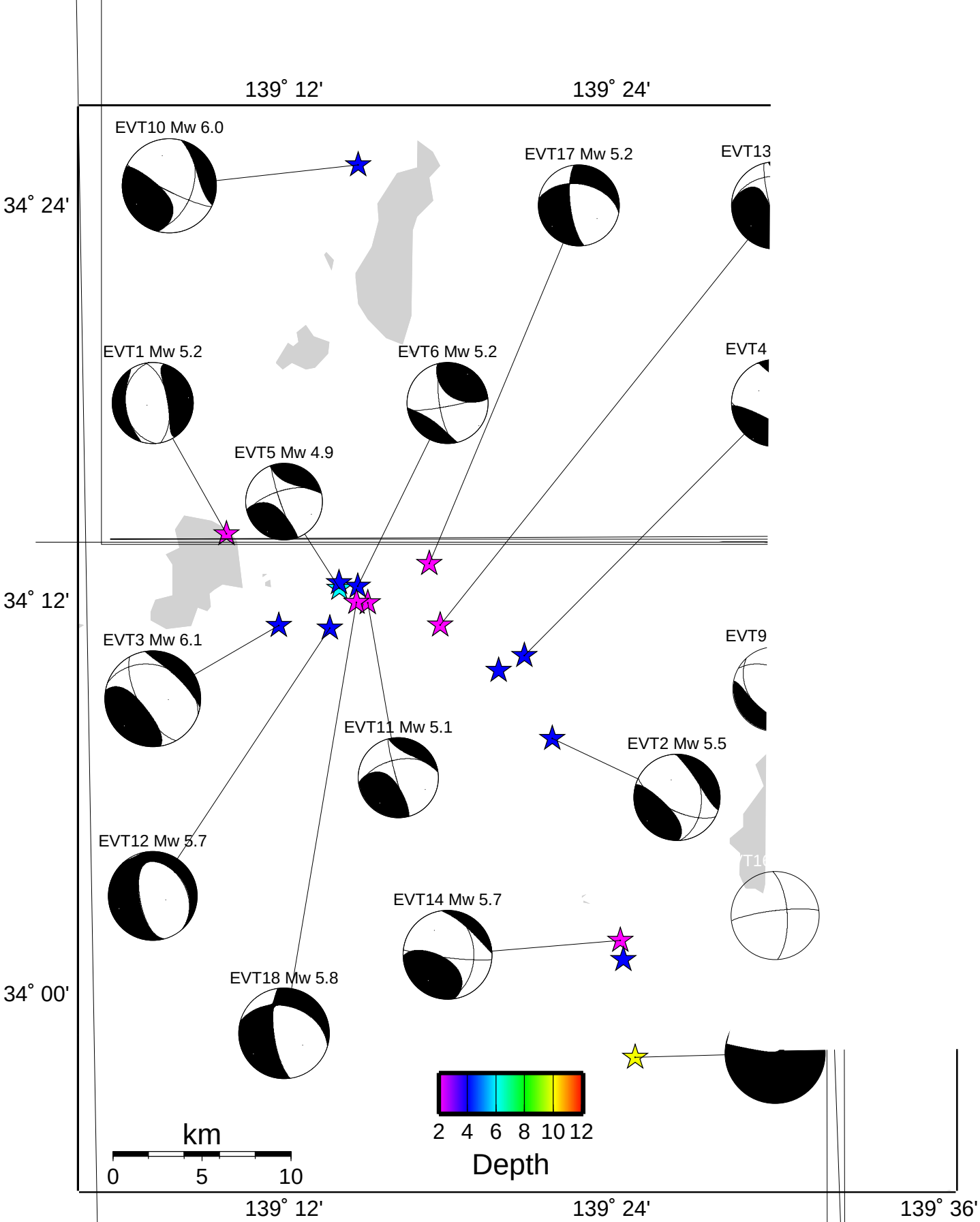

Deviatoric mechanisms (data are bandpass filtered between 0.02 and 0.05 Hz)

Figure 6

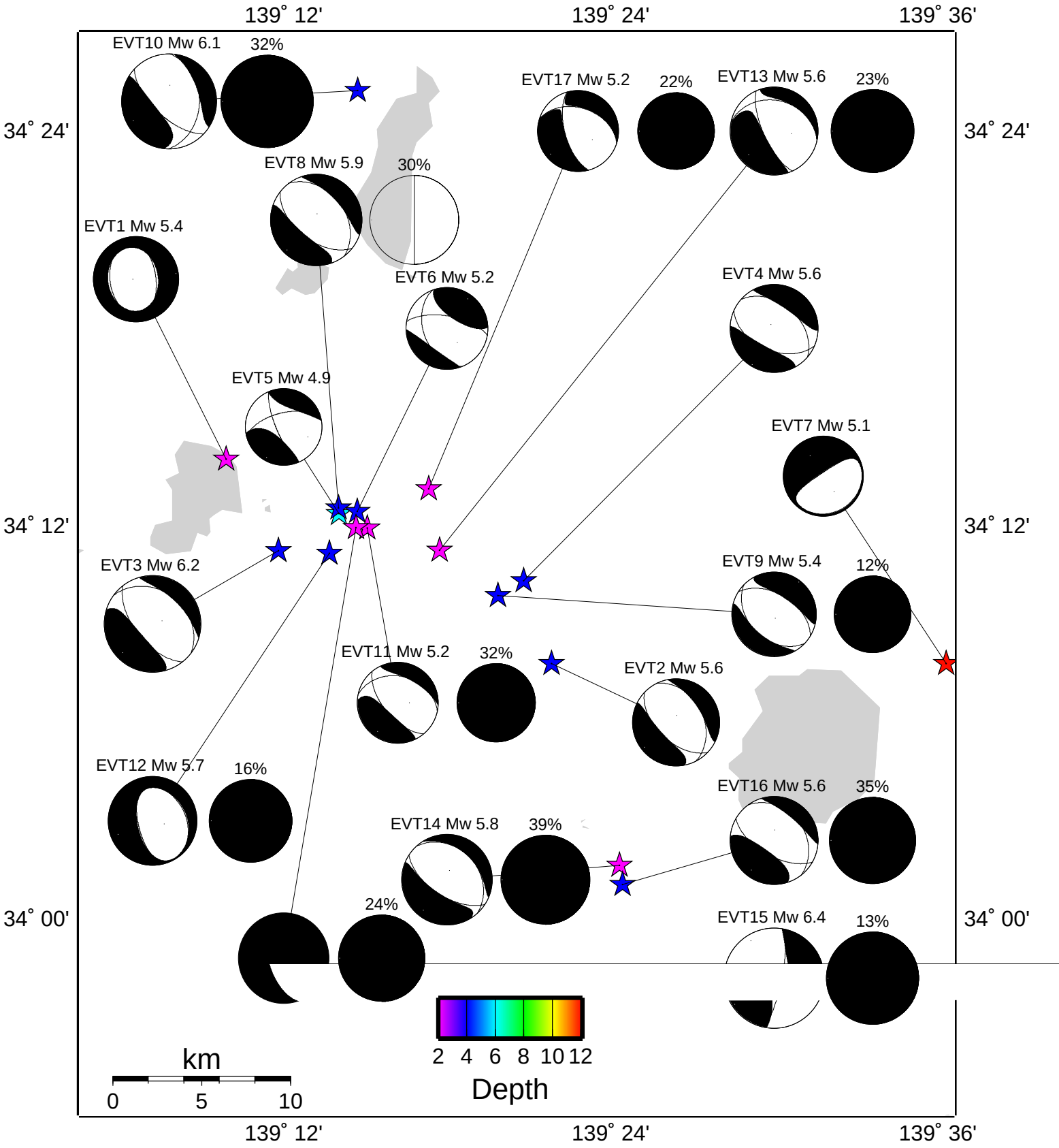

Full moment tensor mechanisms (data are bandpass filtered between 0.02 and 0.05 Hz)

Figure 7

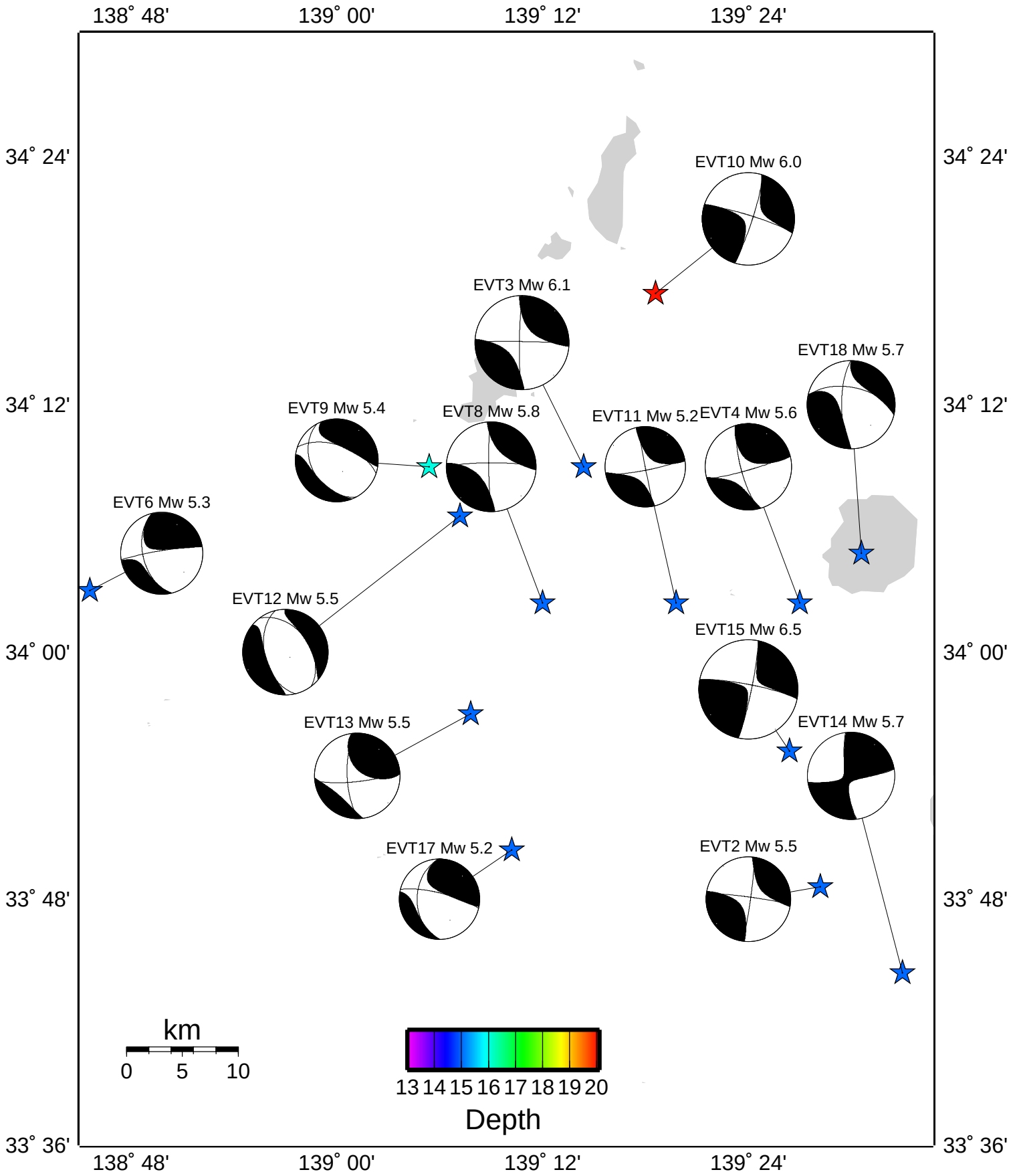

Harvard CMT mechanisms for the events in this study.

Figure 8

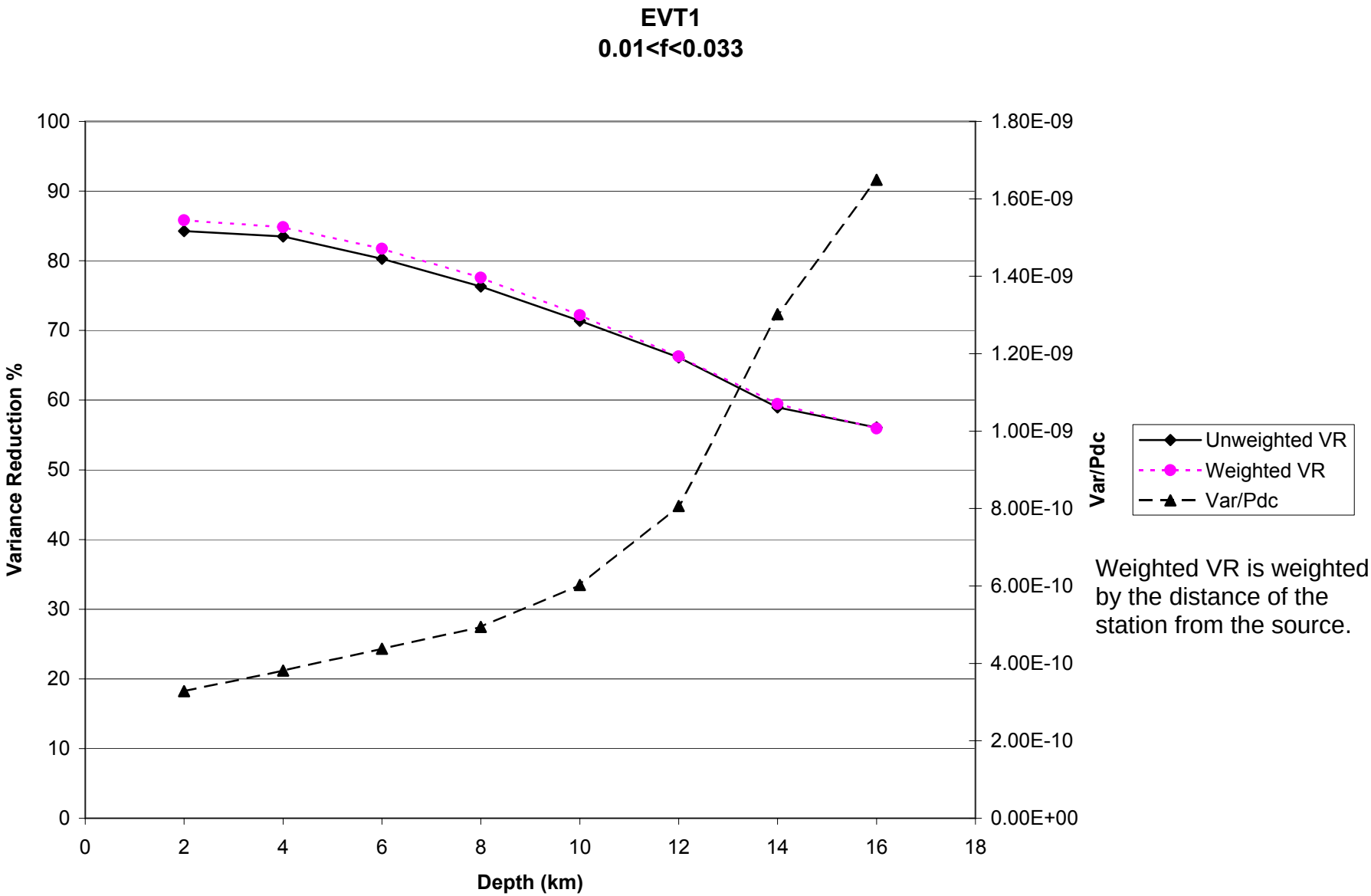

Weighted VR is weighted by the distance of the station from the source.

Figure 9

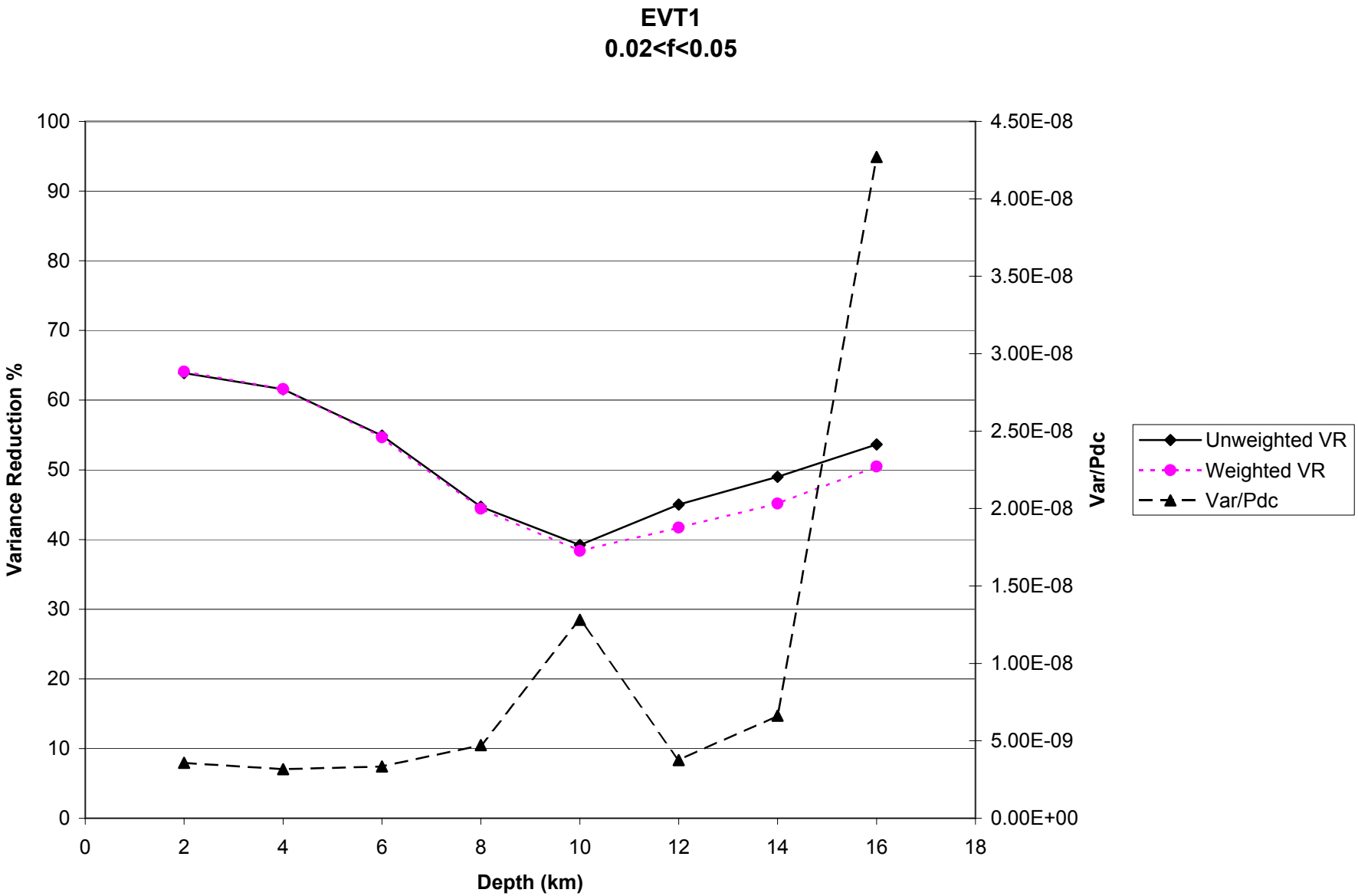
EVT1
0.02<f<0.05
Variance Reduction %
Var/Pdc
Depth (km)
Unweighted VR
Weighted VR
Var/Pdc
100
90
80
70
60
50
40
30
20
10
0
4.50E-08
4.00E-08
3.50E-08
3.00E-08
2.50E-08
2.00E-08
1.50E-08
1.00E-08
5.00E-09
0.00E+00
0
2
4
6
8
10
12
14
16
18

Figure 10

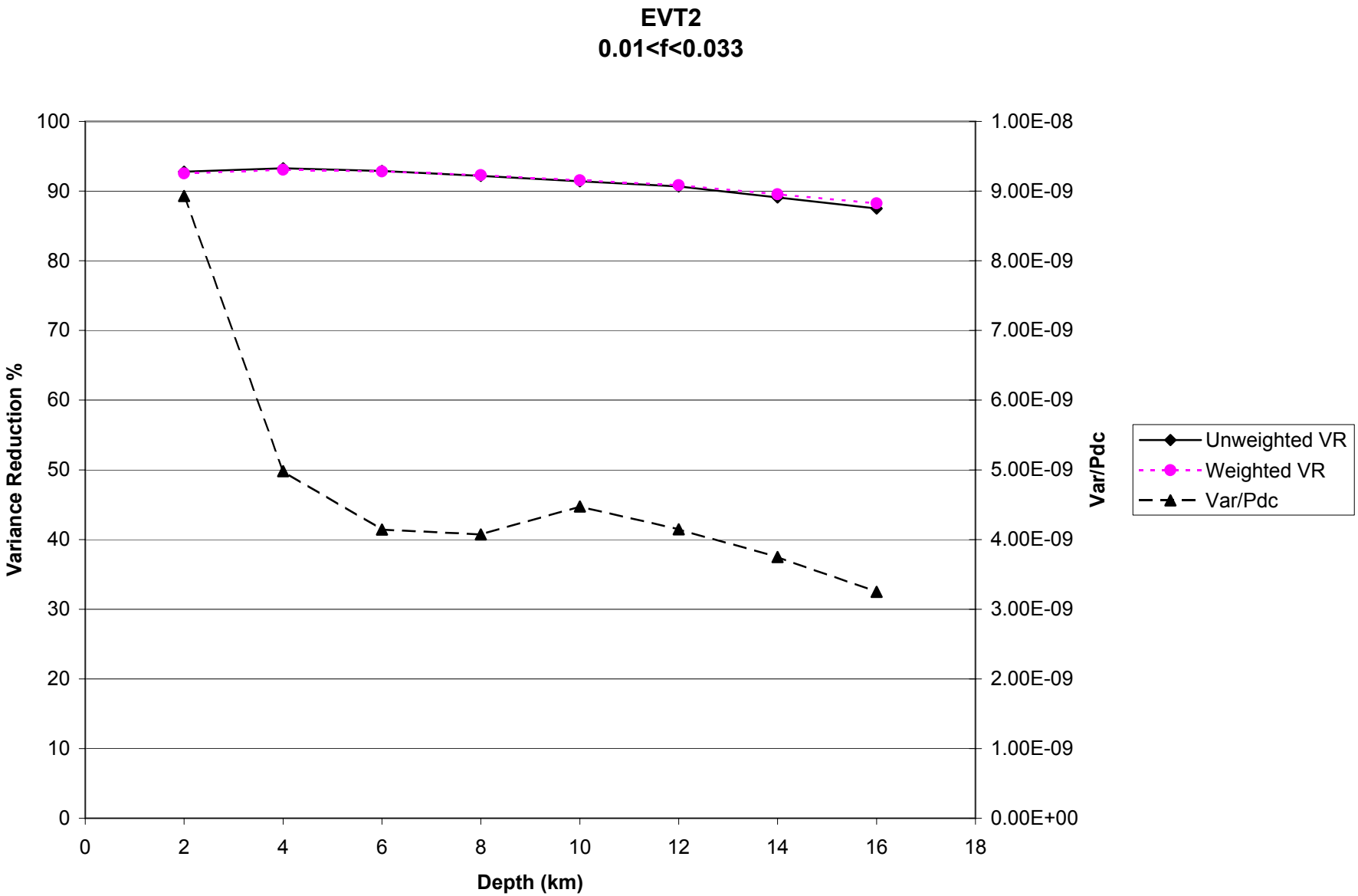
EVT2
0.01<f<0.033
Variance Reduction %
Var/Pdc
Depth (km)
Unweighted VR
Weighted VR
Var/Pdc
100
90
80
70
60
50
40
30
20
10
0
1.00E-08
9.00E-09
8.00E-09
7.00E-09
6.00E-09
5.00E-09
4.00E-09
3.00E-09
2.00E-09
1.00E-09
0.00E+00
0
2
4
6
8
10
12
14
16
18

Figure 11

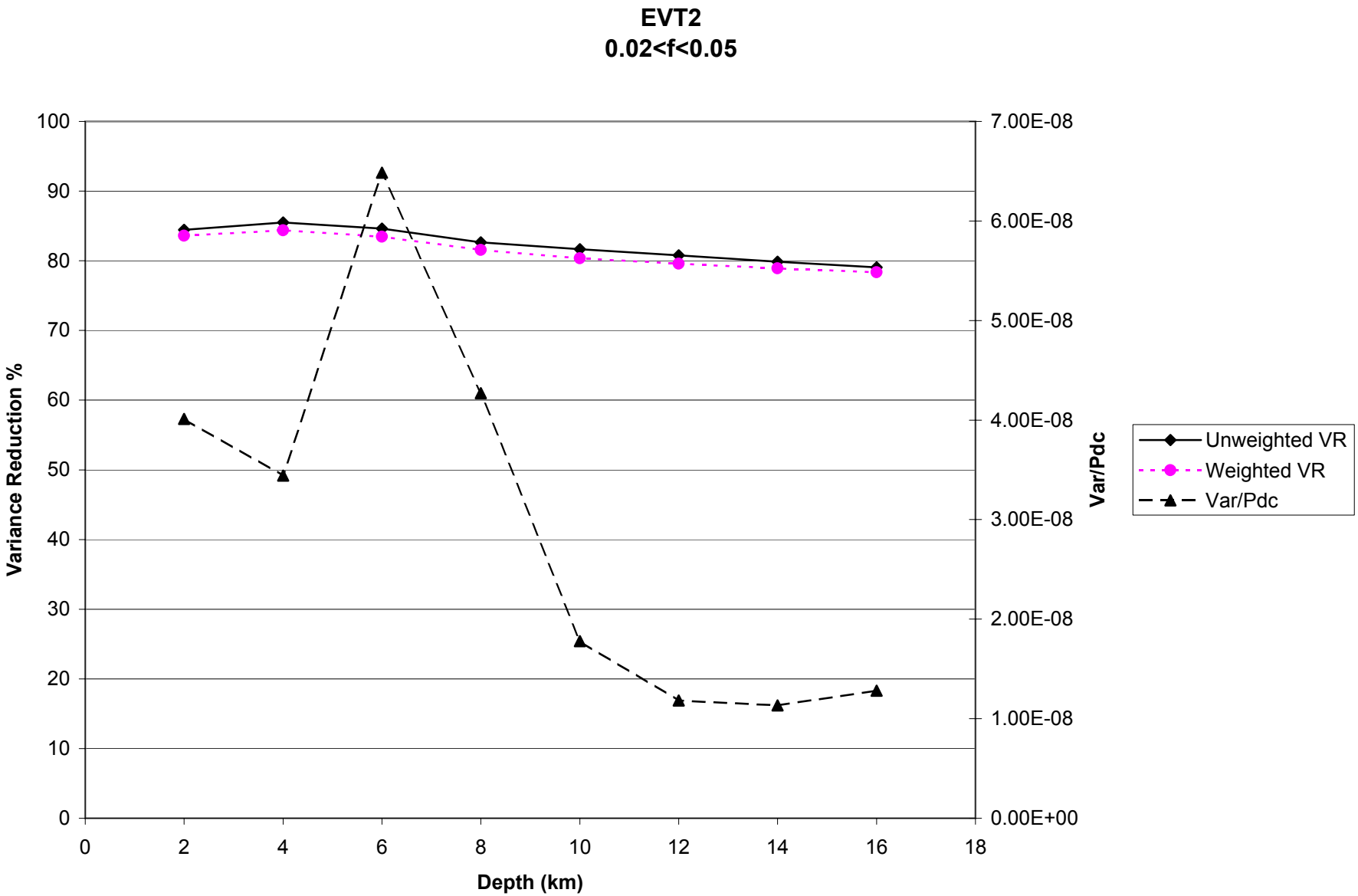
EVT2
0.02<f<0.05
Variance Reduction %
Var/Pdc
Depth (km)
Unweighted VR
Weighted VR
Var/Pdc
100
90
80
70
60
50
40
30
20
10
0
7.00E-08
6.00E-08
5.00E-08
4.00E-08
3.00E-08
2.00E-08
1.00E-08
0.00E+00
0
2
4
6
8
10
12
14
16
18

Figure 12

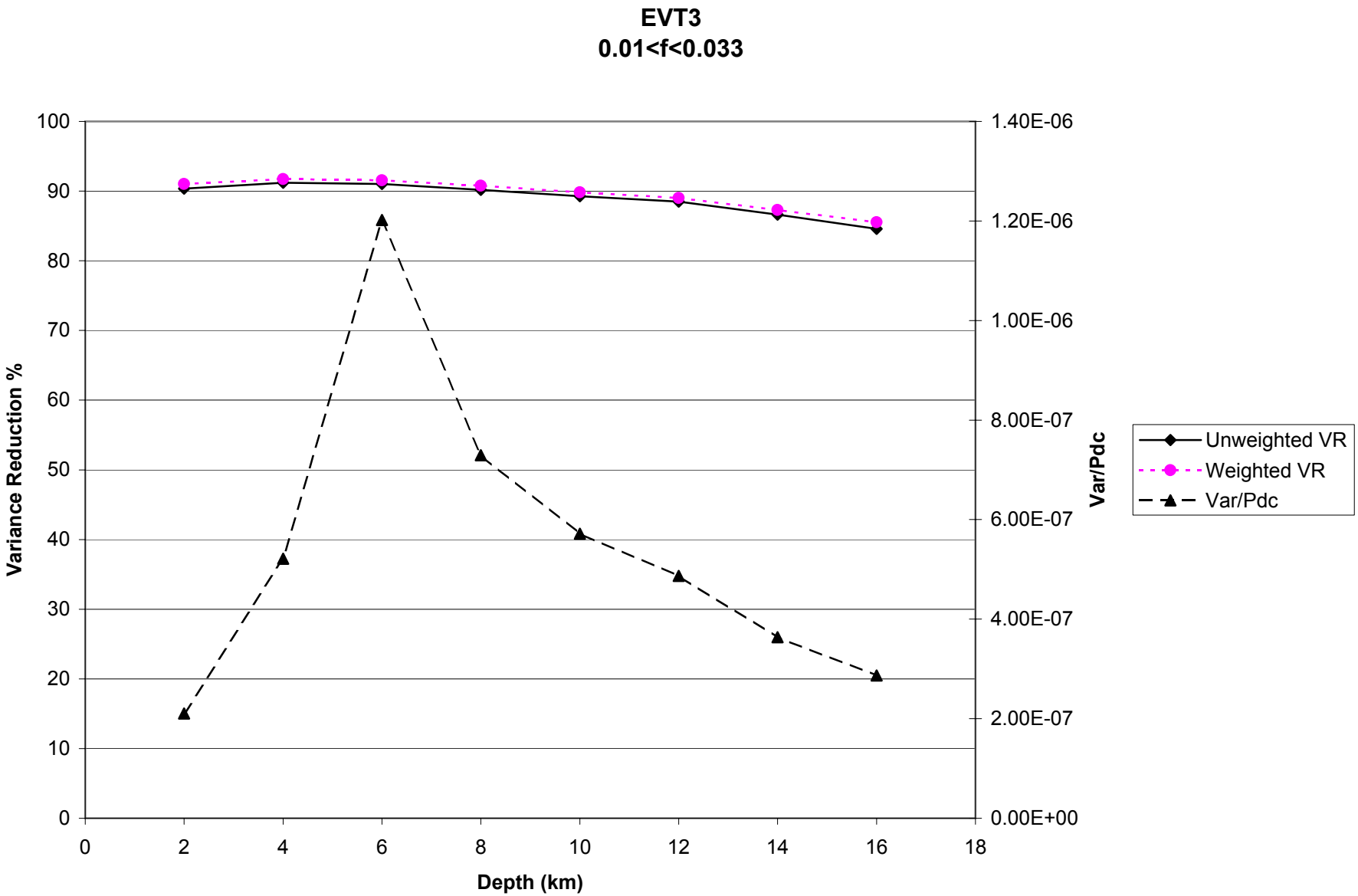
EVT3
0.01<f<0.033
Variance Reduction %
Var/Pdc
Depth (km)
Unweighted VR
Weighted VR
Var/Pdc
100
90
80
70
60
50
40
30
20
10
0
1.40E-06
1.20E-06
1.00E-06
8.00E-07
6.00E-07
4.00E-07
2.00E-07
0.00E+00
0
2
4
6
8
10
12
14
16
18

Figure 13

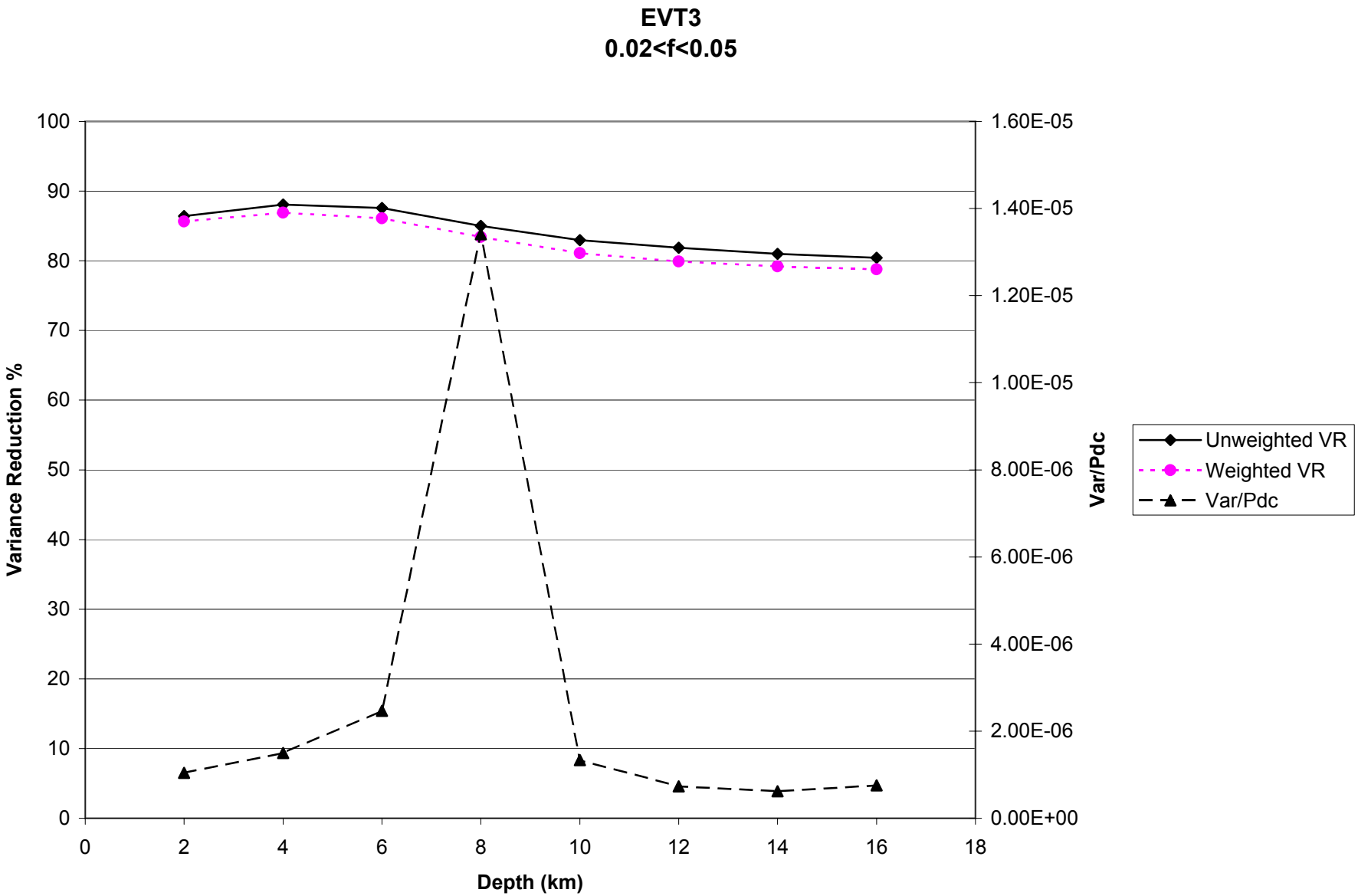
EVT3
0.02<f<0.05
Variance Reduction %
Var/Pdc
Depth (km)
100
90
80
70
60
50
40
30
20
10
0
1.60E-05
1.40E-05
1.20E-05
1.00E-05
8.00E-06
6.00E-06
4.00E-06
2.00E-06
0.00E+00
0
2
4
6
8
10
12
14
16
18
Unweighted VR
Weighted VR
Var/Pdc

Figure 14

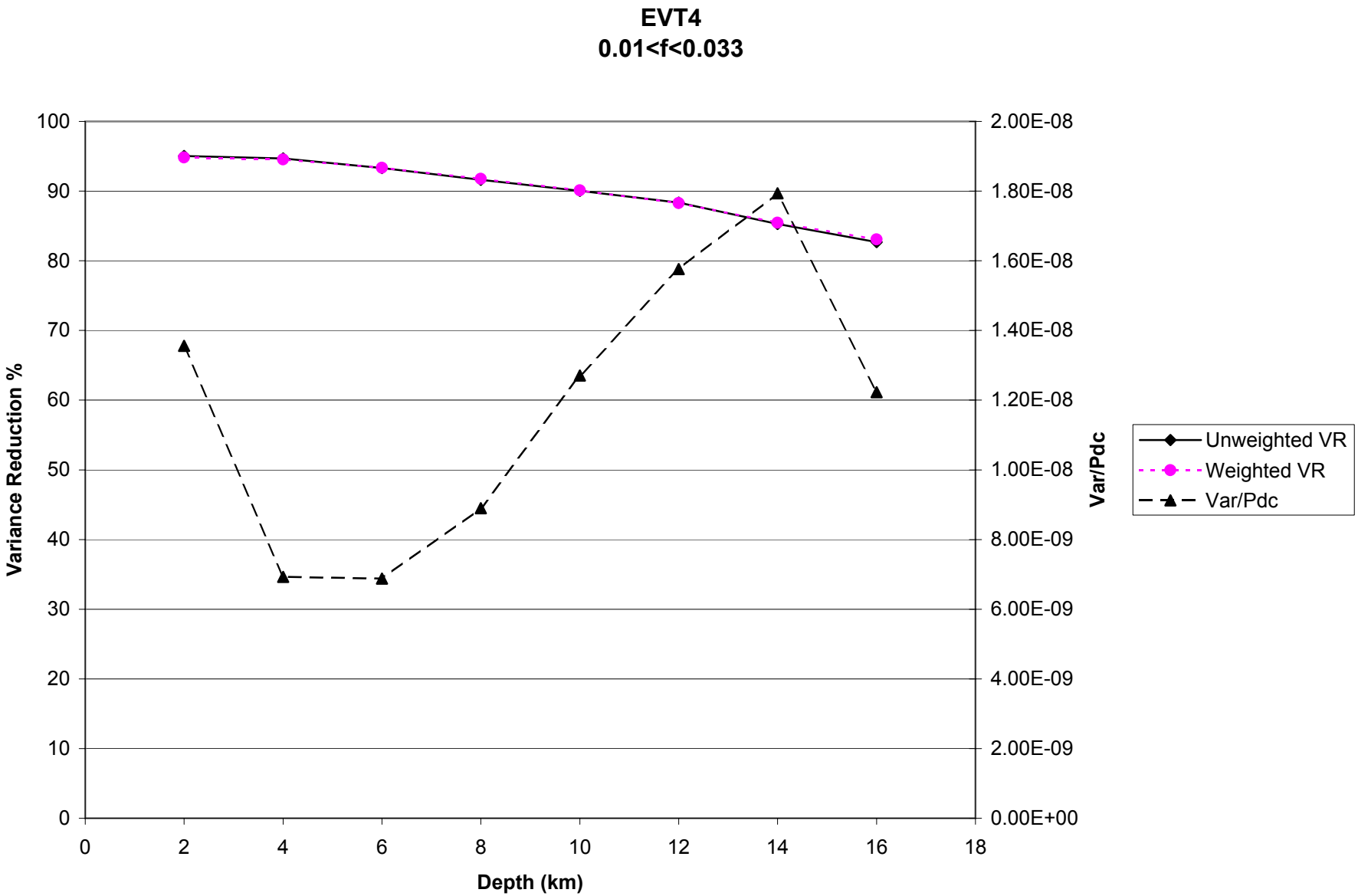
EVT4
0.01<f<0.033
Variance Reduction %
Var/Pdc
Depth (km)
100
90
80
70
60
50
40
30
20
10
0
2.00E-08
1.80E-08
1.60E-08
1.40E-08
1.20E-08
1.00E-08
8.00E-09
6.00E-09
4.00E-09
2.00E-09
0.00E+00
0
2
4
6
8
10
12
14
16
18
Unweighted VR
Weighted VR
Var/Pdc

Figure 15

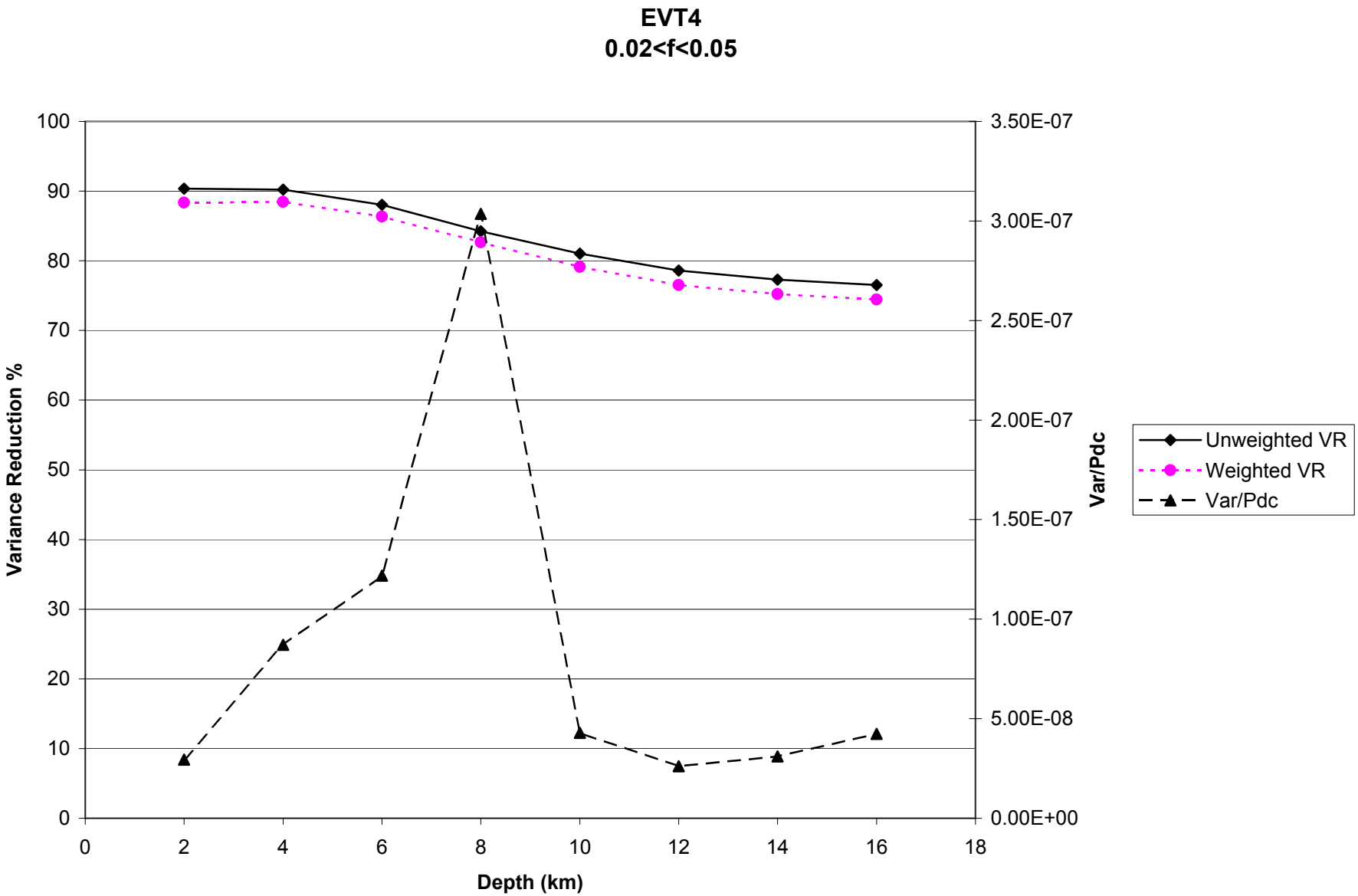
EVT4
0.02<f<0.05
Variance Reduction %
Var/Pdc
Depth (km)
Unweighted VR
Weighted VR
Var/Pdc
100
90
80
70
60
50
40
30
20
10
0
3.50E-07
3.00E-07
2.50E-07
2.00E-07
1.50E-07
1.00E-07
5.00E-08
0.00E+00
0
2
4
6
8
10
12
14
16
18

Figure 16

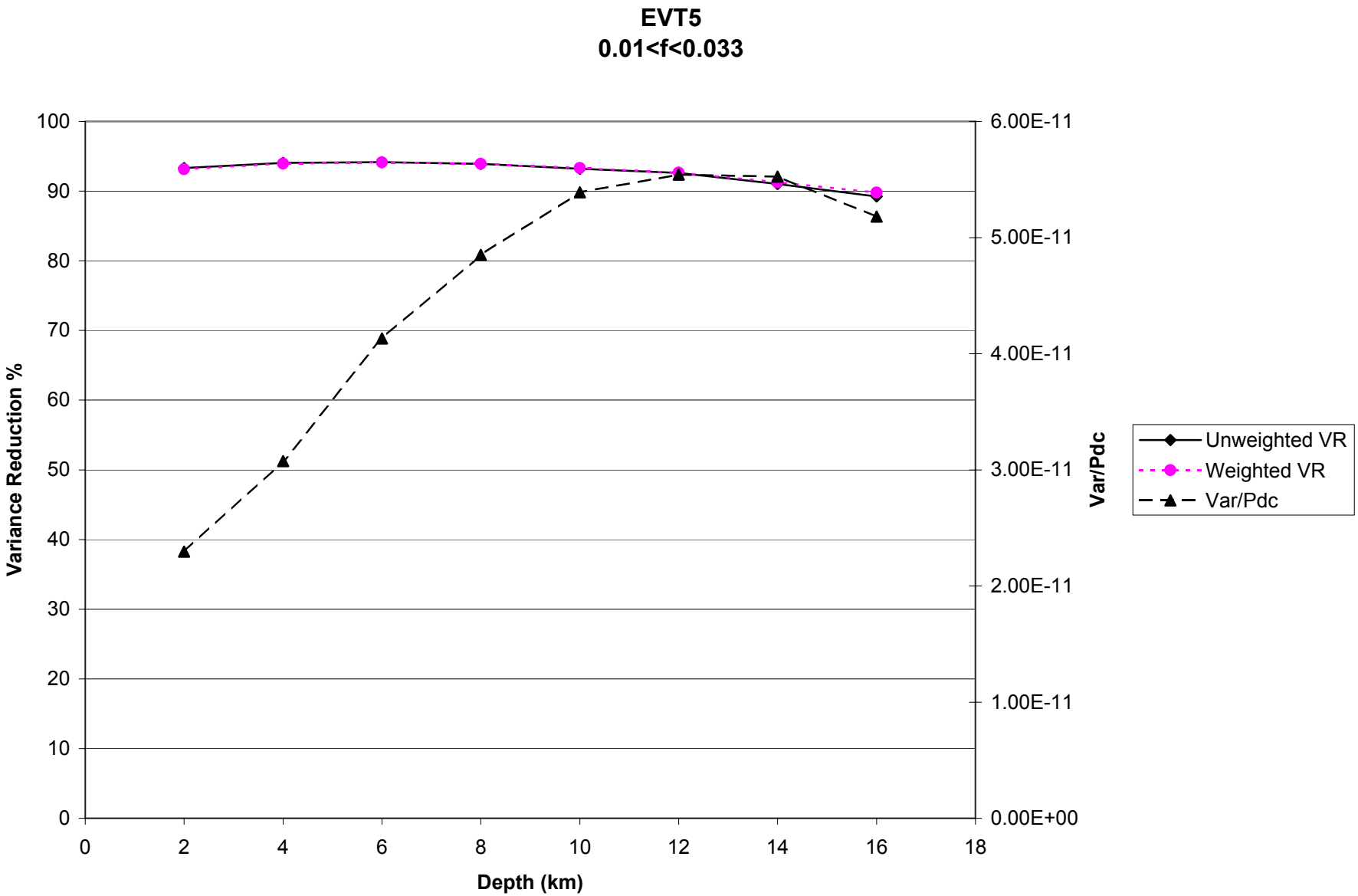
EVT5
0.01<f<0.033
Variance Reduction %
Var/Pdc
Depth (km)
Unweighted VR
Weighted VR
Var/Pdc
100
90
80
70
60
50
40
30
20
10
0
6.00E-11
5.00E-11
4.00E-11
3.00E-11
2.00E-11
1.00E-11
0.00E+00
0
2
4
6
8
10
12
14
16
18

Figure 17

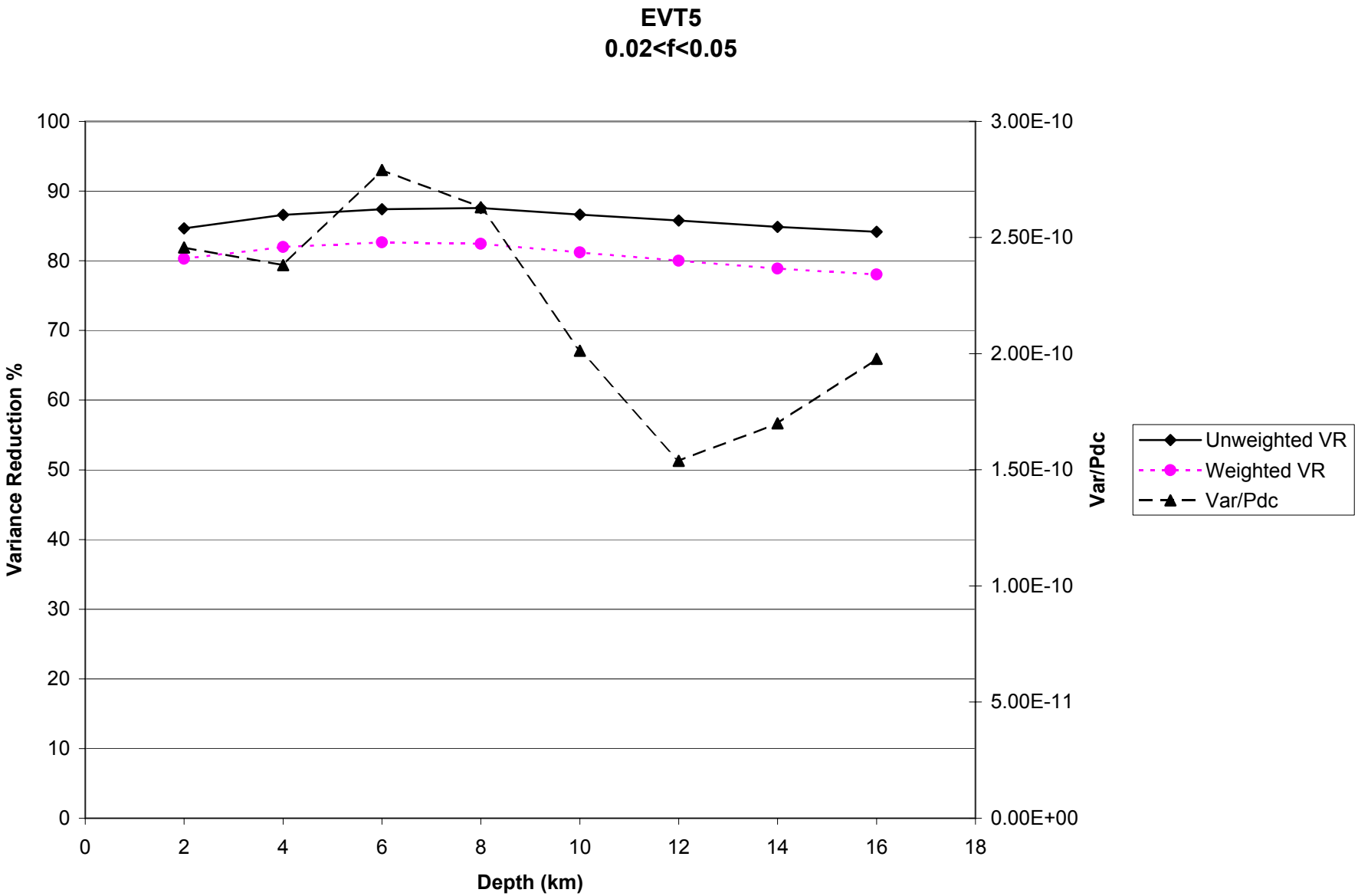
EVT5
0.02<f<0.05
Variance Reduction %
Var/Pdc
Depth (km)
100
90
80
70
60
50
40
30
20
10
0
3.00E-10
2.50E-10
2.00E-10
1.50E-10
1.00E-10
5.00E-11
0.00E+00
0
2
4
6
8
10
12
14
16
18
Unweighted VR
Weighted VR
Var/Pdc

Figure 18

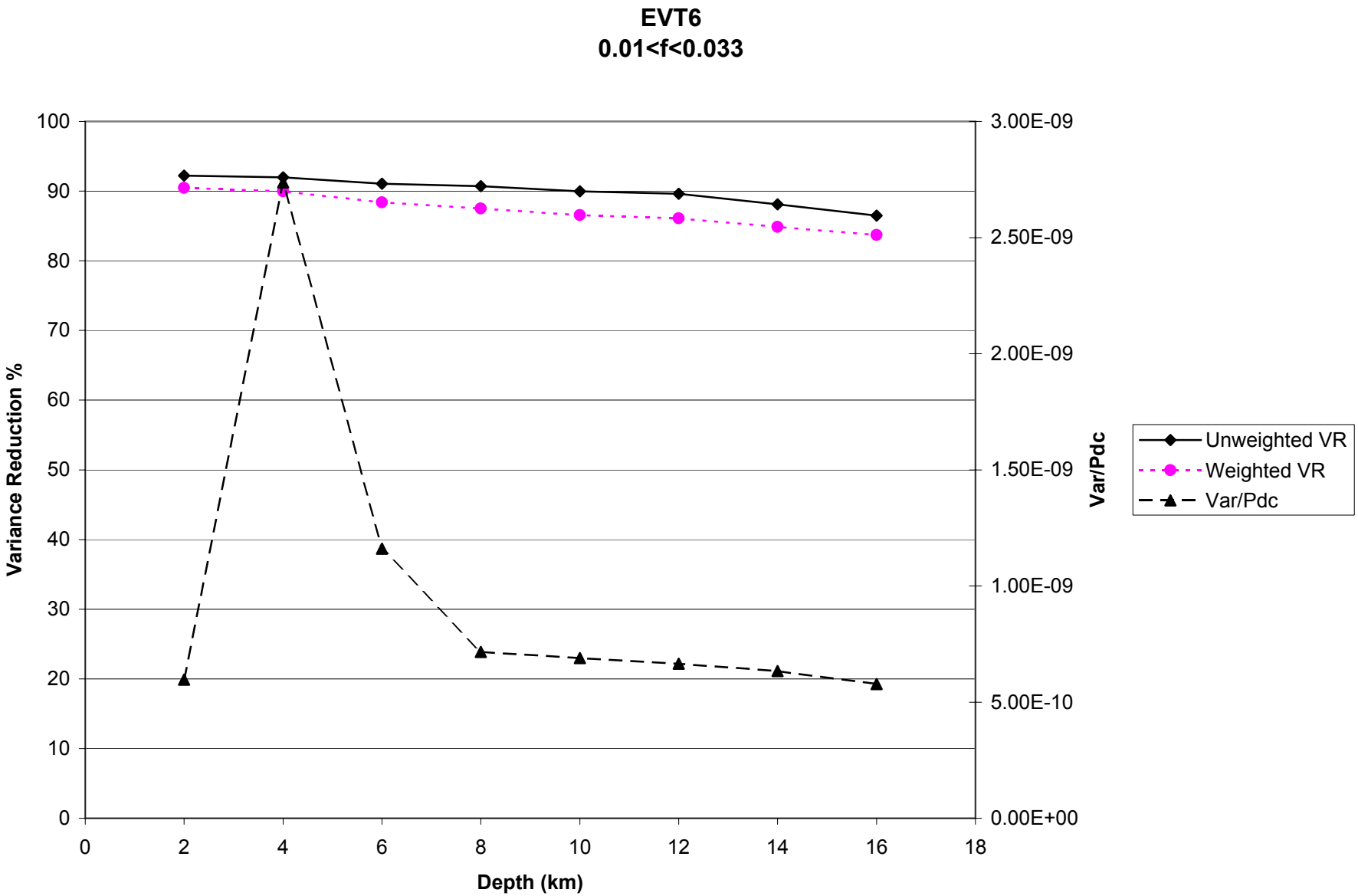
EVT6
0.01<f<0.033
Variance Reduction %
Var/Pdc
Depth (km)
100
90
80
70
60
50
40
30
20
10
0
3.00E-09
2.50E-09
2.00E-09
1.50E-09
1.00E-09
5.00E-10
0.00E+00
0
2
4
6
8
10
12
14
16
18
Unweighted VR
Weighted VR
Var/Pdc

Figure 19

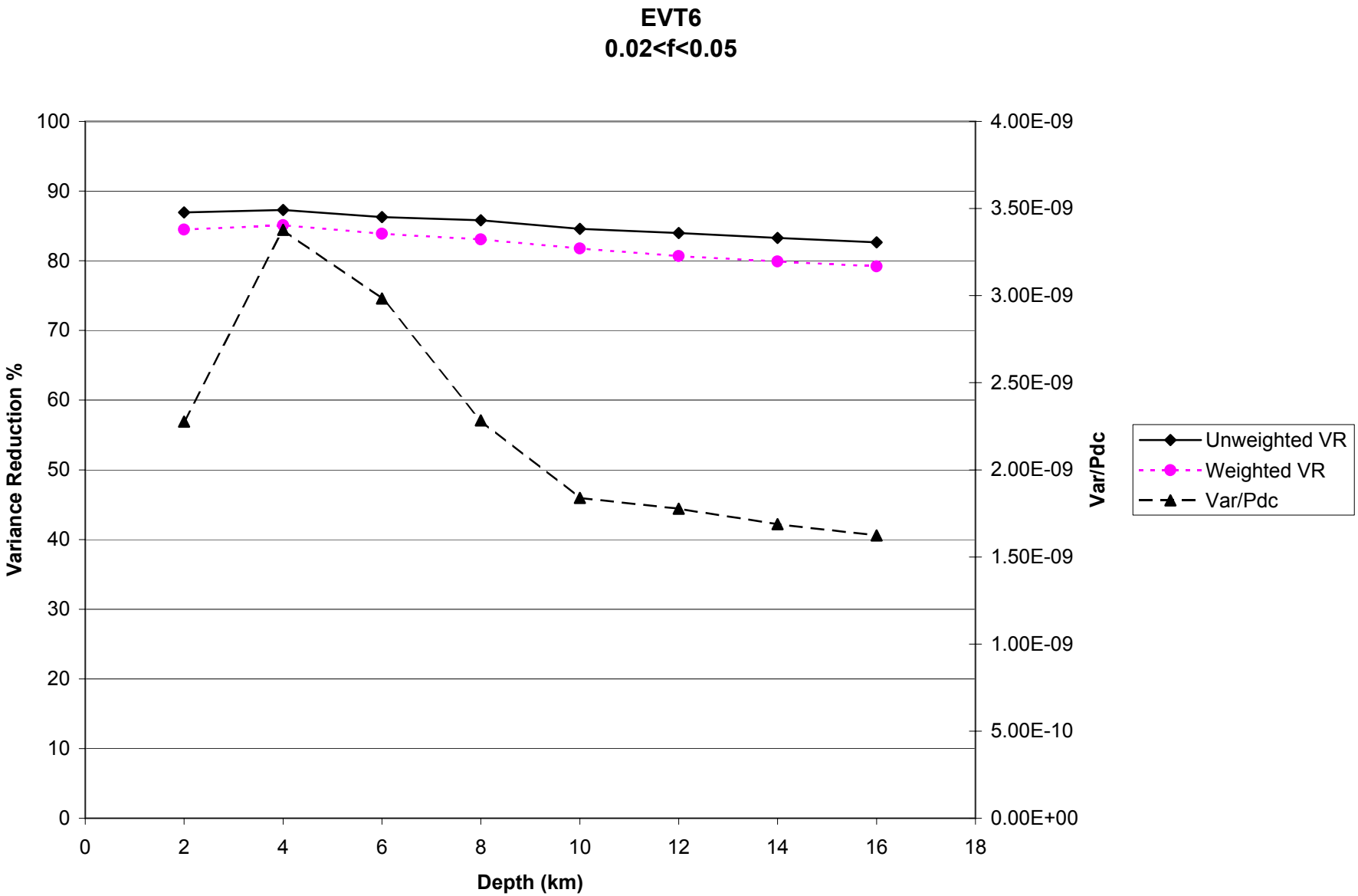
EVT6
0.02<f<0.05
Variance Reduction %
Var/Pdc
Depth (km)
Unweighted VR
Weighted VR
Var/Pdc
100
90
80
70
60
50
40
30
20
10
0
4.00E-09
3.50E-09
3.00E-09
2.50E-09
2.00E-09
1.50E-09
1.00E-09
5.00E-10
0.00E+00
0
2
4
6
8
10
12
14
16
18

Figure 20

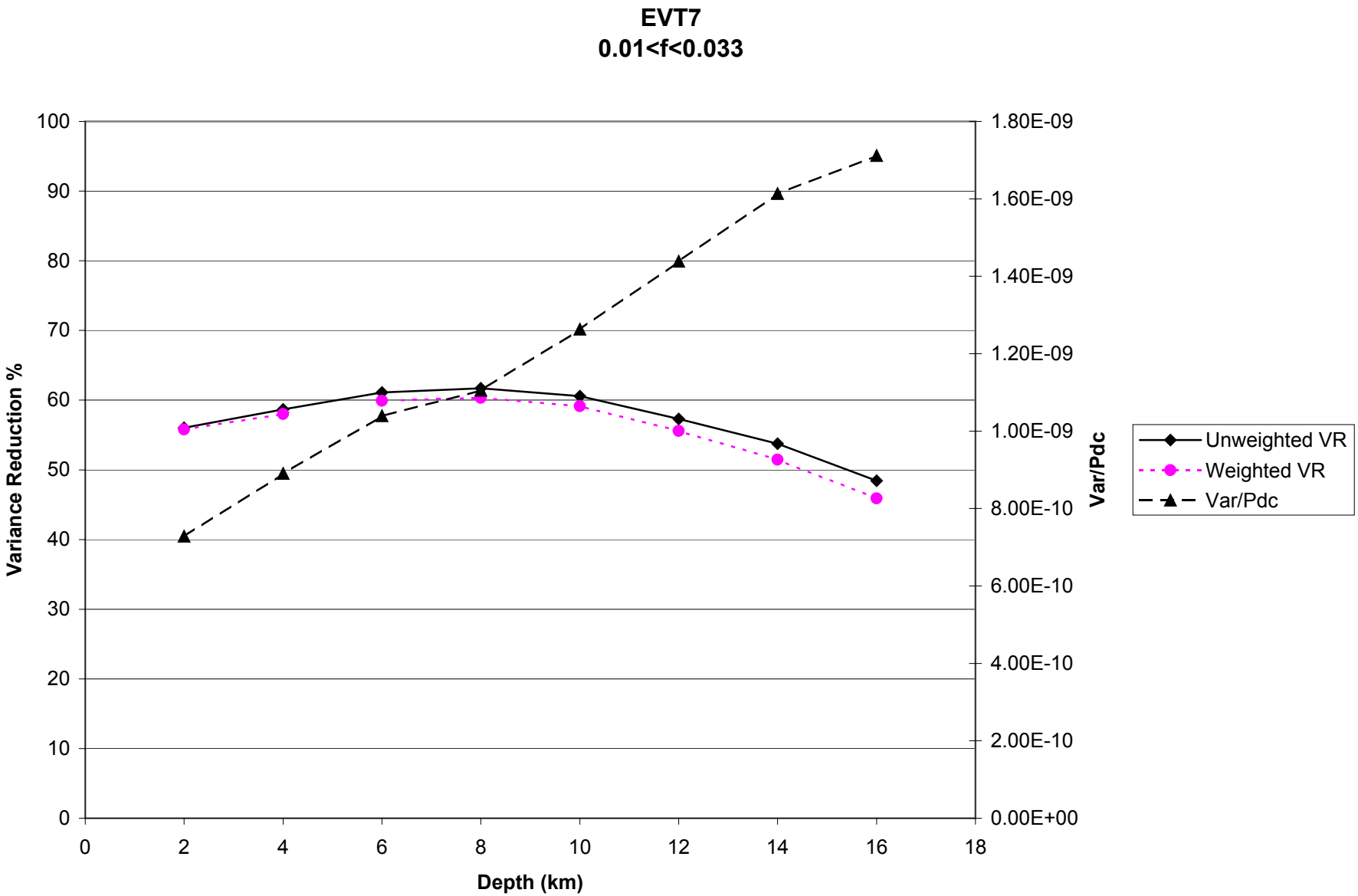
EVT7
0.01<f<0.033
Variance Reduction %
Var/Pdc
Depth (km)
0
10
20
30
40
50
60
70
80
90
100
0.00E+00
2.00E-10
4.00E-10
6.00E-10
8.00E-10
1.00E-09
1.20E-09
1.40E-09
1.60E-09
1.80E-09
0
2
4
6
8
10
12
14
16
18
Unweighted VR
Weighted VR
Var/Pdc

Figure 21

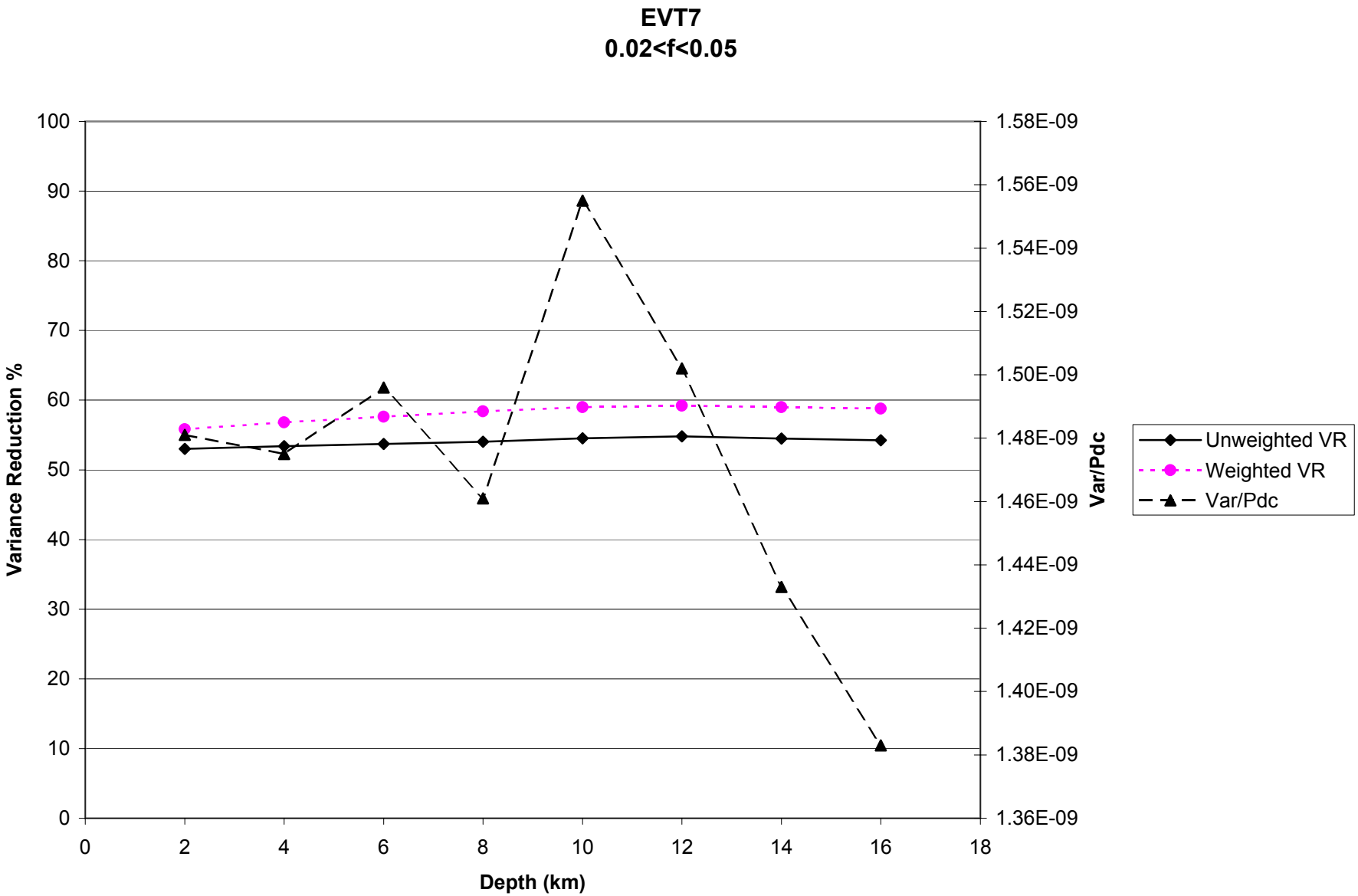
EVT7
0.02<f<0.05
Variance Reduction %
Var/Pdc
Depth (km)
Unweighted VR
Weighted VR
Var/Pdc
100
90
80
70
60
50
40
30
20
10
0
1.58E-09
1.56E-09
1.54E-09
1.52E-09
1.50E-09
1.48E-09
1.46E-09
1.44E-09
1.42E-09
1.40E-09
1.38E-09
1.36E-09
0
2
4
6
8
10
12
14
16
18

Figure 22

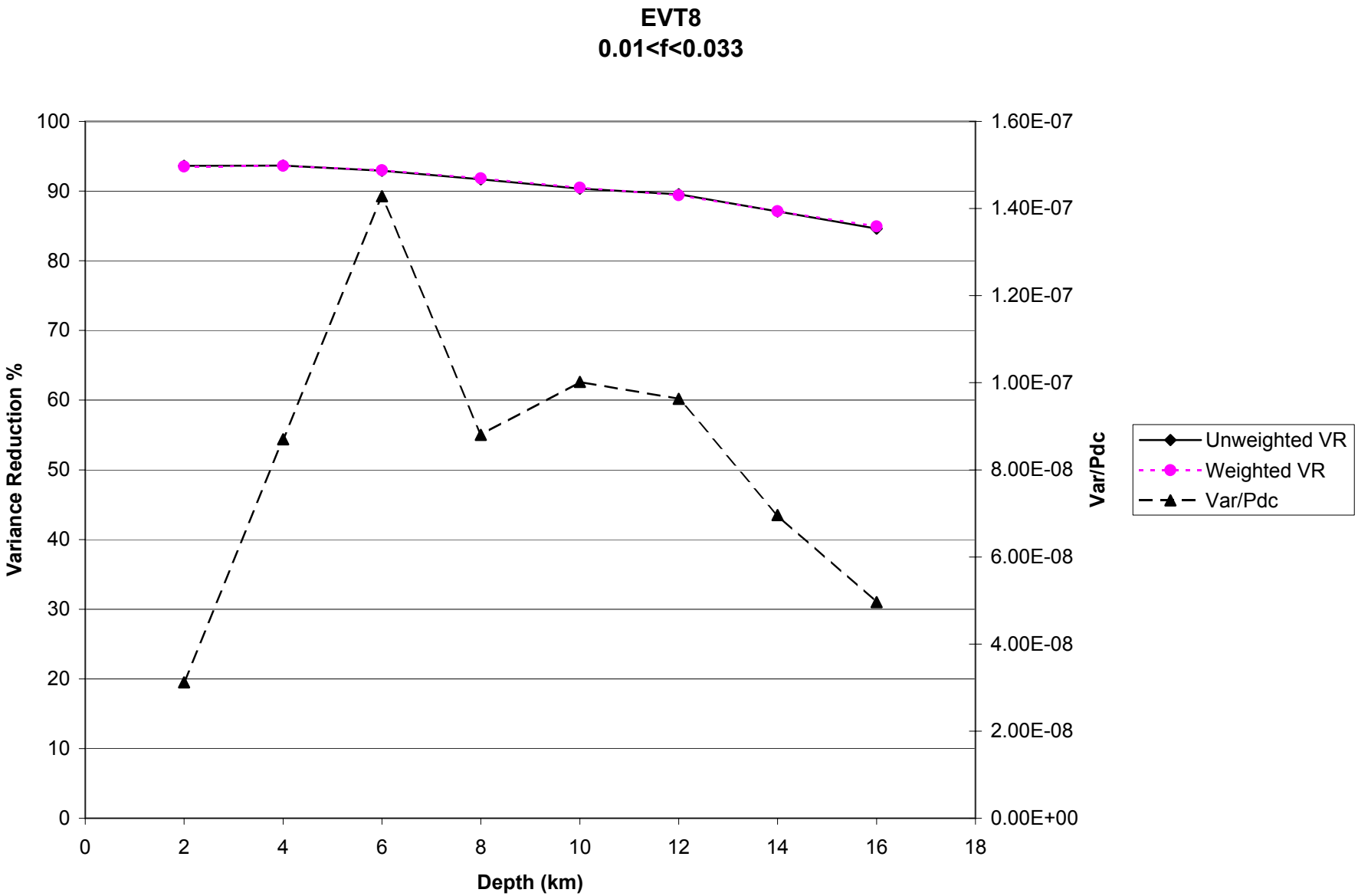
EVT8
0.01<f<0.033
Variance Reduction %
Var/Pdc
Depth (km)
Unweighted VR
Weighted VR
Var/Pdc
100
90
80
70
60
50
40
30
20
10
0
1.60E-07
1.40E-07
1.20E-07
1.00E-07
8.00E-08
6.00E-08
4.00E-08
2.00E-08
0.00E+00
0
2
4
6
8
10
12
14
16
18

Figure 23

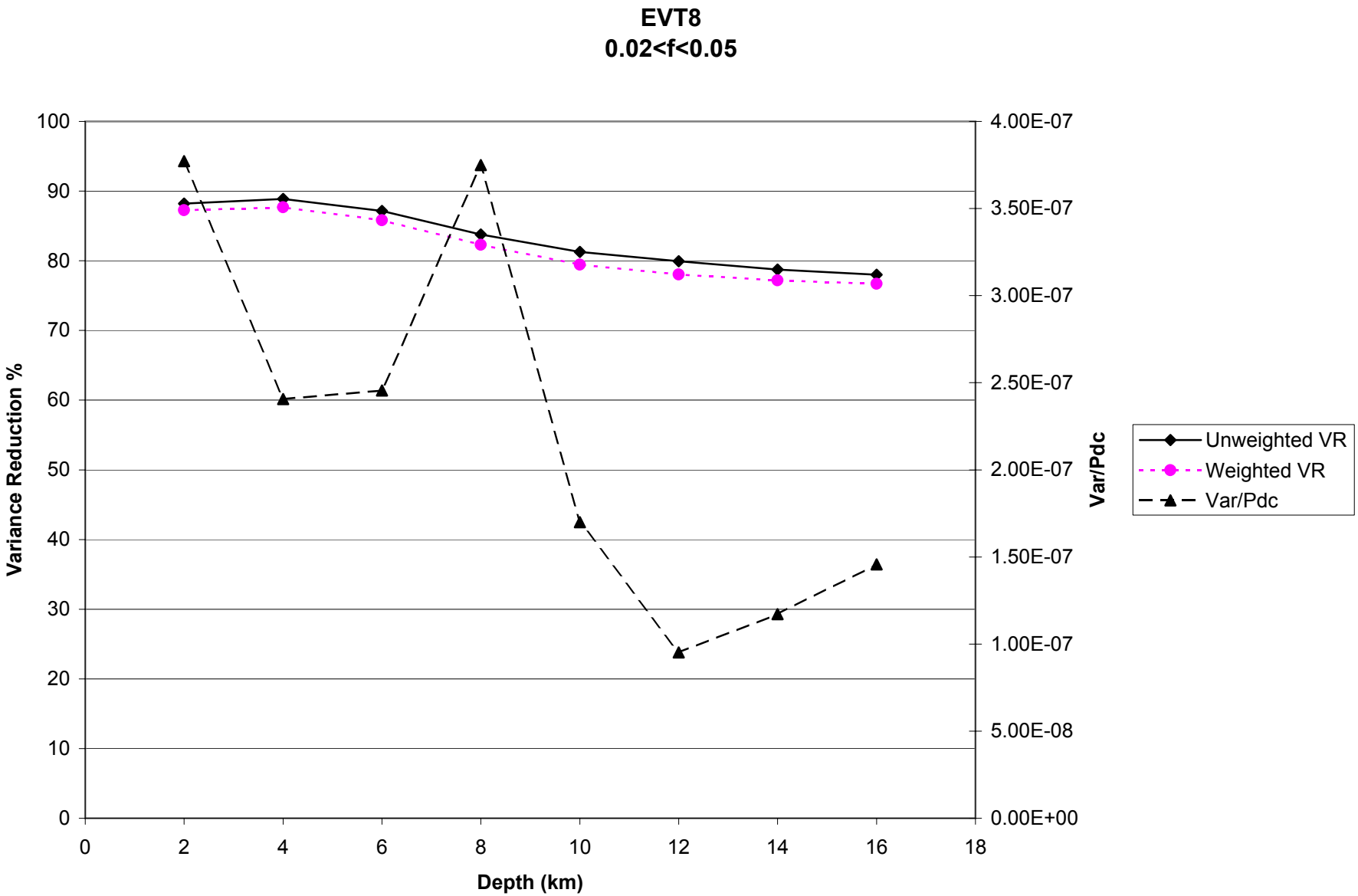
EVT8
0.02<f<0.05
Variance Reduction %
Var/Pdc
Depth (km)
Unweighted VR
Weighted VR
Var/Pdc
100
90
80
70
60
50
40
30
20
10
0
4.00E-07
3.50E-07
3.00E-07
2.50E-07
2.00E-07
1.50E-07
1.00E-07
5.00E-08
0.00E+00
0
2
4
6
8
10
12
14
16
18

Figure 24

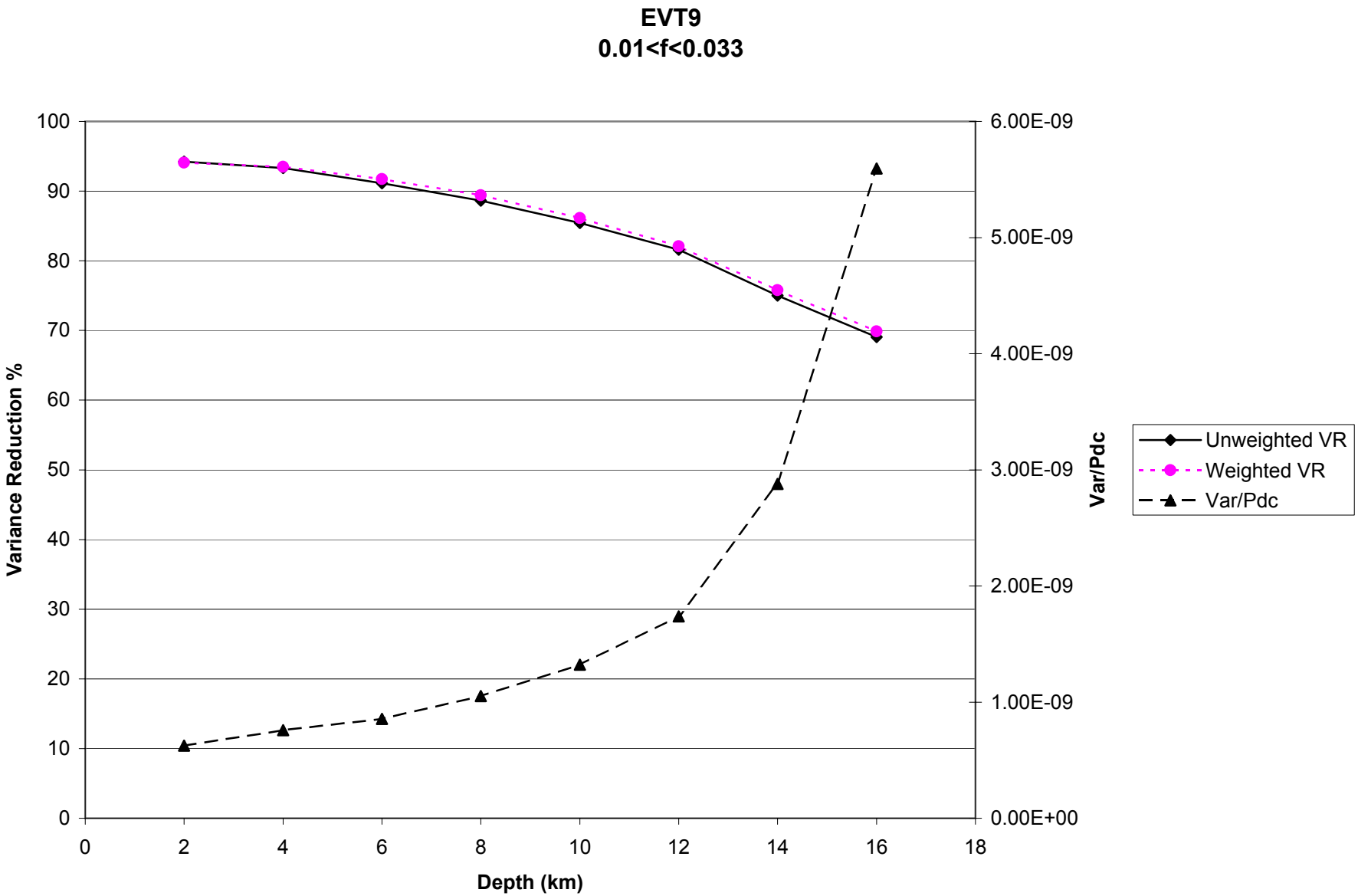
EVT9
0.01<f<0.033
Variance Reduction %
Var/Pdc
Depth (km)
Unweighted VR
Weighted VR
Var/Pdc
100
90
80
70
60
50
40
30
20
10
0
6.00E-09
5.00E-09
4.00E-09
3.00E-09
2.00E-09
1.00E-09
0.00E+00
0
2
4
6
8
10
12
14
16
18

Figure 25

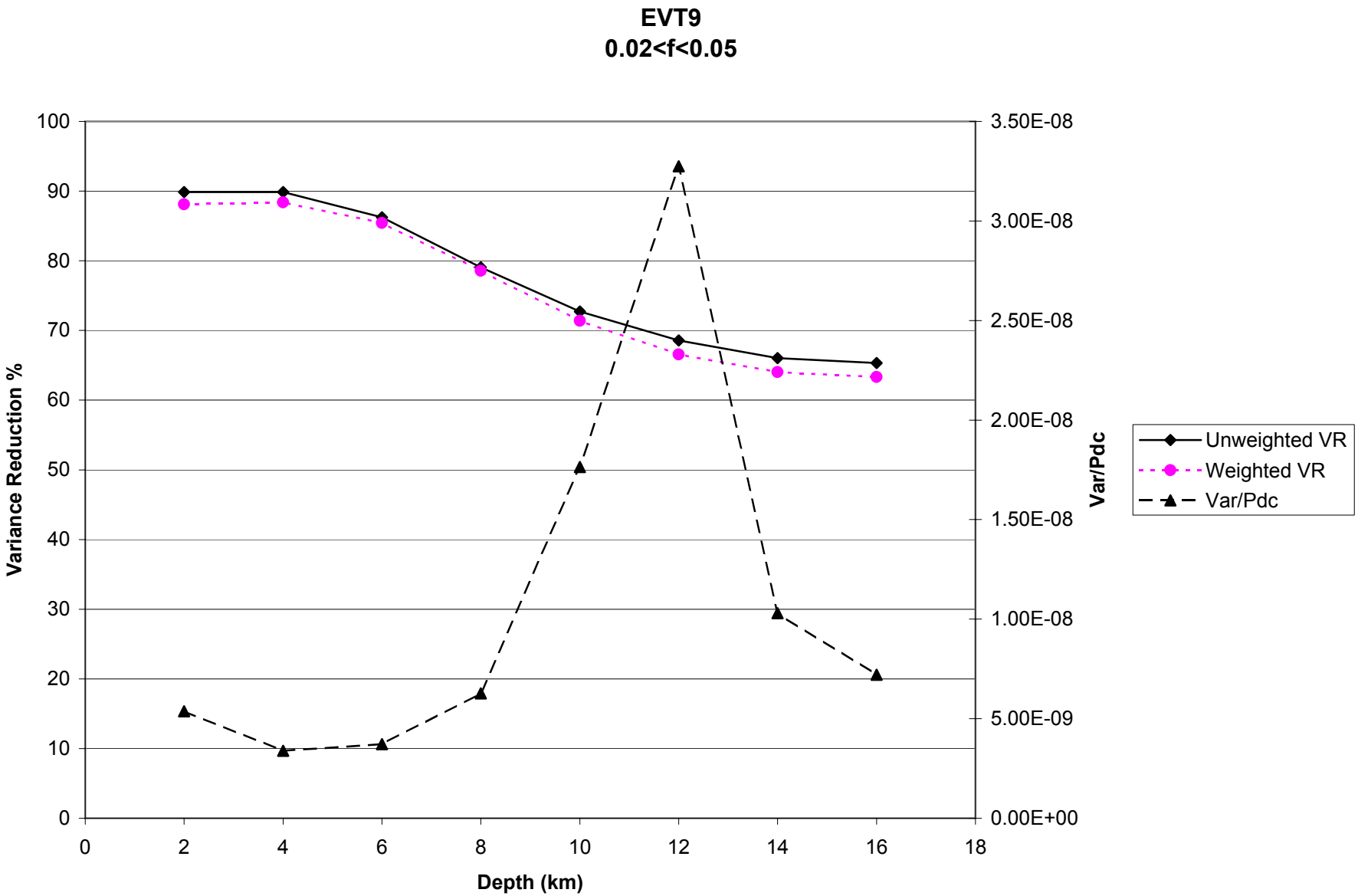
EVT9
0.02<f<0.05
Variance Reduction %
Var/Pdc
Depth (km)
Unweighted VR
Weighted VR
Var/Pdc
100
90
80
70
60
50
40
30
20
10
0
3.50E-08
3.00E-08
2.50E-08
2.00E-08
1.50E-08
1.00E-08
5.00E-09
0.00E+00
0
2
4
6
8
10
12
14
16
18

Figure 26

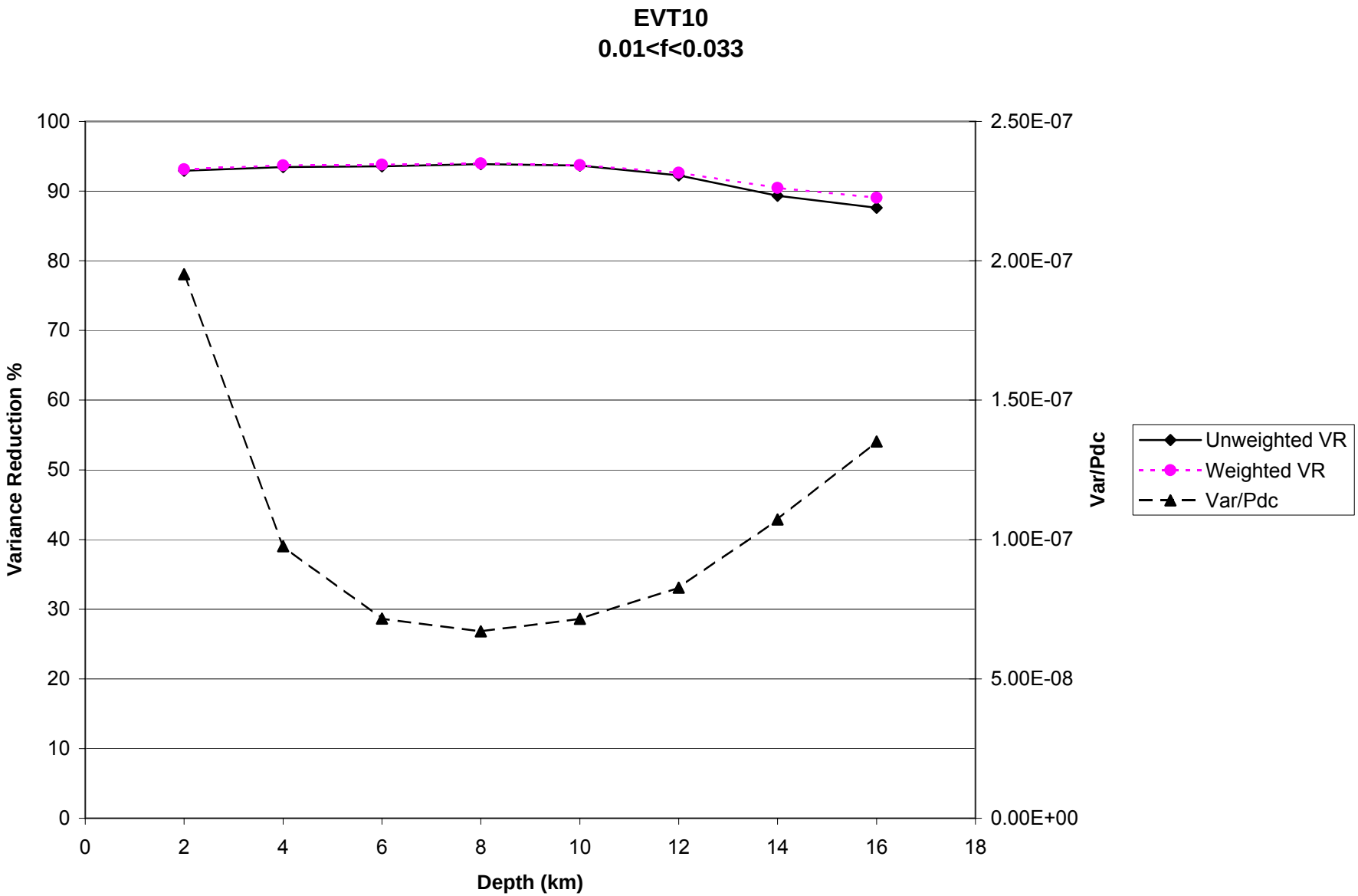
EVT10
0.01<f<0.033
Variance Reduction %
Var/Pdc
Depth (km)
Unweighted VR
Weighted VR
Var/Pdc
100
90
80
70
60
50
40
30
20
10
0
2.50E-07
2.00E-07
1.50E-07
1.00E-07
5.00E-08
0.00E+00
0
2
4
6
8
10
12
14
16
18

Figure 27

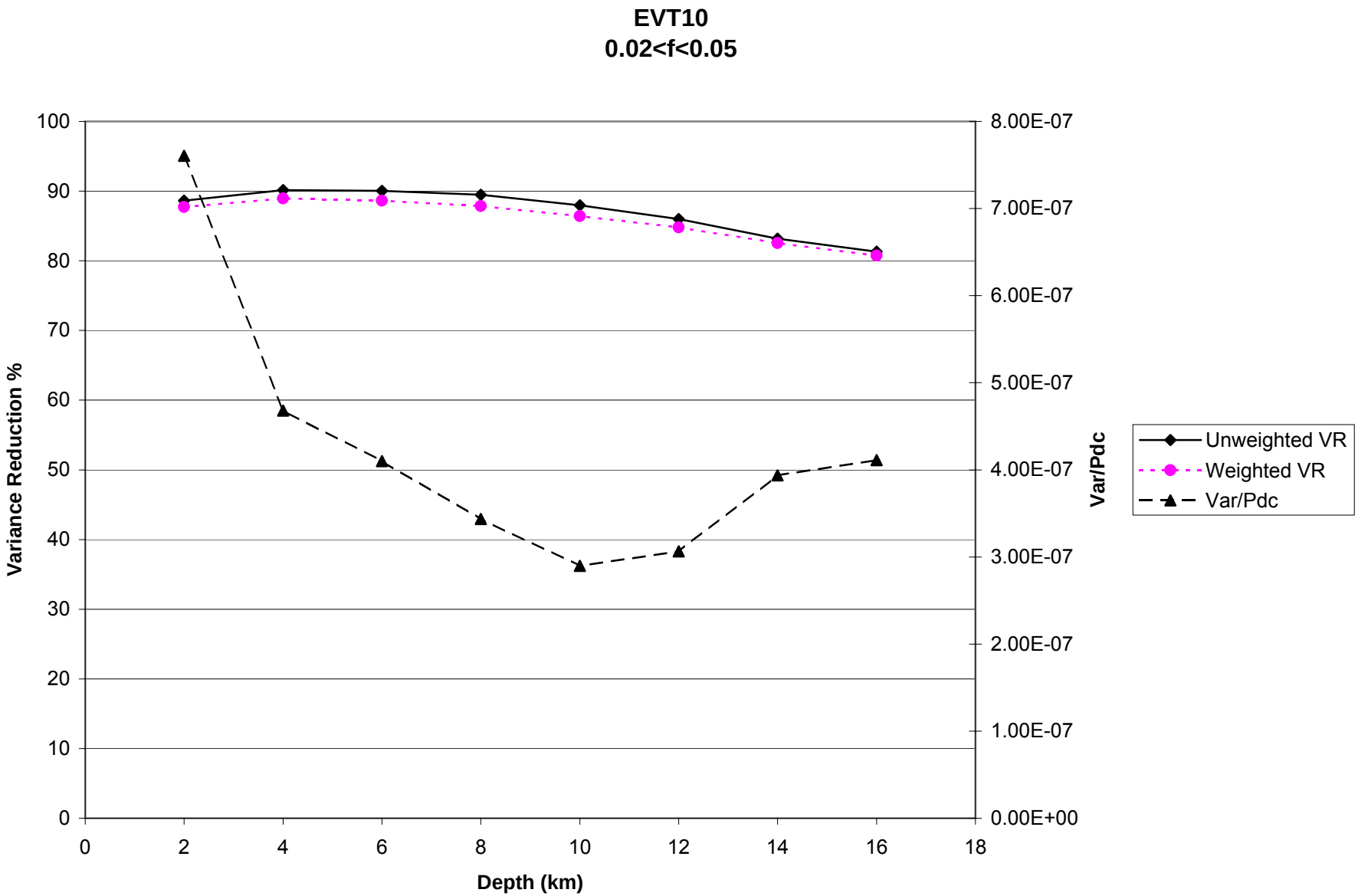
EVT10
0.02<f<0.05
Variance Reduction %
Var/Pdc
Depth (km)
Unweighted VR
Weighted VR
Var/Pdc
0
10
20
30
40
50
60
70
80
90
100
0.00E+00
1.00E-07
2.00E-07
3.00E-07
4.00E-07
5.00E-07
6.00E-07
7.00E-07
8.00E-07
0
2
4
6
8
10
12
14
16
18

Figure 28

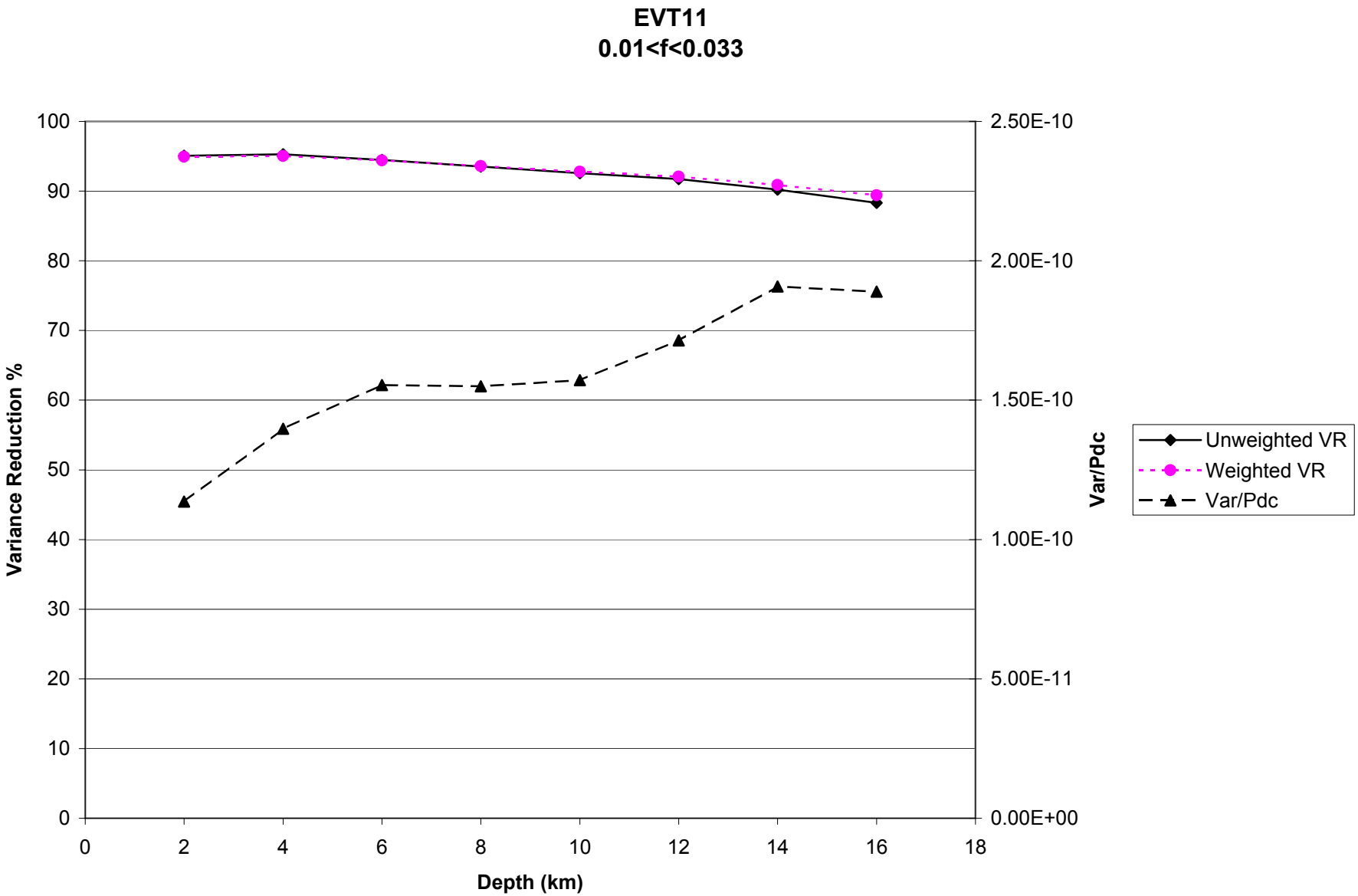
EVT11
0.01<f<0.033
Variance Reduction %
Var/Pdc
Depth (km)
100
90
80
70
60
50
40
30
20
10
0
2.50E-10
2.00E-10
1.50E-10
1.00E-10
5.00E-11
0.00E+00
0
2
4
6
8
10
12
14
16
18
Unweighted VR
Weighted VR
Var/Pdc

Figure 29

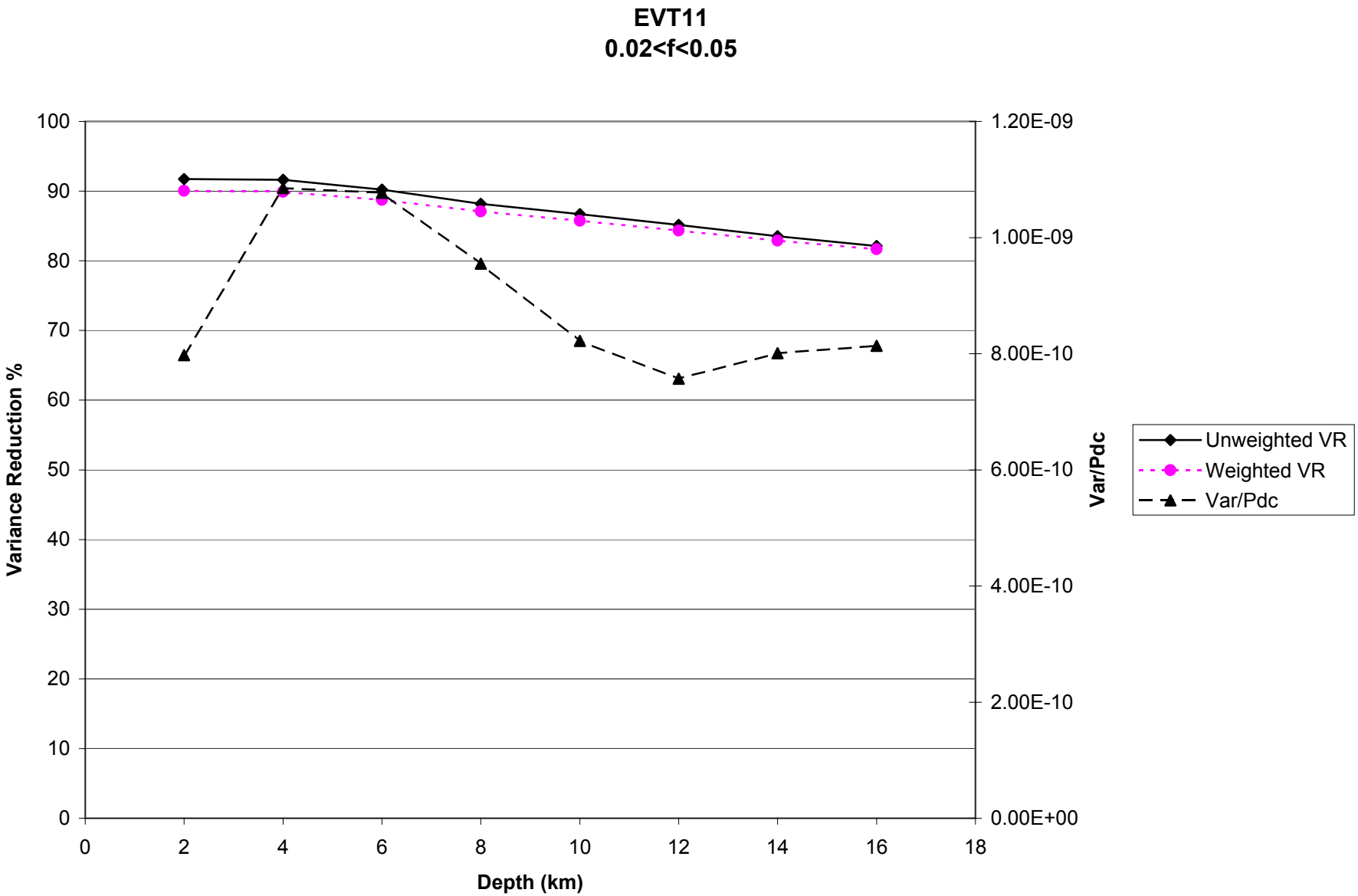
EVT11
0.02<f<0.05
Variance Reduction %
Var/Pdc
Depth (km)
100
90
80
70
60
50
40
30
20
10
0
1.20E-09
1.00E-09
8.00E-10
6.00E-10
4.00E-10
2.00E-10
0.00E+00
0
2
4
6
8
10
12
14
16
18
Unweighted VR
Weighted VR
Var/Pdc

Figure 30

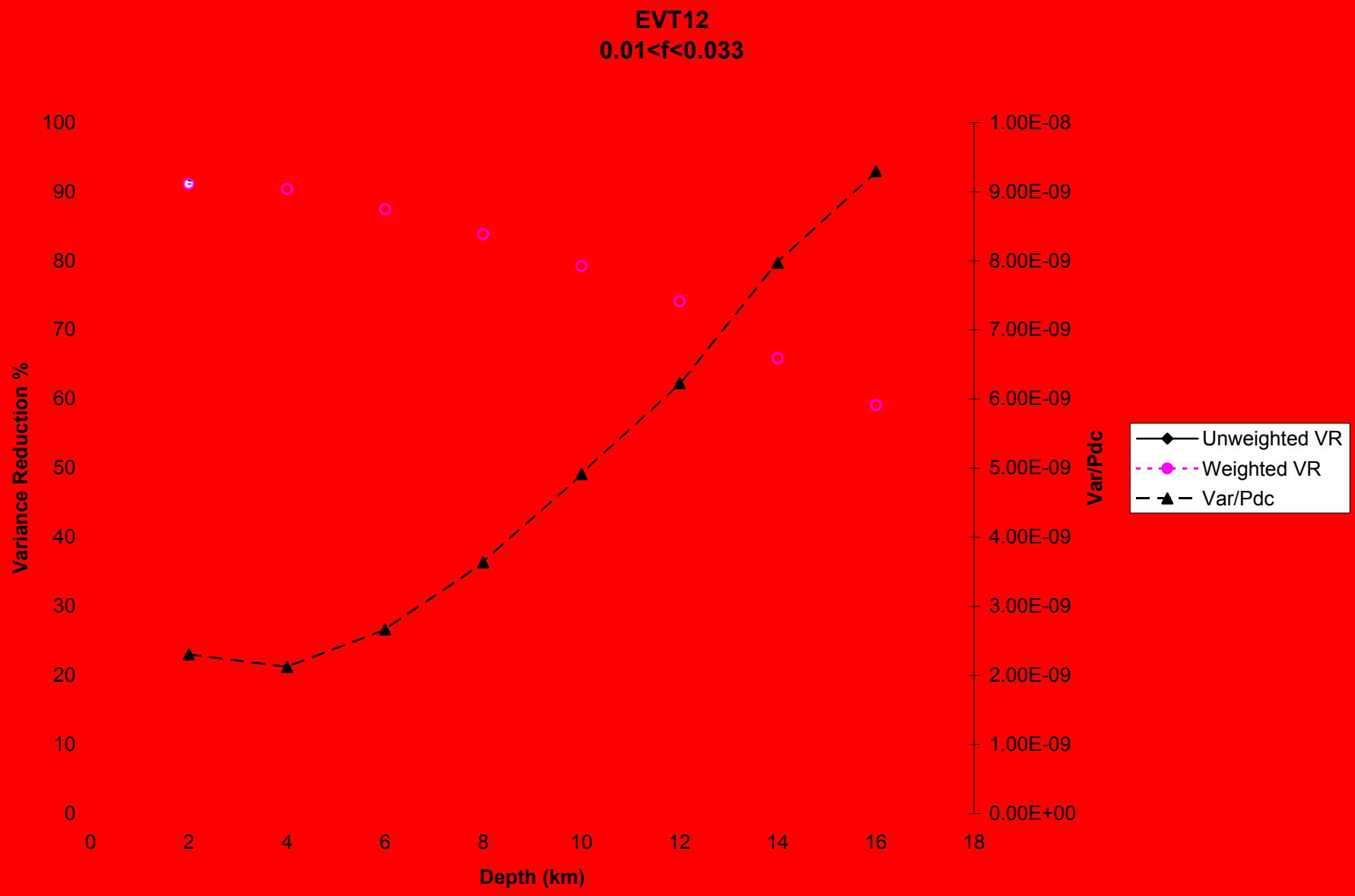
EVT12
0.01<f<0.033
Variance Reduction %
Var/Pdc
Depth (km)
Unweighted VR
Weighted VR
Var/Pdc
100
90
80
70
60
50
40
30
20
10
0
1.00E-08
9.00E-09
8.00E-09
7.00E-09
6.00E-09
5.00E-09
4.00E-09
3.00E-09
2.00E-09
1.00E-09
0.00E+00
0
2
4
6
8
10
12
14
16
18

Figure 31

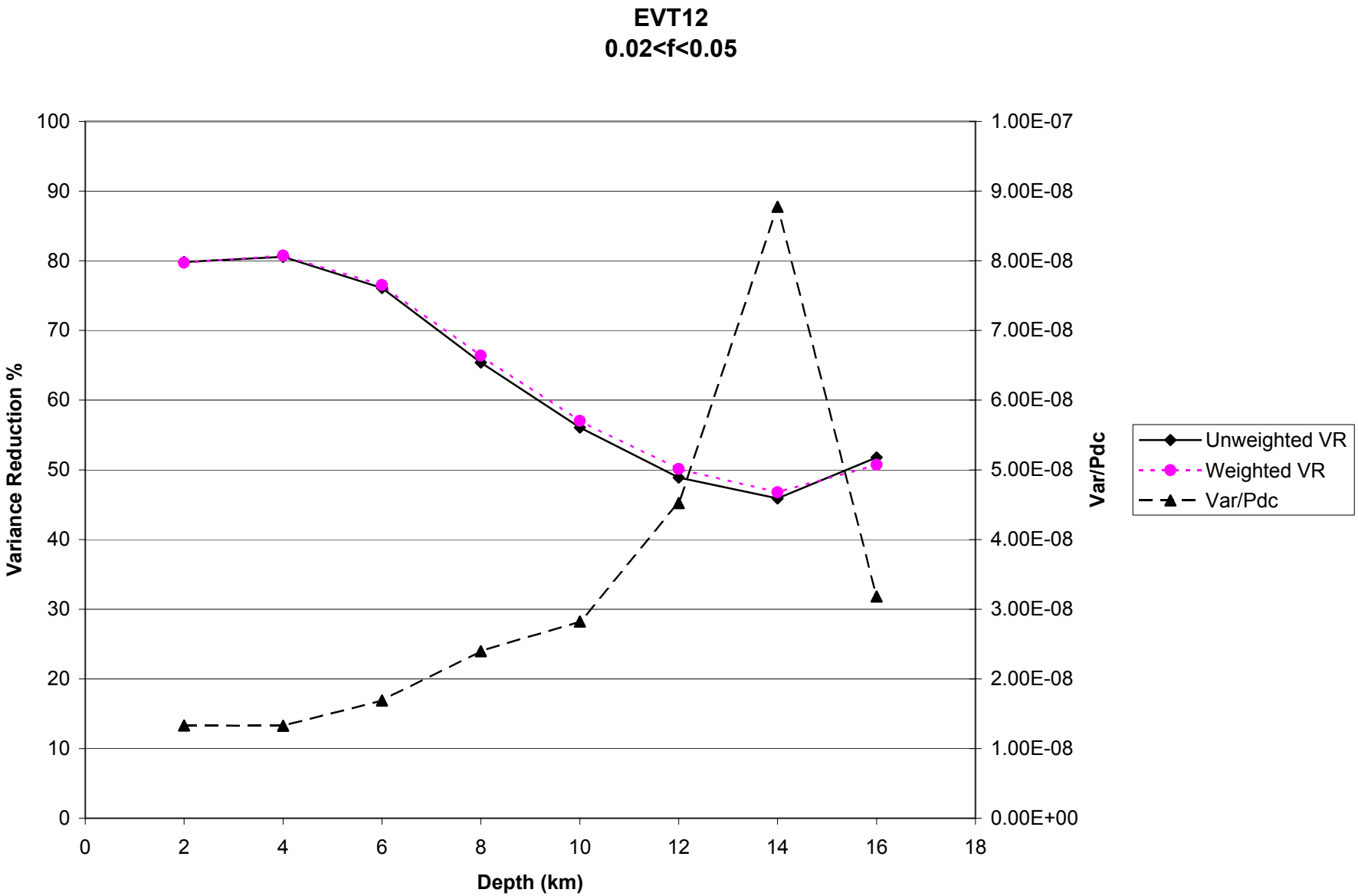
EVT12
0.02<f<0.05
Variance Reduction %
Var/Pdc
Depth (km)
Unweighted VR
Weighted VR
Var/Pdc
100
90
80
70
60
50
40
30
20
10
0
1.00E-07
9.00E-08
8.00E-08
7.00E-08
6.00E-08
5.00E-08
4.00E-08
3.00E-08
2.00E-08
1.00E-08
0.00E+00
0
2
4
6
8
10
12
14
16
18

Figure 32

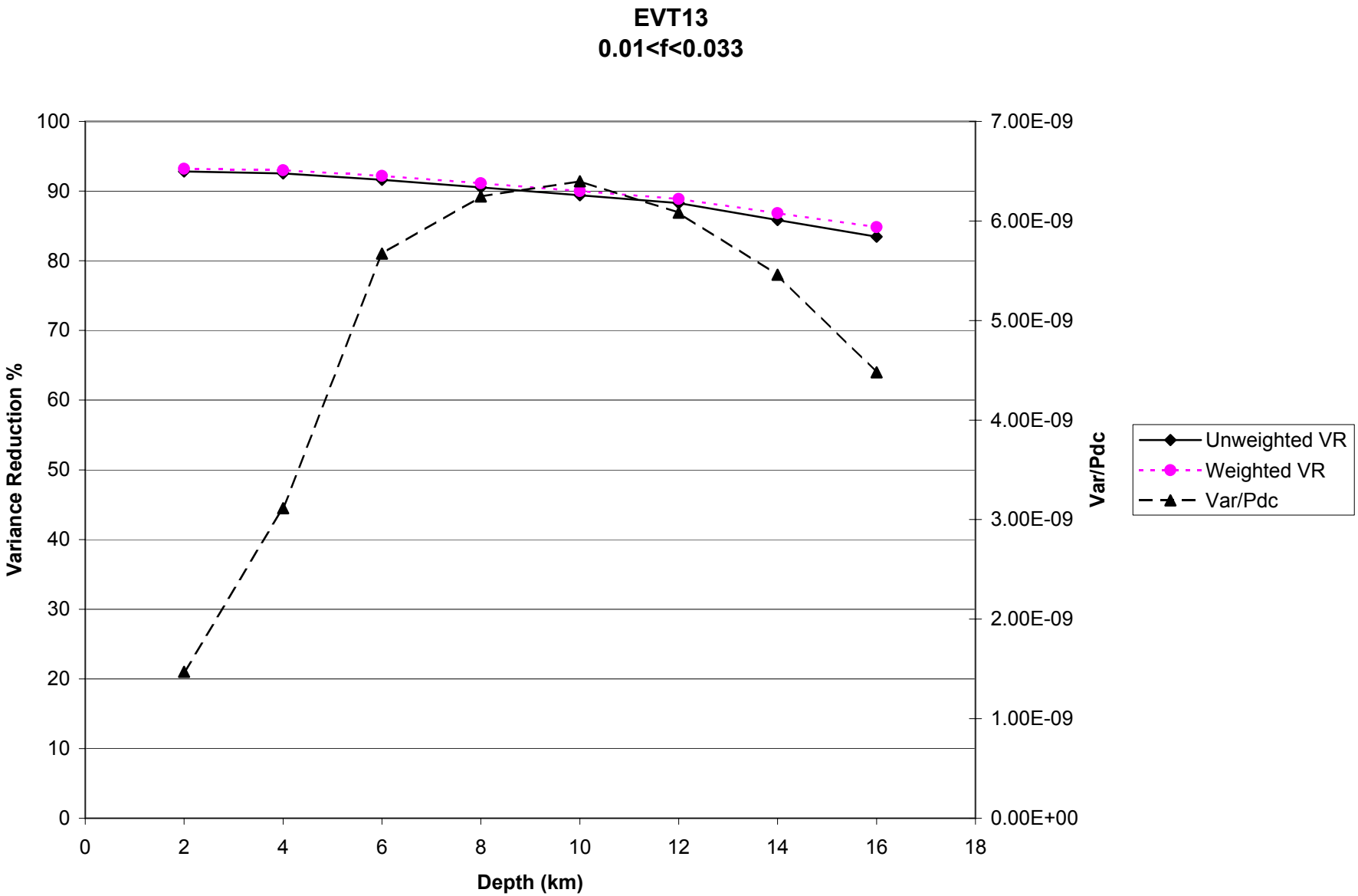
EVT13
0.01<f<0.033
Variance Reduction %
Var/Pdc
Depth (km)
Unweighted VR
Weighted VR
Var/Pdc
100
90
80
70
60
50
40
30
20
10
0
7.00E-09
6.00E-09
5.00E-09
4.00E-09
3.00E-09
2.00E-09
1.00E-09
0.00E+00
0
2
4
6
8
10
12
14
16
18

Figure 33

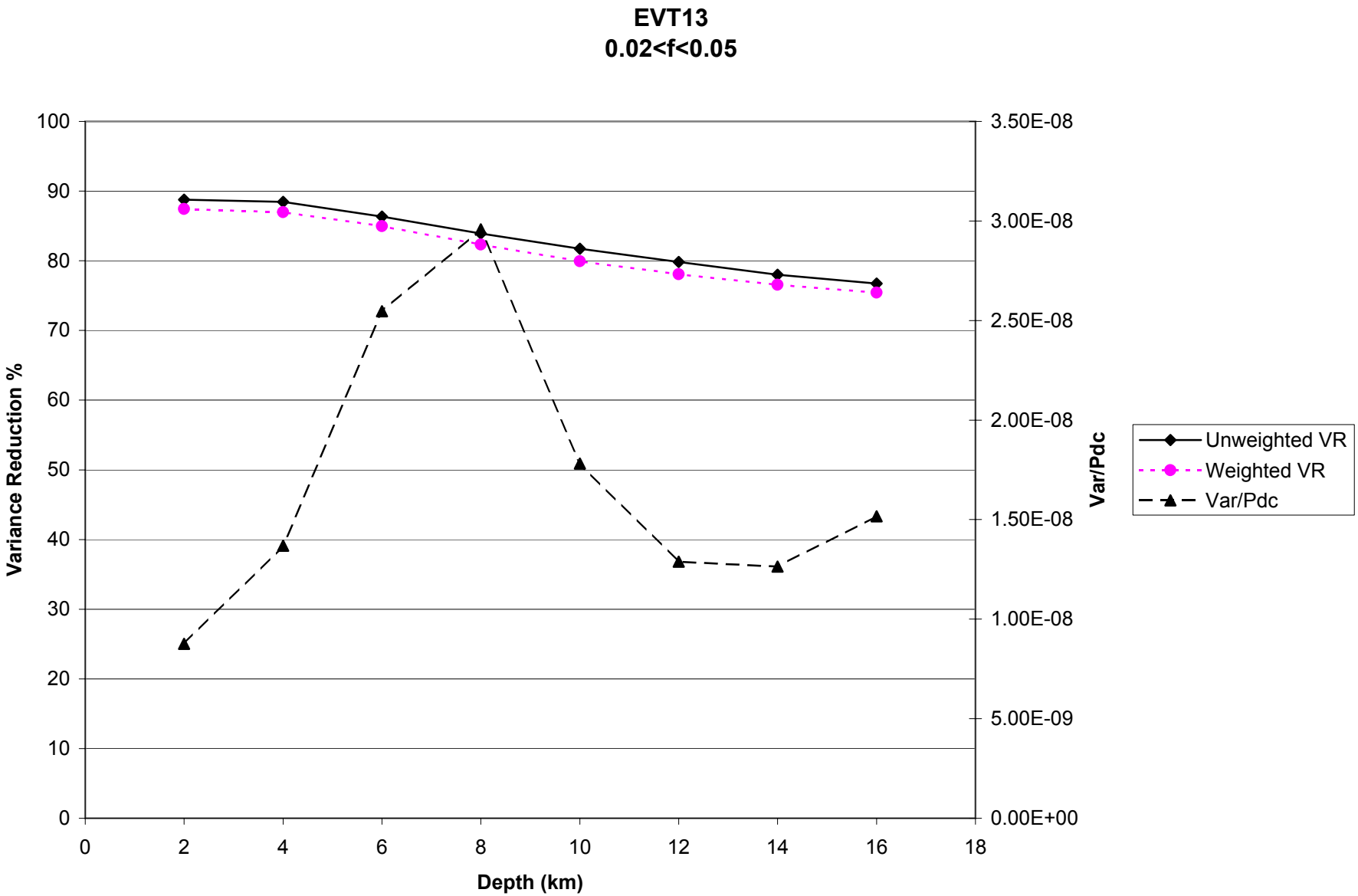
EVT13
0.02<f<0.05
Variance Reduction %
Var/Pdc
Depth (km)
Unweighted VR
Weighted VR
Var/Pdc
100
90
80
70
60
50
40
30
20
10
0
3.50E-08
3.00E-08
2.50E-08
2.00E-08
1.50E-08
1.00E-08
5.00E-09
0.00E+00
0
2
4
6
8
10
12
14
16
18

Figure 34

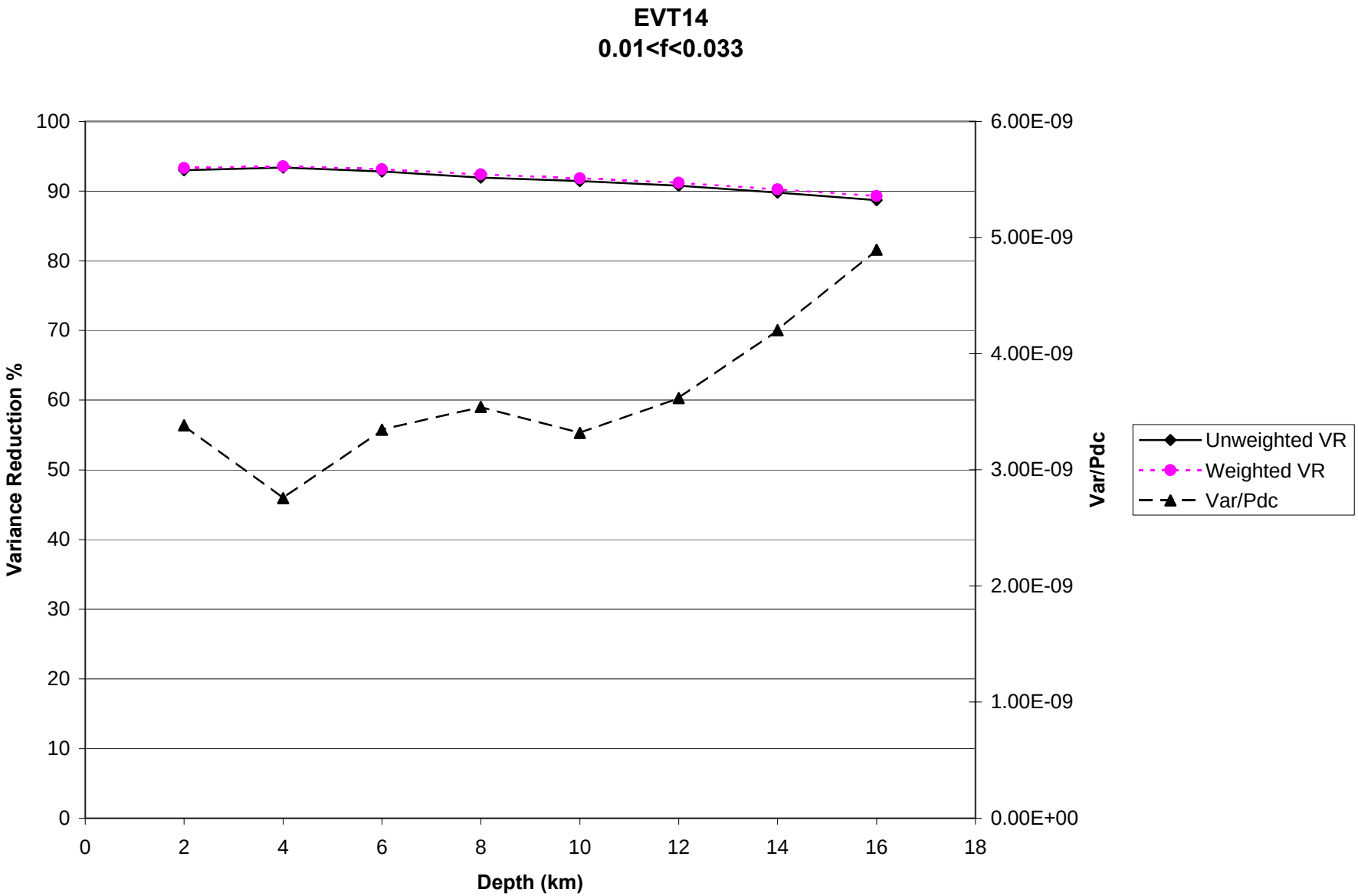
EVT14
0.01<f<0.033
Variance Reduction %
Var/Pdc
Depth (km)
100
90
80
70
60
50
40
30
20
10
0
6.00E-09
5.00E-09
4.00E-09
3.00E-09
2.00E-09
1.00E-09
0.00E+00
0
2
4
6
8
10
12
14
16
18
Unweighted VR
Weighted VR
Var/Pdc

Figure 35

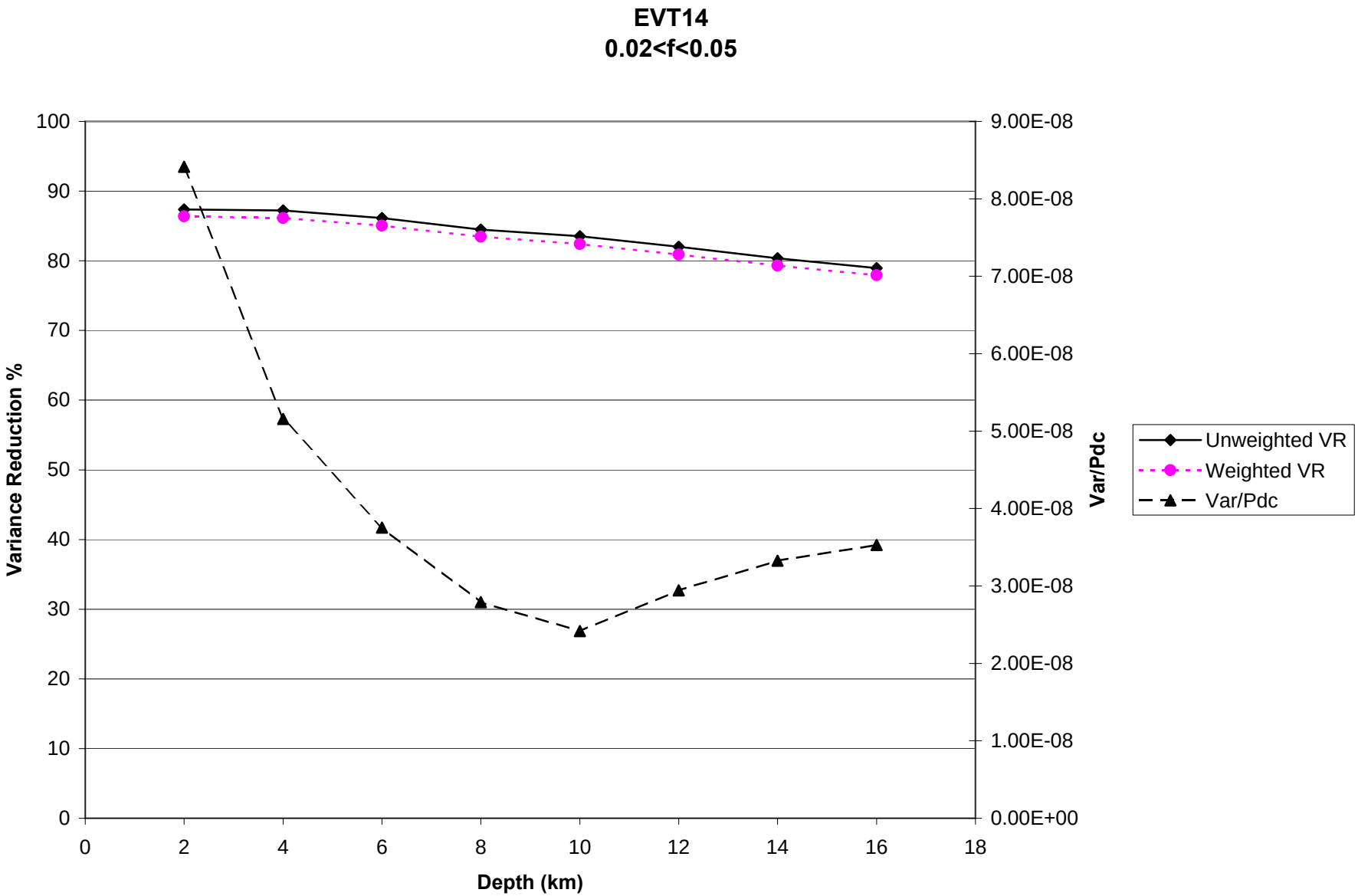
EVT14
0.02<f<0.05
Variance Reduction %
Var/Pdc
Depth (km)
Unweighted VR
Weighted VR
Var/Pdc
100
90
80
70
60
50
40
30
20
10
0
9.00E-08
8.00E-08
7.00E-08
6.00E-08
5.00E-08
4.00E-08
3.00E-08
2.00E-08
1.00E-08
0.00E+00
0
2
4
6
8
10
12
14
16
18

Figure 36

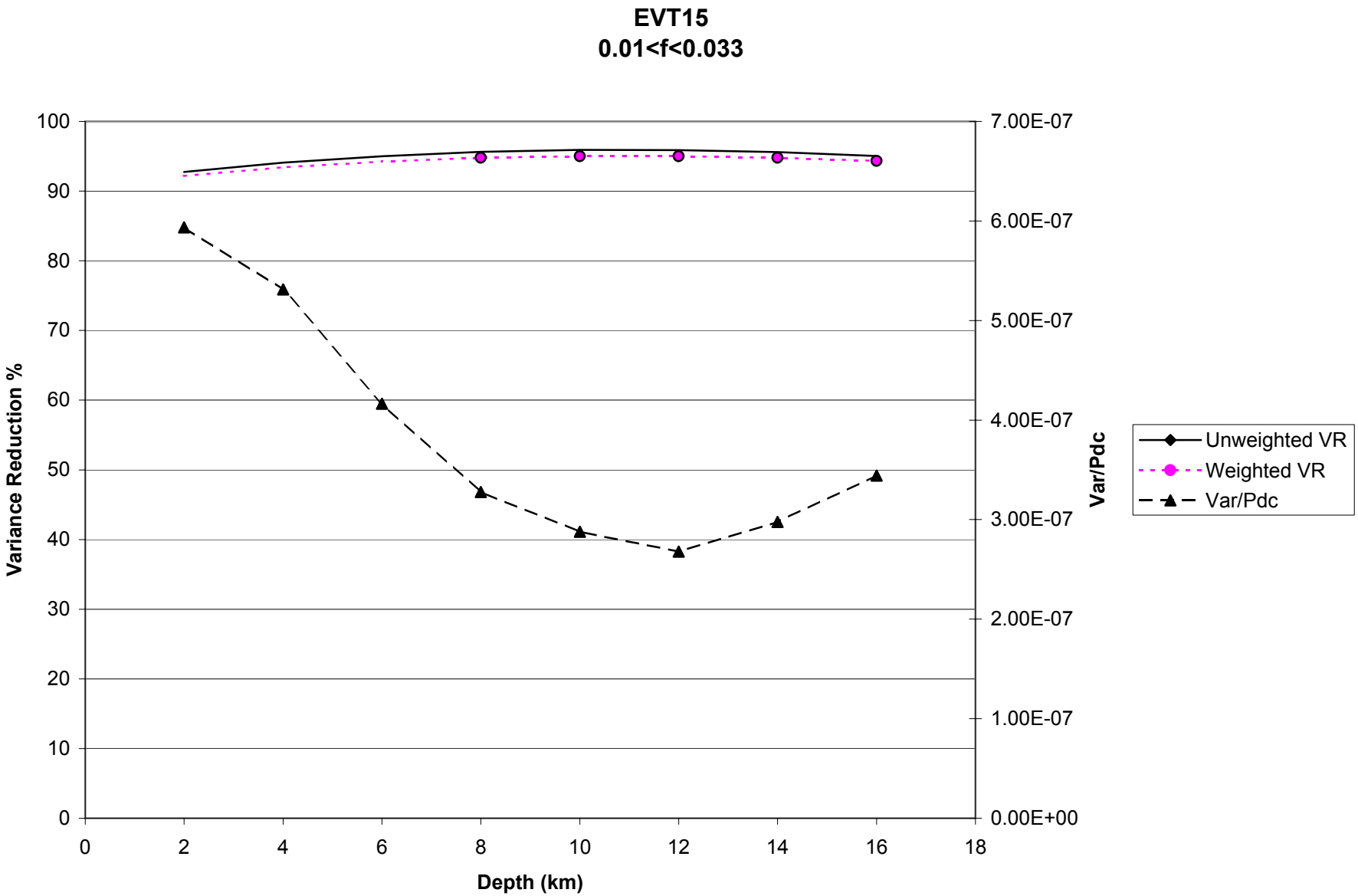
EVT15
0.01<f<0.033
Variance Reduction %
Var/Pdc
Depth (km)
Unweighted VR
Weighted VR
Var/Pdc
100
90
80
70
60
50
40
30
20
10
0
7.00E-07
6.00E-07
5.00E-07
4.00E-07
3.00E-07
2.00E-07
1.00E-07
0.00E+00
0
2
4
6
8
10
12
14
16
18

Figure 37

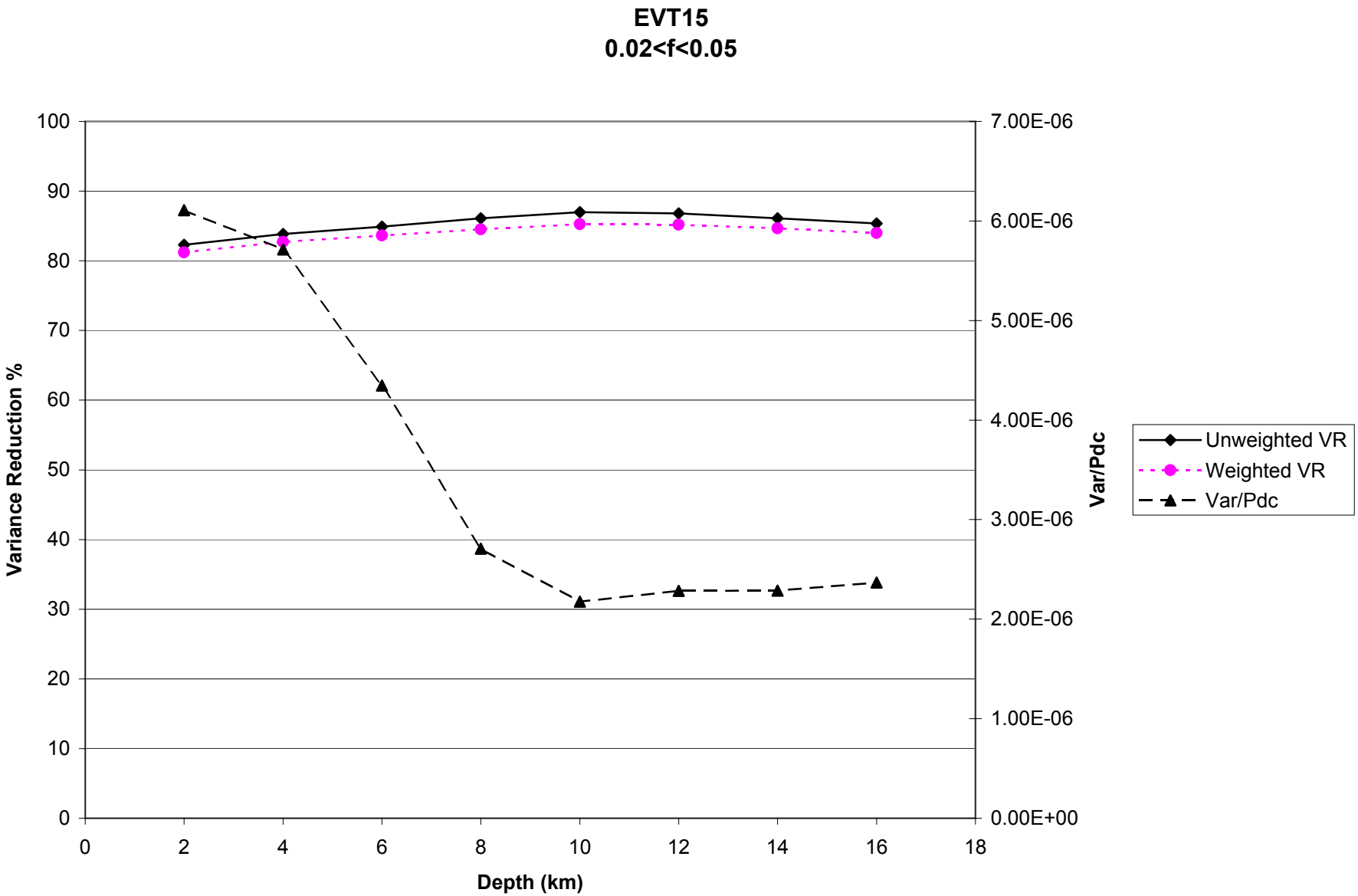
EVT15
0.02<f<0.05
Variance Reduction %
Var/Pdc
Depth (km)
100
90
80
70
60
50
40
30
20
10
0
7.00E-06
6.00E-06
5.00E-06
4.00E-06
3.00E-06
2.00E-06
1.00E-06
0.00E+00
0
2
4
6
8
10
12
14
16
18
Unweighted VR
Weighted VR
Var/Pdc

Figure 38

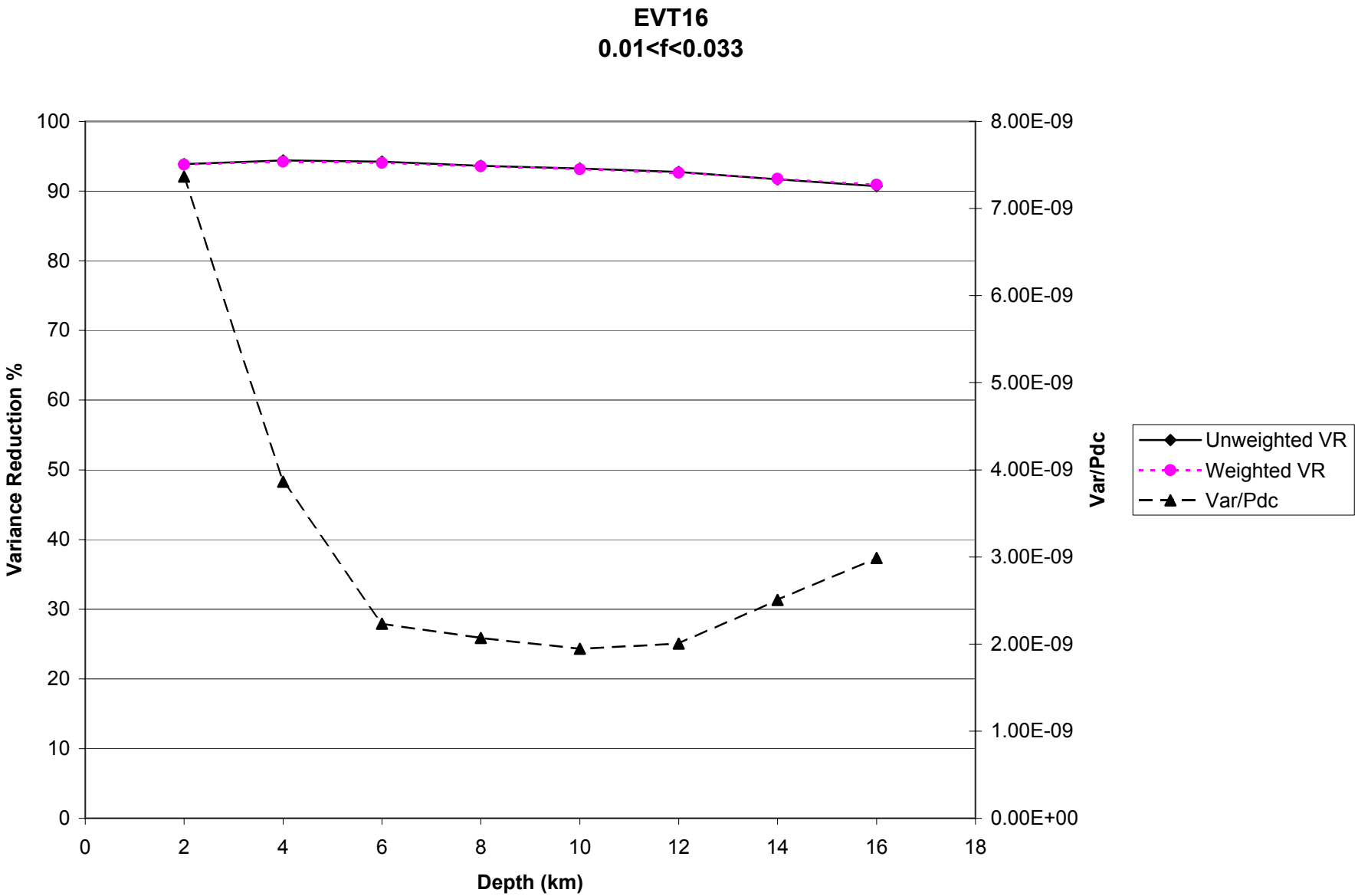
EVT16
0.01<f<0.033
Variance Reduction %
Var/Pdc
Depth (km)
Unweighted VR
Weighted VR
Var/Pdc
100
90
80
70
60
50
40
30
20
10
0
8.00E-09
7.00E-09
6.00E-09
5.00E-09
4.00E-09
3.00E-09
2.00E-09
1.00E-09
0.00E+00
0
2
4
6
8
10
12
14
16
18

Figure 39

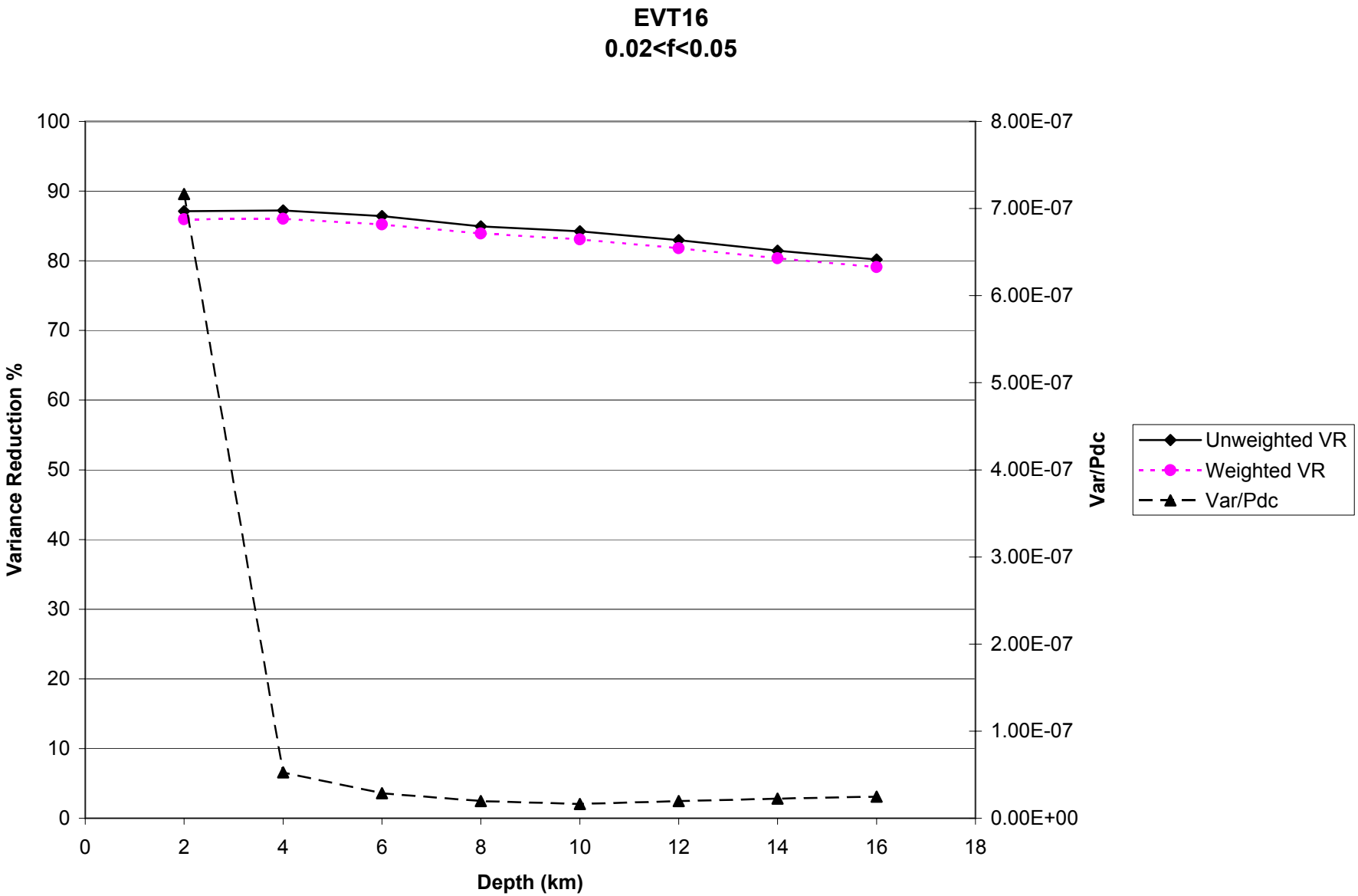
EVT16
0.02<f<0.05
Variance Reduction %
Var/Pdc
Depth (km)
Unweighted VR
Weighted VR
Var/Pdc
100
90
80
70
60
50
40
30
20
10
0
8.00E-07
7.00E-07
6.00E-07
5.00E-07
4.00E-07
3.00E-07
2.00E-07
1.00E-07
0.00E+00
0
2
4
6
8
10
12
14
16
18

Figure 40

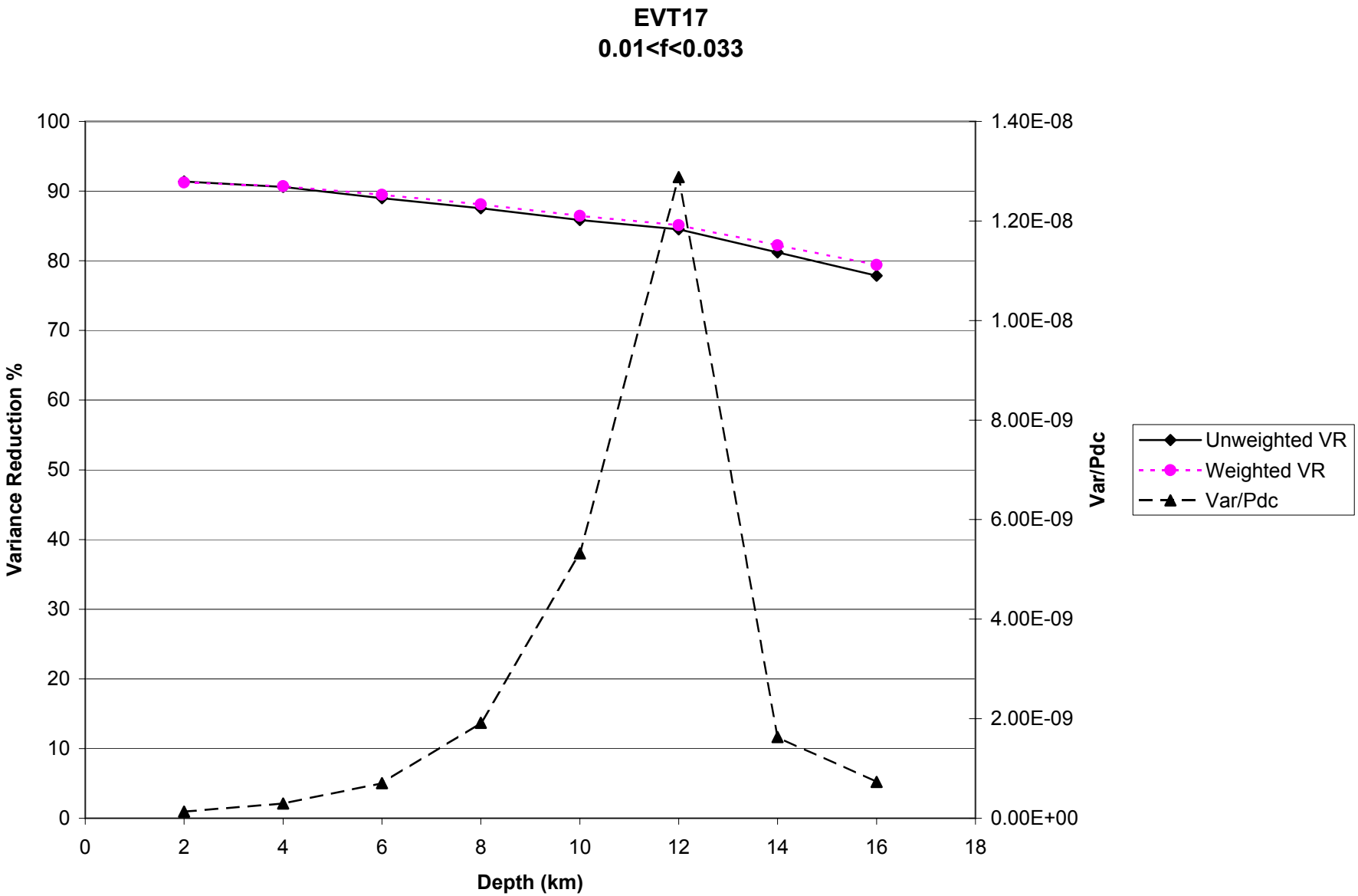
EVT17
0.01<f<0.033
Variance Reduction %
Var/Pdc
Depth (km)
Unweighted VR
Weighted VR
Var/Pdc
100
90
80
70
60
50
40
30
20
10
0
1.40E-08
1.20E-08
1.00E-08
8.00E-09
6.00E-09
4.00E-09
2.00E-09
0.00E+00
0
2
4
6
8
10
12
14
16
18

Figure 41

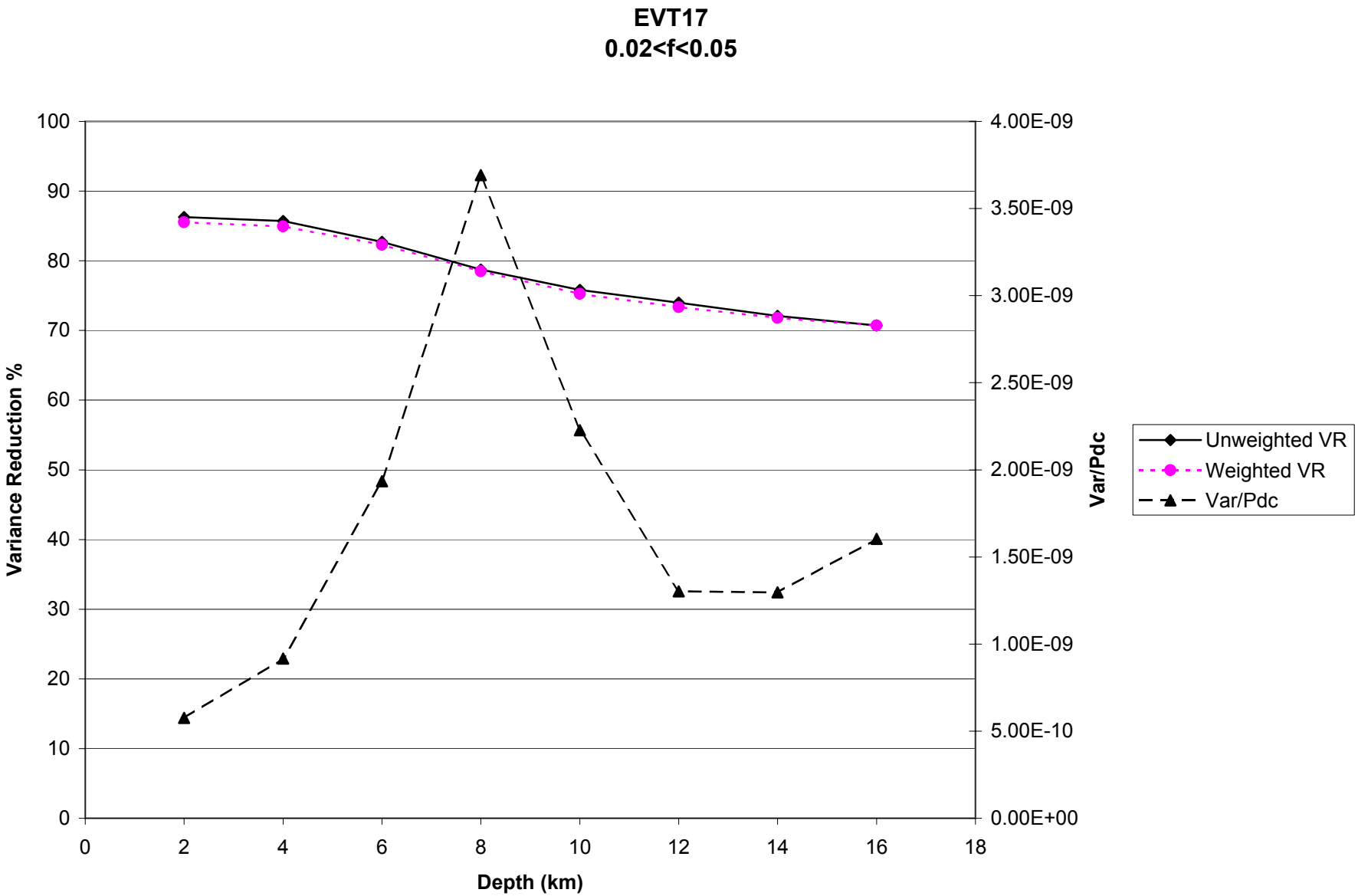
EVT17
0.02<f<0.05
Variance Reduction %
Var/Pdc
Depth (km)
Unweighted VR
Weighted VR
Var/Pdc
100
90
80
70
60
50
40
30
20
10
0
4.00E-09
3.50E-09
3.00E-09
2.50E-09
2.00E-09
1.50E-09
1.00E-09
5.00E-10
0.00E+00
0
2
4
6
8
10
12
14
16
18

Figure 42

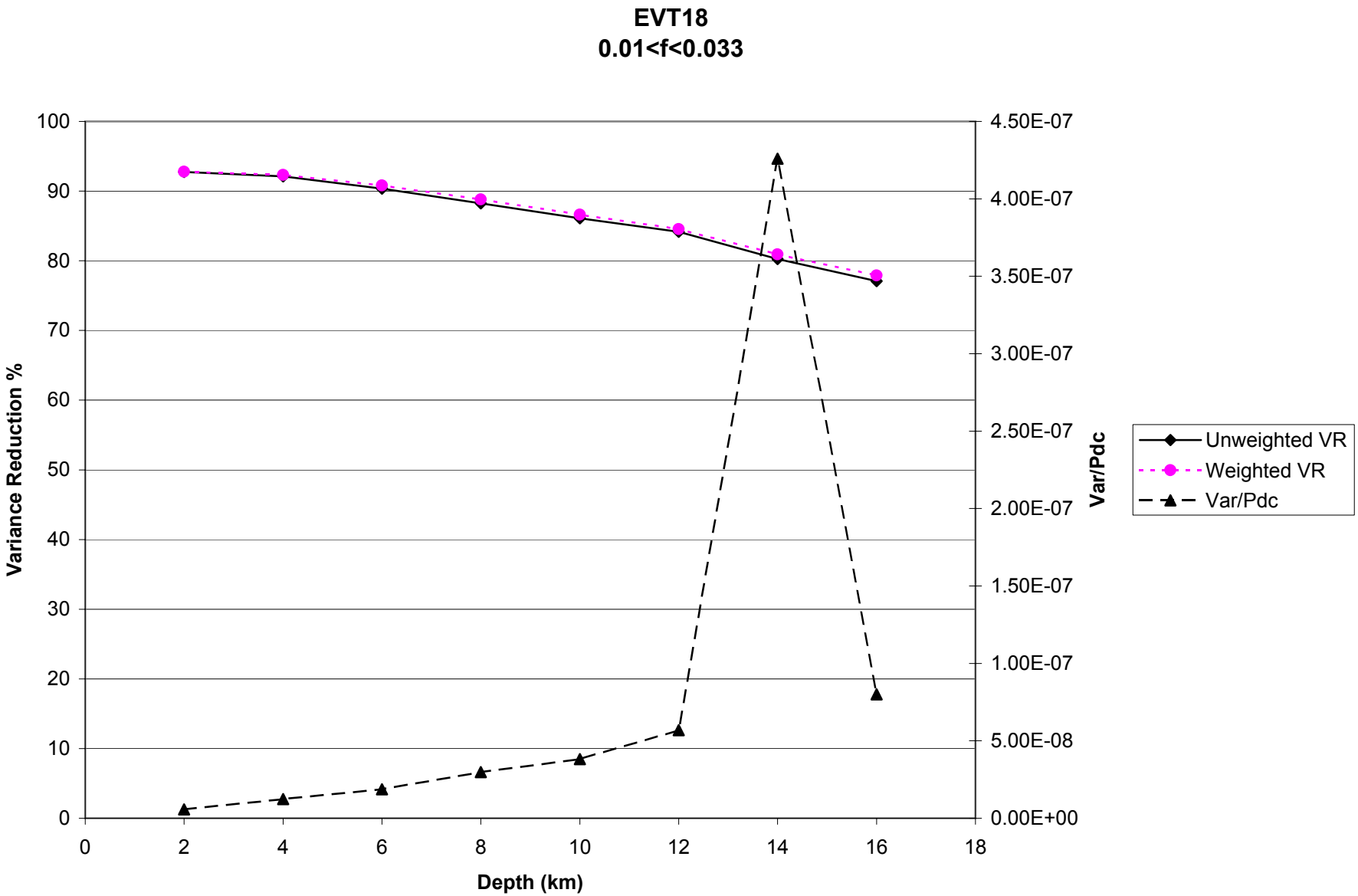
EVT18
0.01<f<0.033
Variance Reduction %
Var/Pdc
Depth (km)
Unweighted VR
Weighted VR
Var/Pdc
0
10
20
30
40
50
60
70
80
90
100
0.00E+00
5.00E-08
1.00E-07
1.50E-07
2.00E-07
2.50E-07
3.00E-07
3.50E-07
4.00E-07
4.50E-07
0
2
4
6
8
10
12
14
16
18

Figure 43

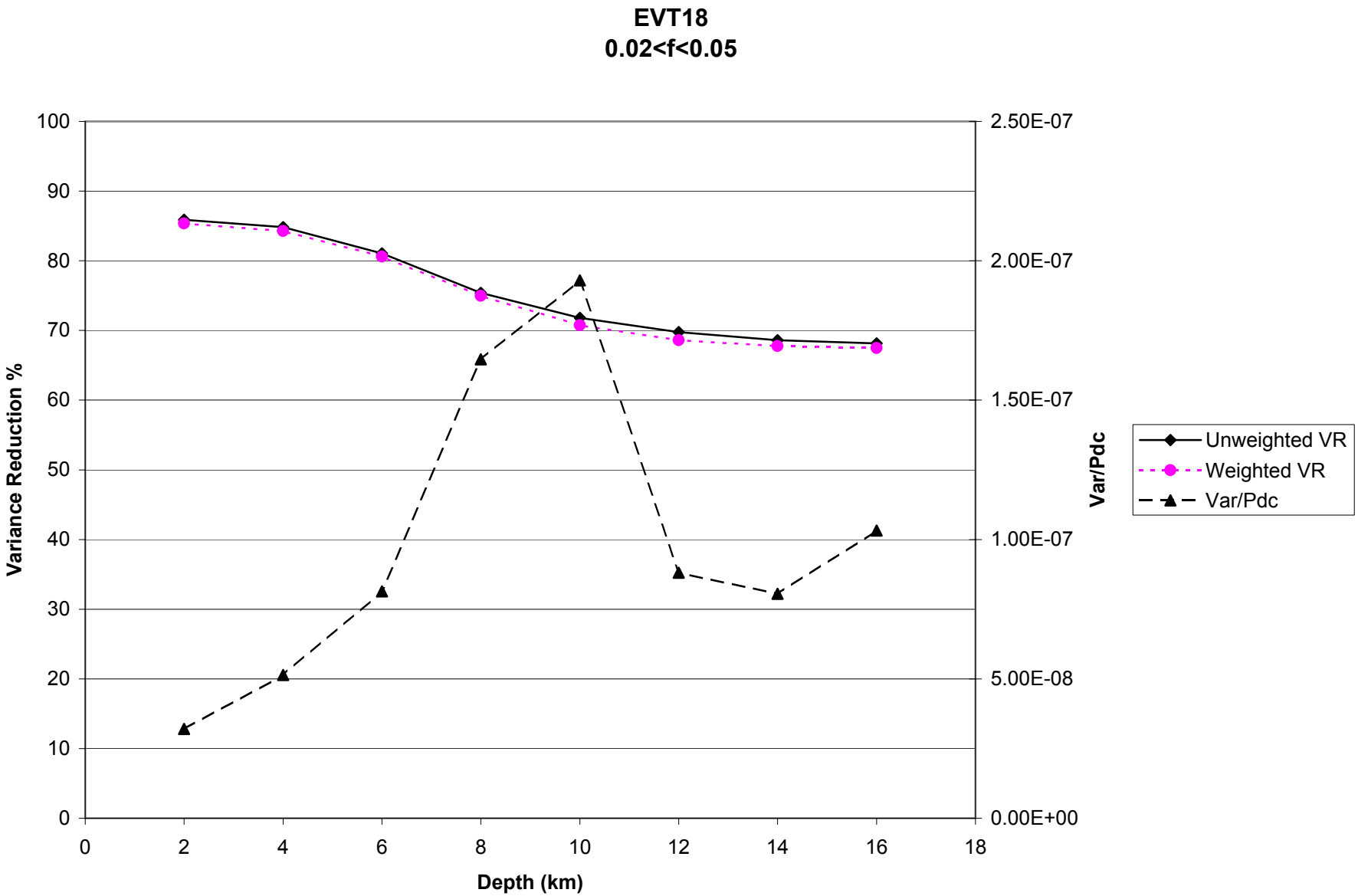
EVT18
0.02<f<0.05
Variance Reduction %
Var/Pdc
Depth (km)
Unweighted VR
Weighted VR
Var/Pdc
100
90
80
70
60
50
40
30
20
10
0
2.50E-07
2.00E-07
1.50E-07
1.00E-07
5.00E-08
0.00E+00
0
2
4
6
8
10
12
14
16
18

Figure 44

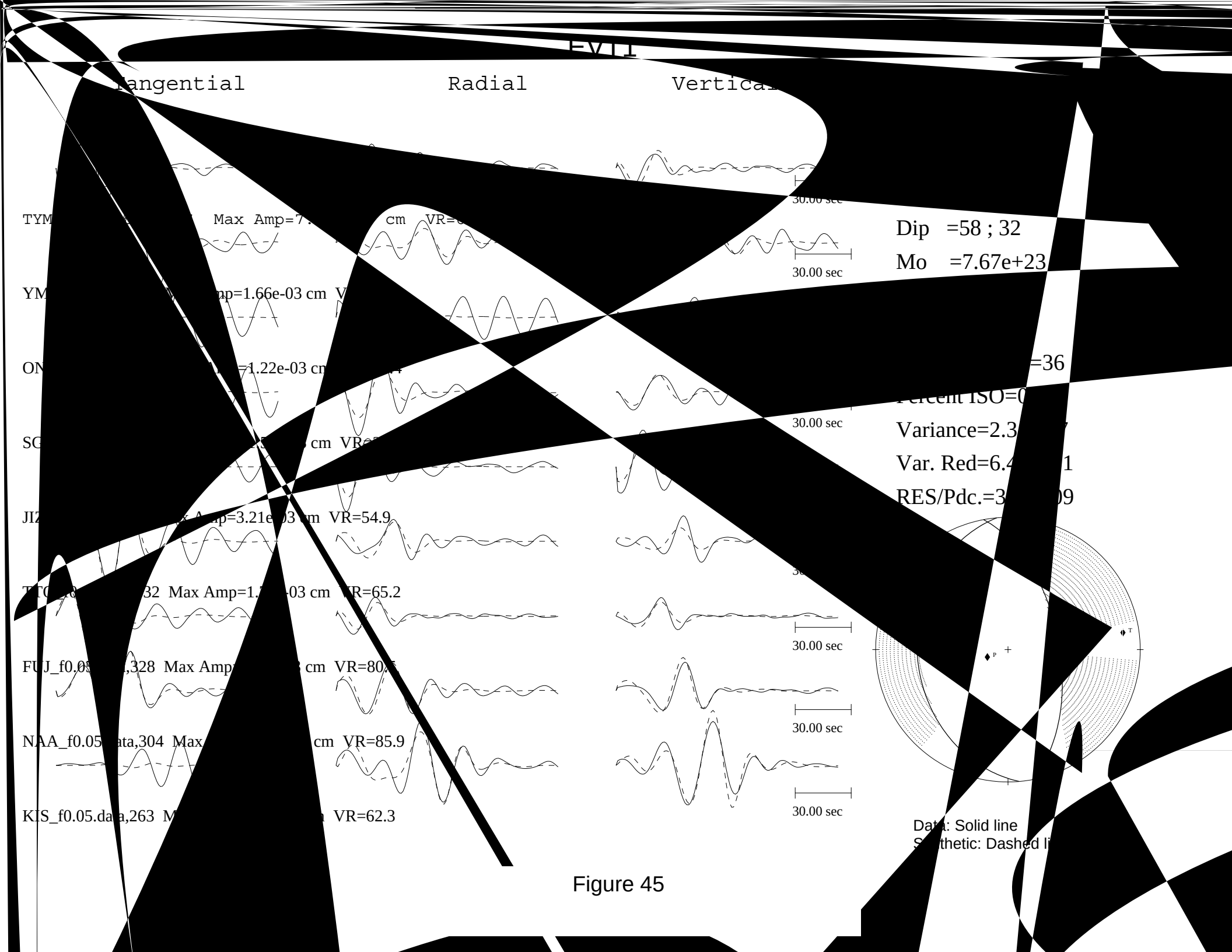
Tangential
Radial
Vertica
Max Amp=7.
cm VR=
30.00 sec
Dip =58 ; 32
Mo =7.67e+23
mp=1.66e-03 cm V
=1.22e-03 cm
=36
Percent ISO=0
Variance=2.3
Var. Red=6.4
1
RES/Pdc.=3
09
cm VR
Amp=3.21e
m VR=54.9
32 Max Amp=1.
-03 cm R=65.2
328 Max Amp=
cm VR=80.
NAA_f0.05
ata,304 Max
cm VR=85.9
KIS_f0.05.da
a,263 M
VR=62.3
Data: Solid line
Synthetic: Dashed li

Figure 45

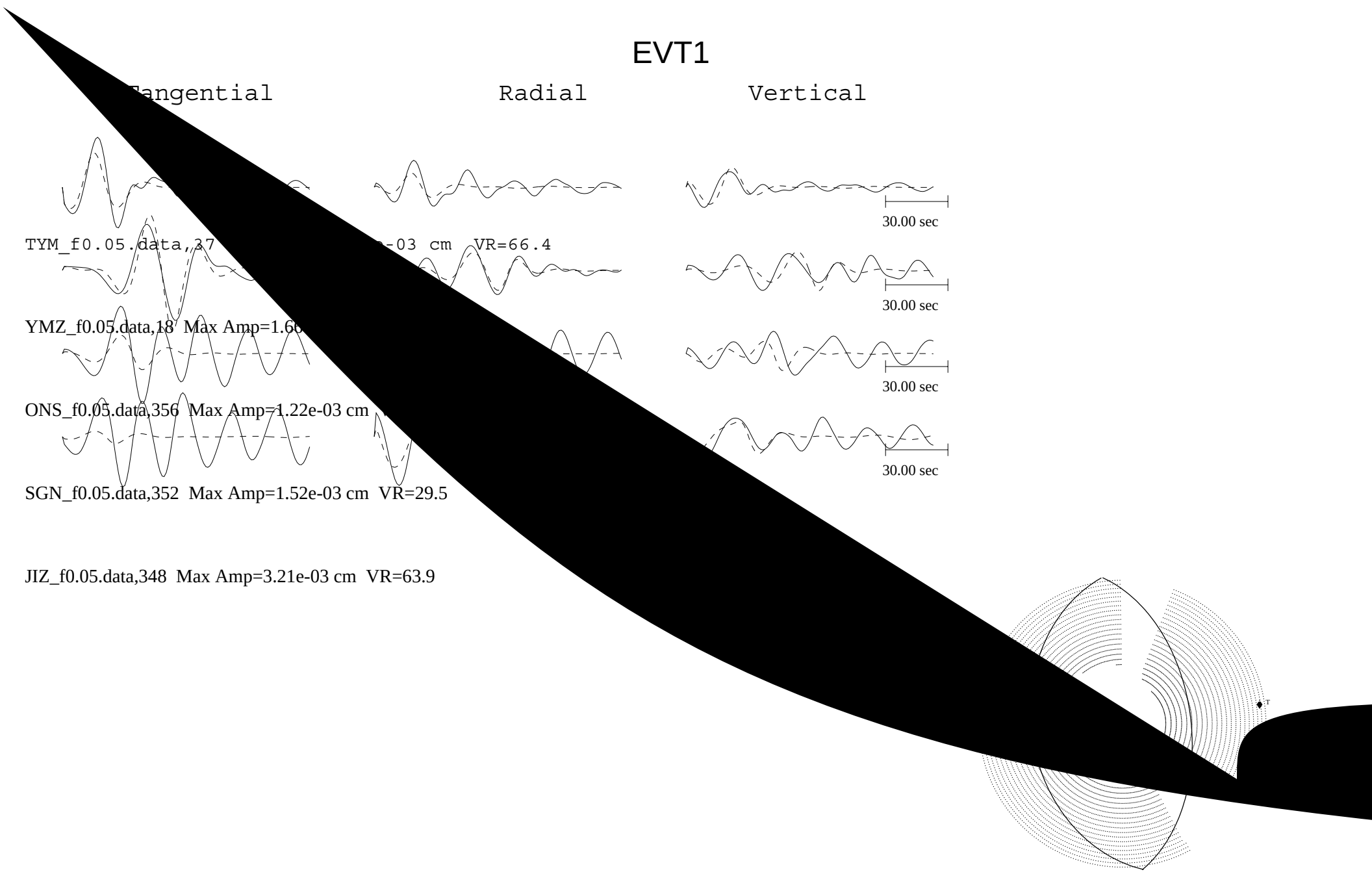
EVT1
Tangential
Radial
Vertical
30.00 sec
30.00 sec
30.00 sec
30.00 sec
TYM_f0.05.data,37
-03 cm VR=66.4
YMZ_f0.05.data,18 Max Amp=1.66
ONS_f0.05.data,356 Max Amp=1.22e-03 cm
SGN_f0.05.data,352 Max Amp=1.52e-03 cm VR=29.5
JIZ_f0.05.data,348 Max Amp=3.21e-03 cm VR=63.9

Figure 46

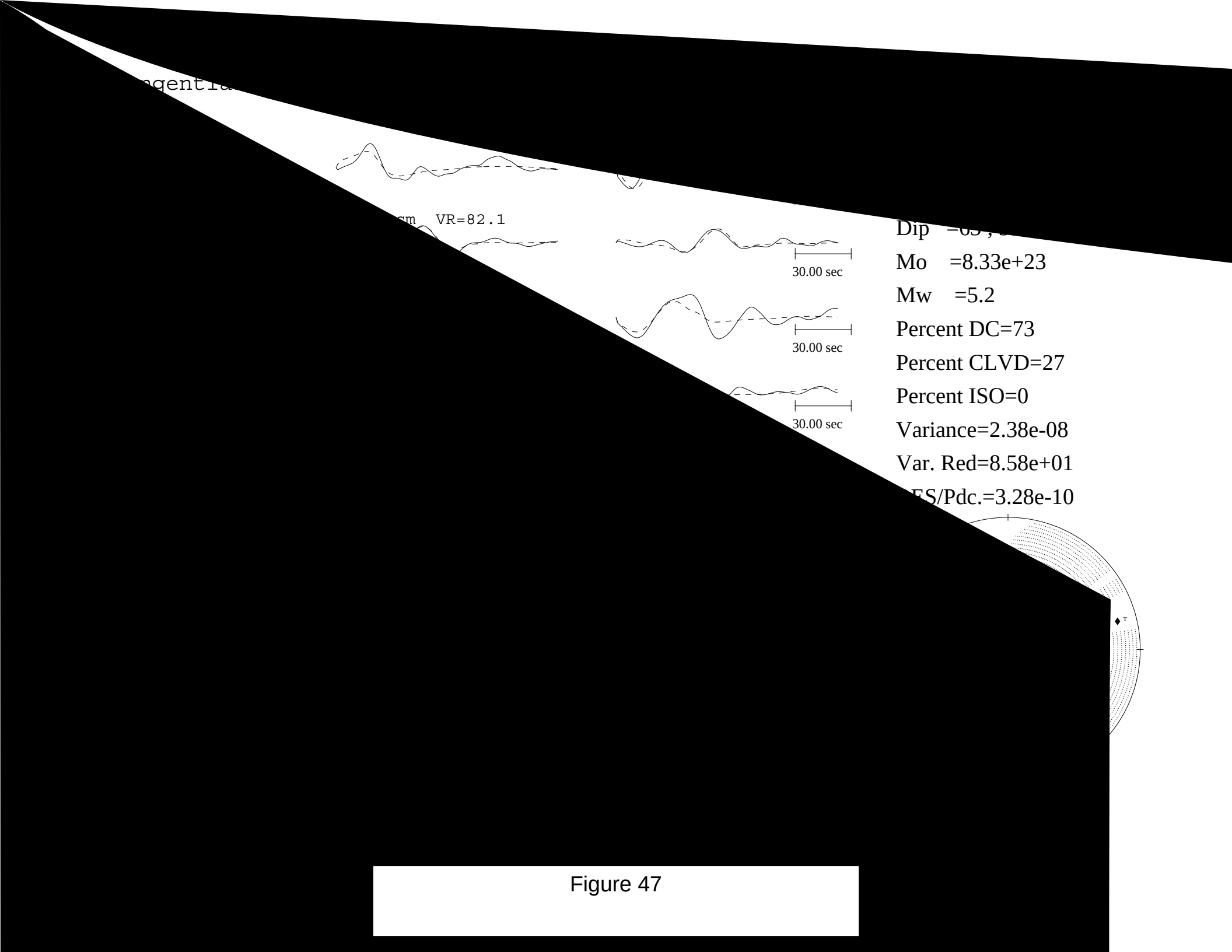
VR=82.1
30.00 sec
30.00 sec
30.00 sec
Dip =
Mo =8.33e+23
Mw =5.2
Percent DC=73
Percent CLVD=27
Percent ISO=0
Variance=2.38e-08
Var. Red=8.58e+01
ES/Pdc.=3.28e-10

Figure 47

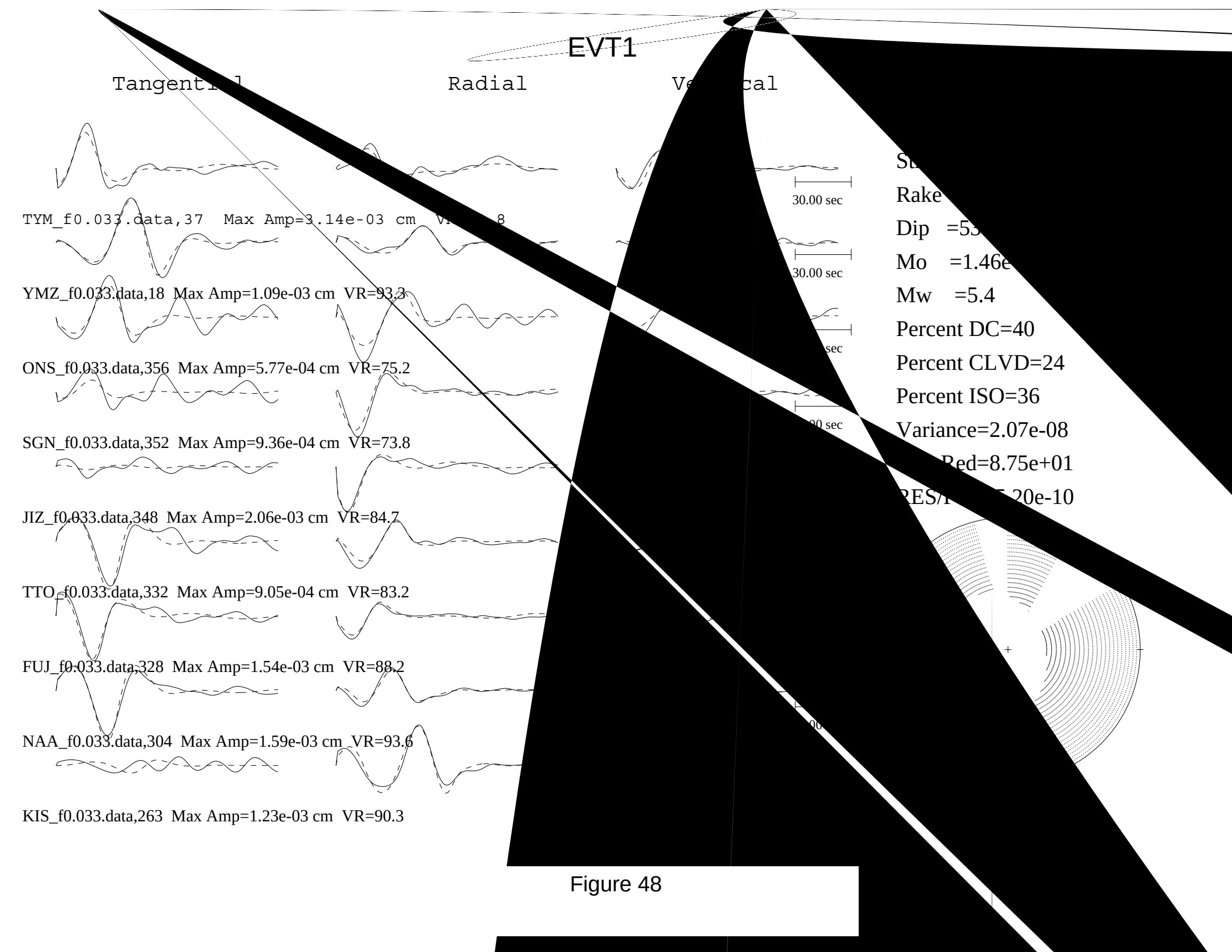
EVT1
Tangential
Radial
Vertical
30.00 sec
30.00 sec
TYM_f0.033.data,37 Max Amp=3.14e-03 cm
YMZ_f0.033.data,18 Max Amp=1.09e-03 cm VR=93.3
ONS_f0.033.data,356 Max Amp=5.77e-04 cm VR=75.2
SGN_f0.033.data,352 Max Amp=9.36e-04 cm VR=73.8
JIZ_f0.033.data,348 Max Amp=2.06e-03 cm VR=84.7
TTO_f0.033.data,332 Max Amp=9.05e-04 cm VR=83.2
FUJ_f0.033.data,328 Max Amp=1.54e-03 cm VR=88.2
NAA_f0.033.data,304 Max Amp=1.59e-03 cm VR=93.6
KIS_f0.033.data,263 Max Amp=1.23e-03 cm VR=90.3
Rake
Dip =53
Mo =1.46e
Mw =5.4
Percent DC=40
Percent CLVD=24
Percent ISO=36
Variance=2.07e-08
Red=8.75e+01
20e-10

Figure 48

EVT2

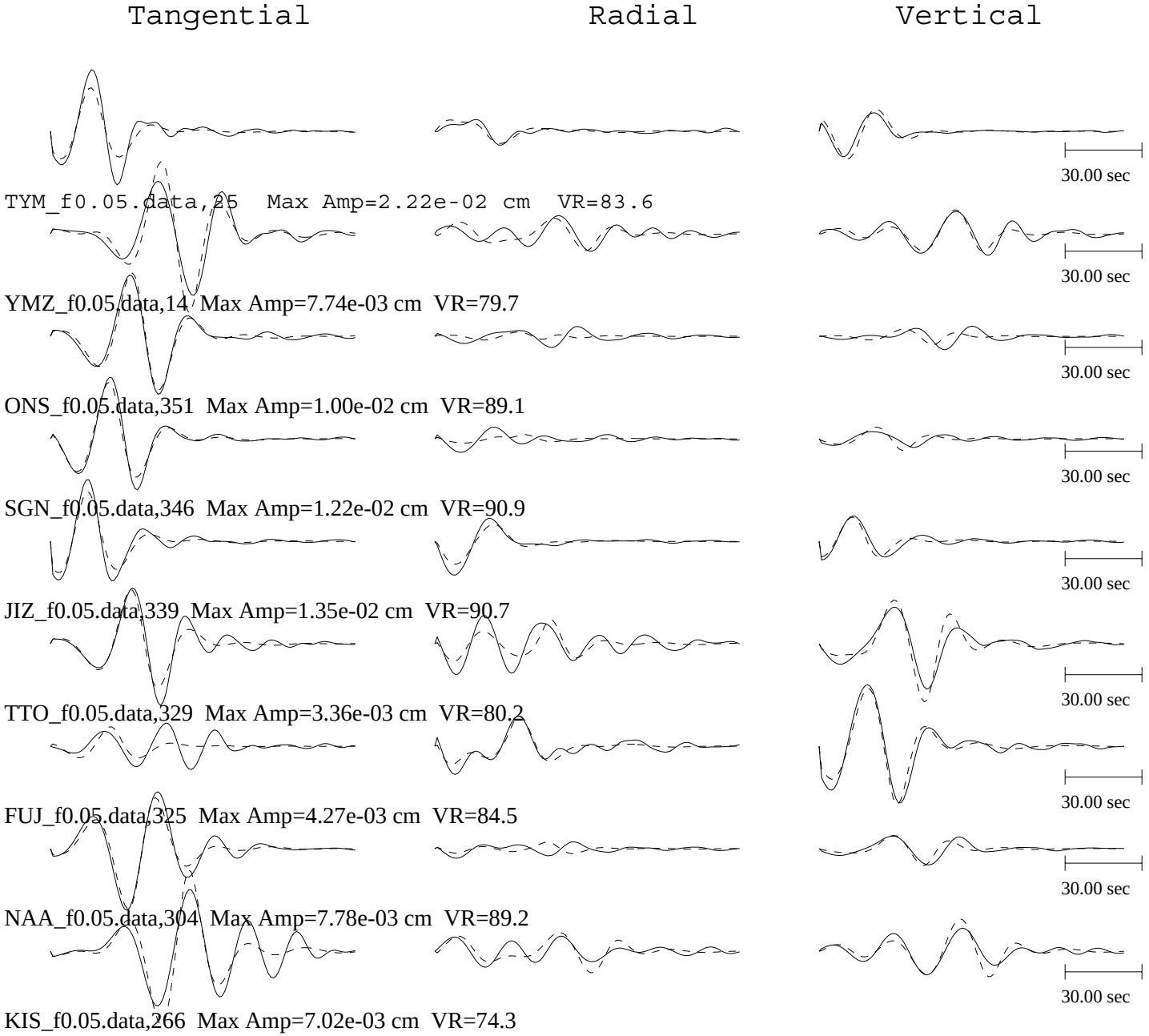

Strike=117 ; 356
Rake =-126 ; -39
Dip =65 ; 43
Mo =2.13e+24
Mw =5.5
Percent DC=23
Percent CLVD=77
Percent ISO=0
Variance=7.77e-07
Var. Red=8.44e+01
RES/Pdc.=3.44e-08

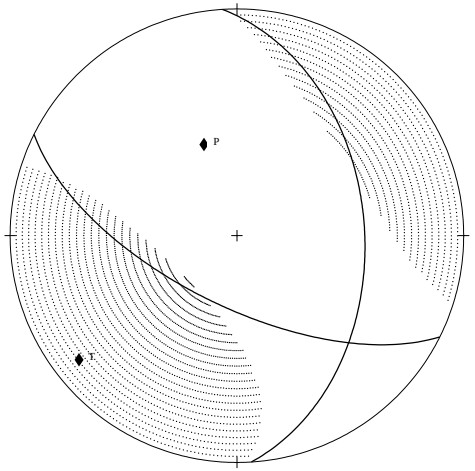

Figure 49

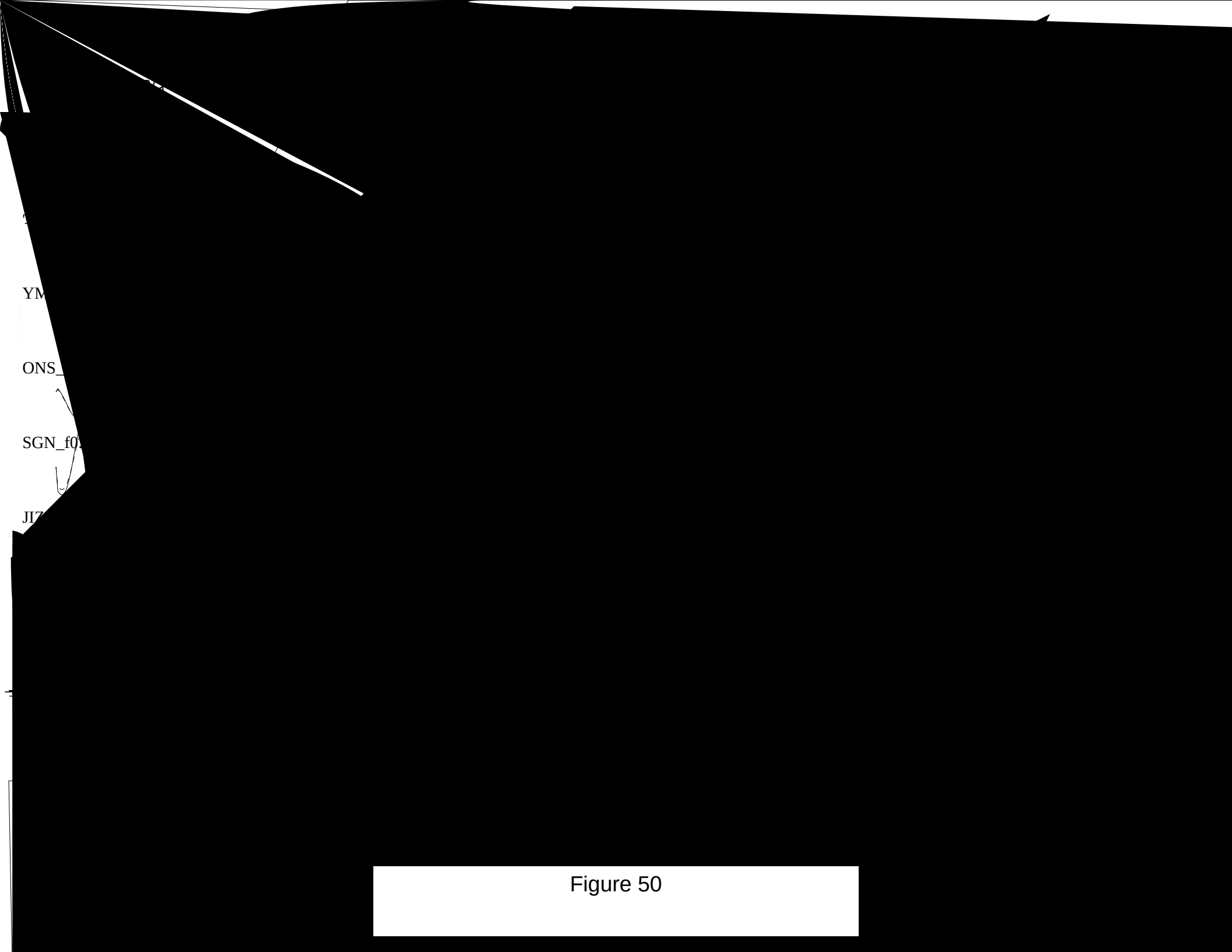

Figure 50

EVT2

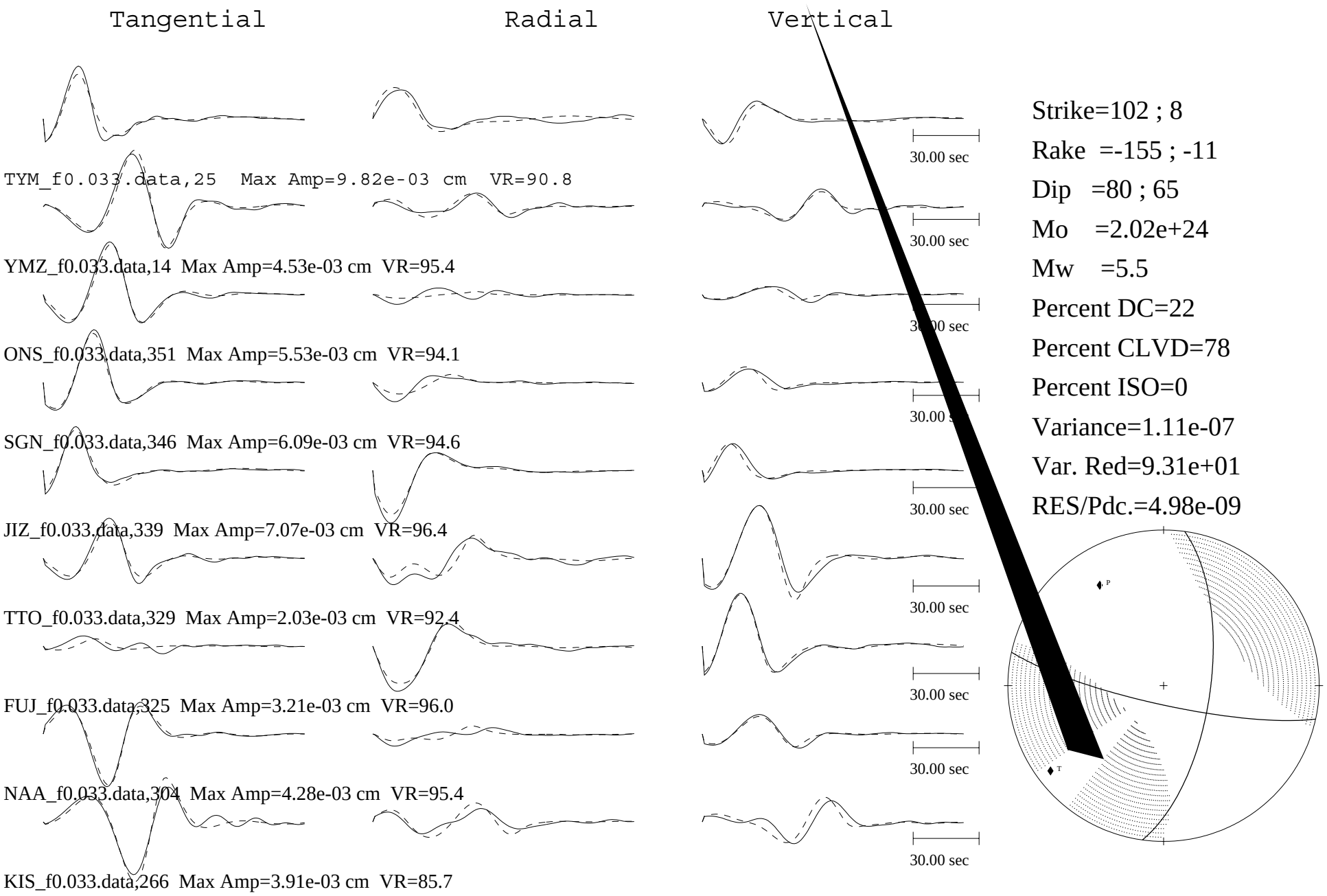

Figure 51

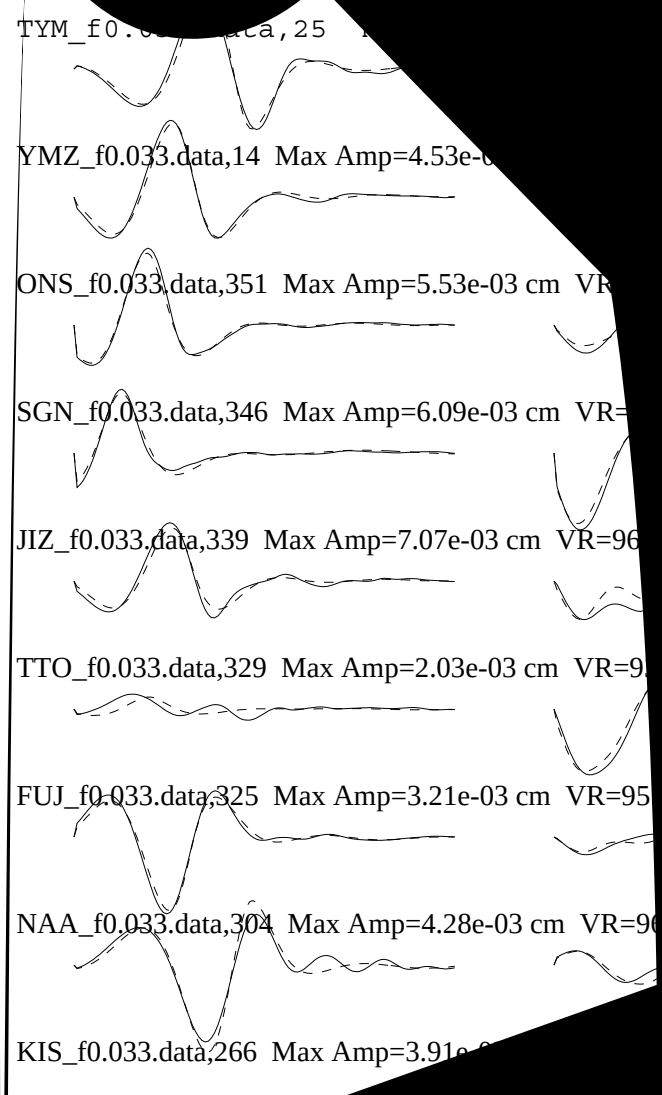
TYM_f0.033.data,25
YMZ_f0.033.data,14 Max Amp=4.53e-0
ONS_f0.033.data,351 Max Amp=5.53e-03 cm VR
SGN_f0.033.data,346 Max Amp=6.09e-03 cm VR=
JIZ_f0.033.data,339 Max Amp=7.07e-03 cm VR=96
TTO_f0.033.data,329 Max Amp=2.03e-03 cm VR=9
FUJ_f0.033.data,325 Max Amp=3.21e-03 cm VR=95
NAA_f0.033.data,304 Max Amp=4.28e-03 cm VR=9
KIS_f0.033.data,266 Max Amp=3.91e-0

Figure 52

EVT3

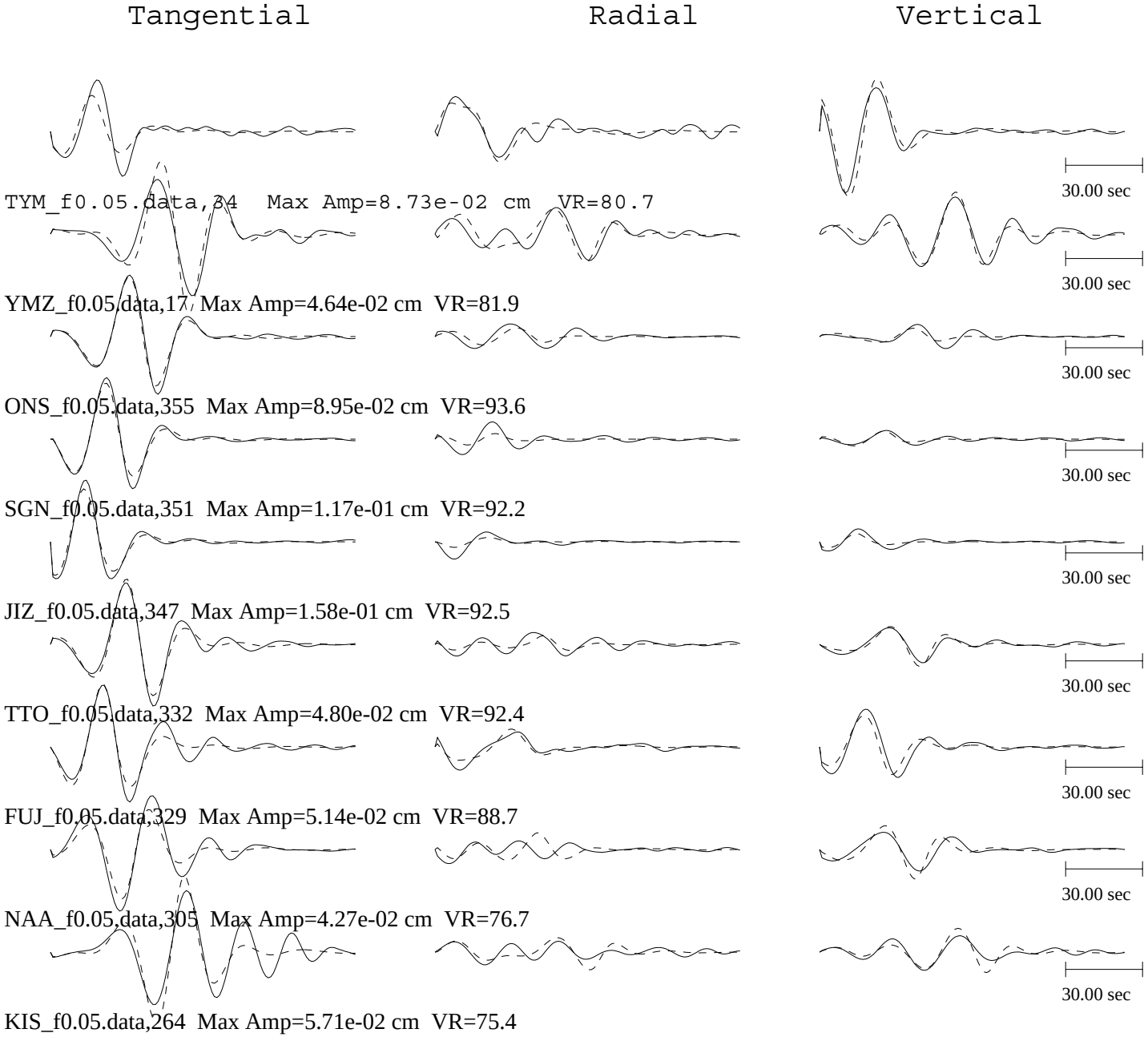

Strike=151 ; 290
Rake =-70 ; -127
Dip =66 ; 31
Mo =1.68e+25
Mw =6.1
Percent DC=25
Percent CLVD=75
Percent ISO=0
Variance=3.69e-05
Var. Red=8.69e+01
RES/Pdc.=1.50e-06

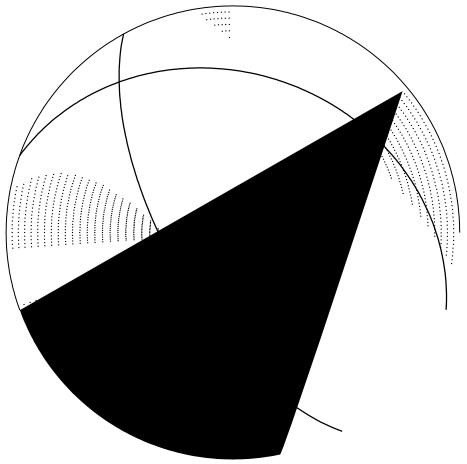

Figure 53

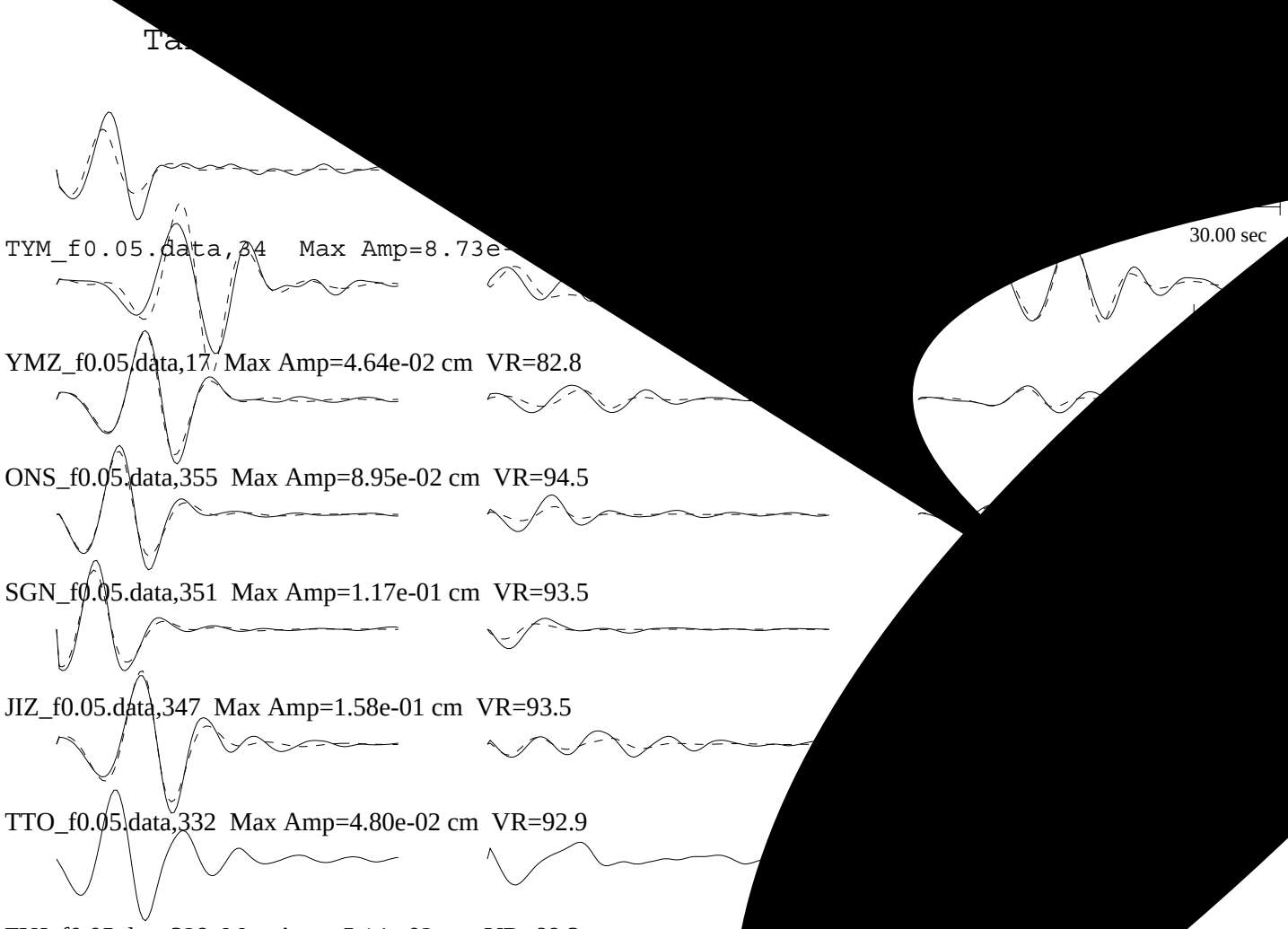
Ta
TYM_f0.05.data,34 Max Amp=8.73e-
YMZ_f0.05.data,17 Max Amp=4.64e-02 cm VR=82.8
ONS_f0.05.data,355 Max Amp=8.95e-02 cm VR=94.5
SGN_f0.05.data,351 Max Amp=1.17e-01 cm VR=93.5
JIZ_f0.05.data,347 Max Amp=1.58e-01 cm VR=93.5
TTO_f0.05.data,332 Max Amp=4.80e-02 cm VR=92.9
FUJ_f0.05.data,329 Max Amp=5.14e-02 cm VR=89.3
30.00 sec

Figure 54

EVT3

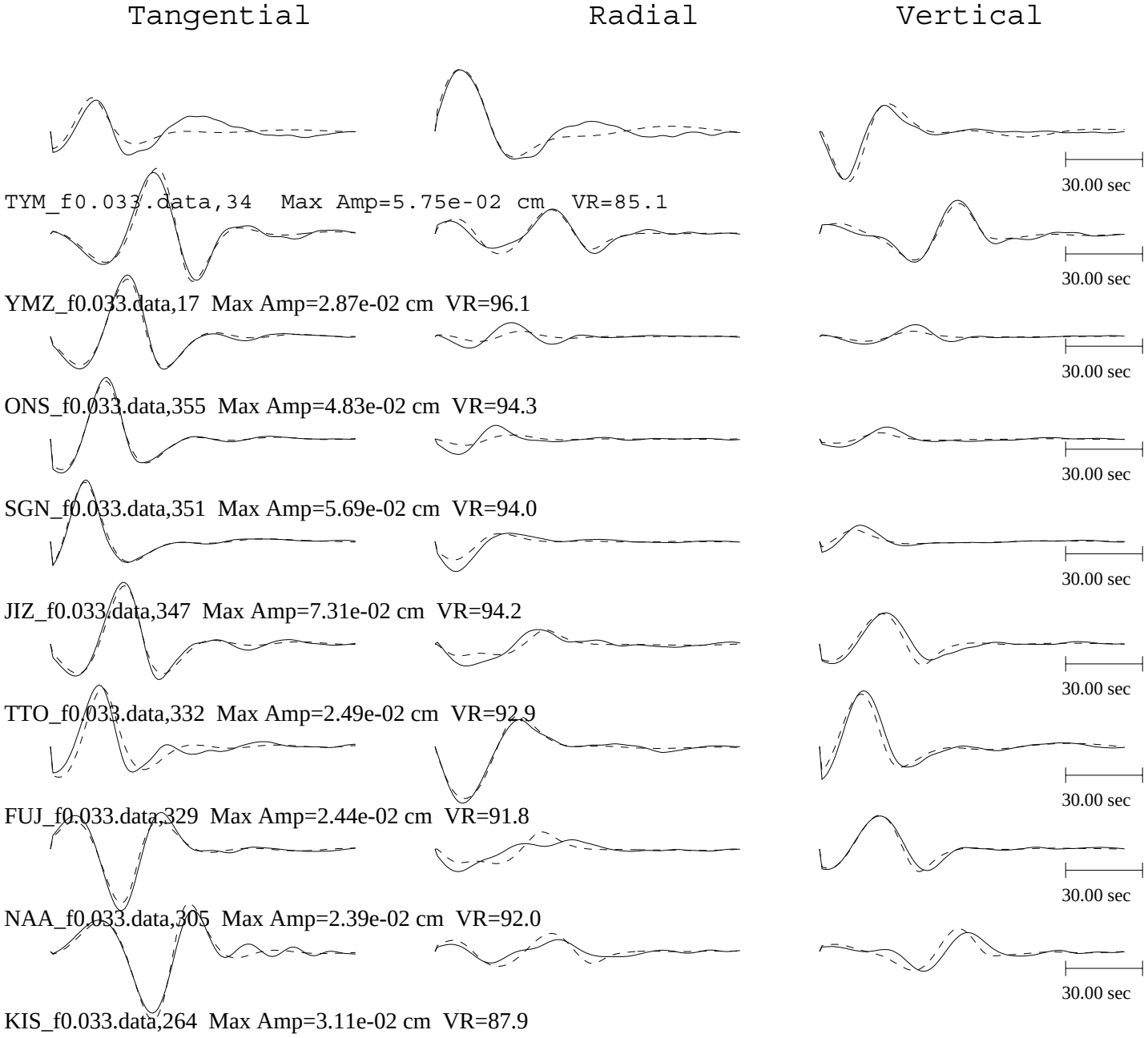

Strike=173 ; 275
Rake =-40 ; -160
Dip =75 ; 52
Mo =1.50e+25
Mw =6.1
Percent DC=17
Percent CLVD=83
Percent ISO=0
Variance=8.79e-06
Var. Red=9.17e+01
RES/Pdc.=5.21e-07

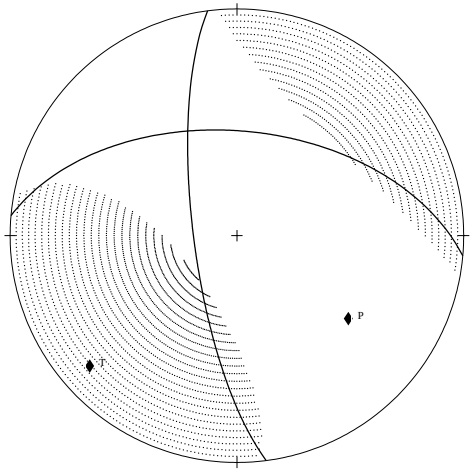

Figure 55

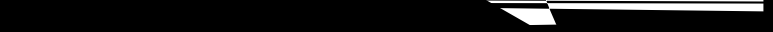

Figure 56

EVT4

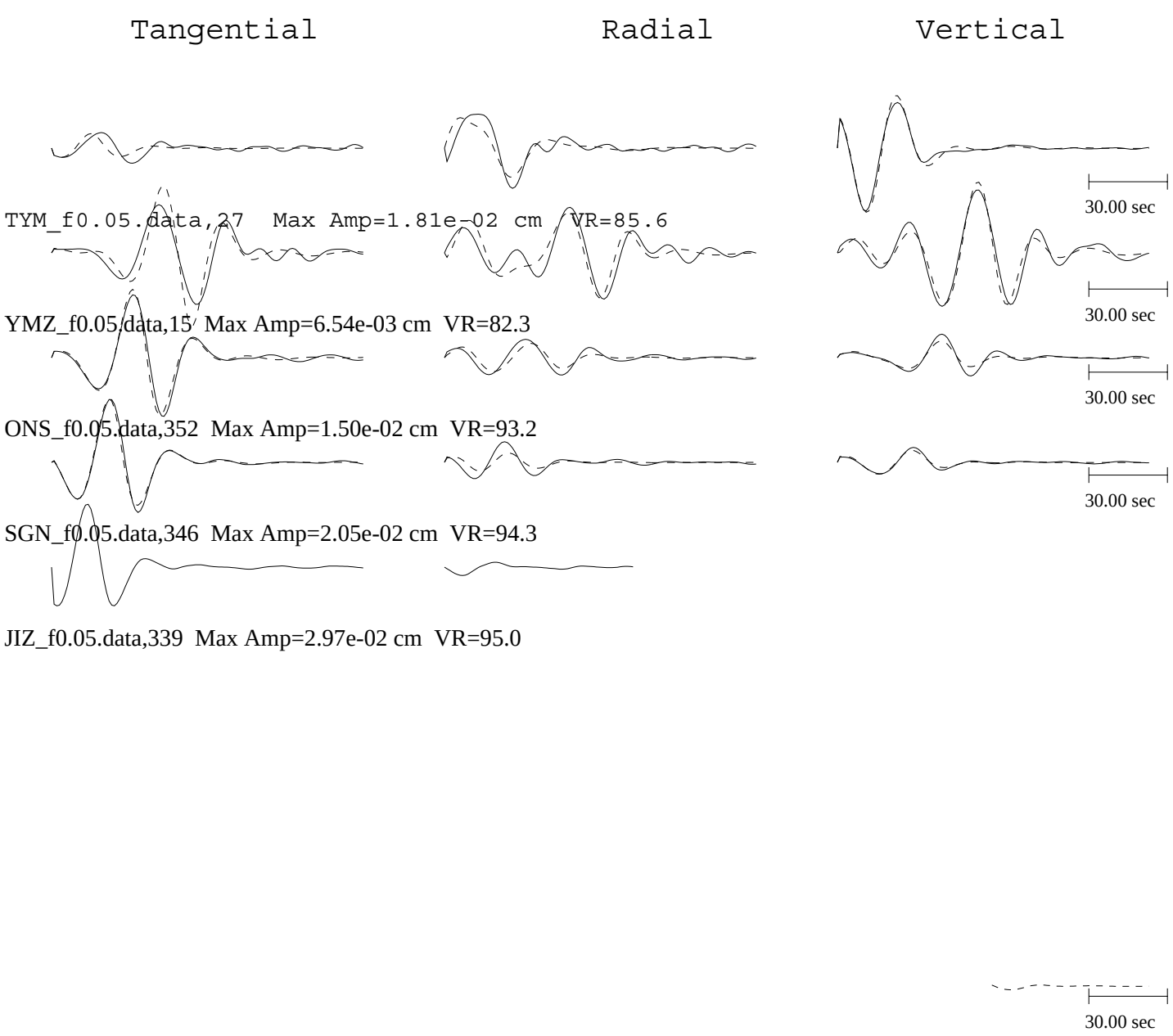

Strike=91 ; 335
Rake =-137 ; -39
Dip =60 ; 54
Mo =2.54e+24
Mw =5.6
Percent DC=12
Percent CLVD=88
Percent ISO=0
Variance=1.07e-06
Var. Red=8.85e+01
RES/Pdc.=8.71e-08

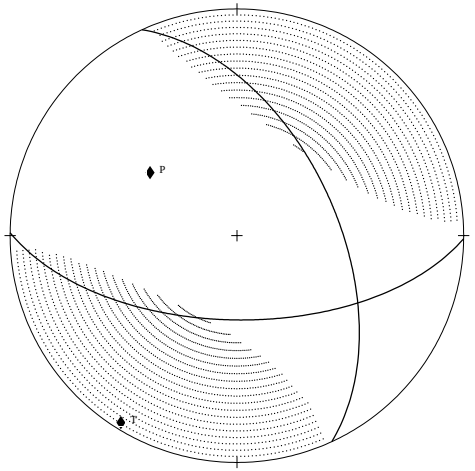

Figure 57

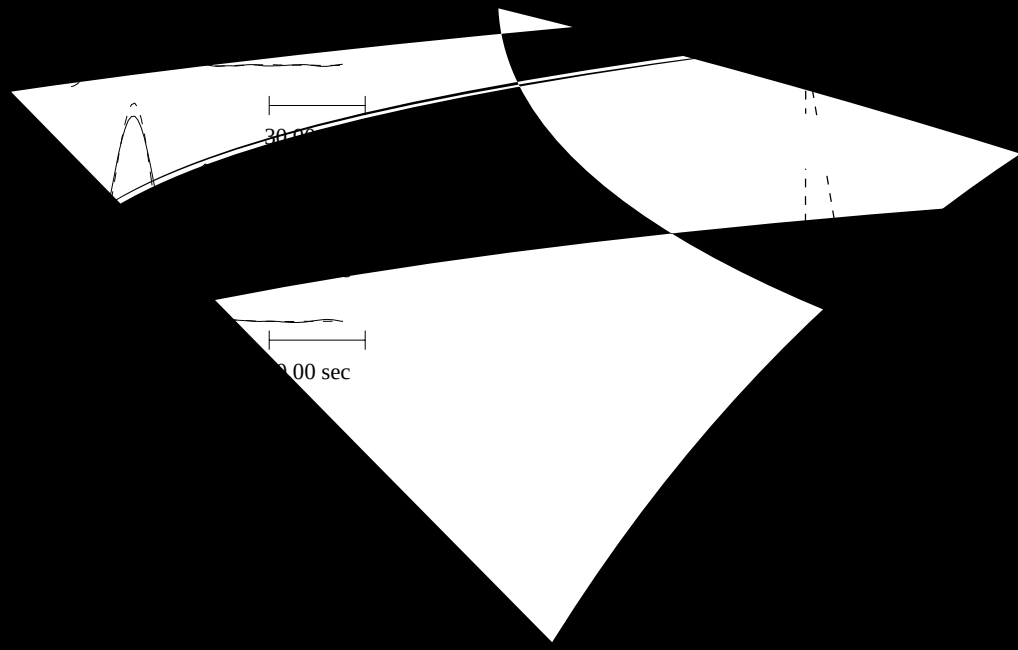

Figure 58

EVT4

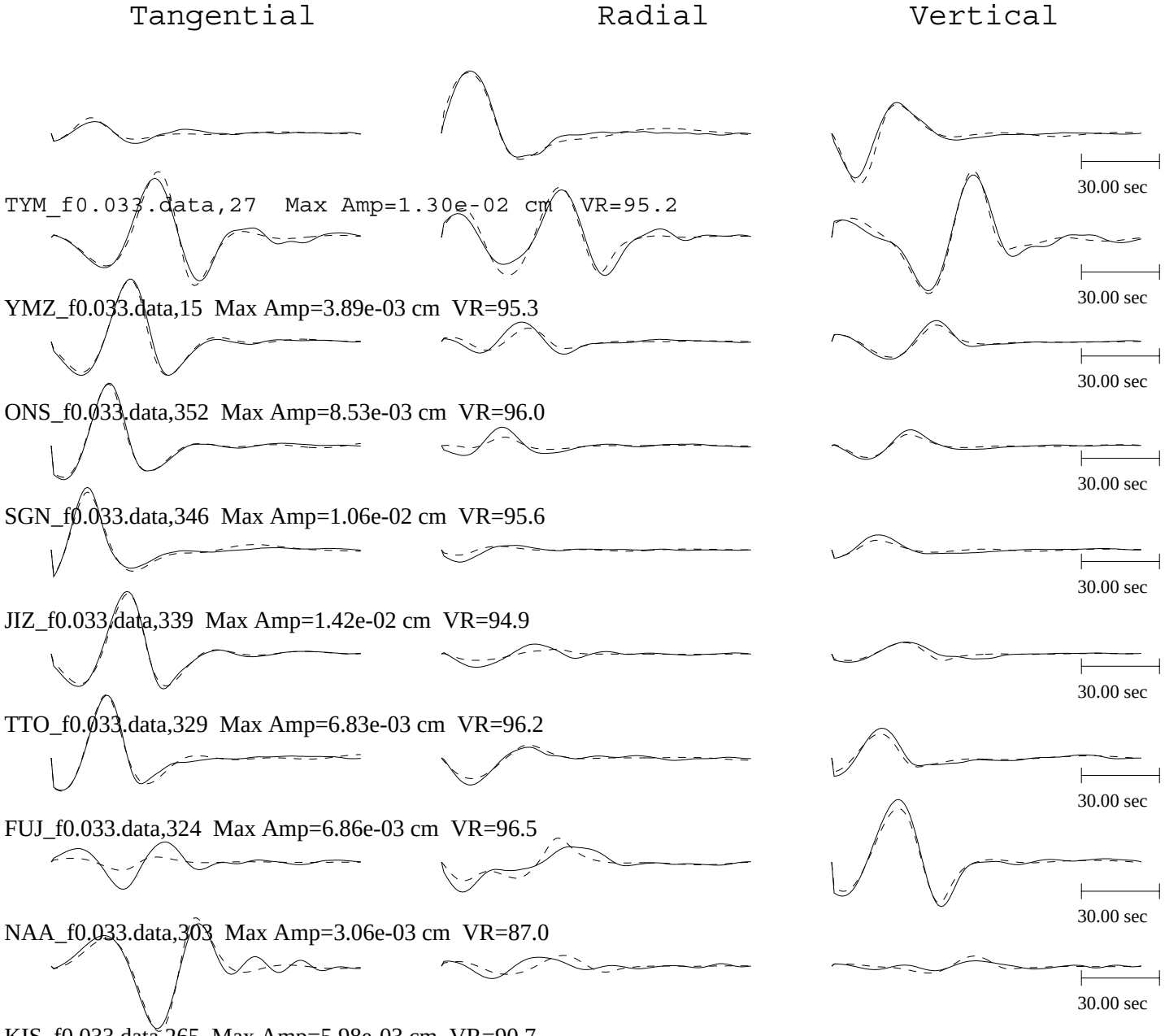

Strike=89 ; 347
Rake =-142 ; -20
Dip =74 ; 54
Mo =2.65e+24
Mw =5.6
Percent DC=13
Percent CLVD=87
Percent ISO=0
Variance=1.79e-07
Var. Red=9.48e+01
RES/Pdc.=1.36e-08

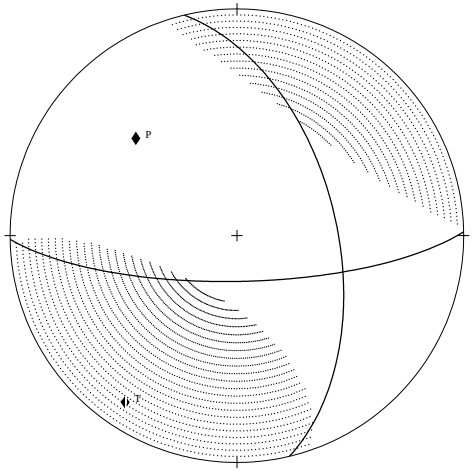

Figure 59

Figure 60

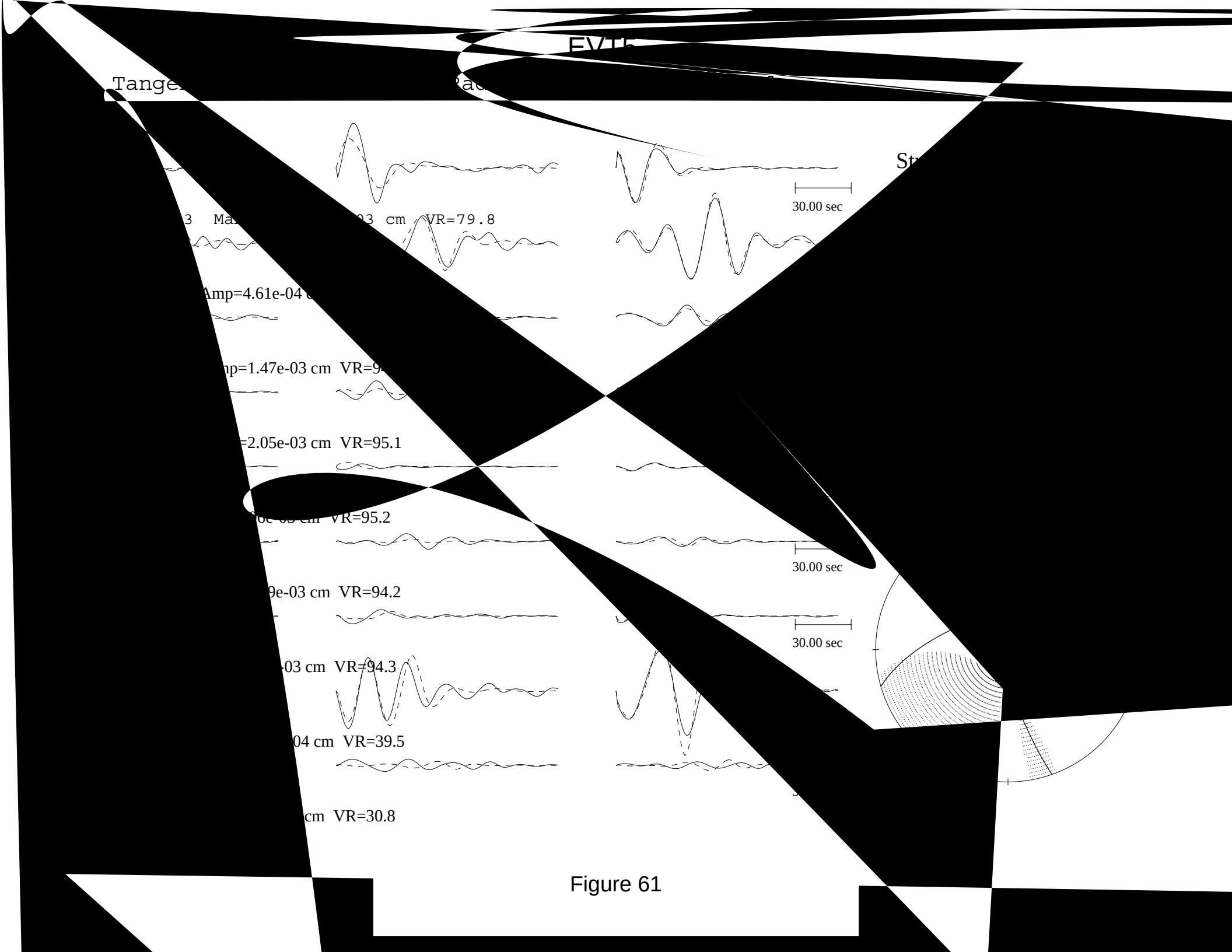

Figure 61

EVT5

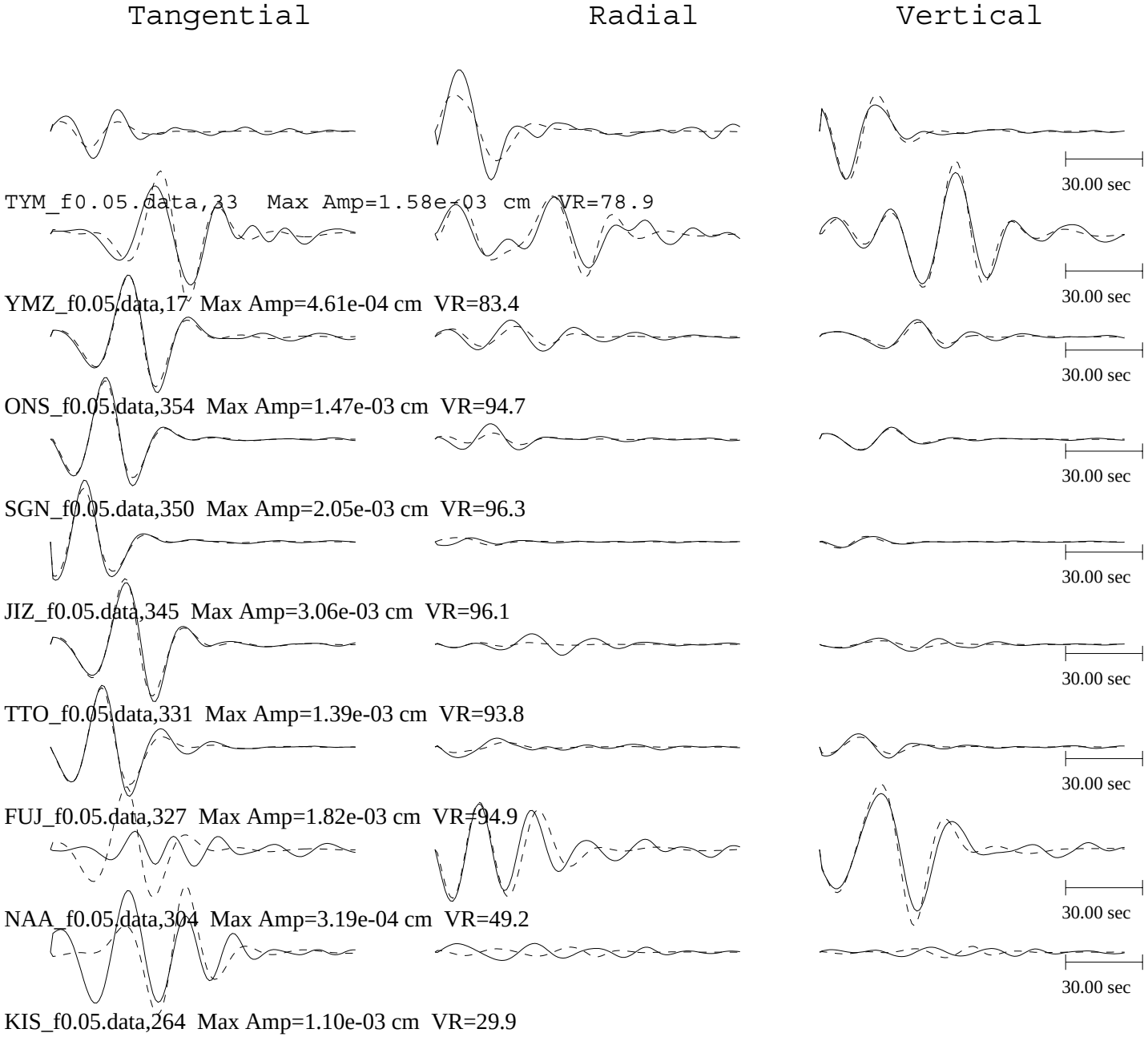

Strike=157 ; 256
Rake =-31 ; -162
Dip =75 ; 60
Mo =2.54e+23
Mw =4.9
Percent DC=27
Percent CLVD=55
Percent ISO=18
Variance=1.27e-08
Var. Red=8.30e+01
RES/Pdc.=4.69e-10

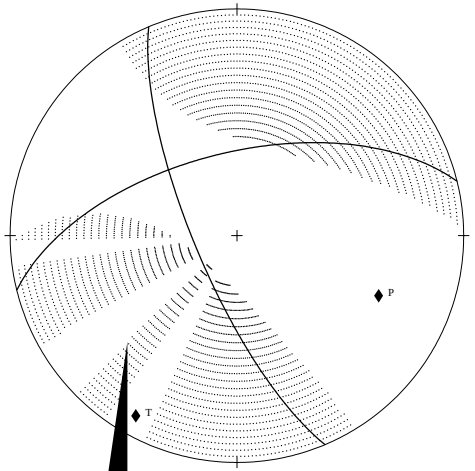

Figure 62

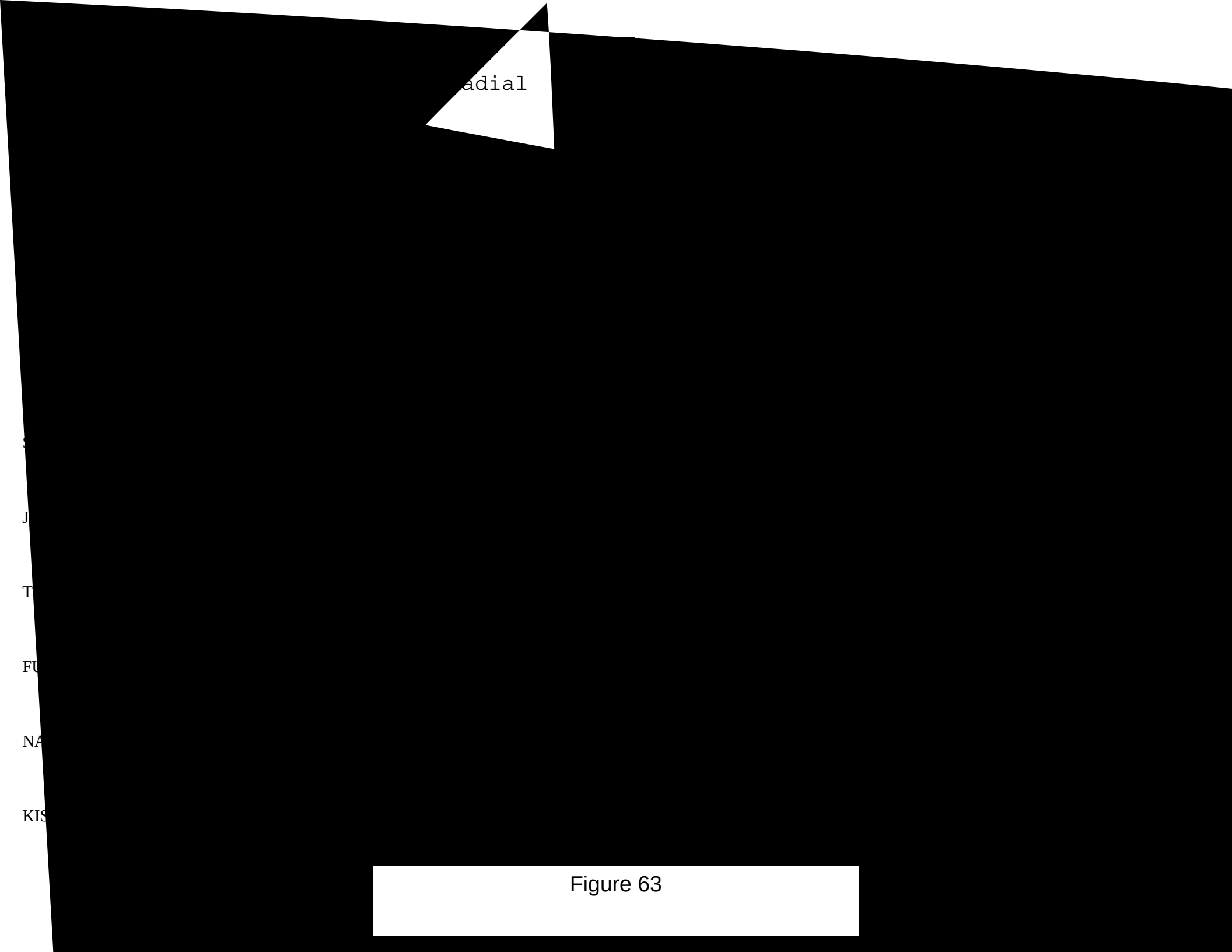

Figure 63

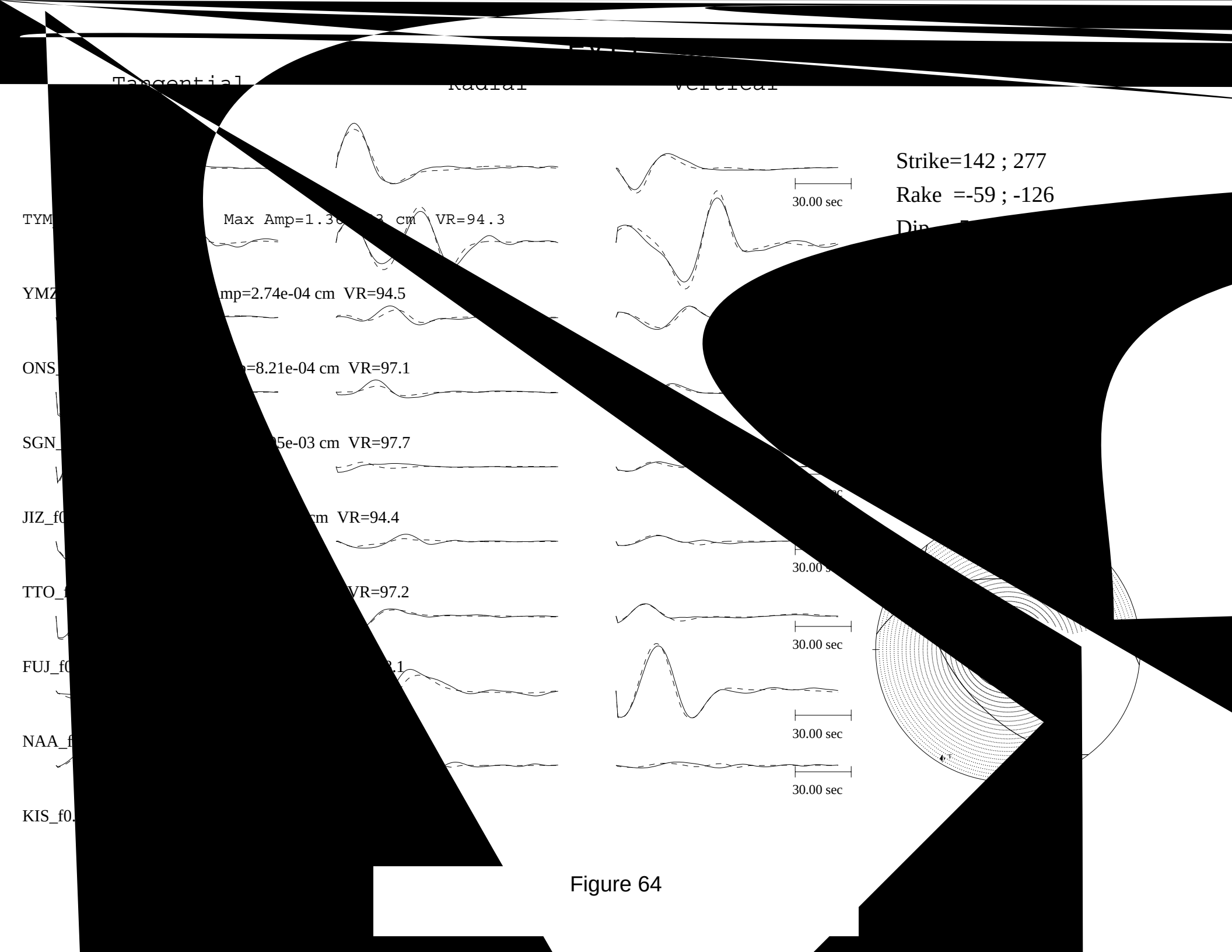
Tangential
Radial
Vertical
Strike=142 ; 277
Rake =-59 ; -126
TYM
Max Amp=1.3
cm VR=94.3
YMZ
mp=2.74e-04 cm VR=94.5
ONS
=8.21e-04 cm VR=97.1
SGN
5e-03 cm VR=97.7
JIZ_f0
cm VR=94.4
TTO
VR=97.2
FUJ_f0
NAA_f
KIS_f0.
30.00 sec
30.00 sec
30.00 sec
30.00 sec

Figure 64

EVT6

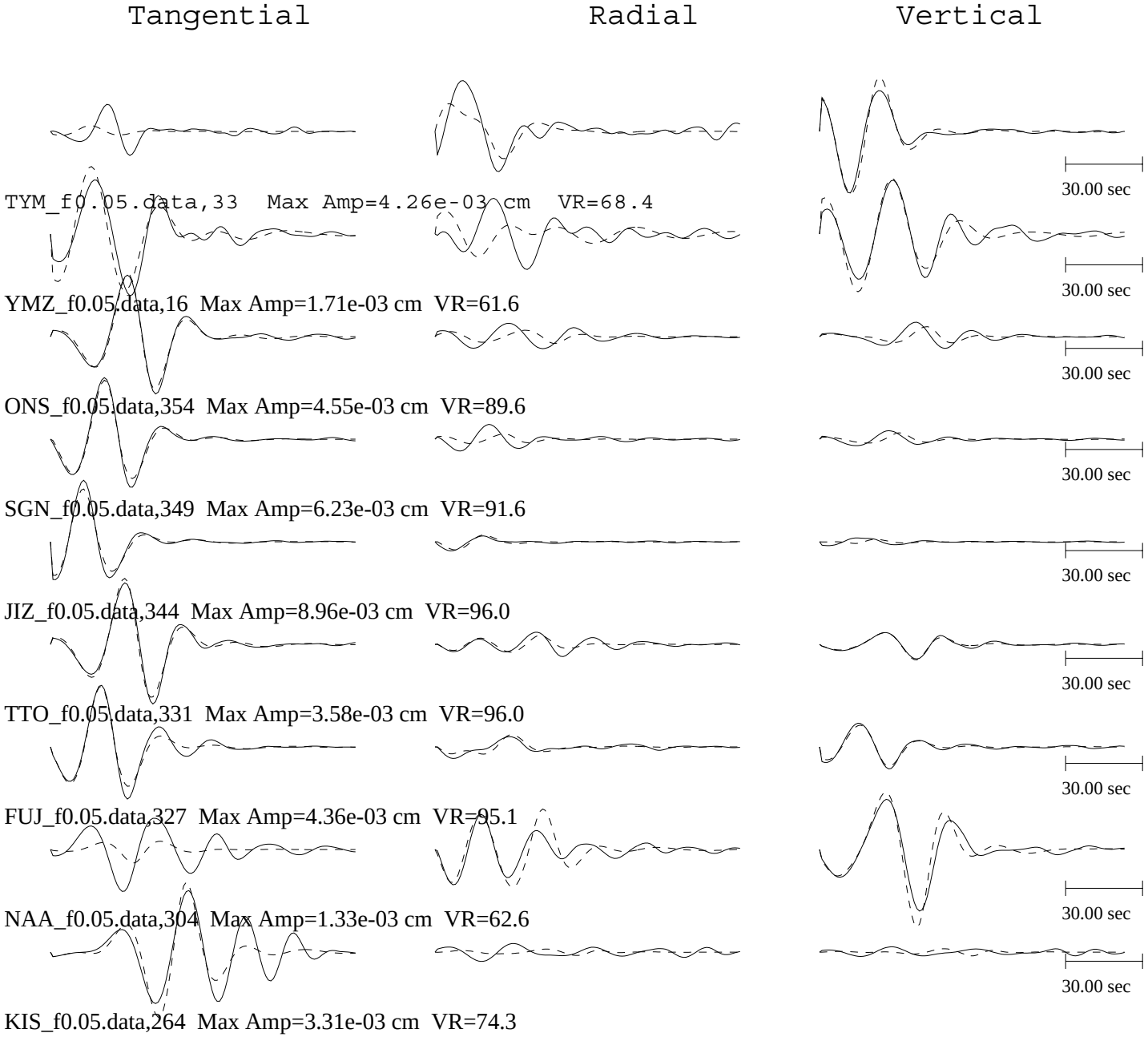

Strike=79 ; 171
Rake =163 ; 7
Dip =83 ; 73
Mo =7.27e+23
Mw =5.2
Percent DC=33
Percent CLVD=67
Percent ISO=0
Variance=1.12e-07
Var. Red=8.51e+01
RES/Pdc.=3.38e-09

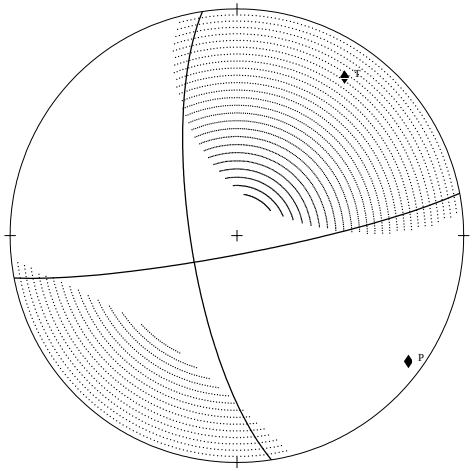

Figure 65


TYM_f0
Amp=4.26e-03
VR=2
YM
Am
3 cm VR=67.8
=89.9
SGN_f0.05
ta,349
Amp=6.23e
cm VR=92.7

Figure 66

EVT6

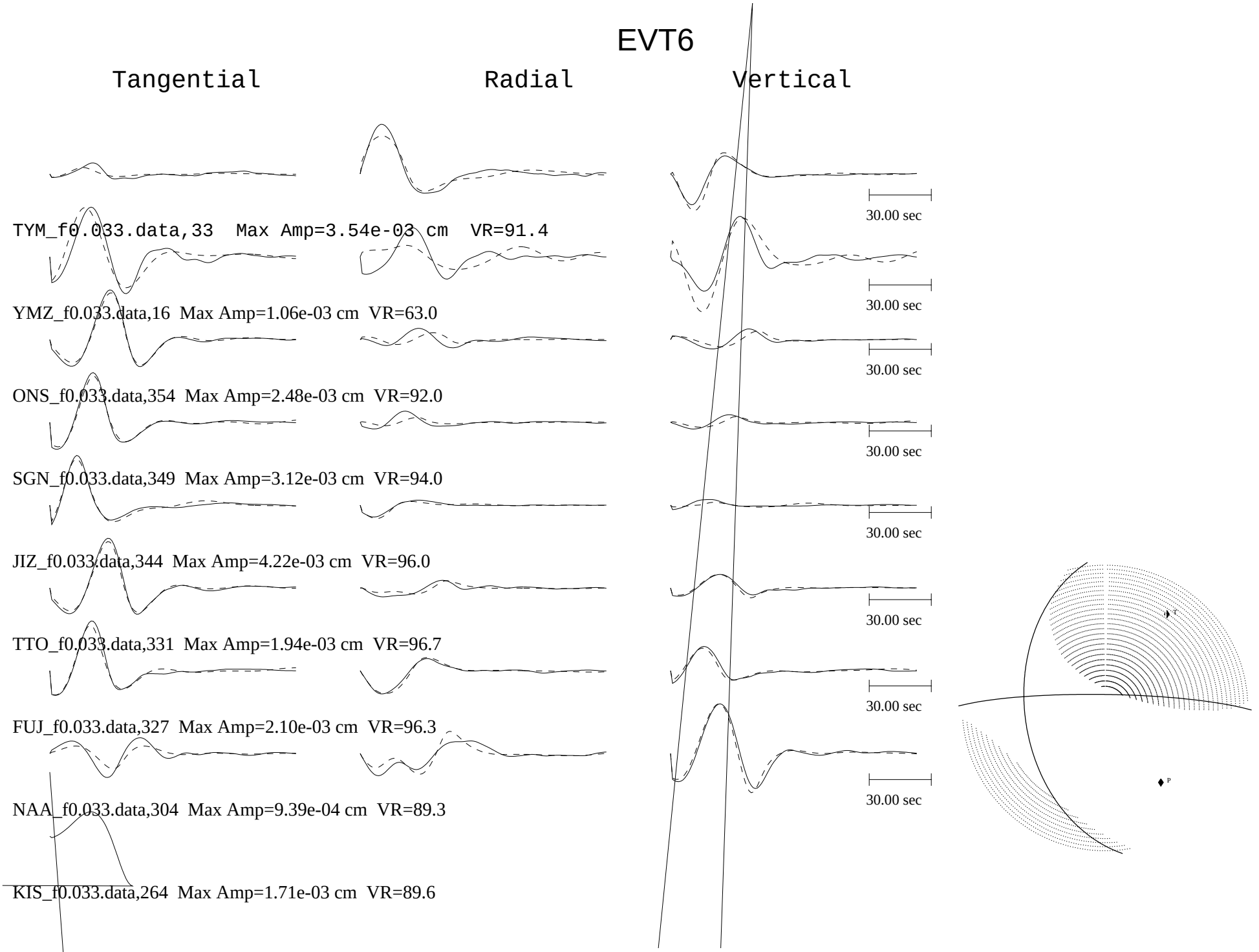

Figure 67

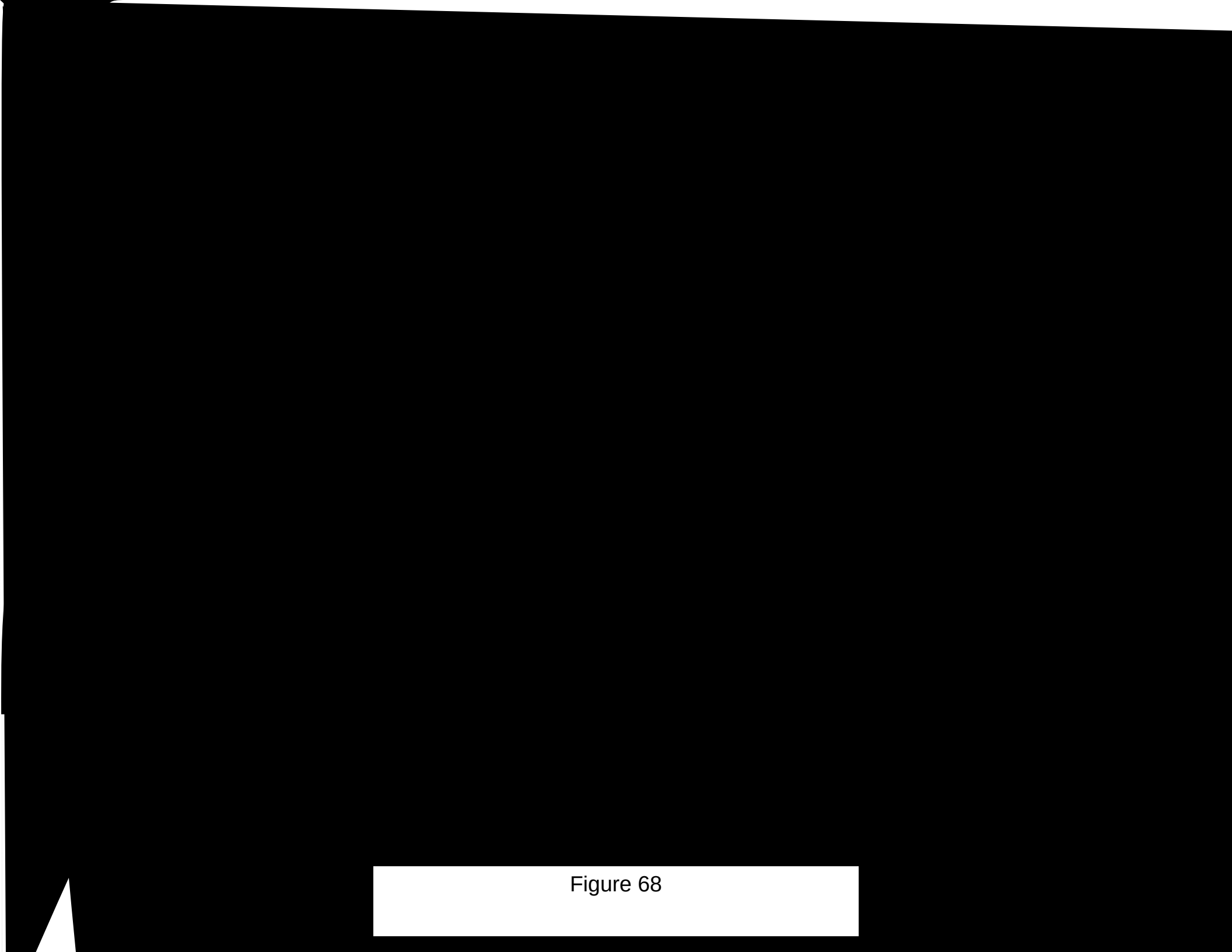

Figure 68

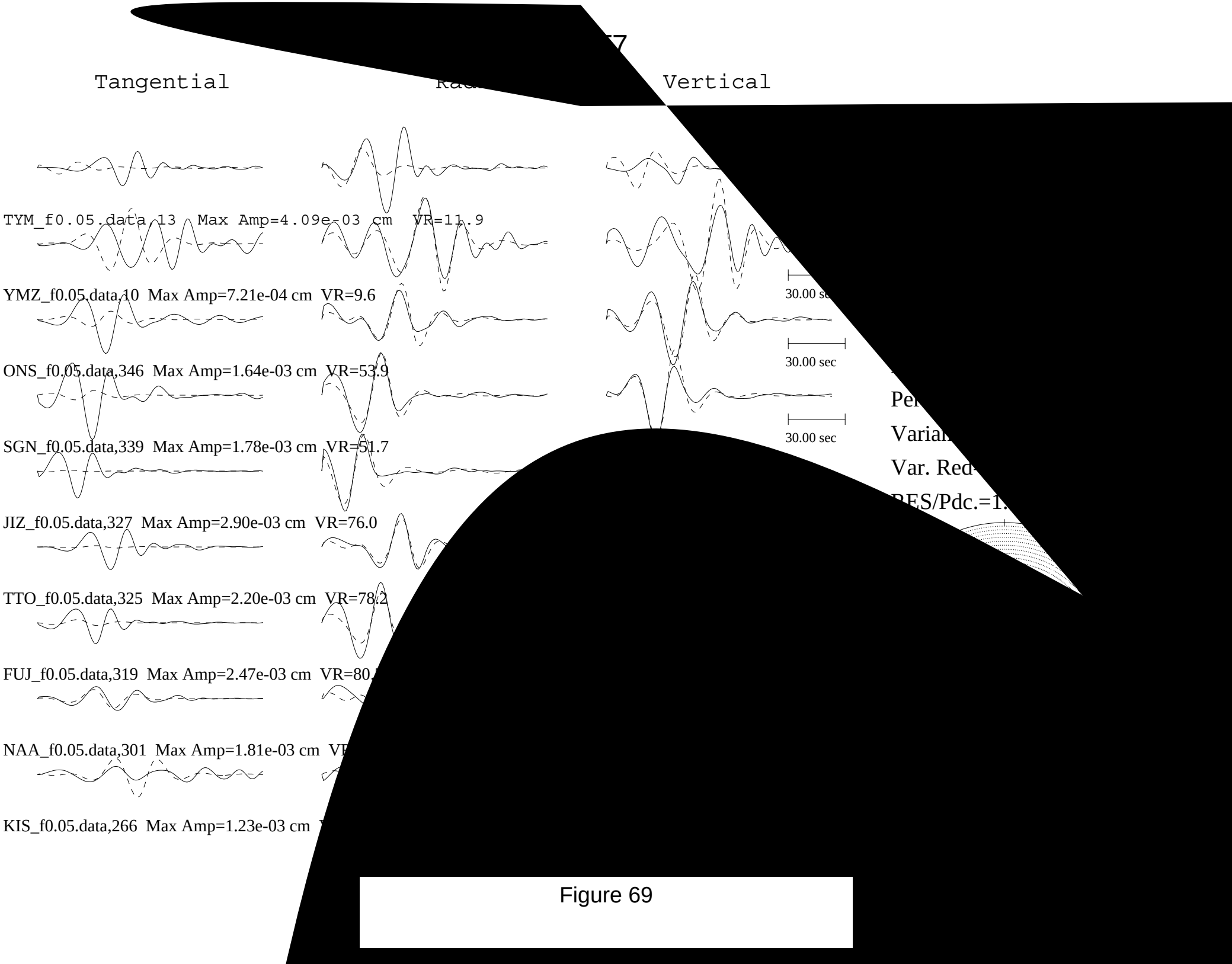
Tangential
Vertical
TYM_f0.05.data,13 Max Amp=4.09e-03 cm VR=11.9
YMZ_f0.05.data,10 Max Amp=7.21e-04 cm VR=9.6
ONS_f0.05.data,346 Max Amp=1.64e-03 cm VR=53.9
SGN_f0.05.data,339 Max Amp=1.78e-03 cm VR=51.7
JIZ_f0.05.data,327 Max Amp=2.90e-03 cm VR=76.0
TTO_f0.05.data,325 Max Amp=2.20e-03 cm
FUJ_f0.05.data,319 Max Amp=2.47e-03 cm
NAA_f0.05.data,301 Max Amp=1.81e-03 cm
KIS_f0.05.data,266 Max Amp=1.23e-03 cm
30.00 sec
30.00 sec
30.00 sec

Figure 69

EVT7

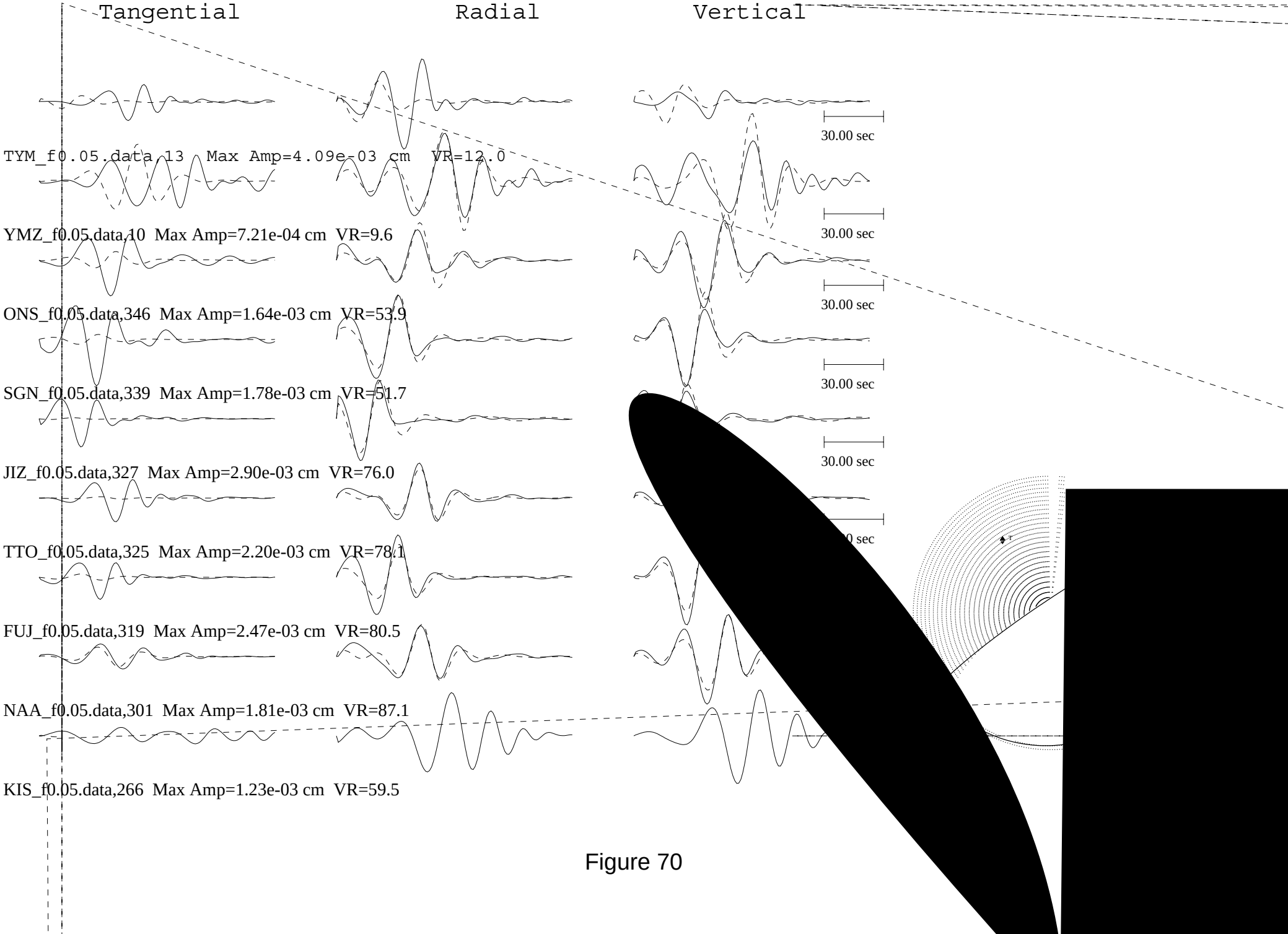

Figure 70

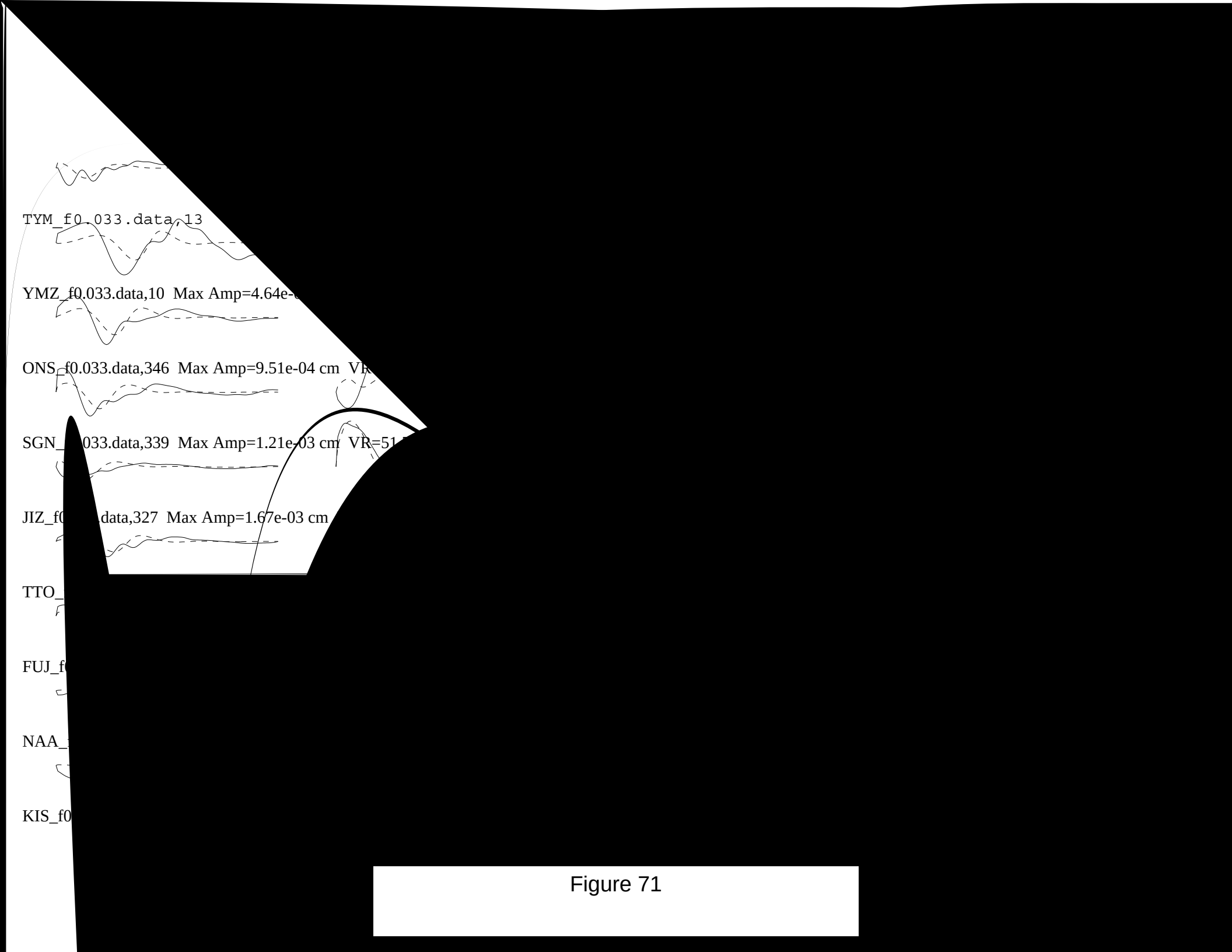
TYM_f0.033.data,13
YMZ_f0.033.data,10 Max Amp=4.64e-
ONS_f0.033.data,346 Max Amp=9.51e-04 cm
SGN_ 033.data,339 Max Amp=1.21e-03 cm
JIZ_f data,327 Max Amp=1.67e-03 cm
TTO_
FUJ_f
NAA_
KIS_f0

Figure 71

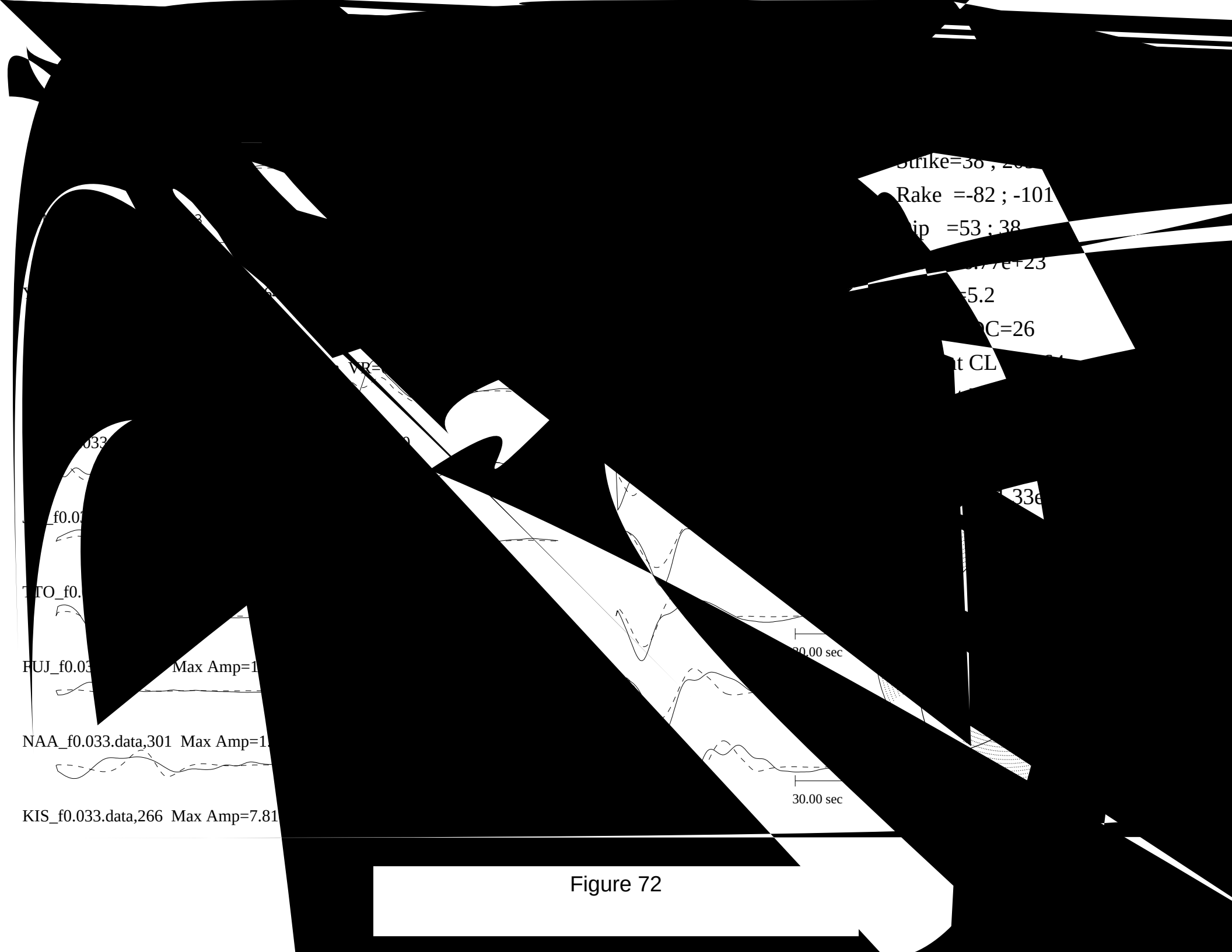
Rake =-82 ; -101
ip =53 ; 38
=5.2
C=26
t CL
33e
TTO_f0.
Max Amp=1
30.00 sec
NAA_f0.033.data,301 Max Amp=1
30.00 sec
KIS_f0.033.data,266 Max Amp=7.81

Figure 72

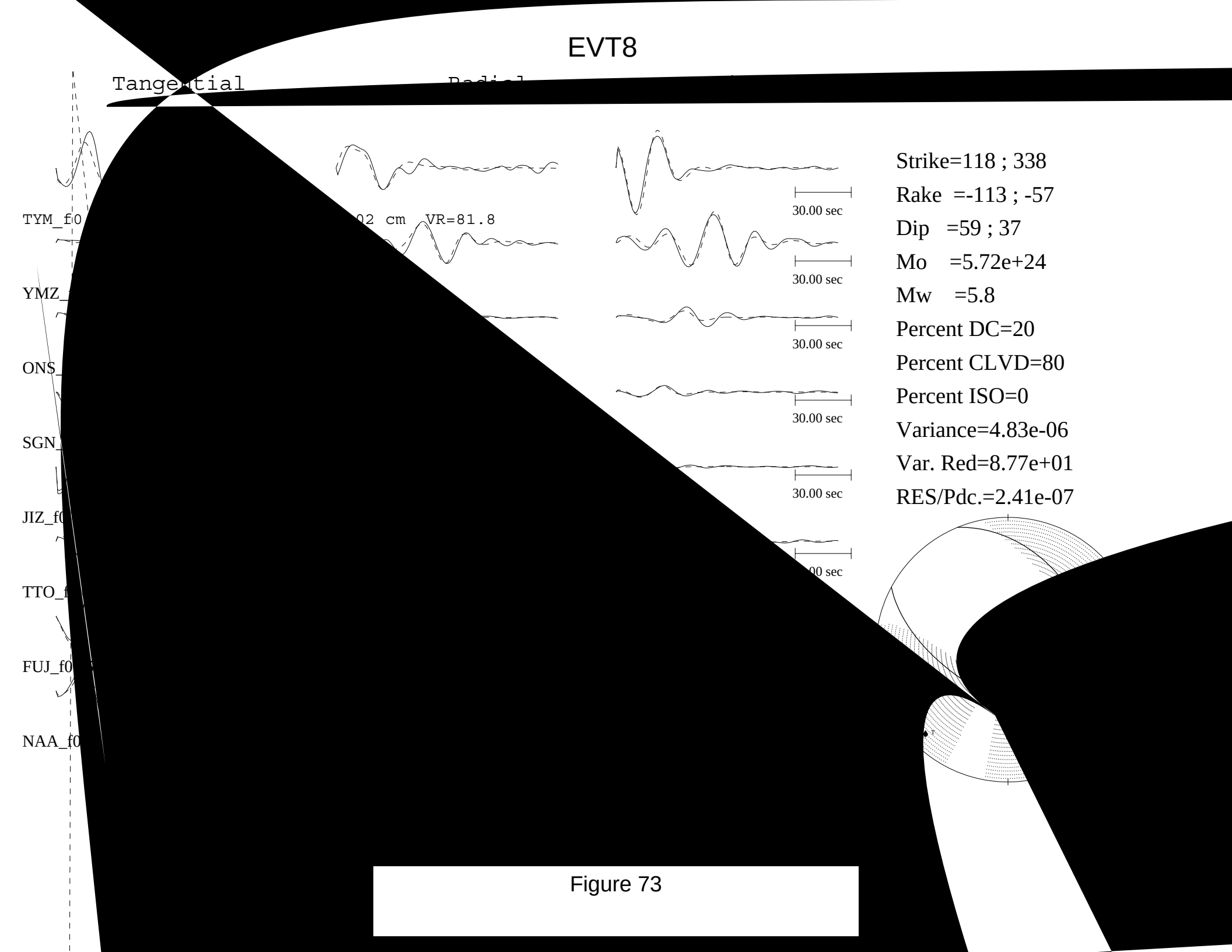
EVT8
Tangential
Radial
TYM_f0
YMZ_
ONS_
SGN_
JIZ_f0
TTO_f
FUJ_f0
NAA_f0
02 cm VR=81.8
30.00 sec
30.00 sec
30.00 sec
30.00 sec
30.00 sec
Strike=118 ; 338
Rake =-113 ; -57
Dip =59 ; 37
Mo =5.72e+24
Mw =5.8
Percent DC=20
Percent CLVD=80
Percent ISO=0
Variance=4.83e-06
Var. Red=8.77e+01
RES/Pdc.=2.41e-07

Figure 73

Figure 74

Figure 75

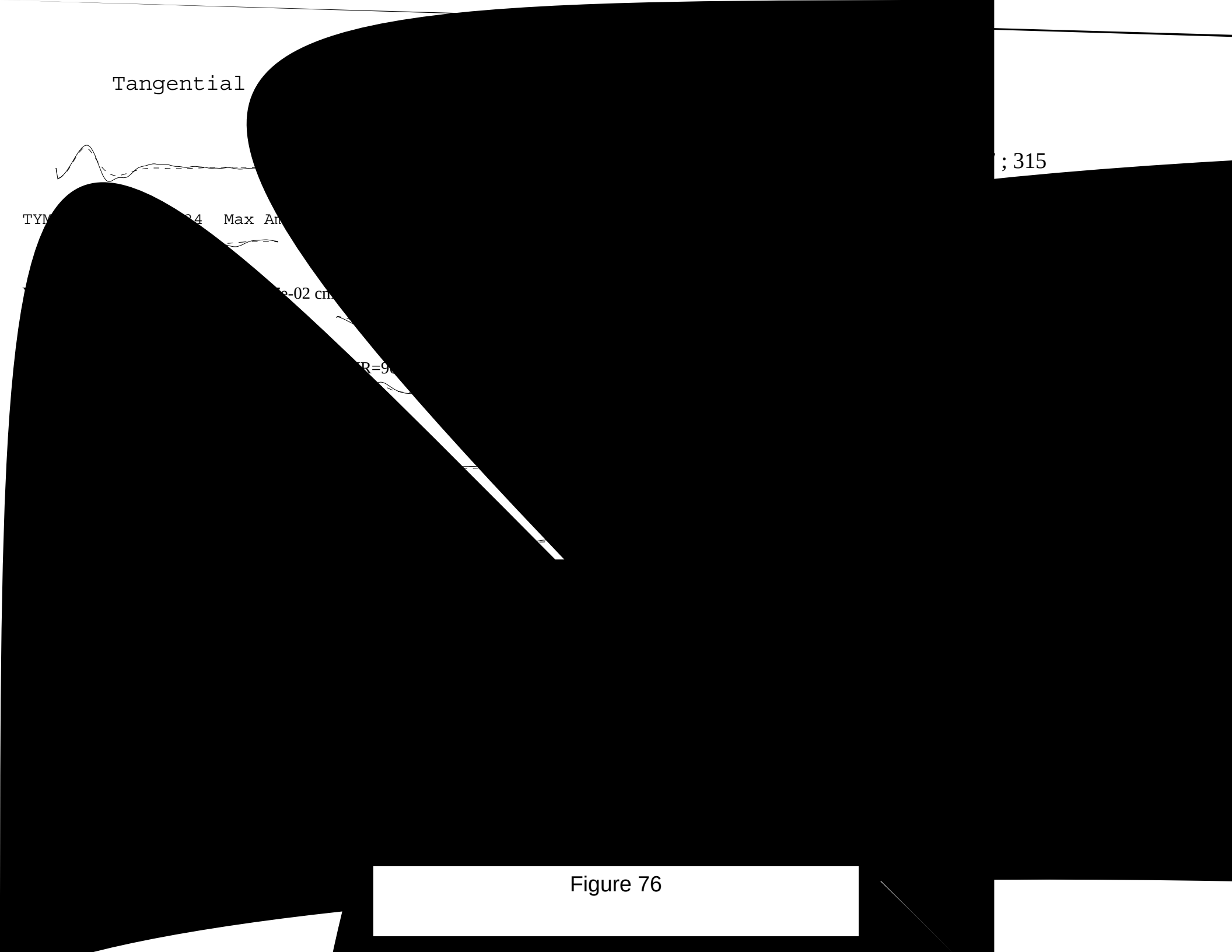

Figure 76

Figure 77

EVT9

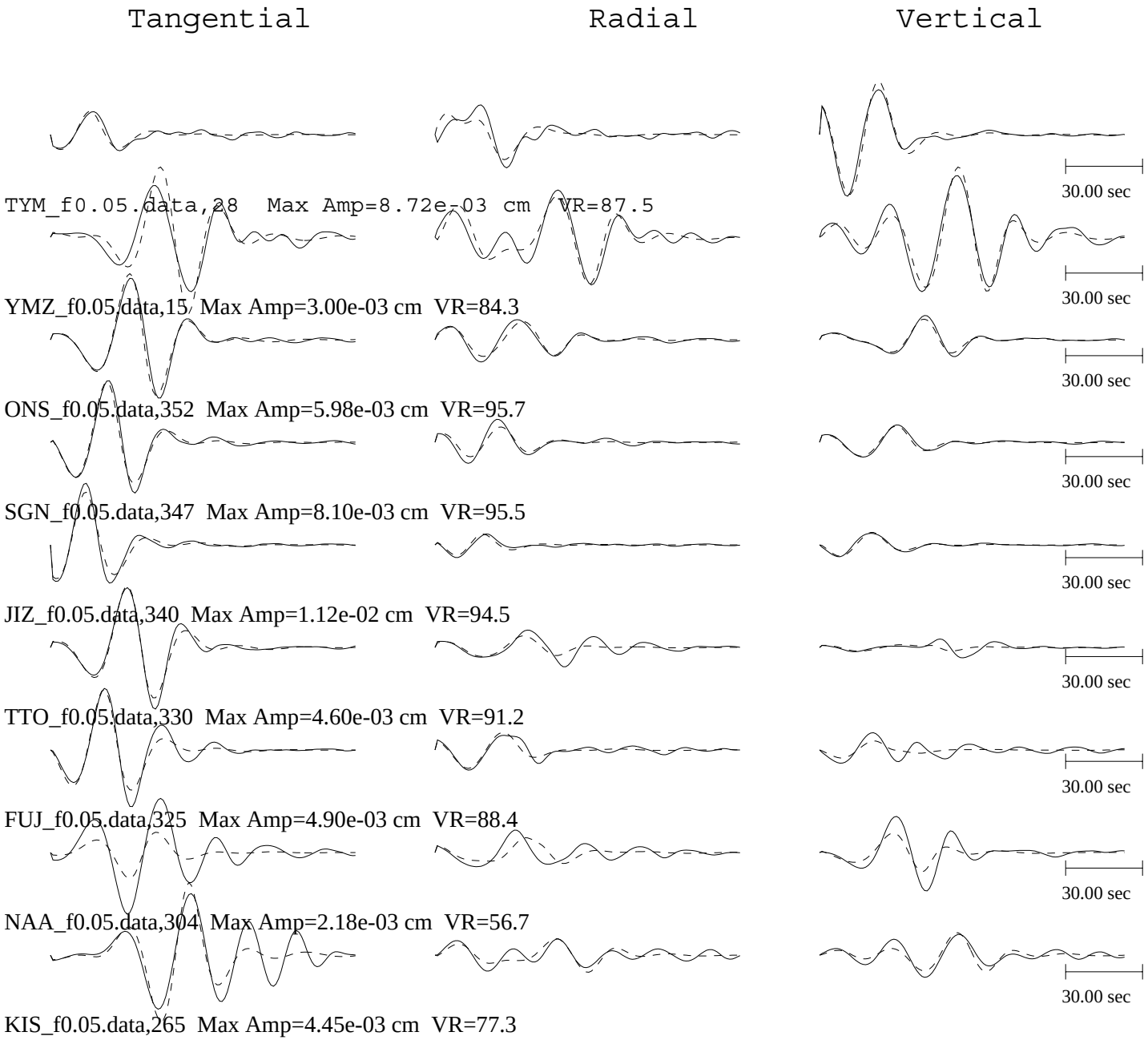

Strike=301 ; 134
Rake =-98 ; -80
Dip =51 ; 40
Mo =1.49e+24
Mw =5.4
Percent DC=58
Percent CLVD=29
Percent ISO=12
Variance=1.82e-07
Var. Red=8.85e+01
RES/Pdc.=3.13e-09

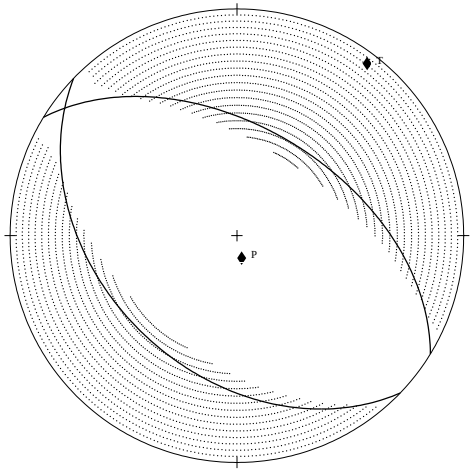

Figure 78

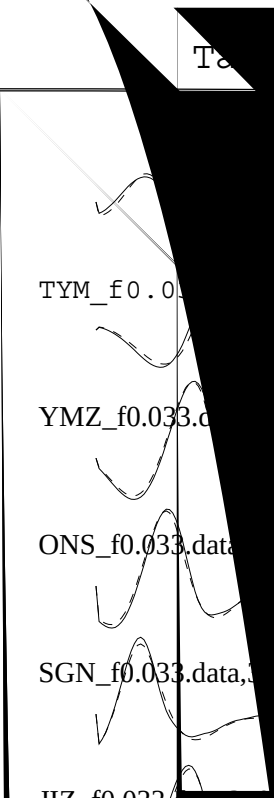
TYM_f0.0
YMZ_f0.033.d
ONS_f0.033.data
SGN_f0.033.data,
JIZ_f0.033.
TTO_f0.033
FUJ_f0.033
NAA_f0.03
KIS_f0.033

Figure 79

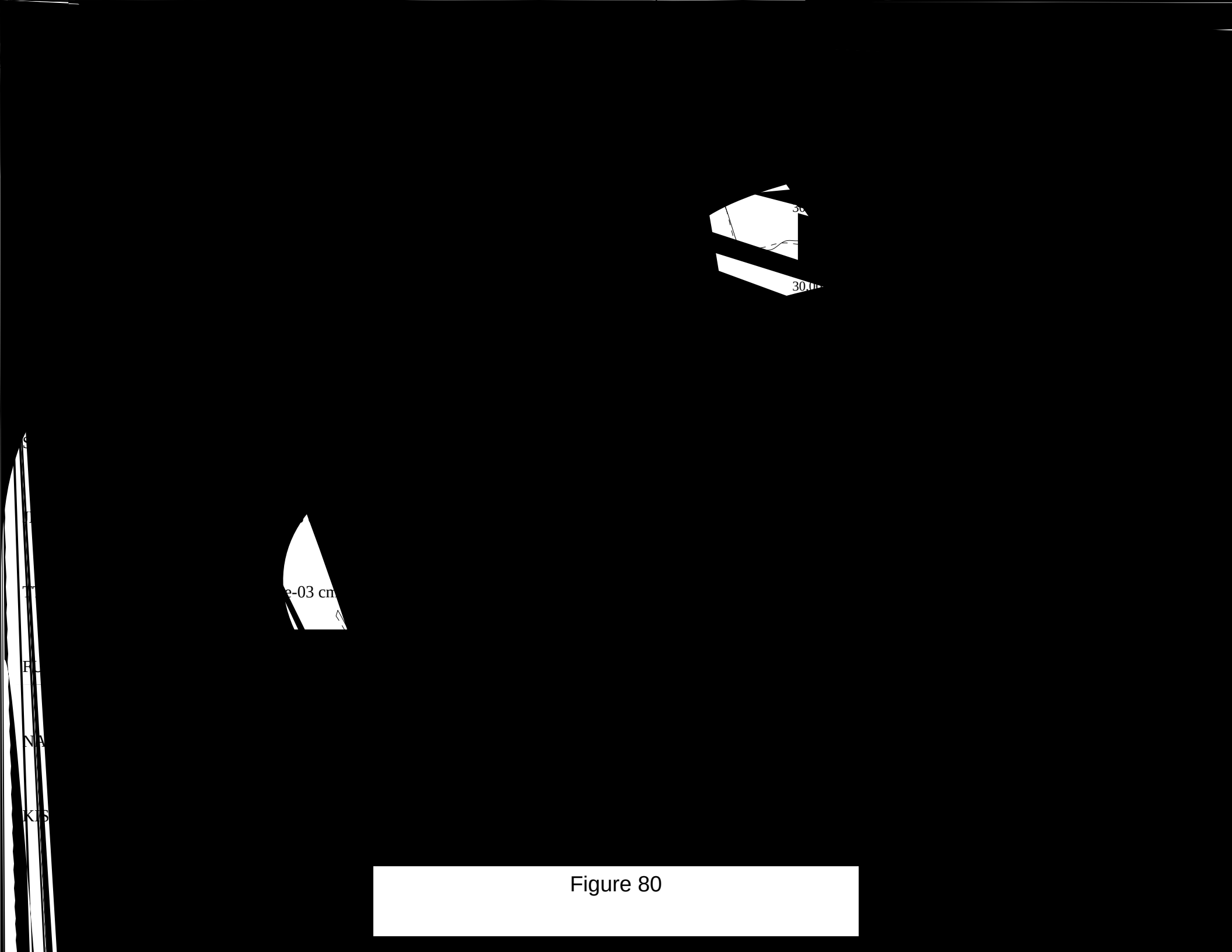

Figure 80

EVT10

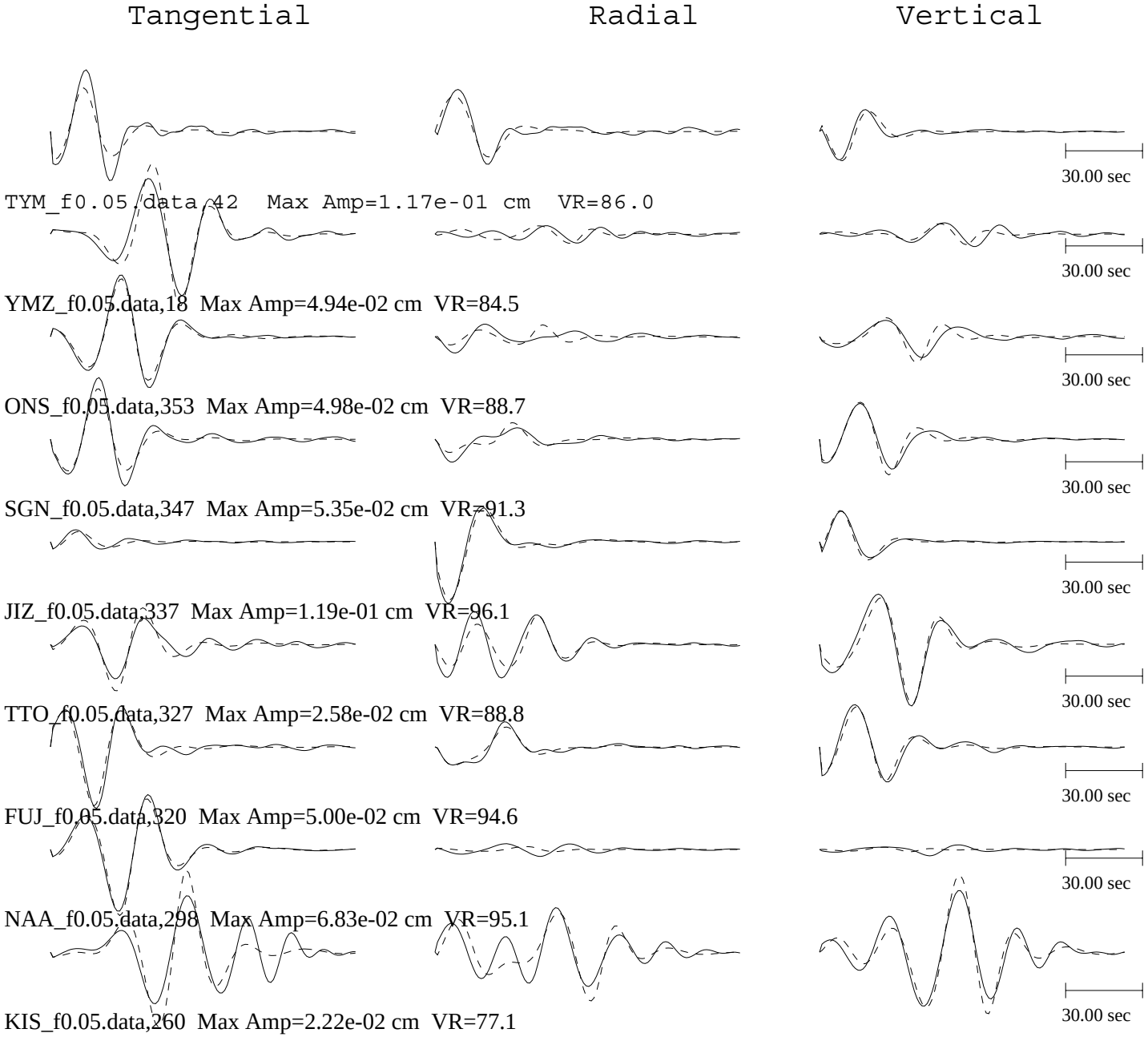

Strike=117 ; 19
Rake =-138 ; -12
Dip =81 ; 48
Mo =1.28e+25
Mw =6.0
Percent DC=45
Percent CLVD=55
Percent ISO=0
Variance=2.09e-05
Var. Red=8.89e+01
RES/Pdc.=4.68e-07

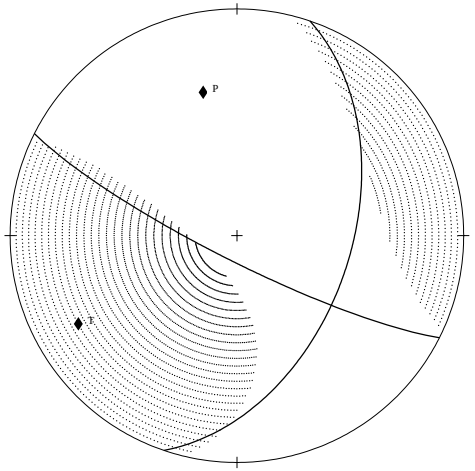

Figure 81

EVT10

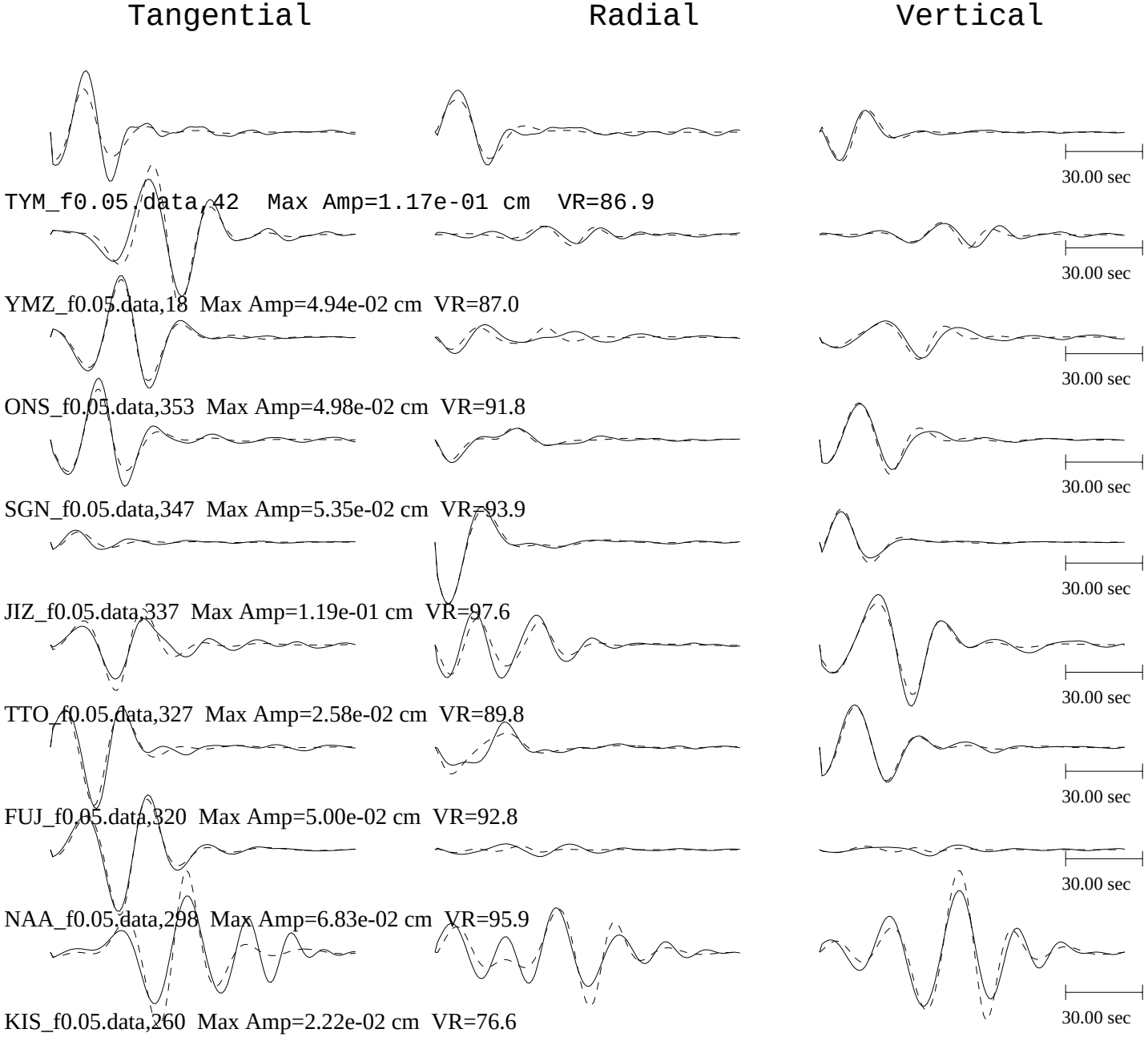

Strike=133 ; 1
Rake =-116 ; -48
Dip =64 ; 36
Mo =1.48e+25
Mw =6.1
Percent DC=36
Percent CLVD=32
Percent ISO=32
Variance=1.85e-05
Var. Red=9.01e+01
RES/Pdc.=5.15e-07

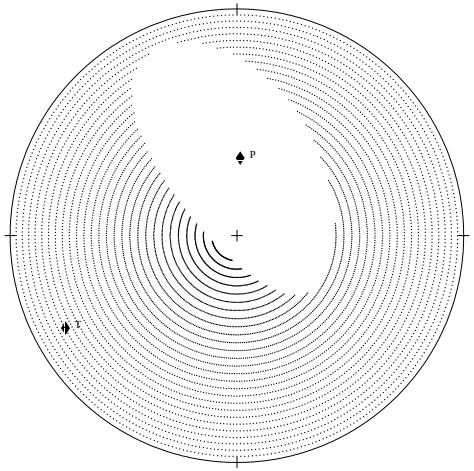

Figure 82

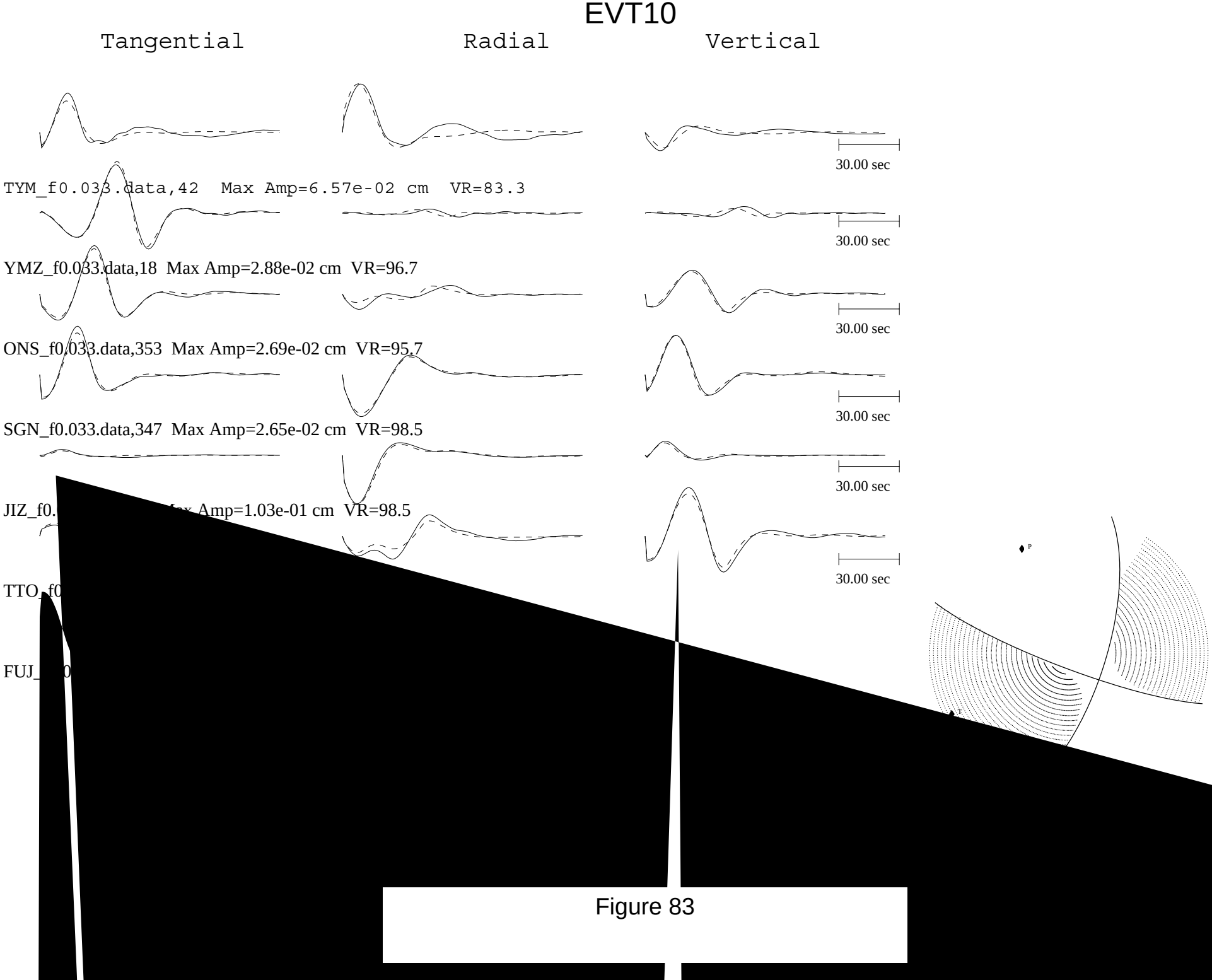
EVT10
Tangential
Radial
Vertical
30.00 sec
TYM_f0.033.data,42 Max Amp=6.57e-02 cm VR=83.3
YMZ_f0.033.data,18 Max Amp=2.88e-02 cm VR=96.7
ONS_f0.033.data,353 Max Amp=2.69e-02 cm VR=95.7
SGN_f0.033.data,347 Max Amp=2.65e-02 cm VR=98.5
JIZ_f0.
Amp=1.03e-01 cm VR=98.5
TTO_f0
FUJ_
P

Figure 83

EVT10

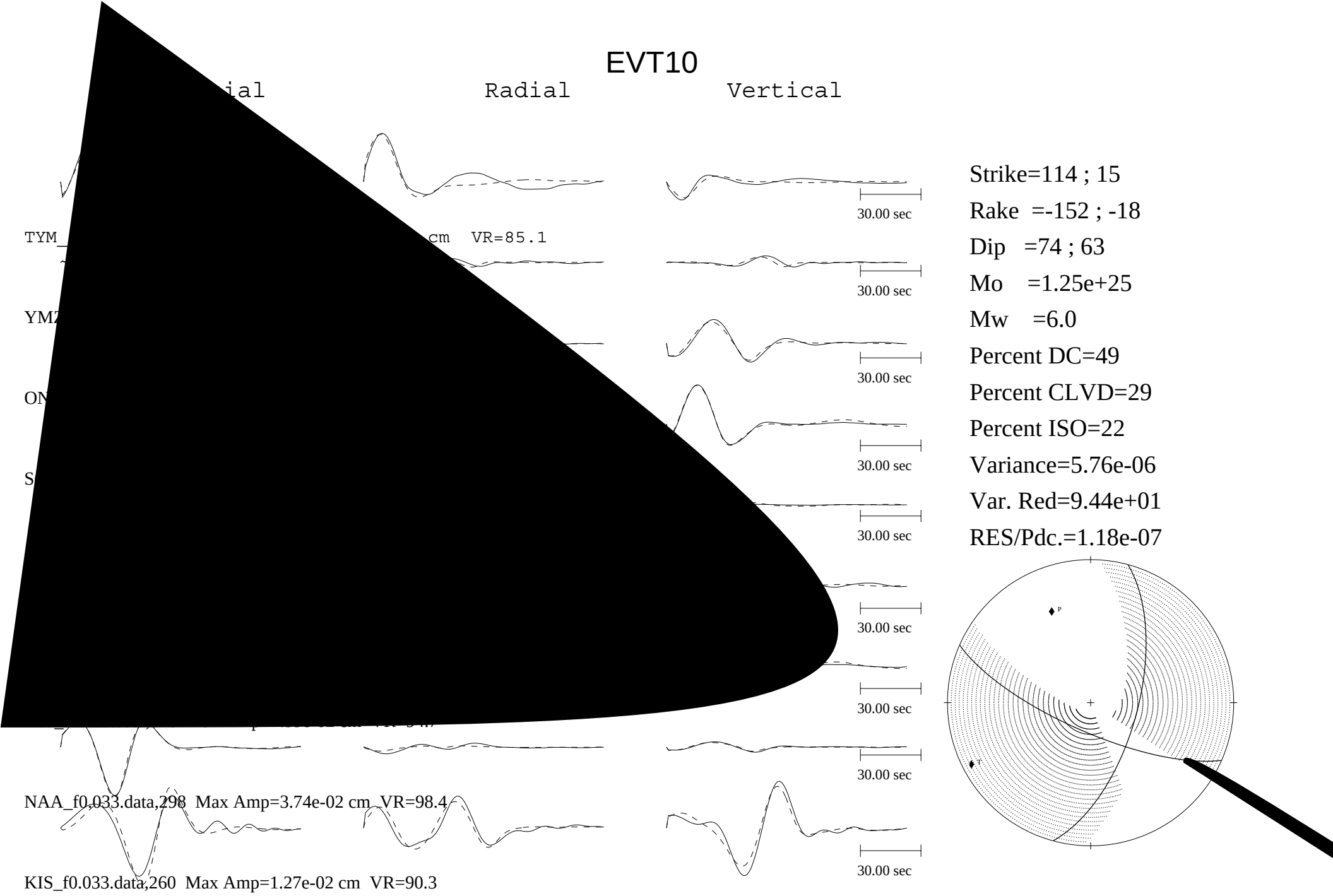

Strike=114 ; 15
Rake =-152 ; -18
Dip =74 ; 63
Mo =1.25e+25
Mw =6.0
Percent DC=49
Percent CLVD=29
Percent ISO=22
Variance=5.76e-06
Var. Red=9.44e+01
RES/Pdc.=1.18e-07

Figure 84

EVT11

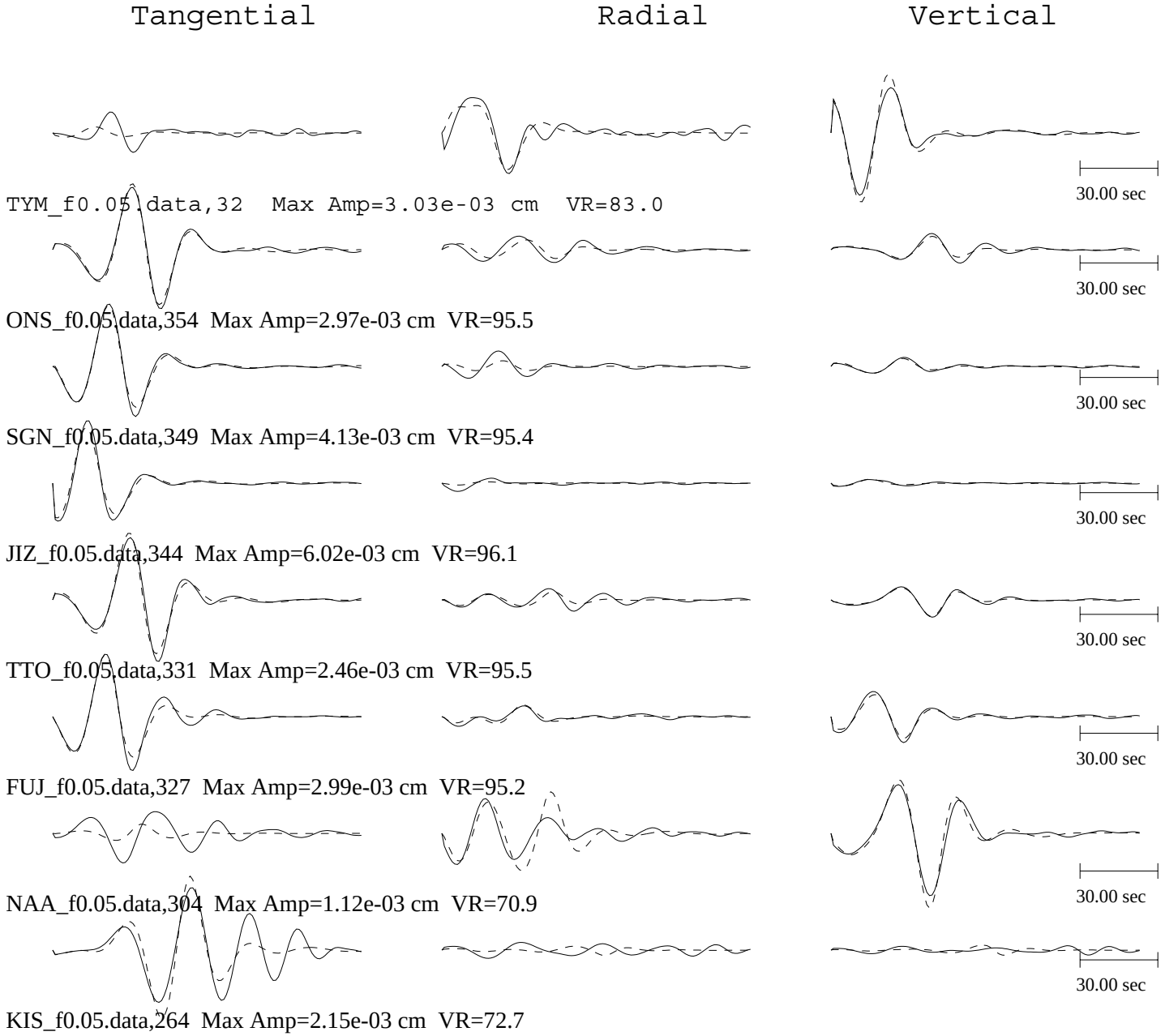

Strike=164 ; 258
Rake =-37 ; -174
Dip =85 ; 53
Mo =5.47e+23
Mw =5.1
Percent DC=45
Percent CLVD=55
Percent ISO=0
Variance=3.56e-08
Var. Red=9.00e+01
RES/Pdc.=7.98e-10

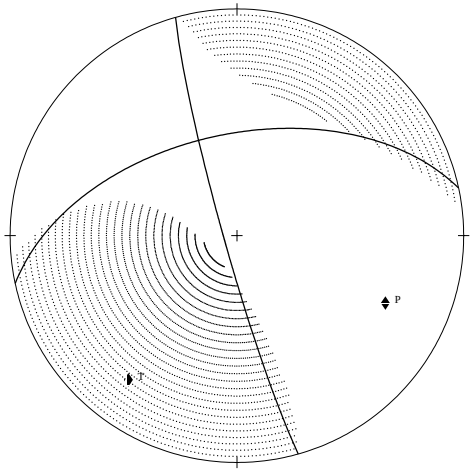

Figure 85

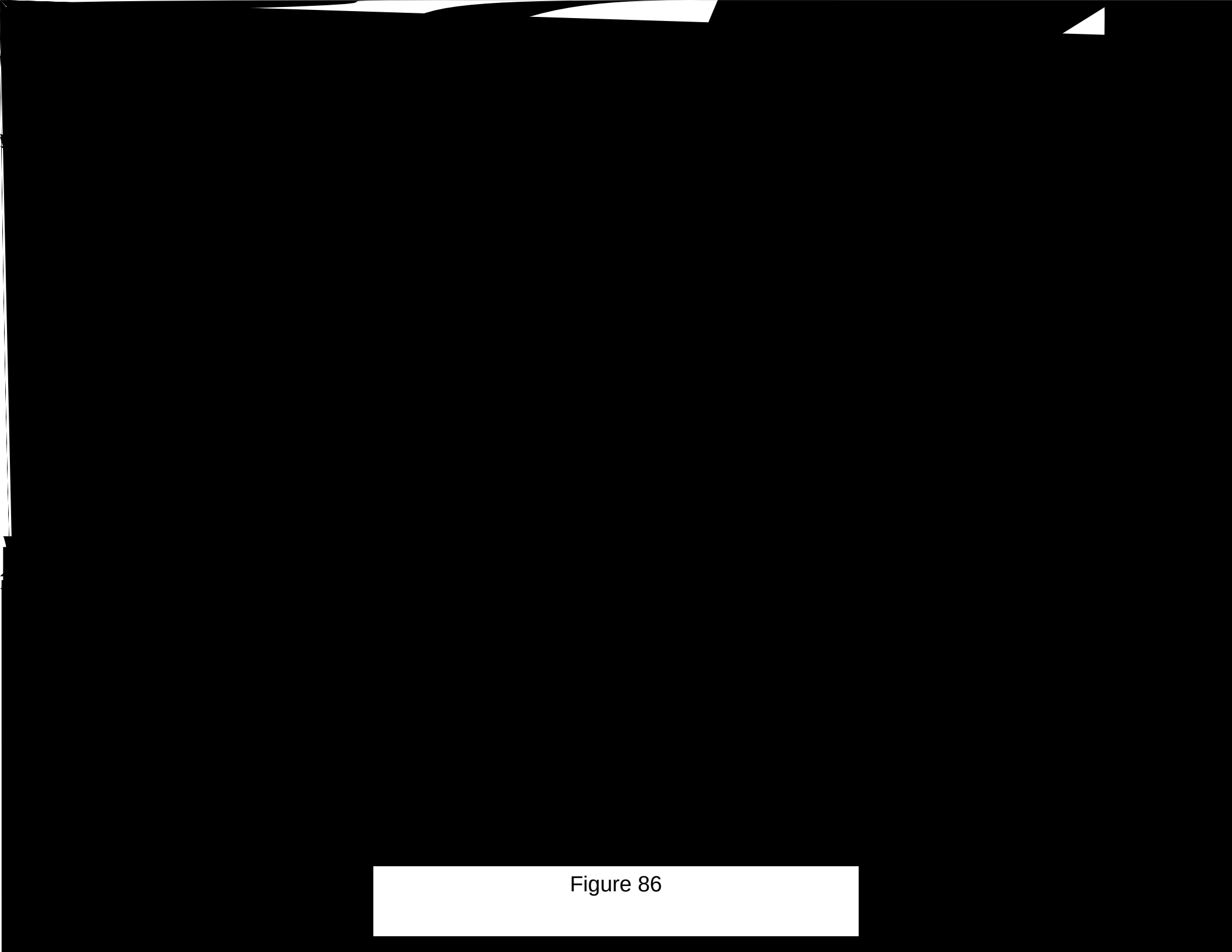

Figure 86

EVT11

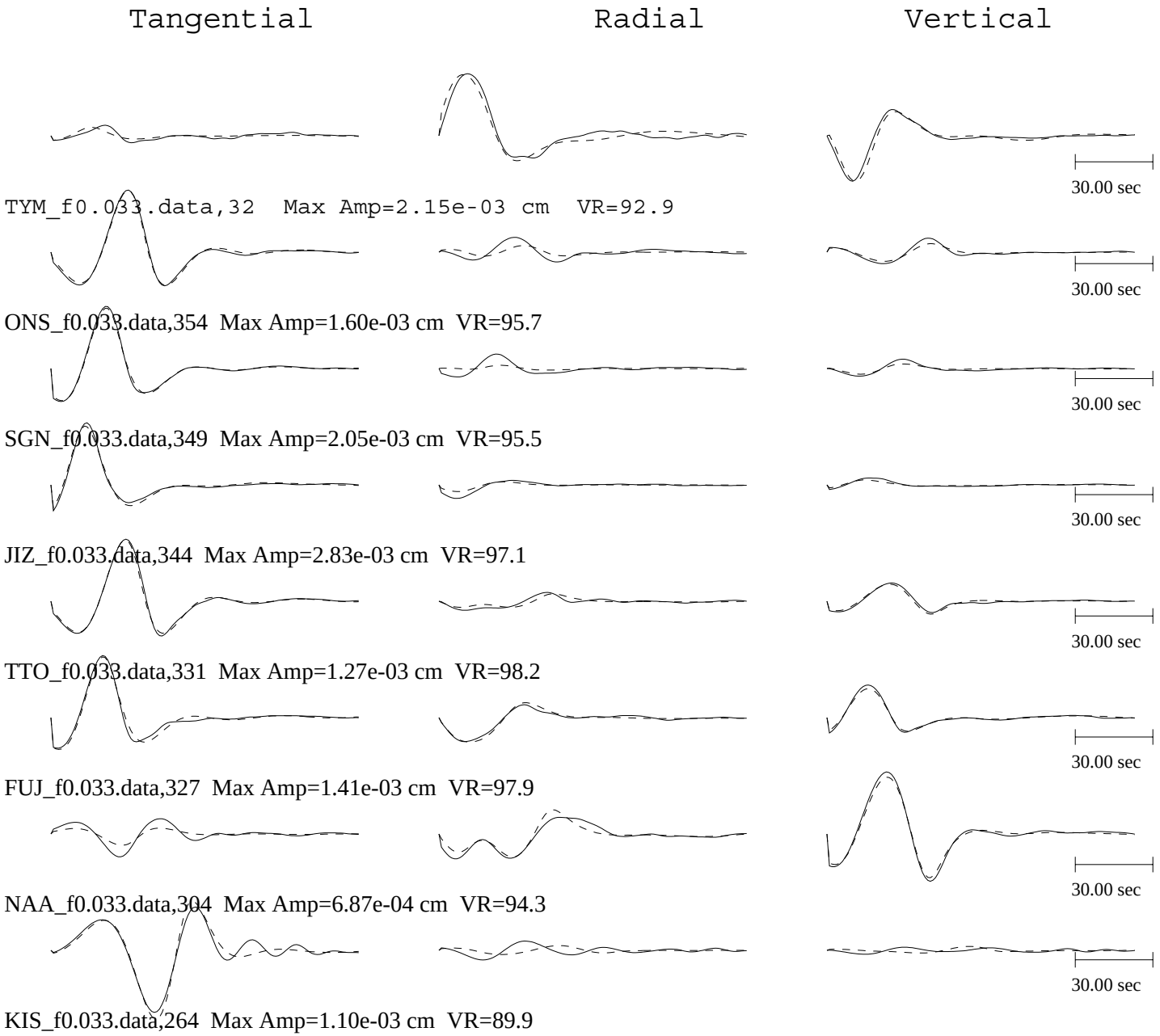

Strike=351 ; 261
Rake =8 ; 178
Dip =88 ; 82
Mo =4.69e+23
Mw =5.1
Percent DC=42
Percent CLVD=58
Percent ISO=0
Variance=5.90e-09
Var. Red=9.50e+01
RES/Pdc.=1.40e-10

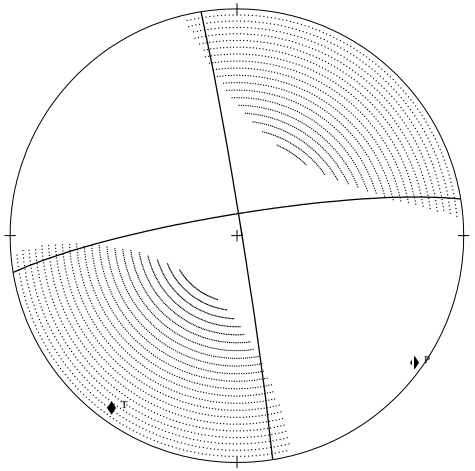

Figure 87

EVT11

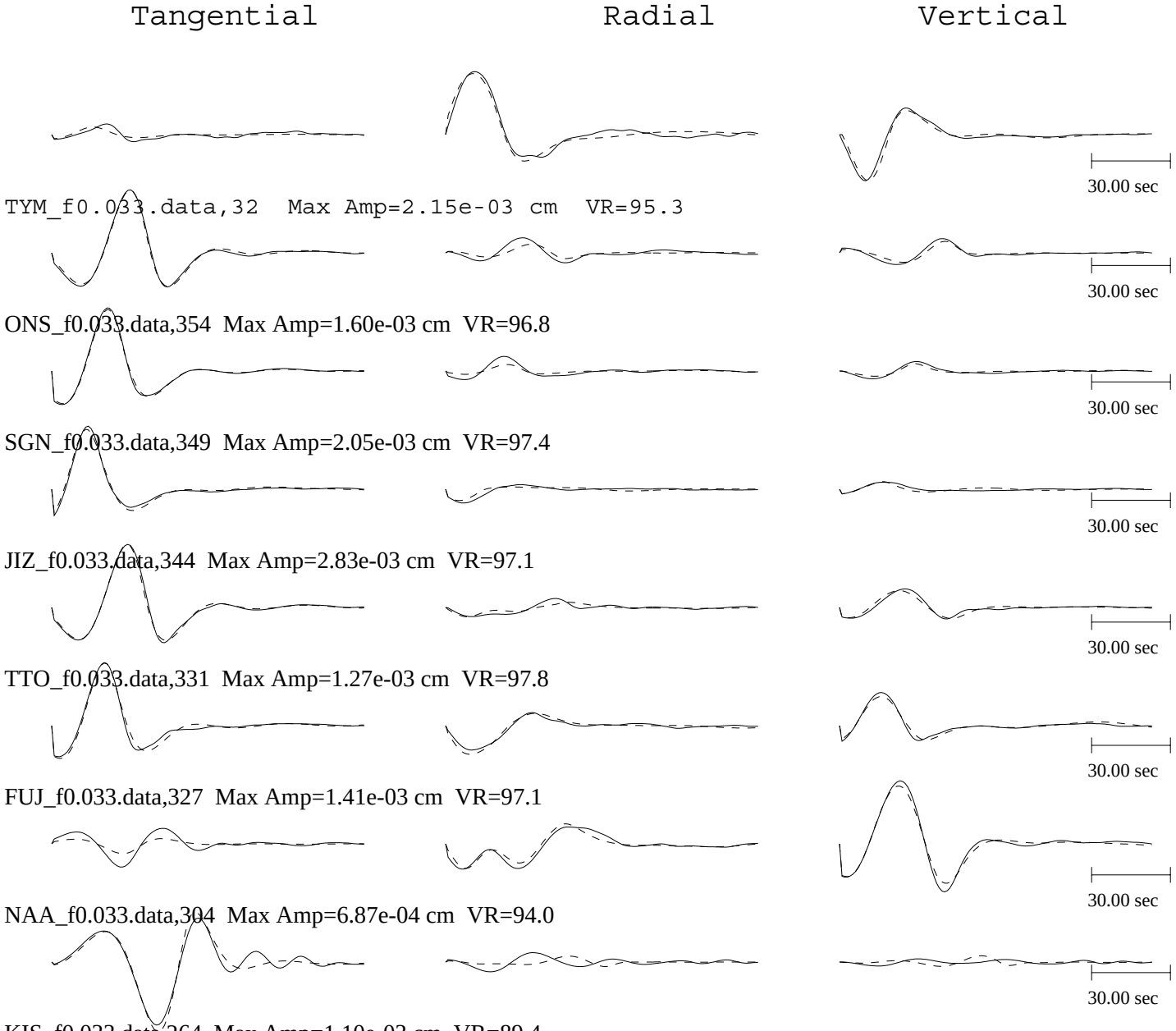

Strike=127 ; 305
Rake =-89 ; -91
Dip =49 ; 41
Mo =6.46e+23
Mw =5.2
Percent DC=29
Percent CLVD=32
Percent ISO=39
Variance=4.76e-09
Var. Red=9.58e+01
RES/Pdc.=1.62e-10

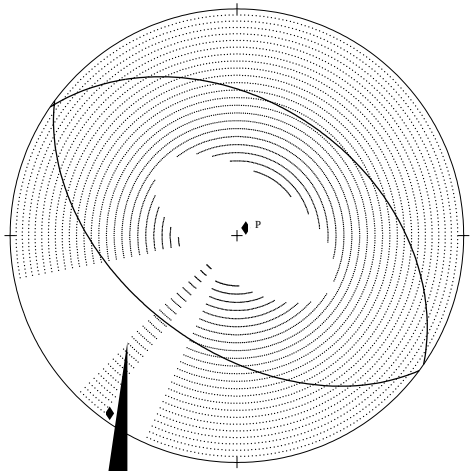

Figure 88

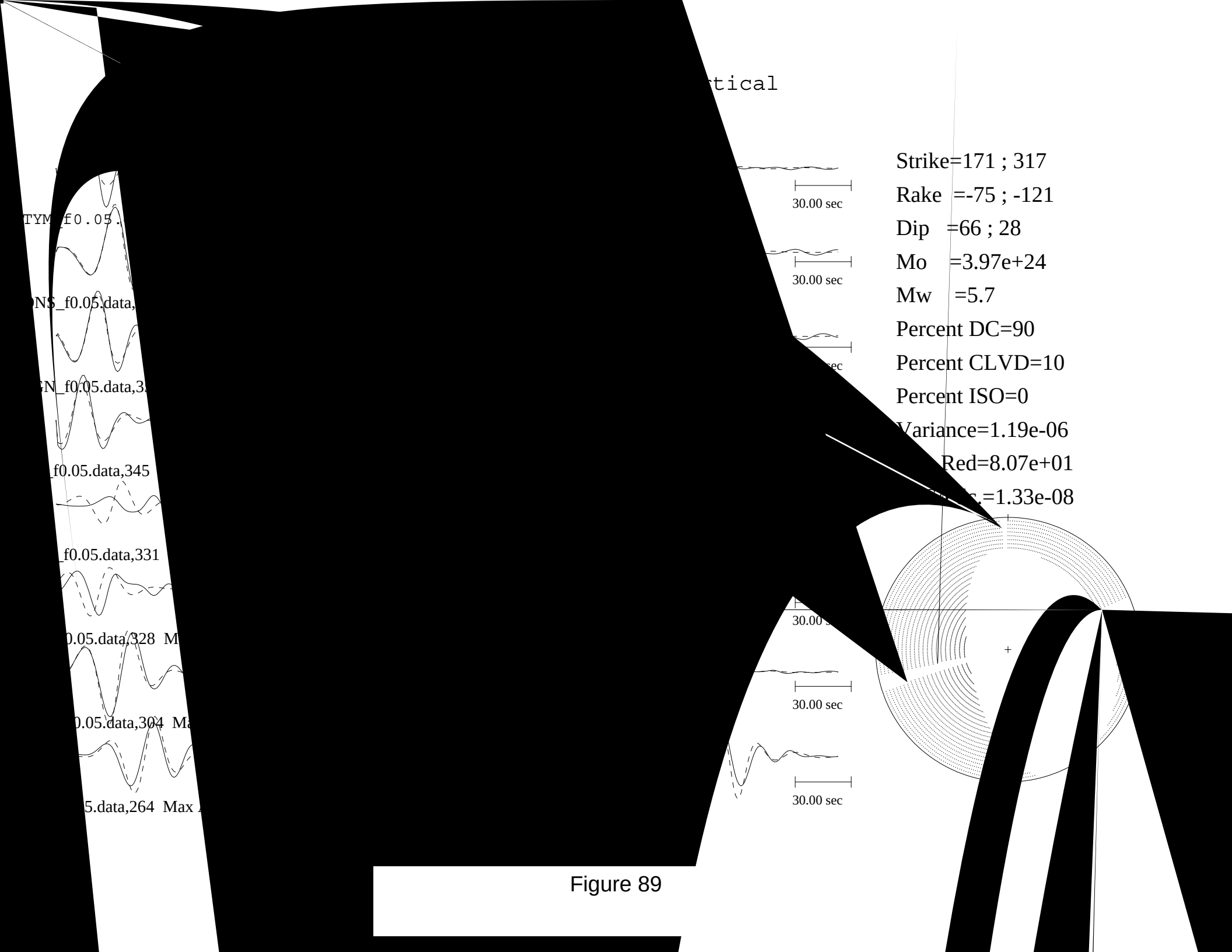
tical
TYM_f0.05.
NS_f0.05.data,
N_f0.05.data,3
f0.05.data,345
_f0.05.data,331
0.05.data,328 M
0.05.data,304 Ma
5.data,264 Max
30.00 sec
30.00 sec
30.00 sec
30.00 sec
Strike=171 ; 317
Rake =-75 ; -121
Dip =66 ; 28
Mo =3.97e+24
Mw =5.7
Percent DC=90
Percent CLVD=10
Percent ISO=0
Variance=1.19e-06
Red=8.07e+01
=1.33e-08

Figure 89

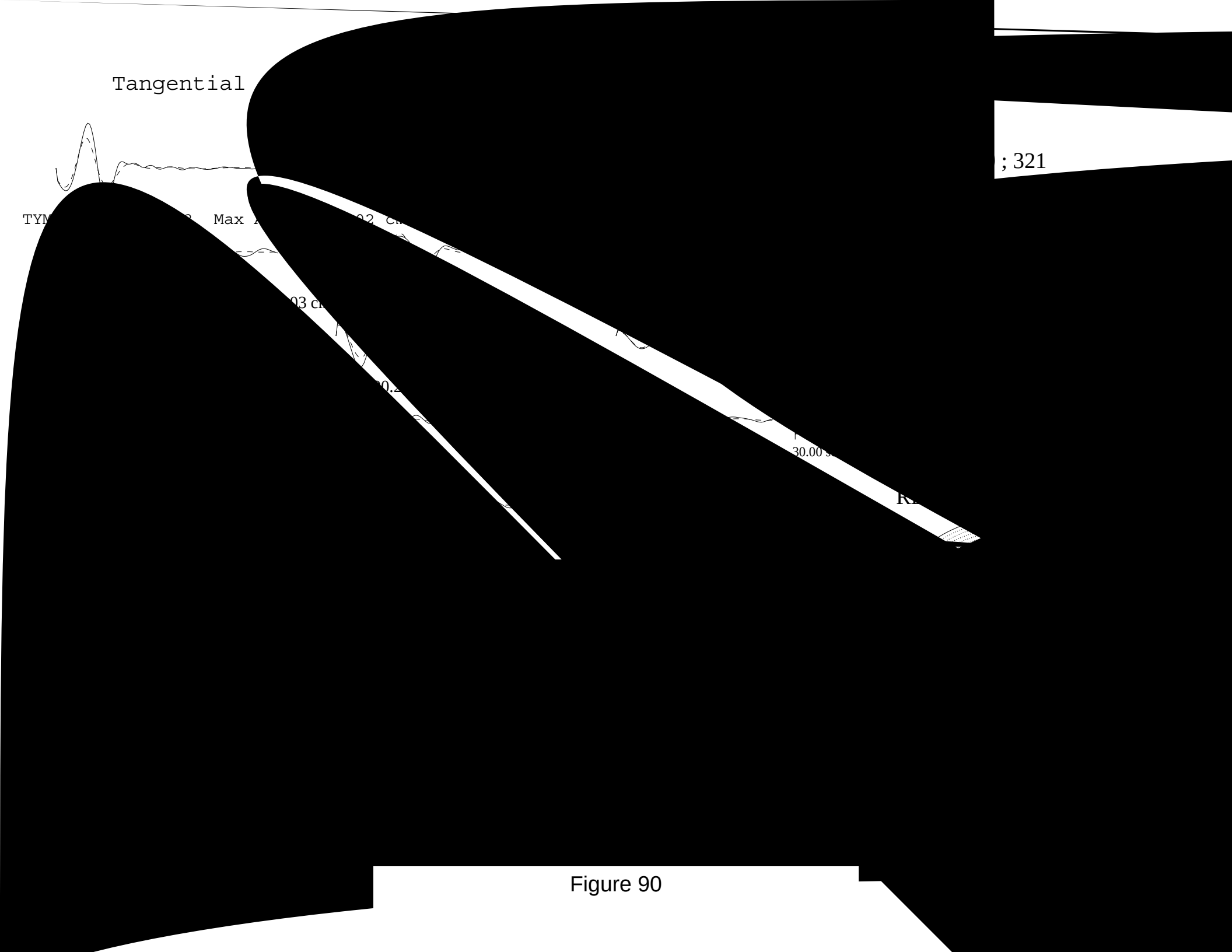

Figure 90

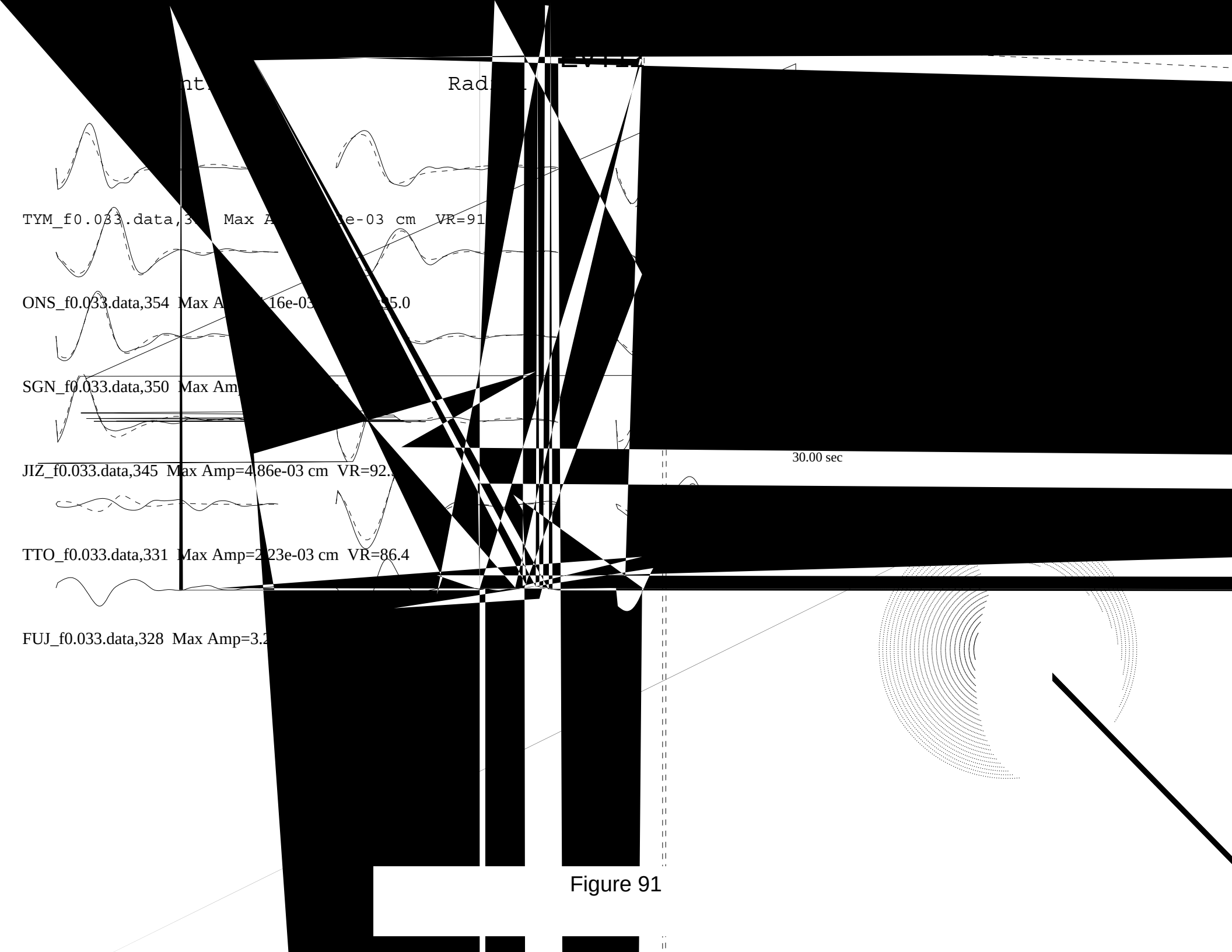
TYM_f0.033.data,3
Max A
e-03 cm VR=91
ONS_f0.033.data,354 Max A
16e-03
25.0
SGN_f0.033.data,350 Max Am
JIZ_f0.033.data,345 Max Amp=4.86e-03 cm VR=92.
TTO_f0.033.data,331 Max Amp=2.23e-03 cm VR=86.4
FUJ_f0.033.data,328 Max Amp=3.2
30.00 sec

Figure 91

Figure 92

EVT13

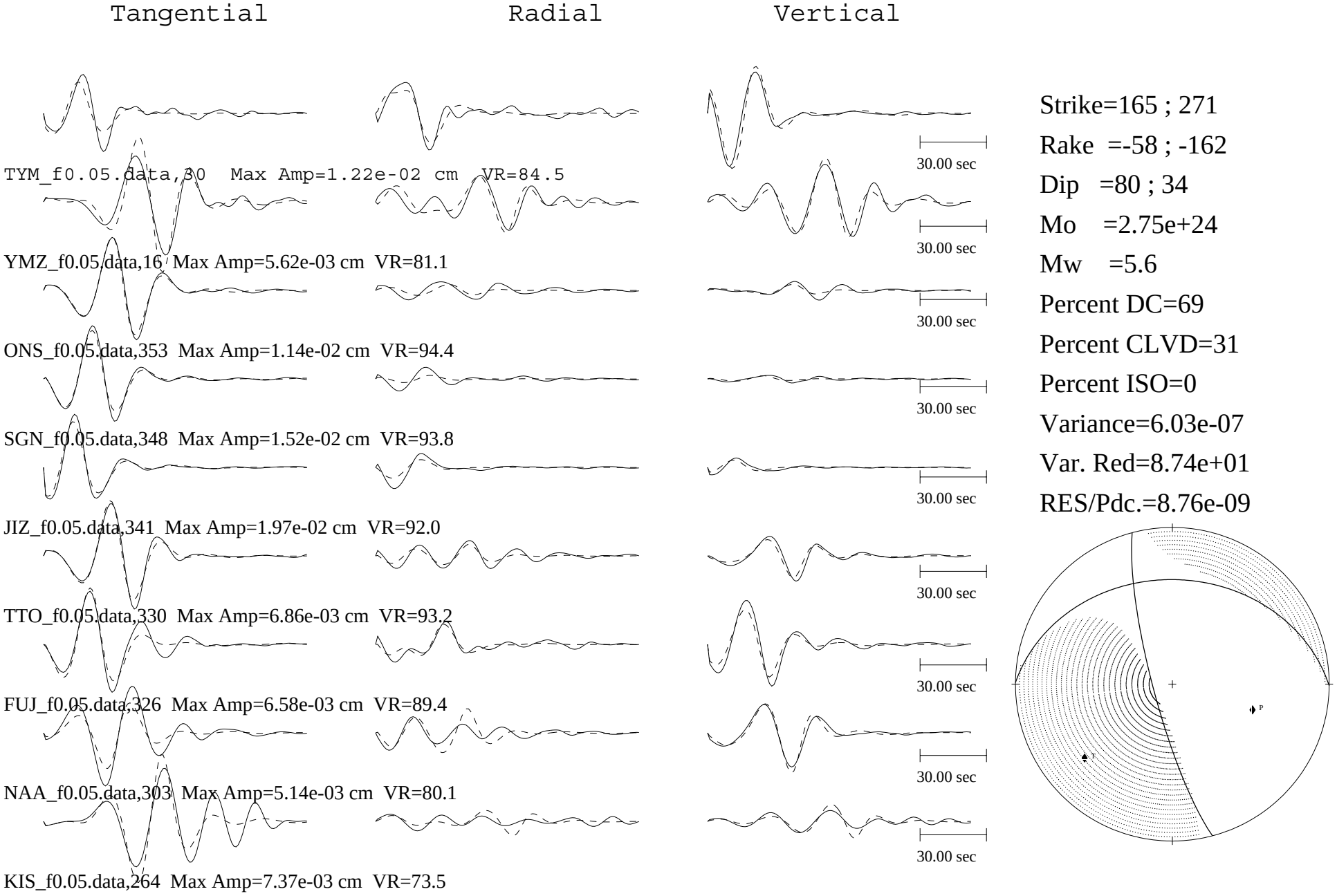

Figure 93

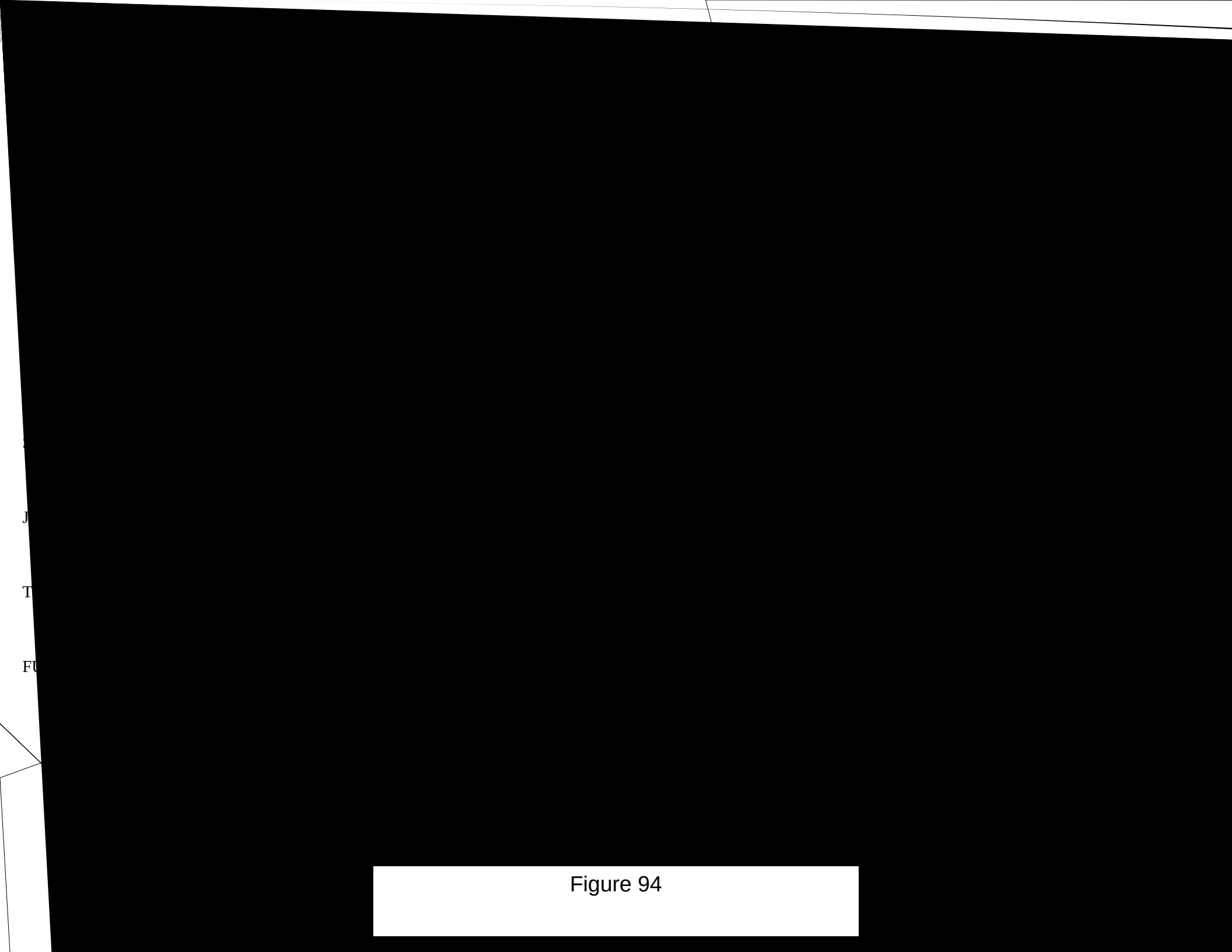

Figure 94

EVT13

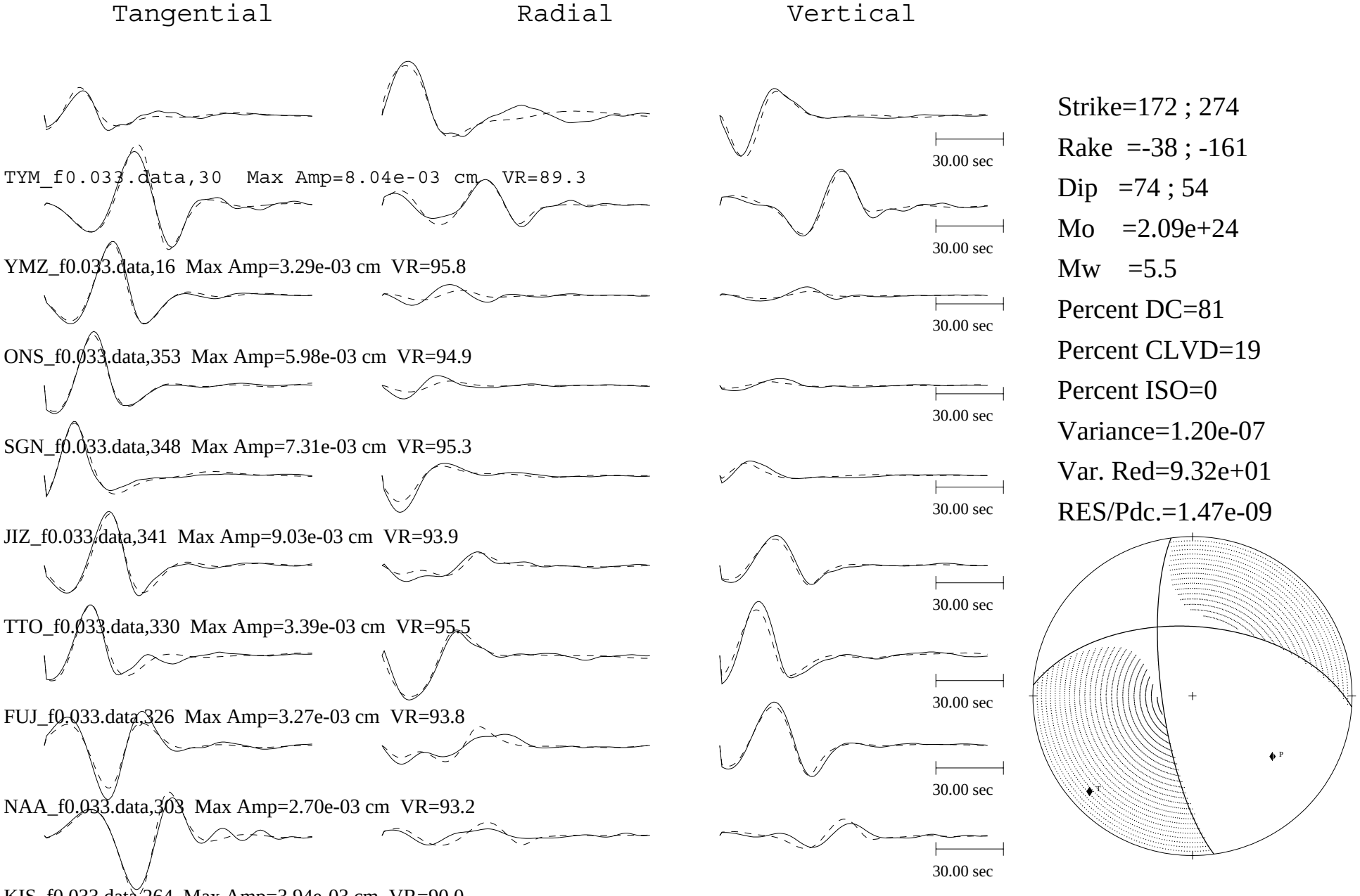

Figure 95

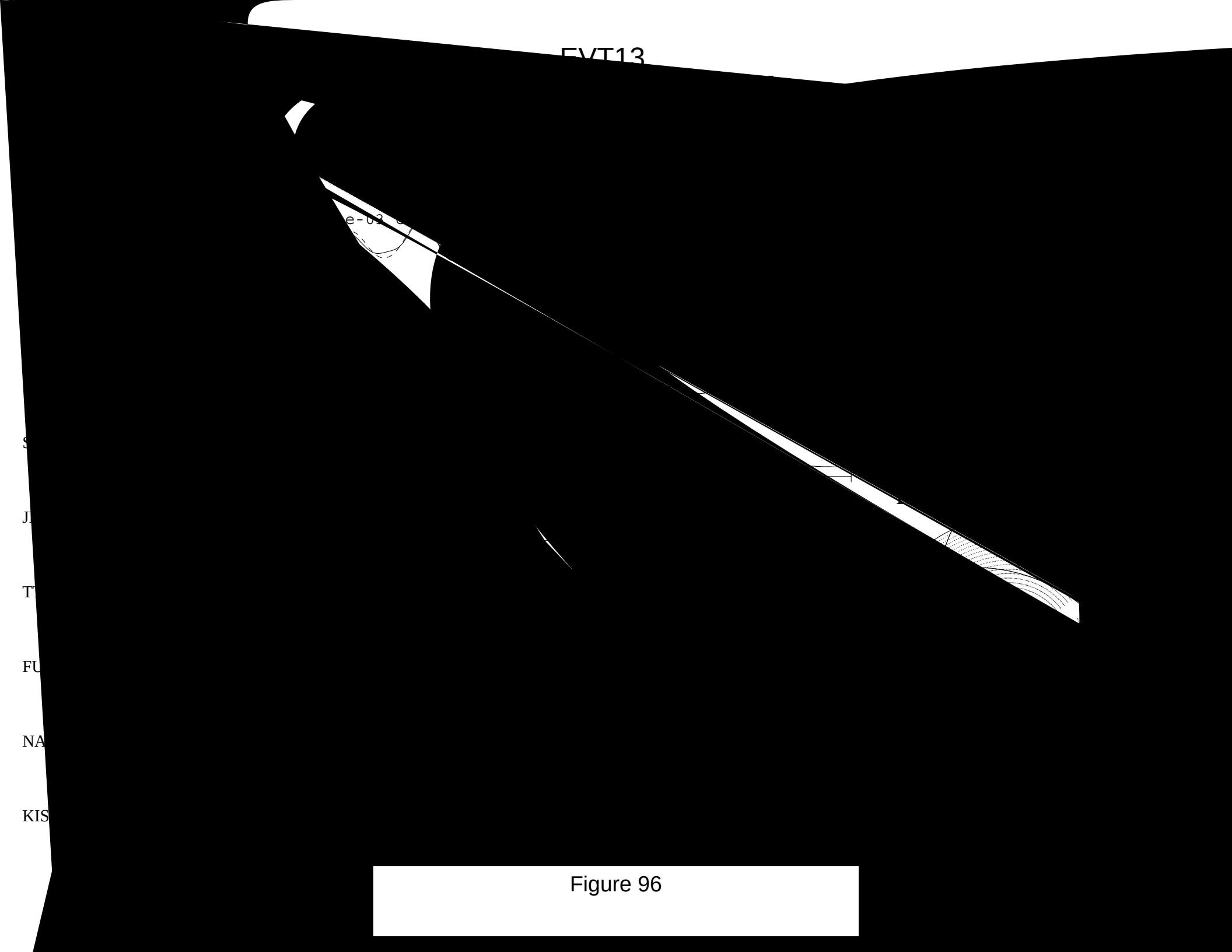

Figure 96

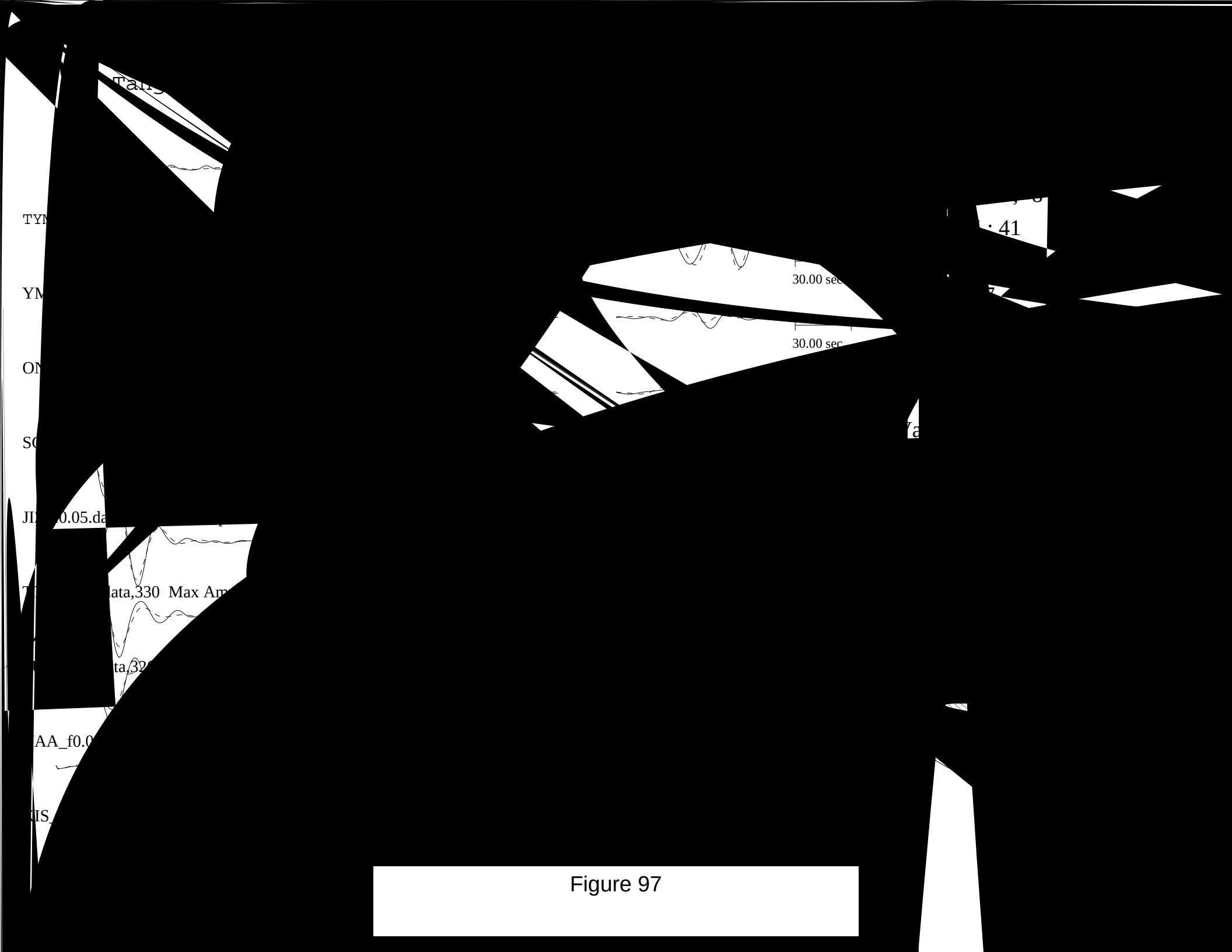

Figure 97

EVT14

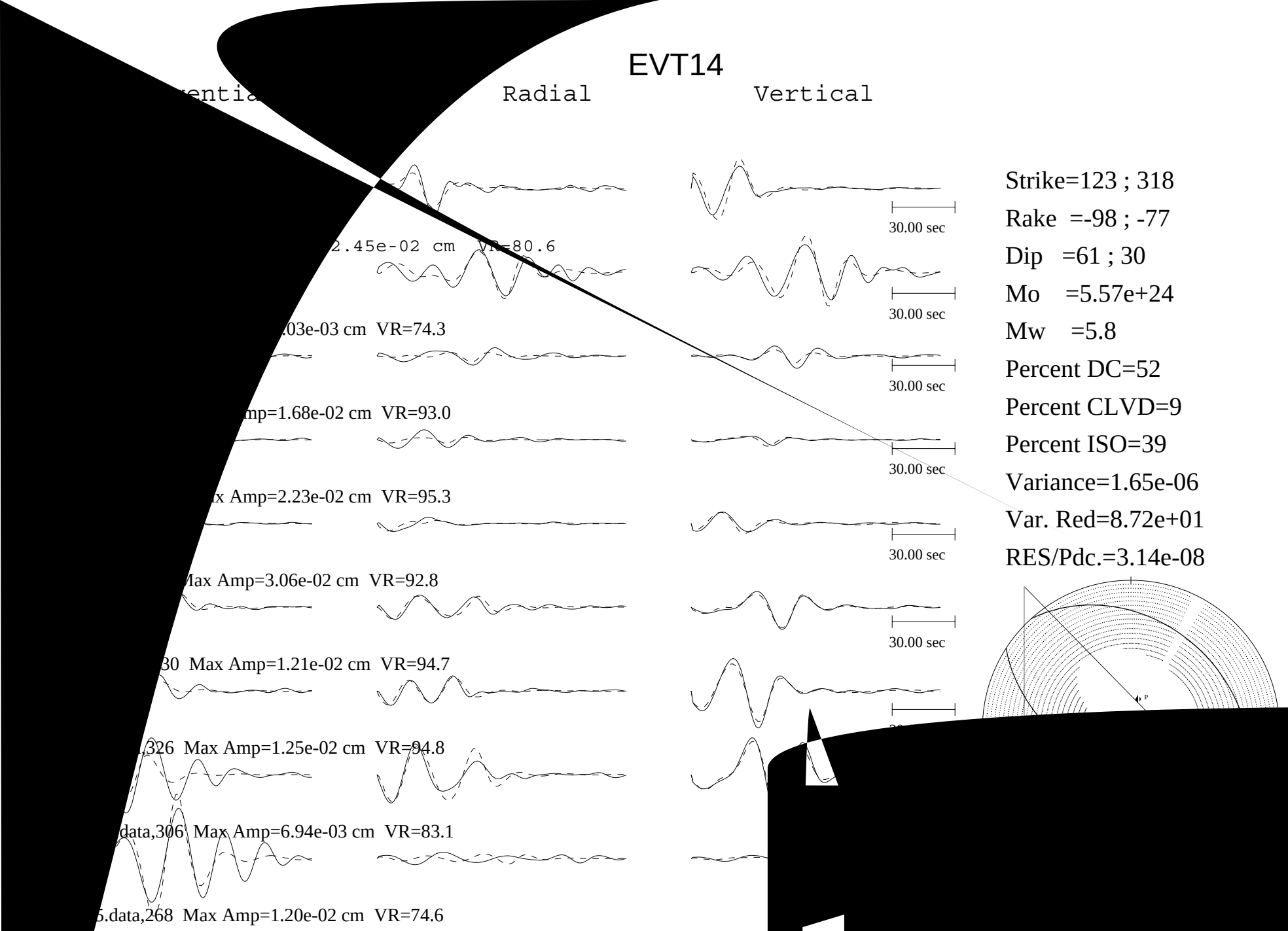

Figure 98

Figure 99

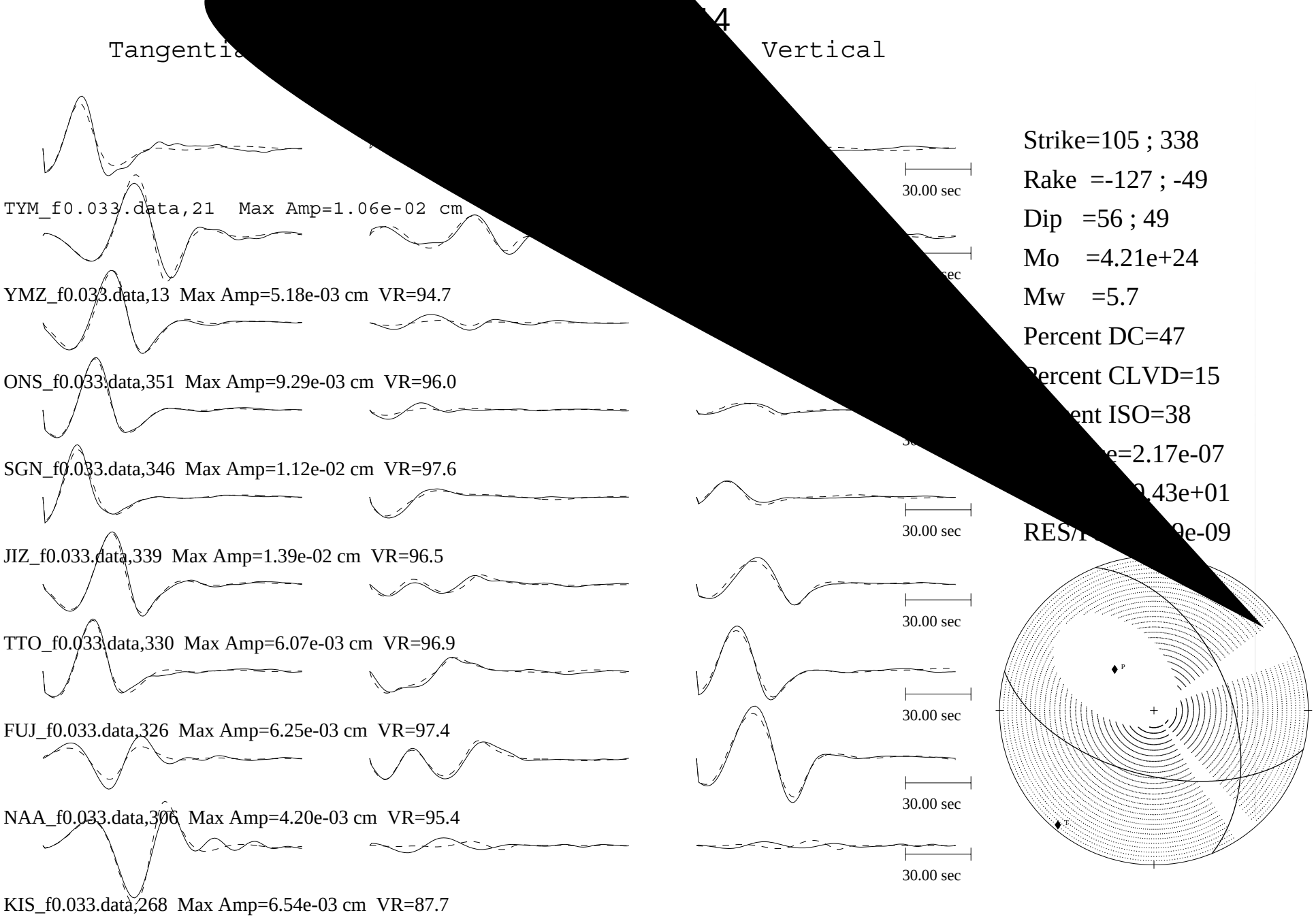
Tangentia
Vertical
TYM_f0.033.data,21 Max Amp=1.06e-02 cm
YMZ_f0.033.data,13 Max Amp=5.18e-03 cm VR=94.7
ONS_f0.033.data,351 Max Amp=9.29e-03 cm VR=96.0
SGN_f0.033.data,346 Max Amp=1.12e-02 cm VR=97.6
JIZ_f0.033.data,339 Max Amp=1.39e-02 cm VR=96.5
TTO_f0.033.data,330 Max Amp=6.07e-03 cm VR=96.9
FUJ_f0.033.data,326 Max Amp=6.25e-03 cm VR=97.4
NAA_f0.033.data,306 Max Amp=4.20e-03 cm VR=95.4
KIS_f0.033.data,268 Max Amp=6.54e-03 cm VR=87.7
30.00 sec
Strike=105 ; 338
Rake =-127 ; -49
Dip =56 ; 49
Mo =4.21e+24
Mw =5.7
Percent DC=47
Percent CLVD=15
ent ISO=38
e=2.17e-07
.43e+01
9e-09

Figure 100

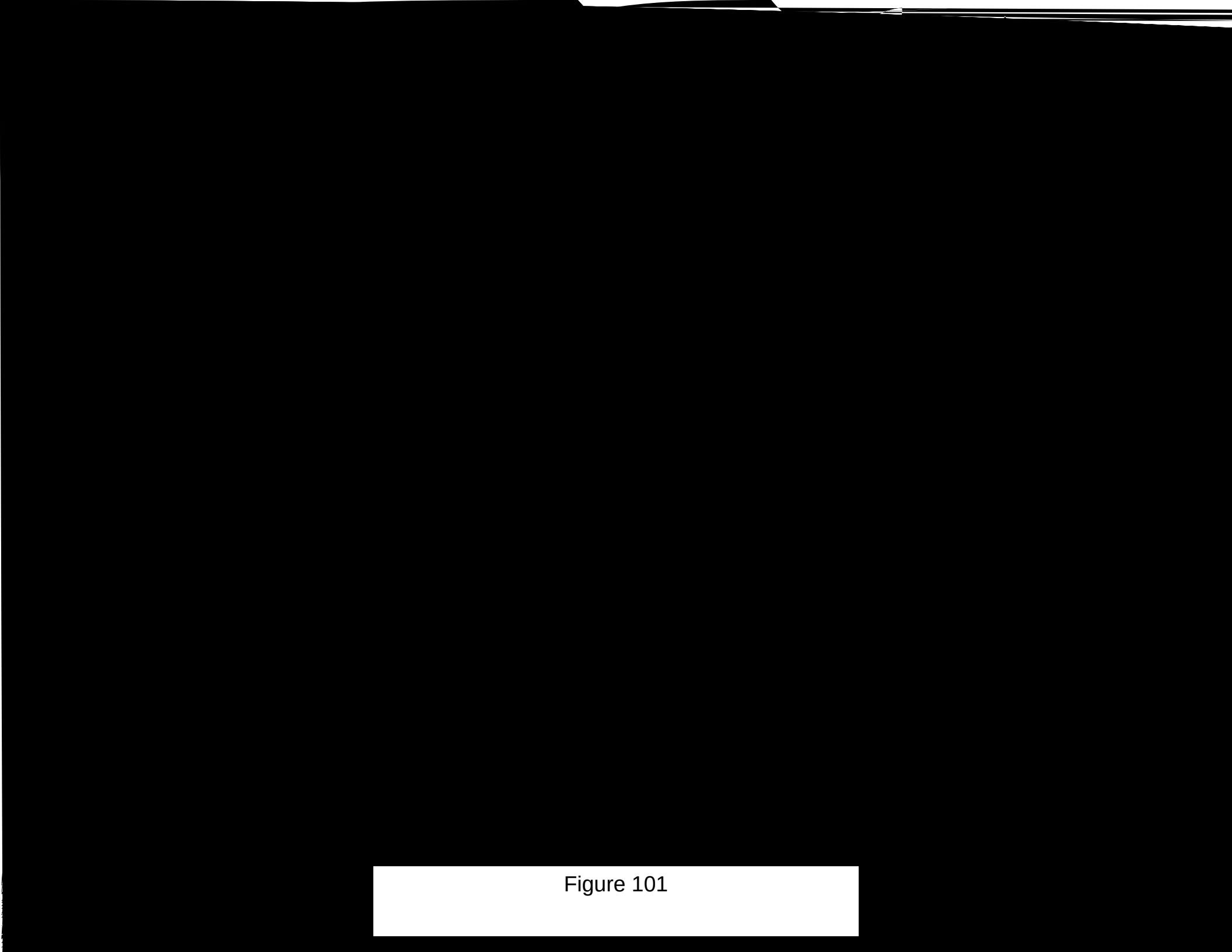

Figure 101

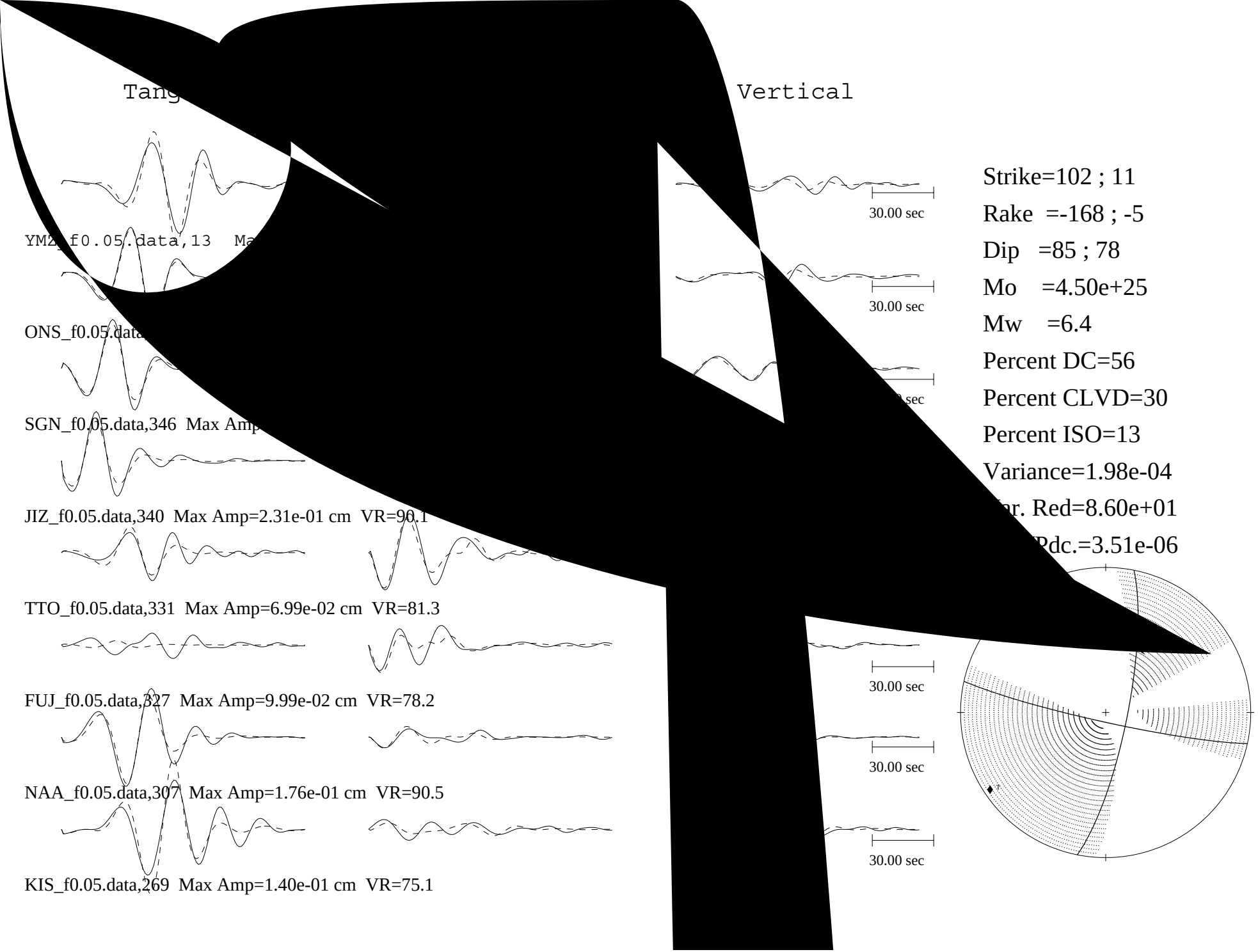
Tang
Vertical
YMZ_f0.05.data,13 Ma
ONS_f0.05.data
SGN_f0.05.data,346 Max Amp
JIZ_f0.05.data,340 Max Amp=2.31e-01 cm VR=90.1
TTO_f0.05.data,331 Max Amp=6.99e-02 cm VR=81.3
FUJ_f0.05.data,327 Max Amp=9.99e-02 cm VR=78.2
NAA_f0.05.data,307 Max Amp=1.76e-01 cm VR=90.5
KIS_f0.05.data,269 Max Amp=1.40e-01 cm VR=75.1
30.00 sec
30.00 sec
sec
30.00 sec
30.00 sec
30.00 sec
Strike=102 ; 11
Rake =-168 ; -5
Dip =85 ; 78
Mo =4.50e+25
Mw =6.4
Percent DC=56
Percent CLVD=30
Percent ISO=13
Variance=1.98e-04
r. Red=8.60e+01
Pdc.=3.51e-06

Figure 102


EVT15
Radial
Vertical
Strike=103 ; 13
Rake =-168 ; -3
=87 ; 78
13e+2
30.00 sec
Percent ISO=
Variance=2.6
Red=9.
RES/Pdc.=2
07
Max Amp=1.14e-01 cm
VR=98.0
VR=95.0
VR=97.5
VR=87.3

Figure 103

EVT15

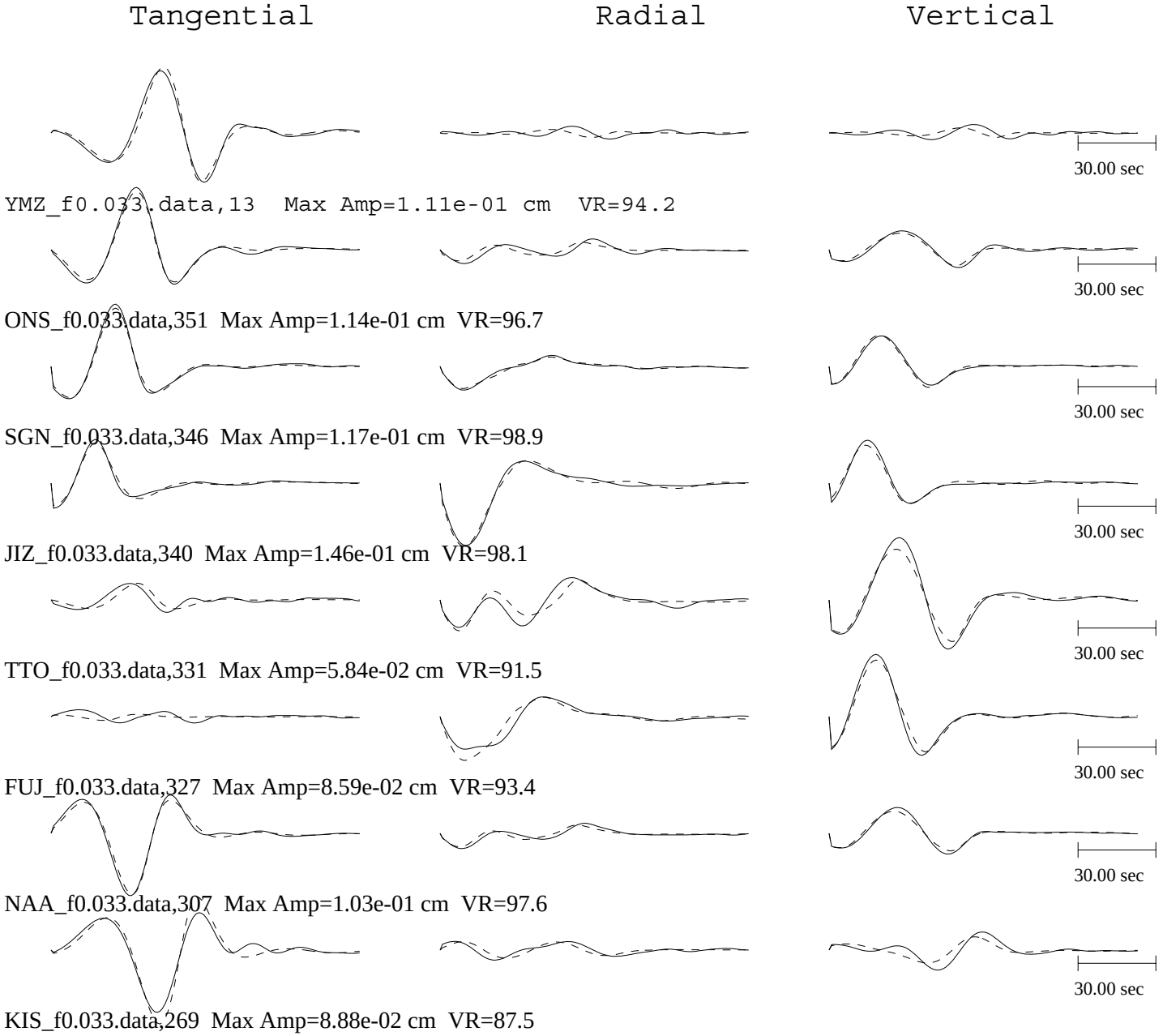

Strike=103 ; 12
Rake =-168 ; -4
Dip =86 ; 78
Mo =5.14e+25
Mw =6.4
Percent DC=79
Percent CLVD=13
Percent ISO=8
Variance=2.59e-05
Var. Red=9.51e+01
RES/Pdc.=3.28e-07

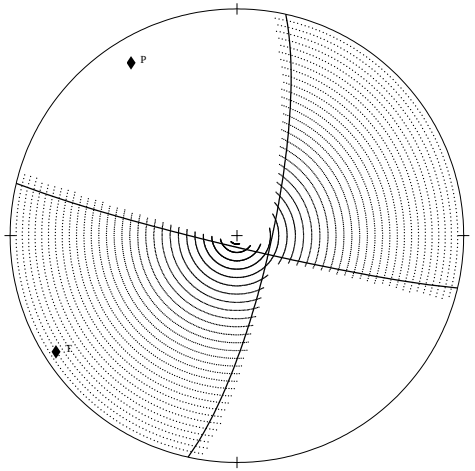

Figure 104

EVT16

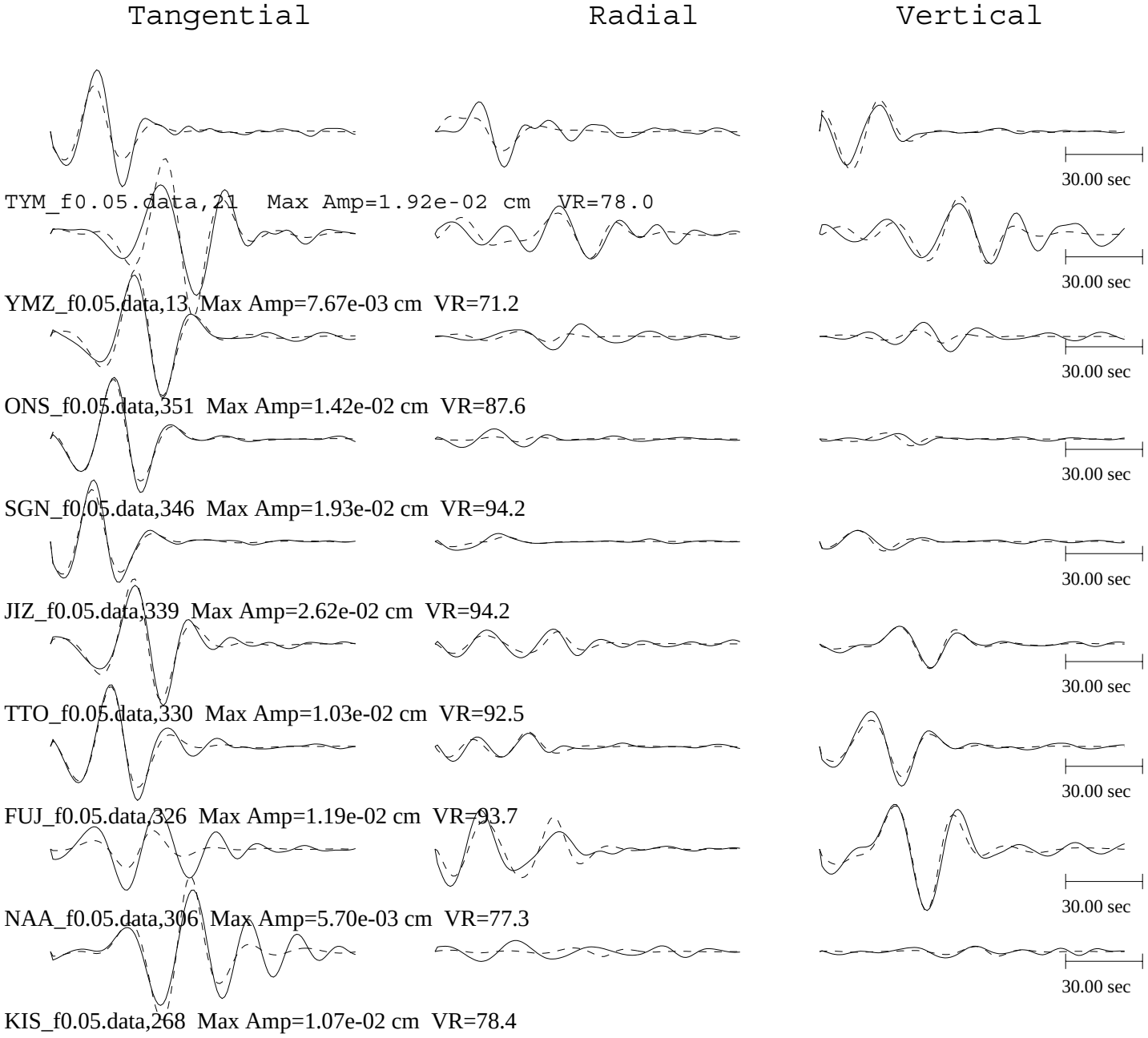

Strike=263 ; 357
Rake =157 ; 10
Dip =81 ; 68
Mo =2.77e+24
Mw =5.6
Percent DC=24
Percent CLVD=76
Percent ISO=0
Variance=1.27e-06
Var. Red=8.60e+01
RES/Pdc.=5.27e-08

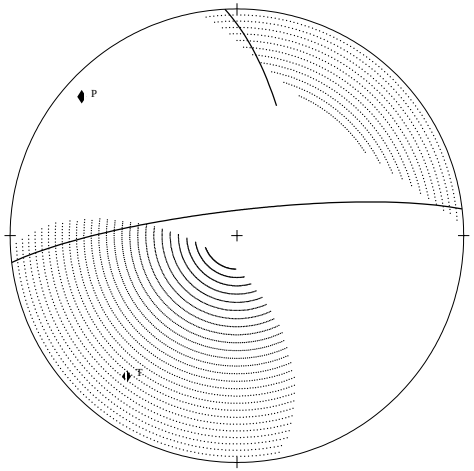

Figure 105

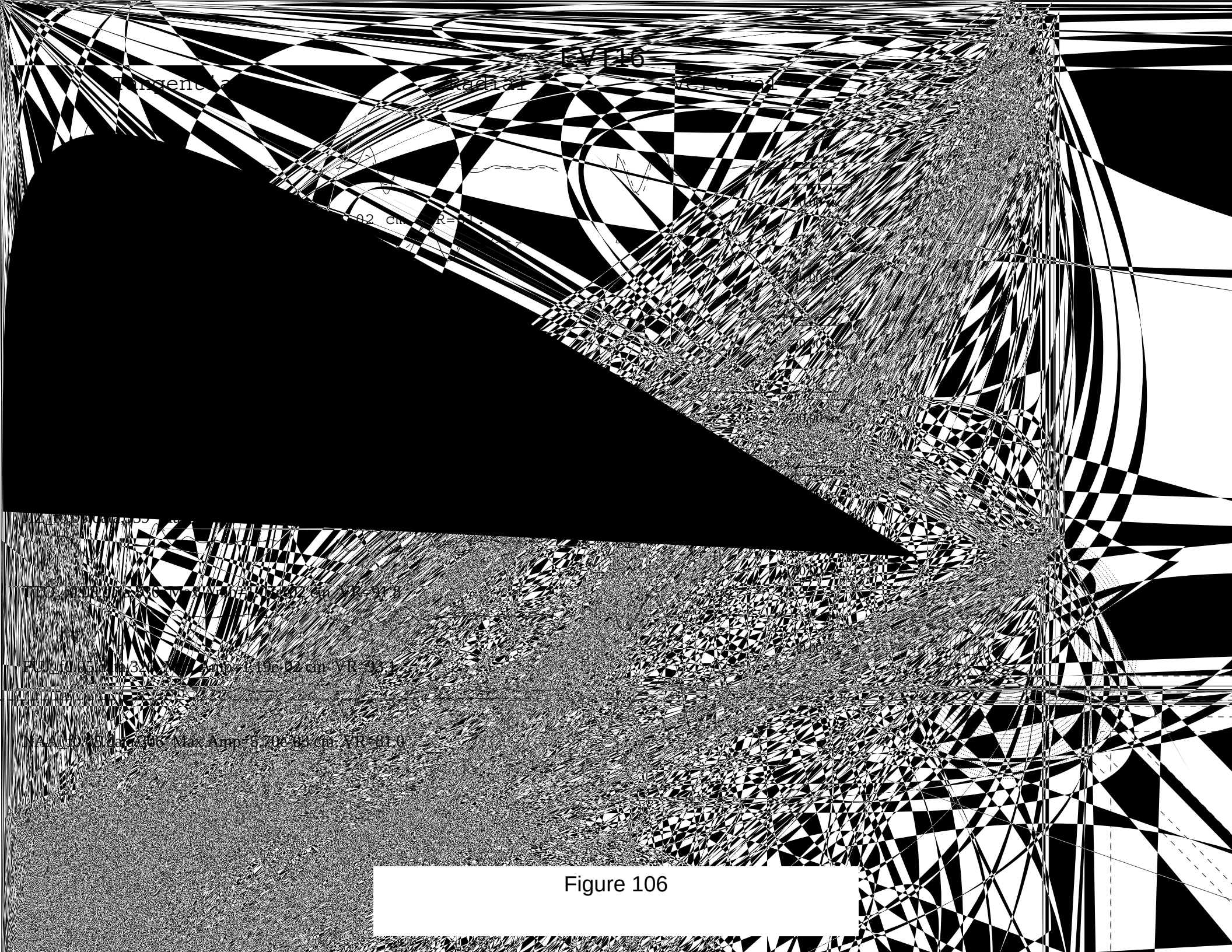

Figure 106

EVT16

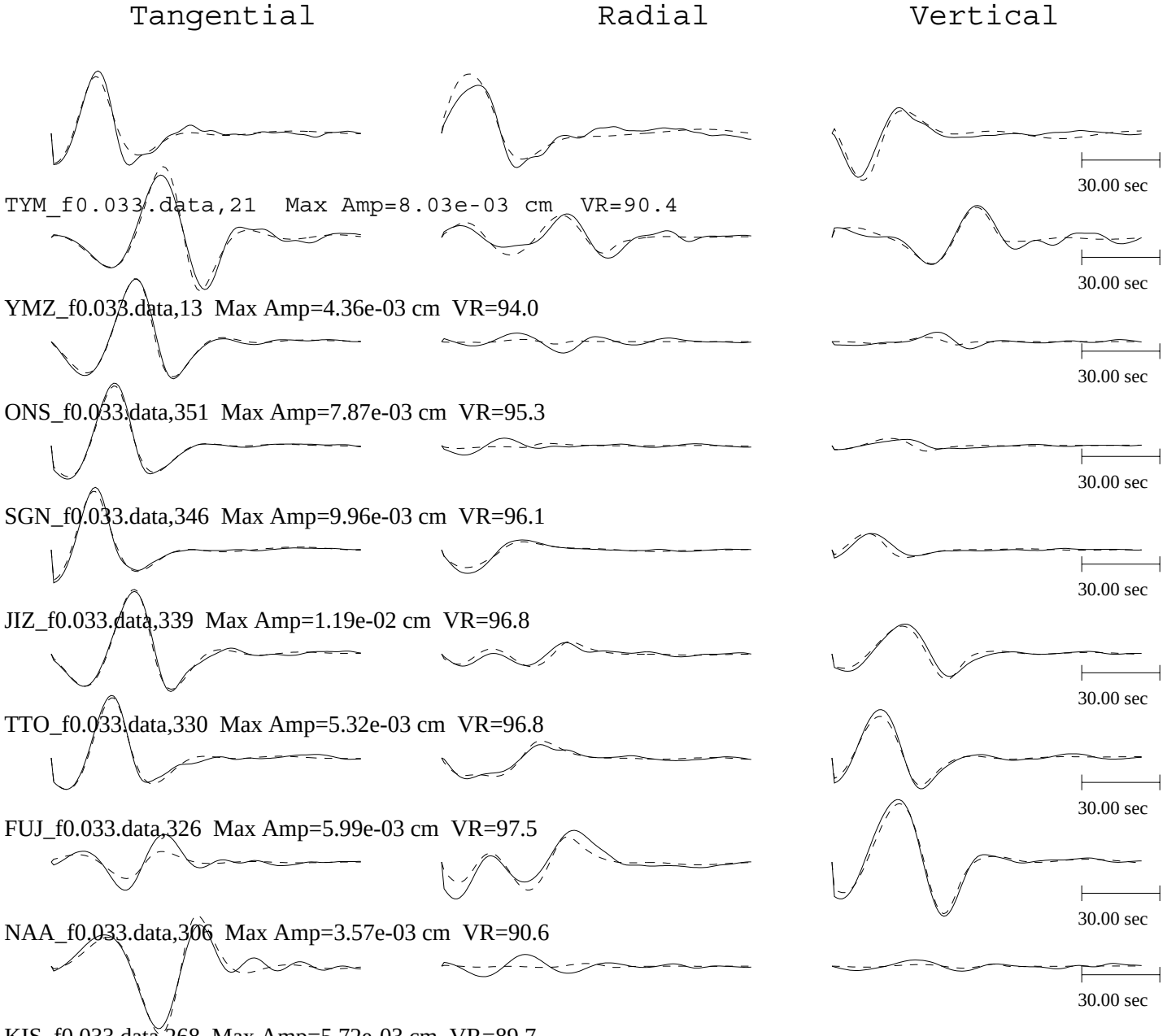

Strike=264 ; 358
Rake =155 ; 9
Dip =82 ; 65
Mo =2.86e+24
Mw =5.6
Percent DC=39
Percent CLVD=61
Percent ISO=0
Variance=1.53e-07
Var. Red=9.42e+01
RES/Pdc.=3.86e-09

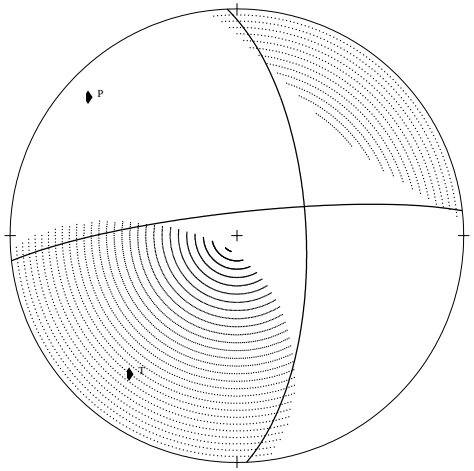

Figure 107

EVT16

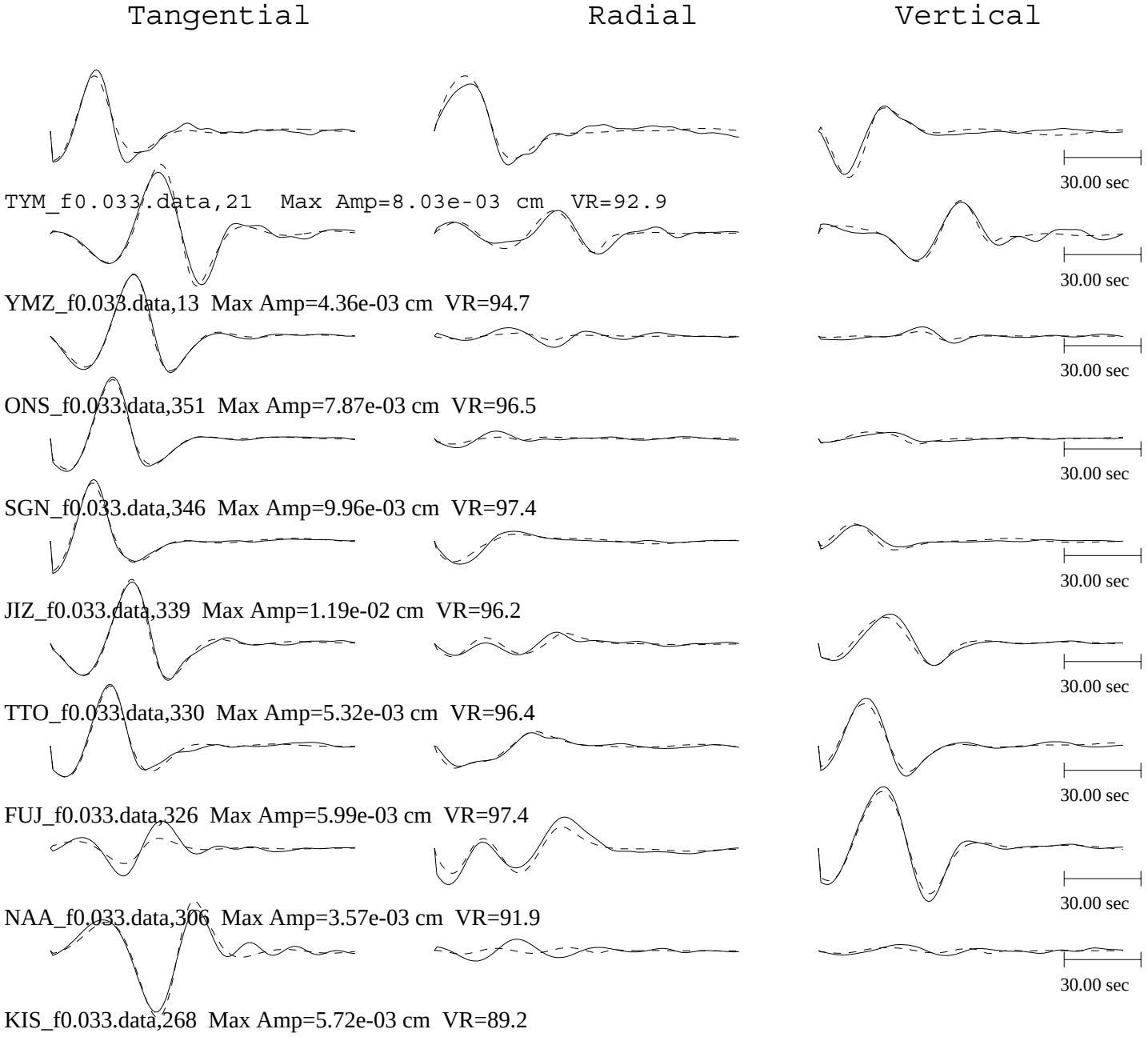

Strike=122 ; 319
Rake =-99 ; -75
Dip =60 ; 32
Mo =3.48e+24
Mw =5.7
Percent DC=24
Percent CLVD=37
Percent ISO=38
Variance=1.32e-07
Var. Red=9.49e+01
RES/Pdc.=5.38e-09

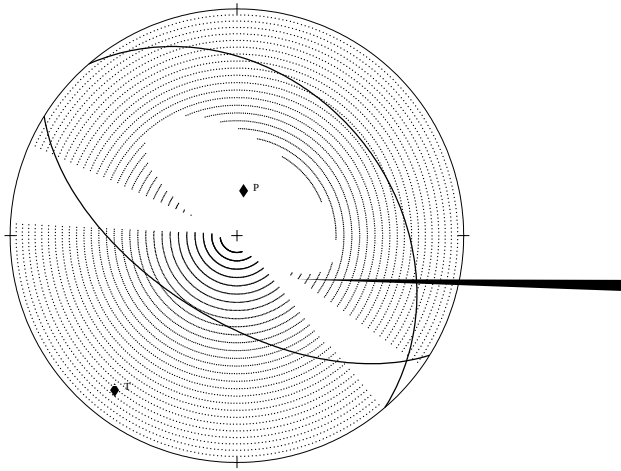

Figure 108

EVT17

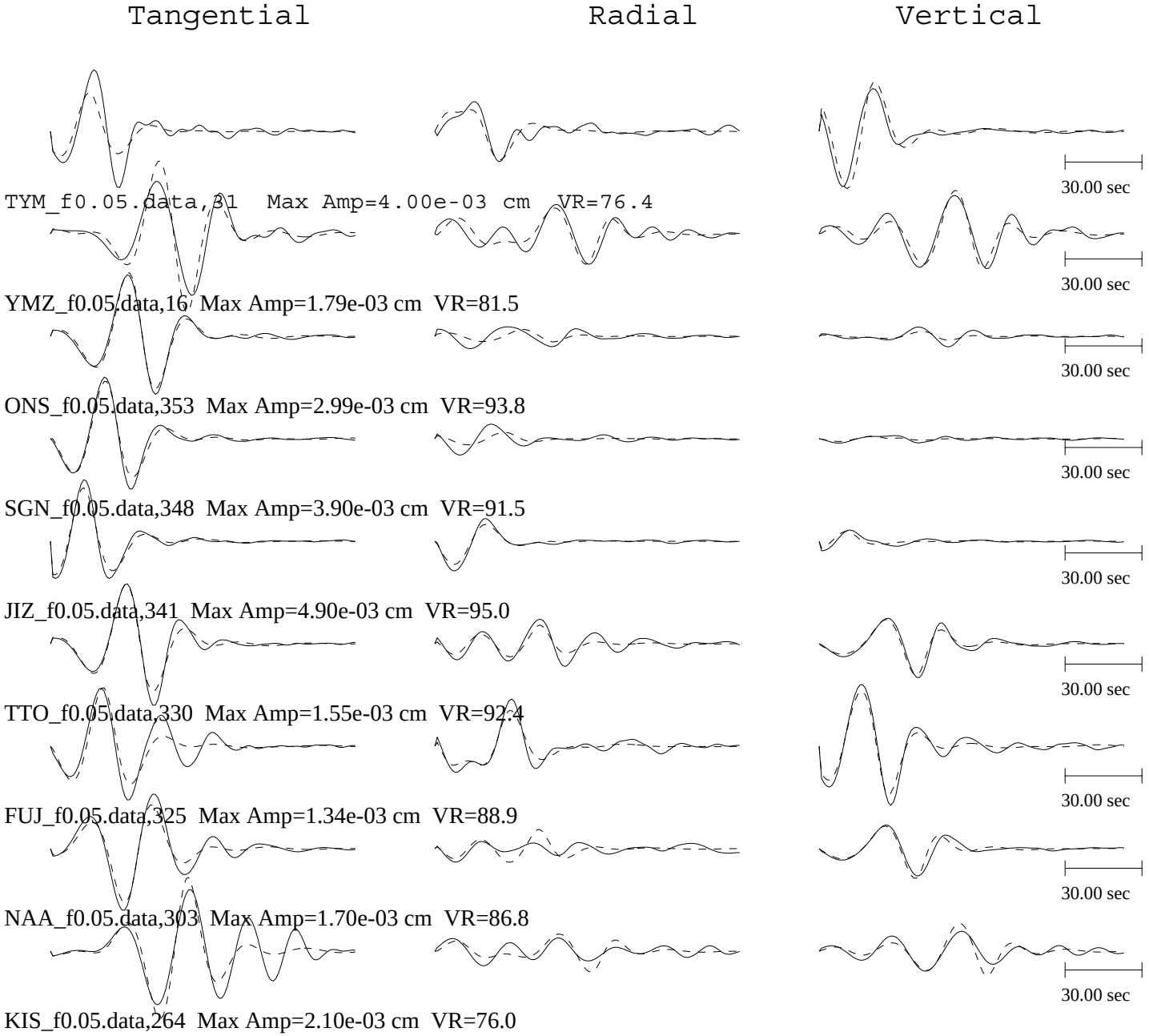

Strike=173 ; 280
Rake =-46 ; -156
Dip =73 ; 46
Mo =6.62e+23
Mw =5.2
Percent DC=100
Percent CLVD=0
Percent ISO=0
Variance=5.75e-08
Var. Red=8.56e+01
RES/Pdc.=5.75e-10

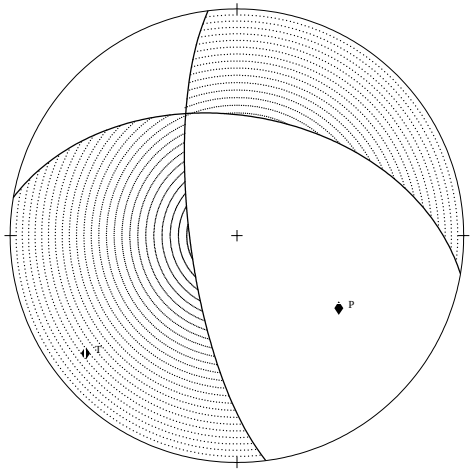

Figure 109

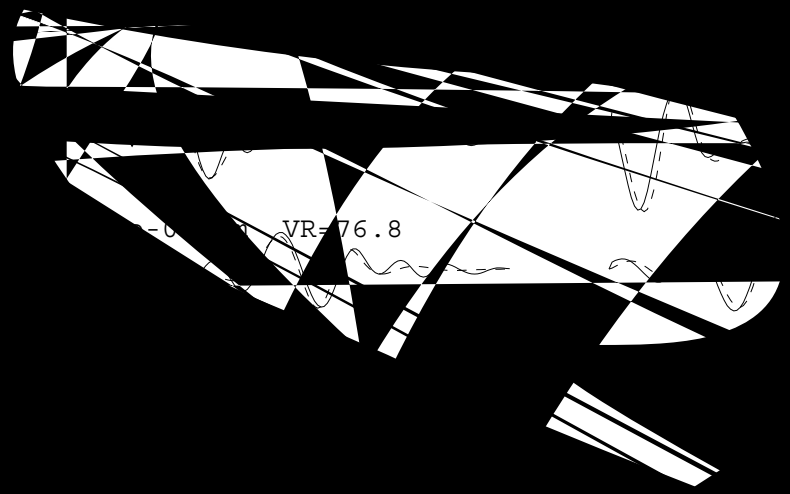

Figure 110


Tangential
Radial
Vertical
30.00 sec
30.00 sec
30.00 sec
30.00 sec
30.00 sec

Figure 111

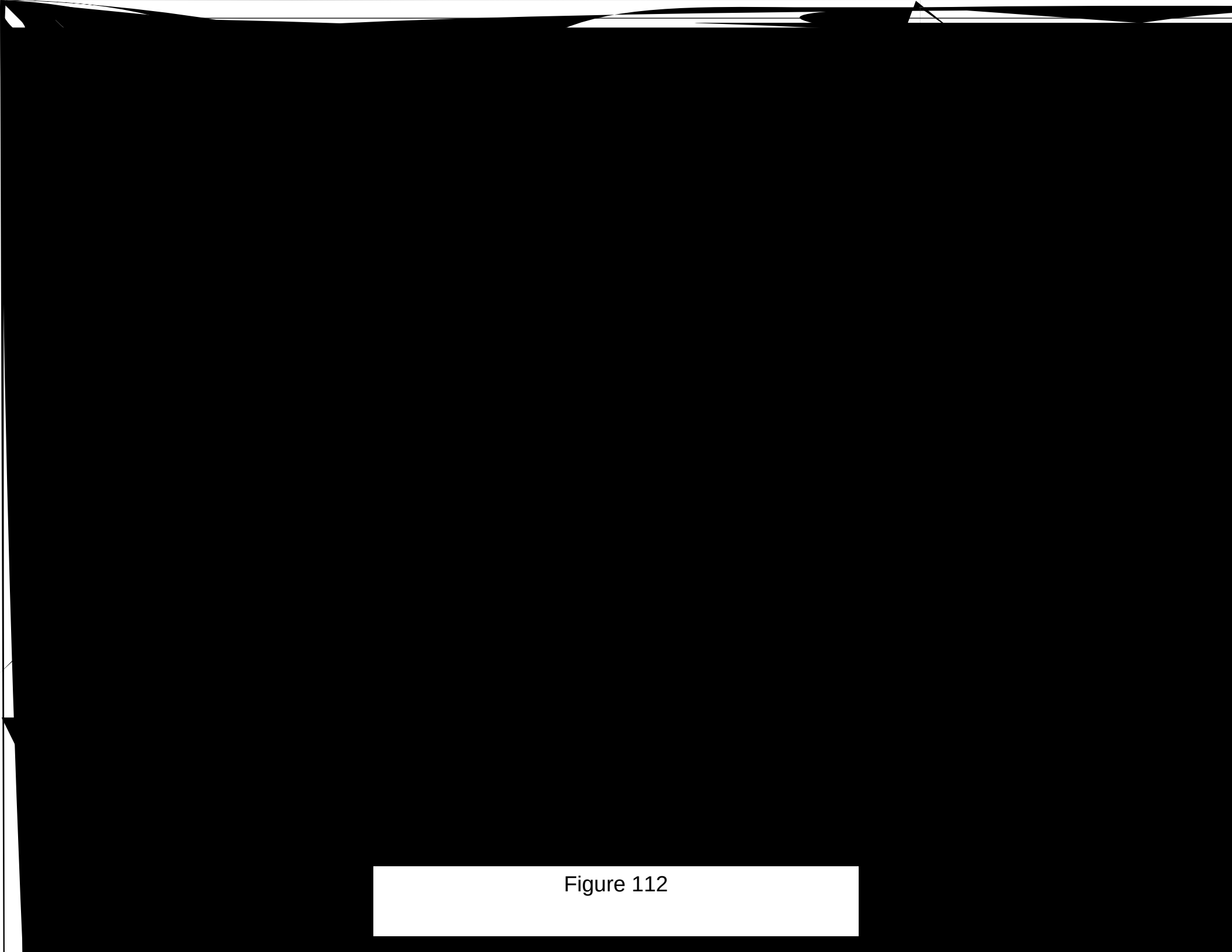

Figure 112

EVT18

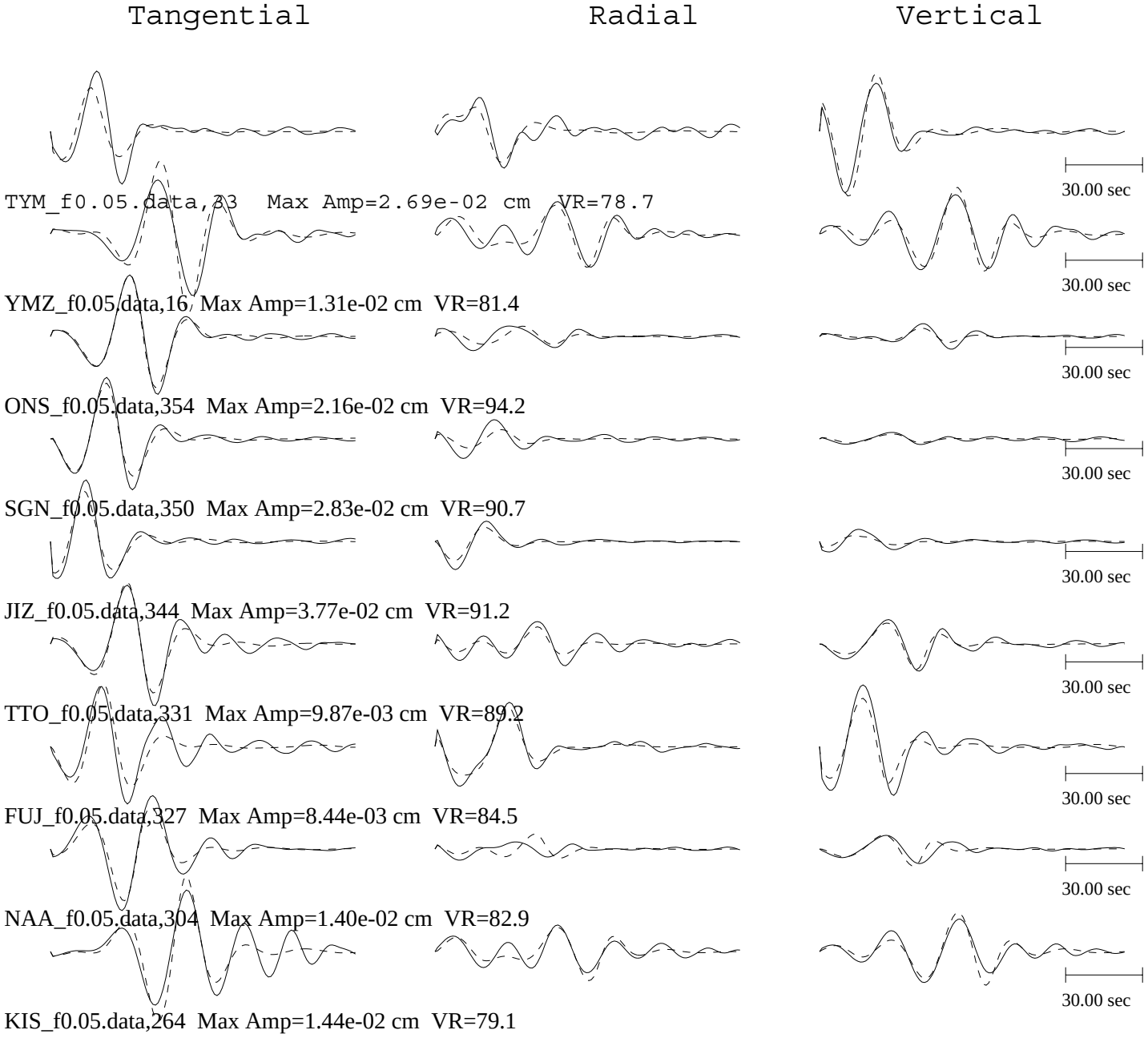

Strike=172 ; 286
Rake =-55 ; -151
Dip =72 ; 39
Mo =5.46e+24
Mw =5.8
Percent DC=99
Percent CLVD=1
Percent ISO=0
Variance=3.17e-06
Var. Red=8.54e+01
RES/Pdc.=3.21e-08

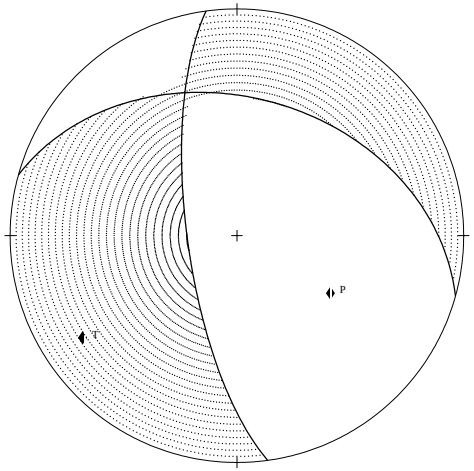

Figure 113

EVT18

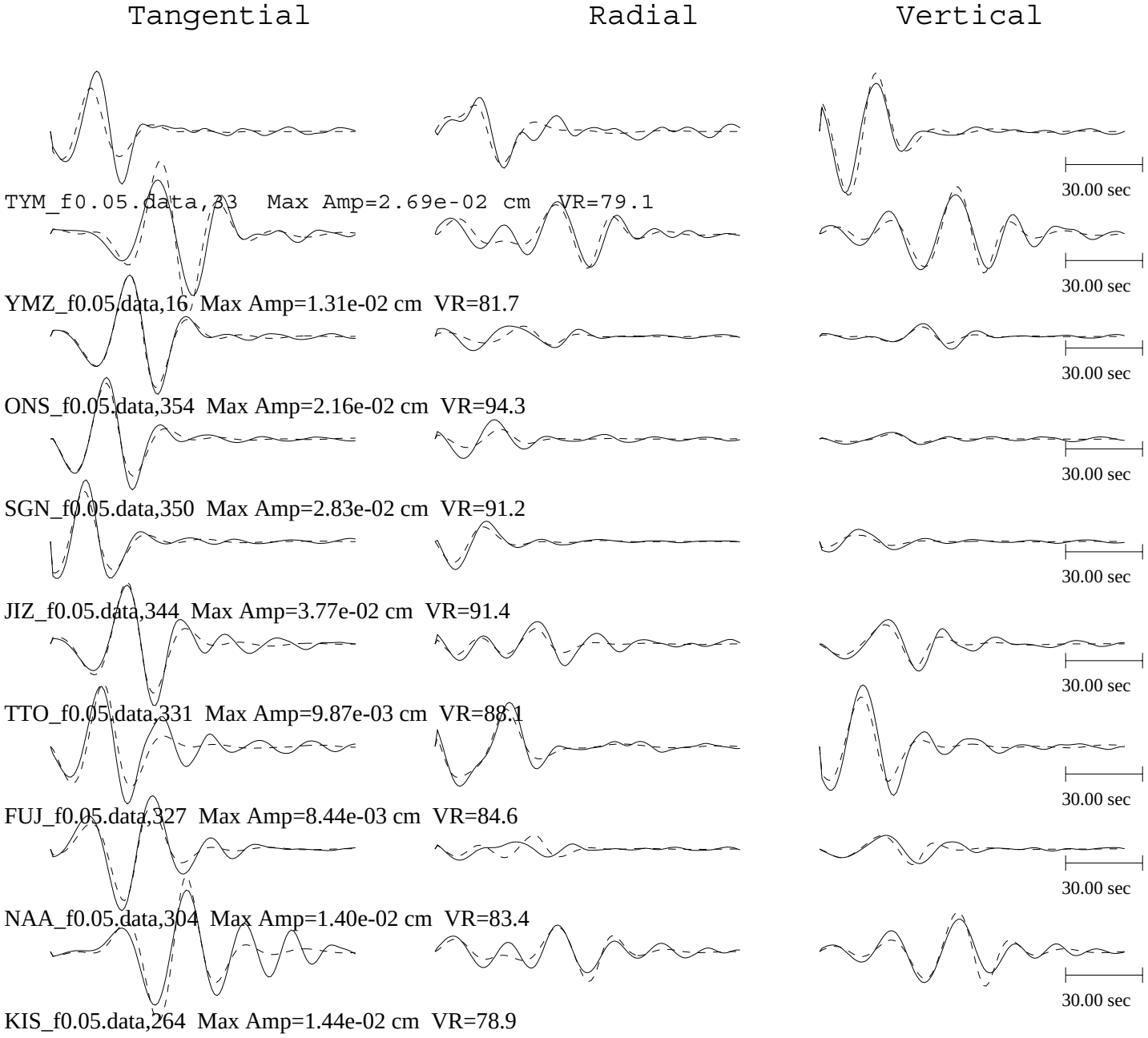

Strike=163 ; 295
Rake =-63 ; -131
Dip =63 ; 37
Mo =6.37e+24
Mw =5.8
Percent DC=69
Percent CLVD=7
Percent ISO=24
Variance=3.11e-06
Var. Red=8.55e+01
RES/Pdc.=4.52e-08

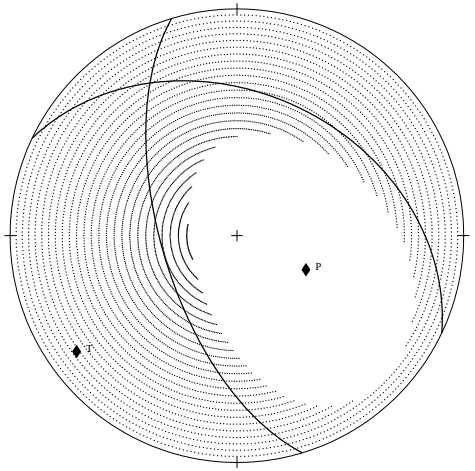

Figure 114

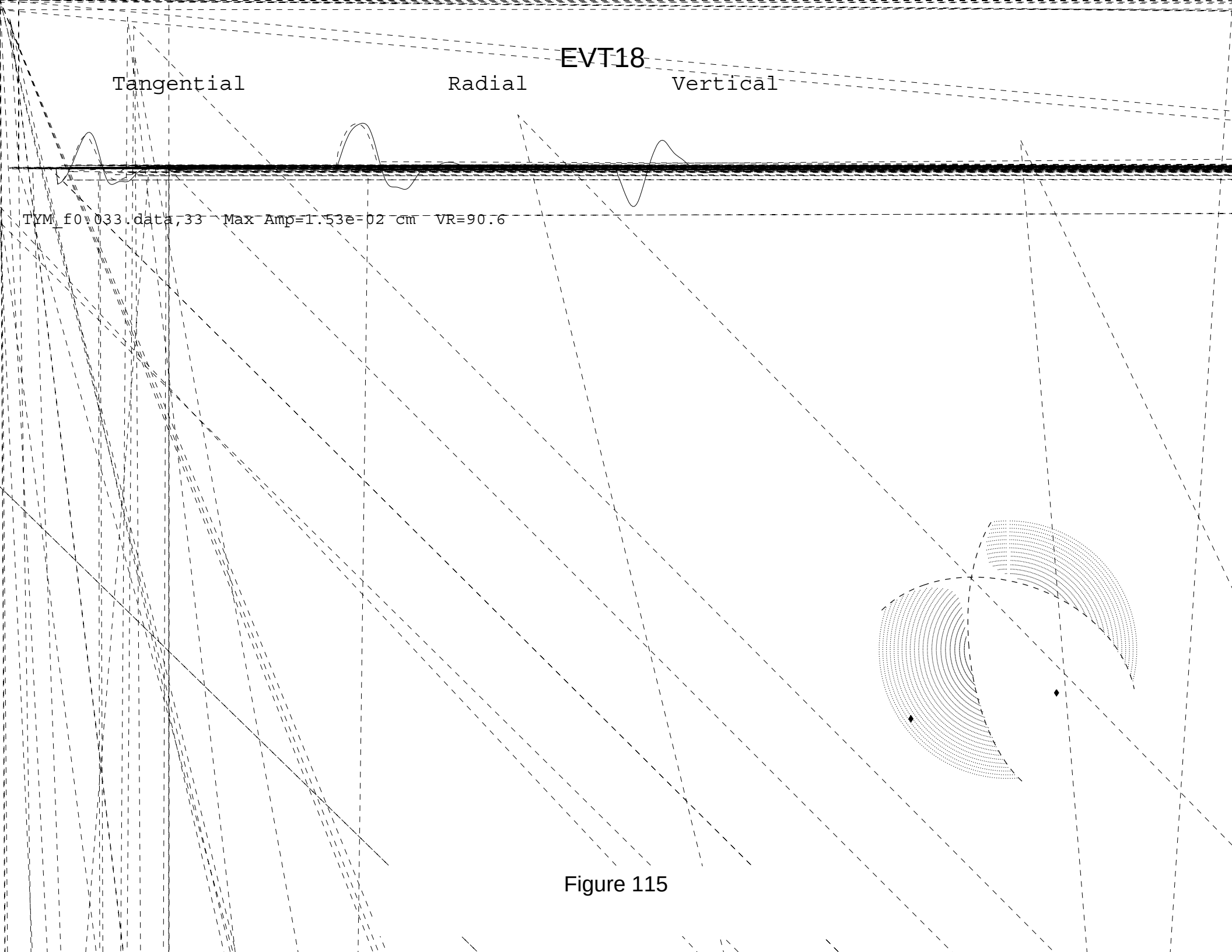
EVT18
Tangential
Radial
Vertical
TYM_f0.033.data,33 Max Amp=1.53e-02 cm VR=90.6

Figure 115

EVT18

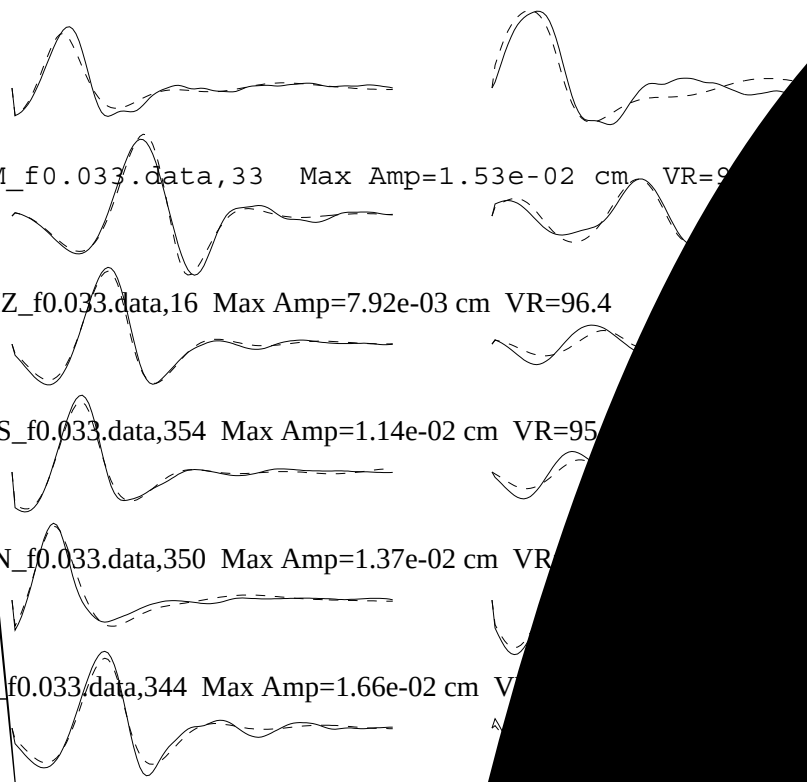

Figure 116

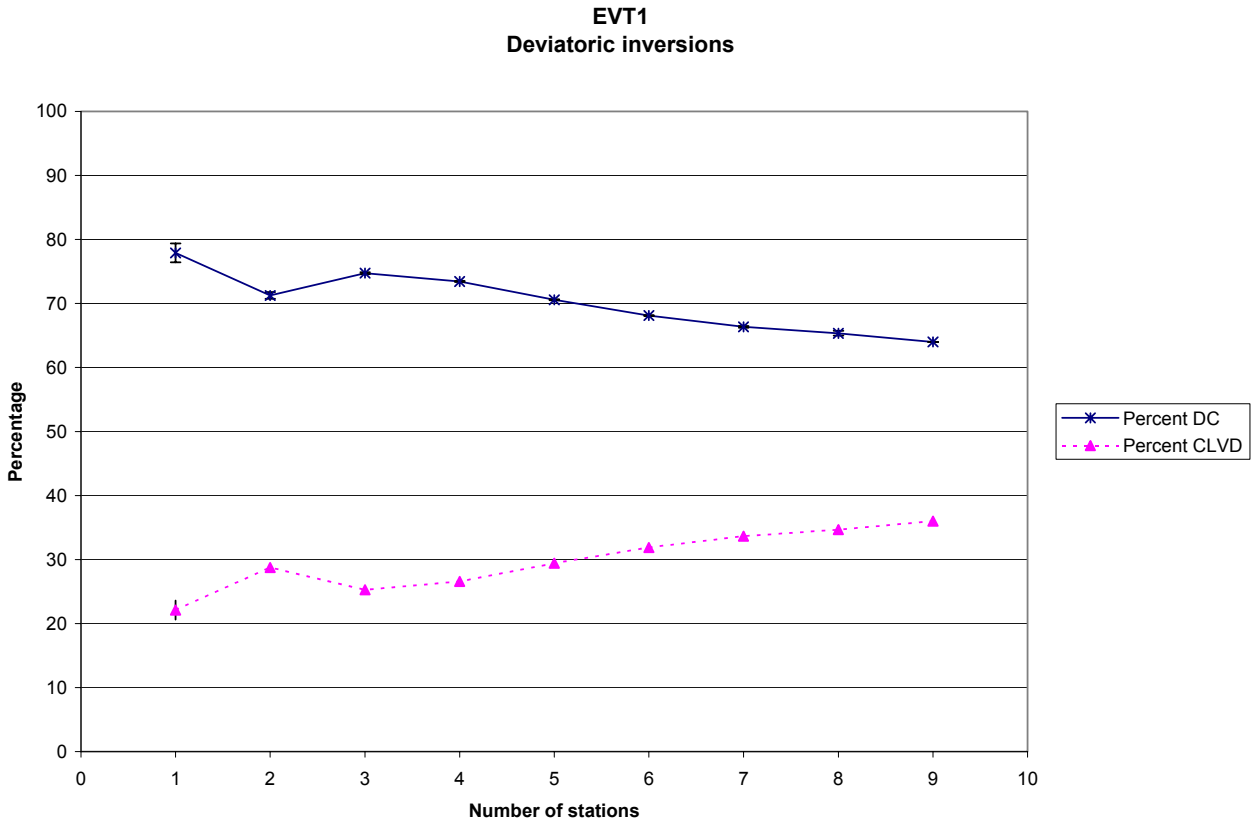
EVT1
Deviatoric inversions
Percentage
Number of stations
Percent DC
Percent CLVD

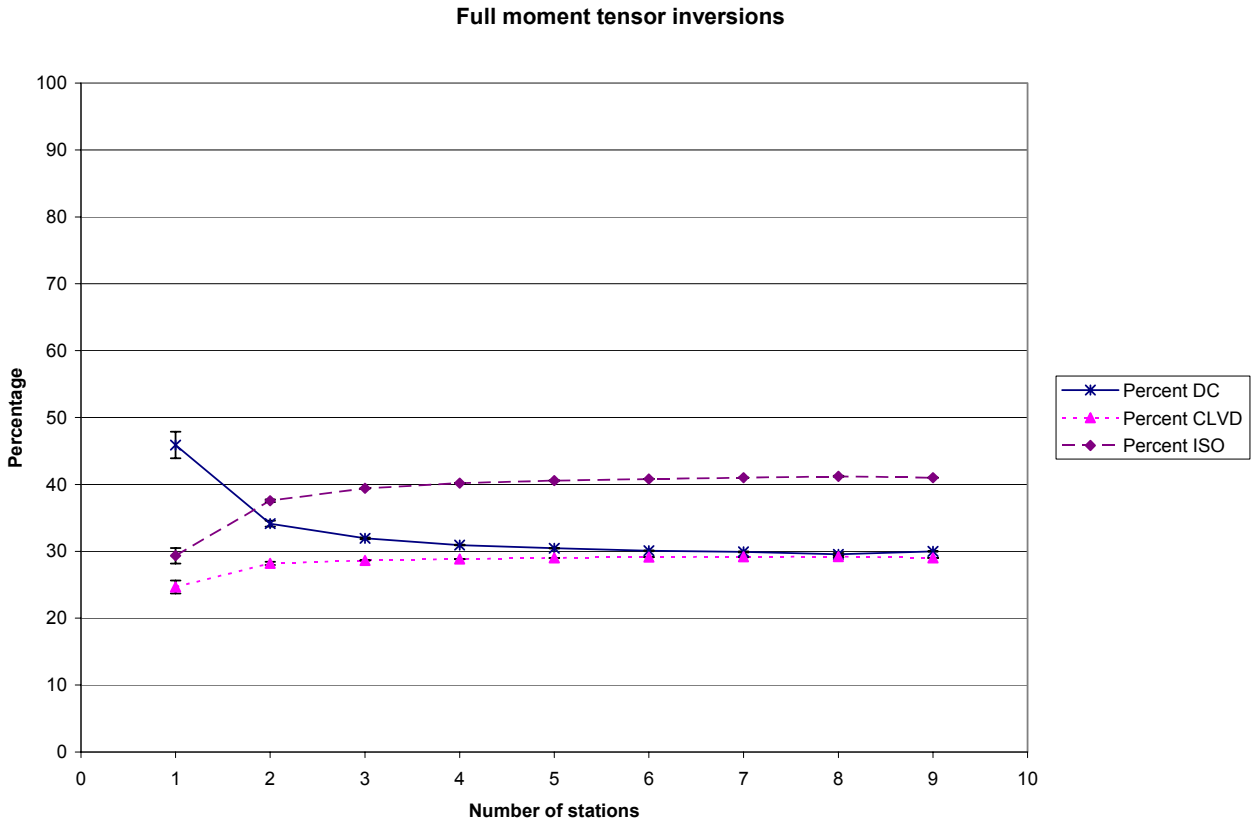
Full moment tensor inversions
Percentage
Number of stations
Percent DC
Percent CLVD
Percent ISO

Figure 117

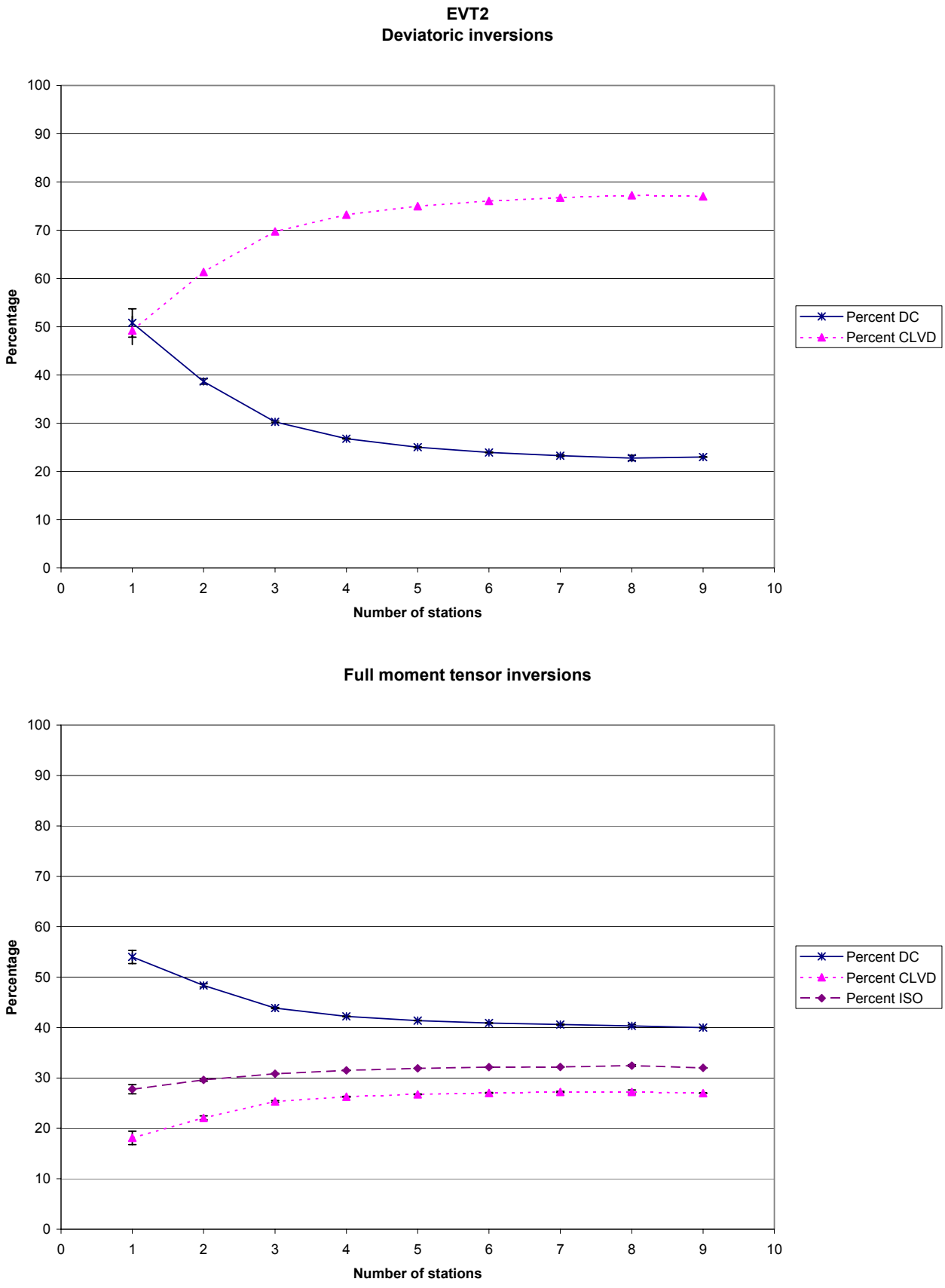
EVT2
Deviatoric inversions
Percentage
Number of stations
Percent DC
Percent CLVD
Full moment tensor inversions
Percentage
Number of stations
Percent DC
Percent CLVD
Percent ISO

Figure 118

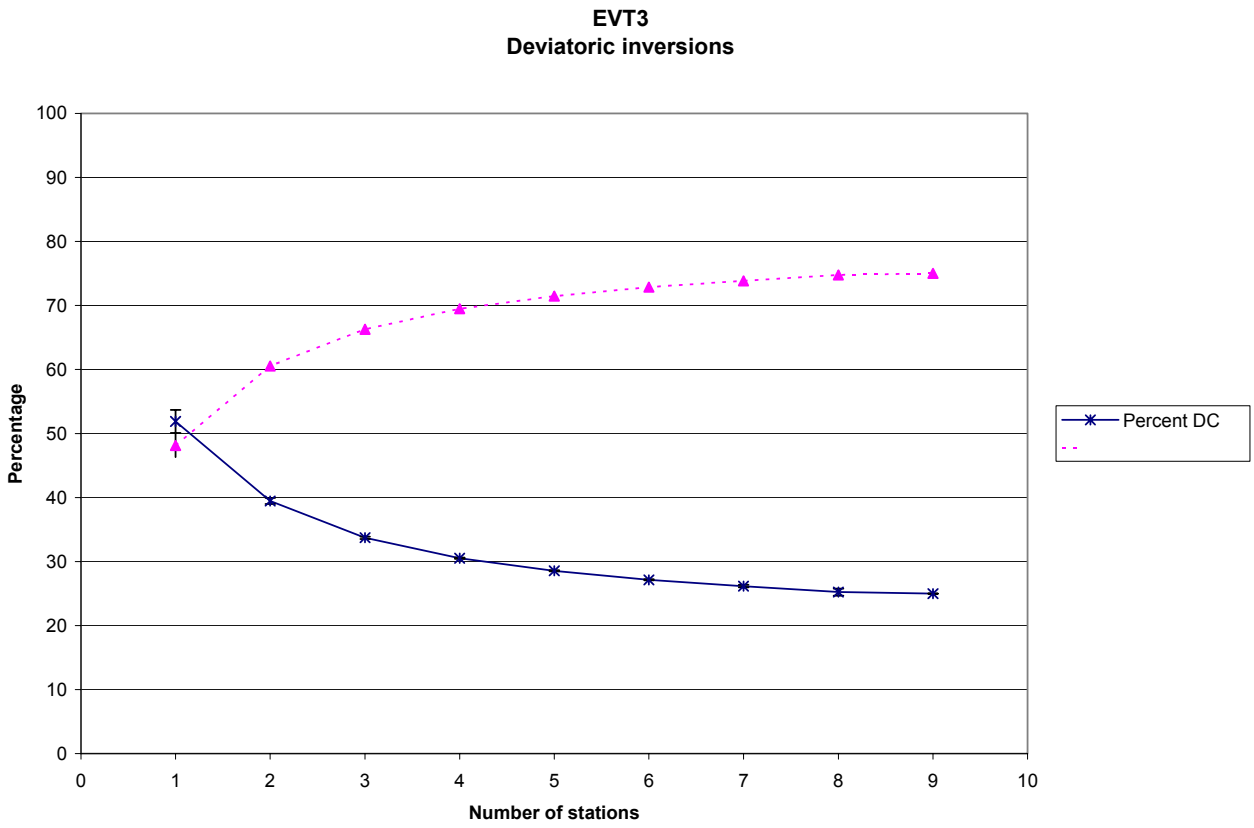
EVT3
Deviatoric inversions
Percentage
Number of stations
Percent DC

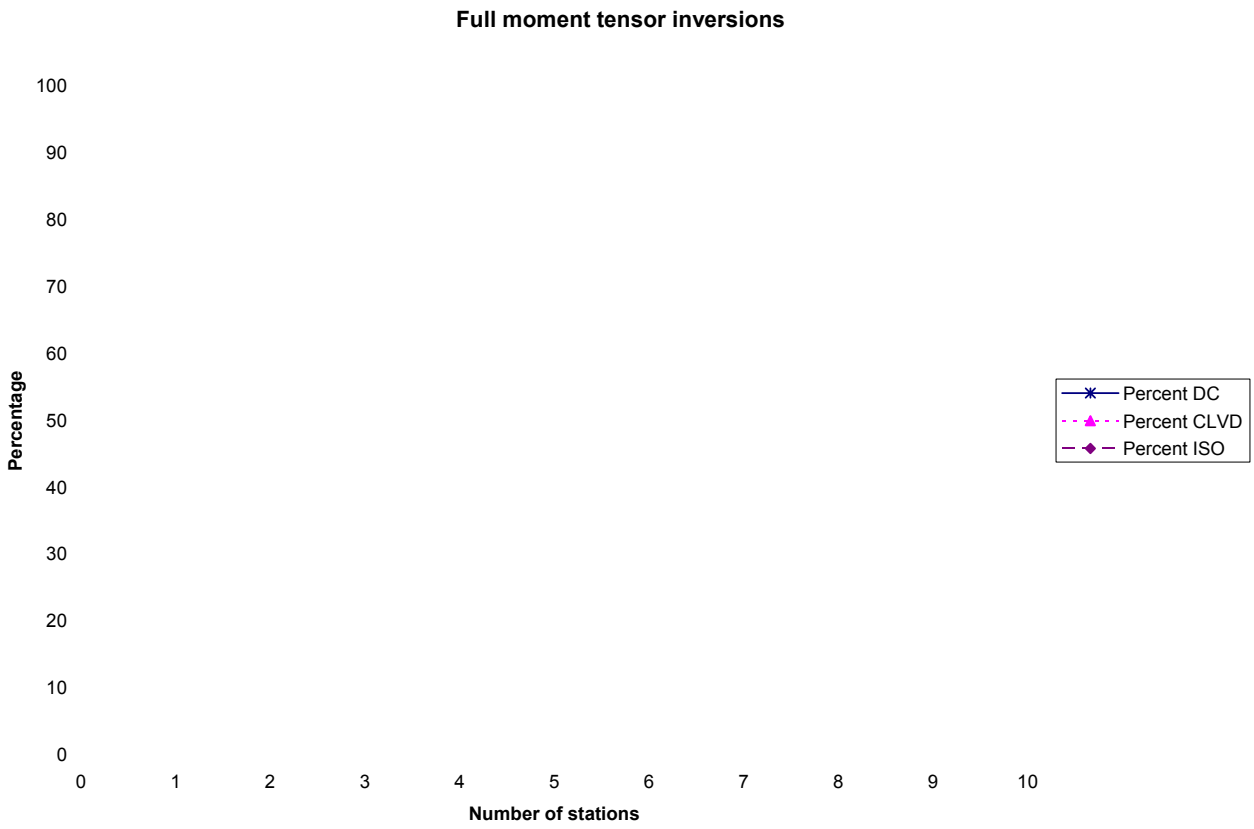
Full moment tensor inversions
Percentage
Number of stations
Percent DC
Percent CLVD
Percent ISO

Figure 119

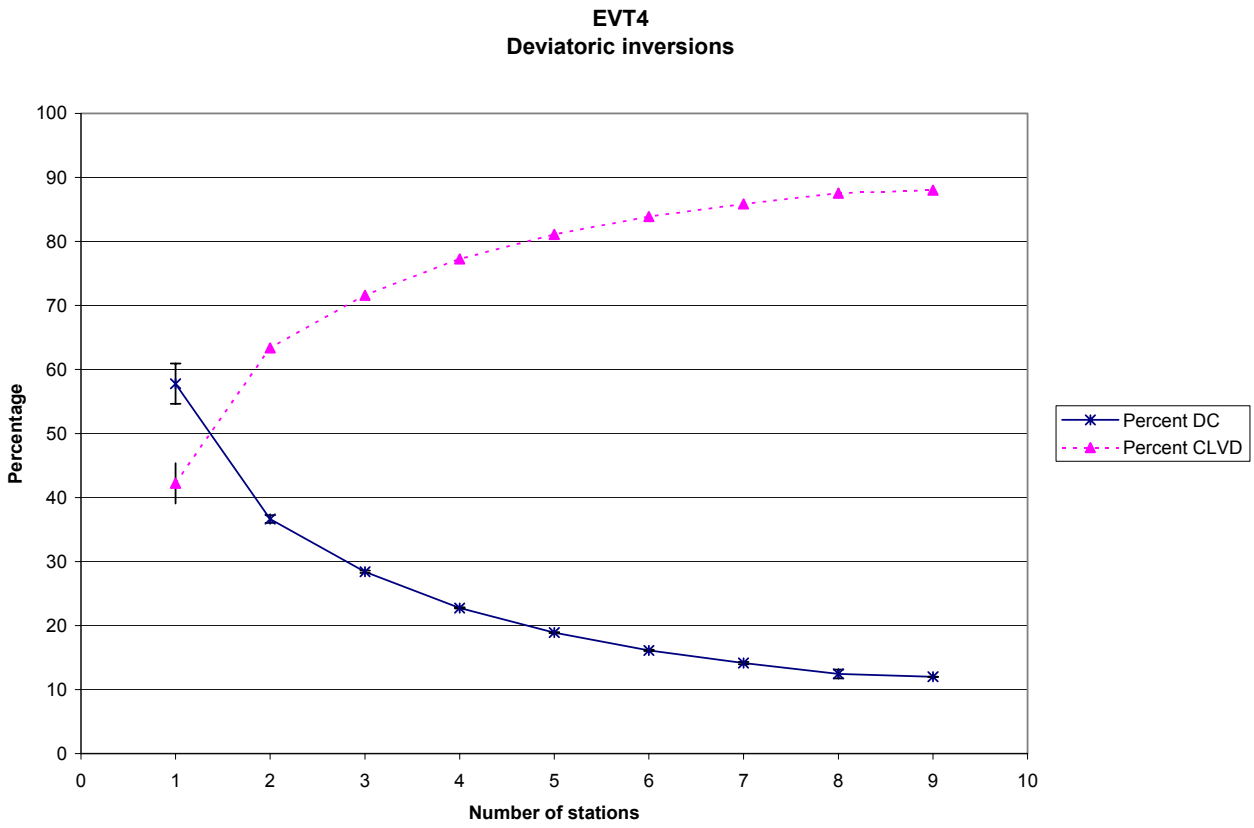
EVT4
Deviatoric inversions
Percentage
Number of stations
Percent DC
Percent CLVD

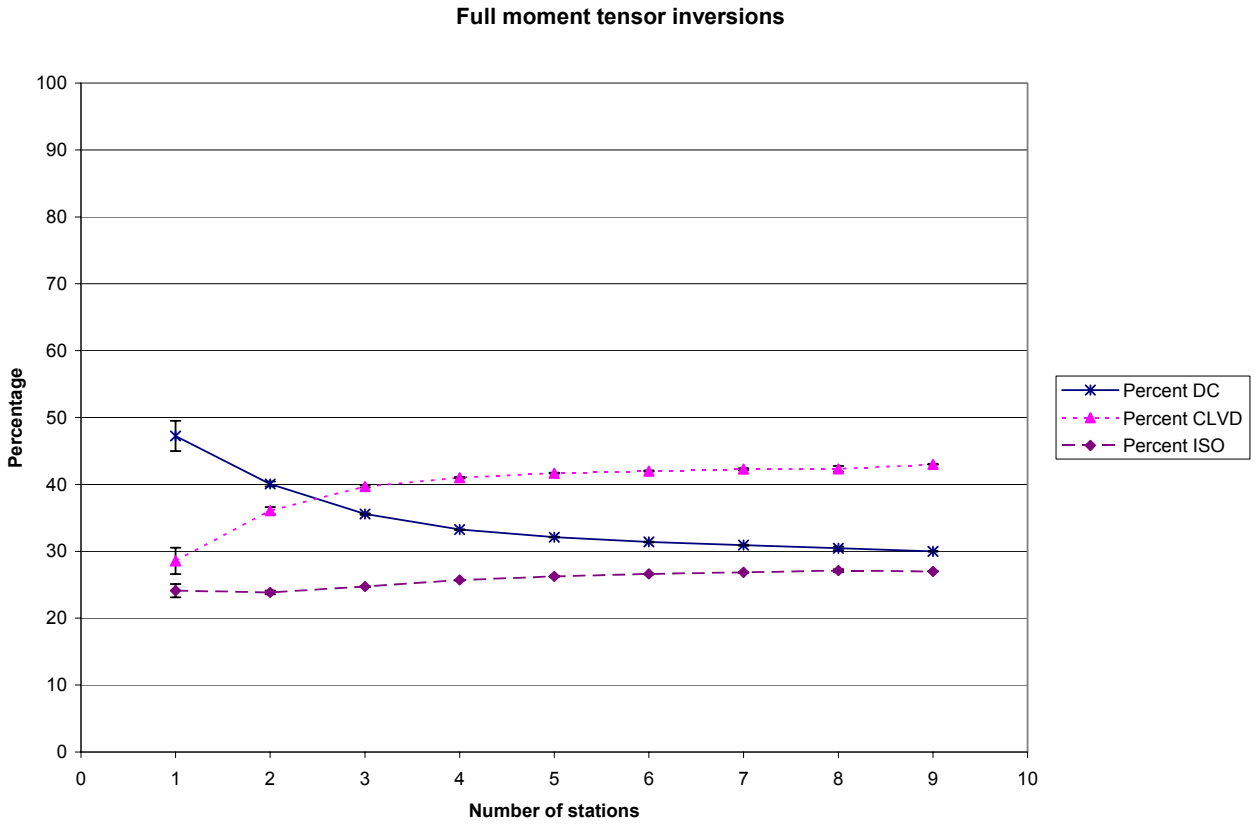
Full moment tensor inversions
Percentage
Number of stations
Percent DC
Percent CLVD
Percent ISO

Figure 120

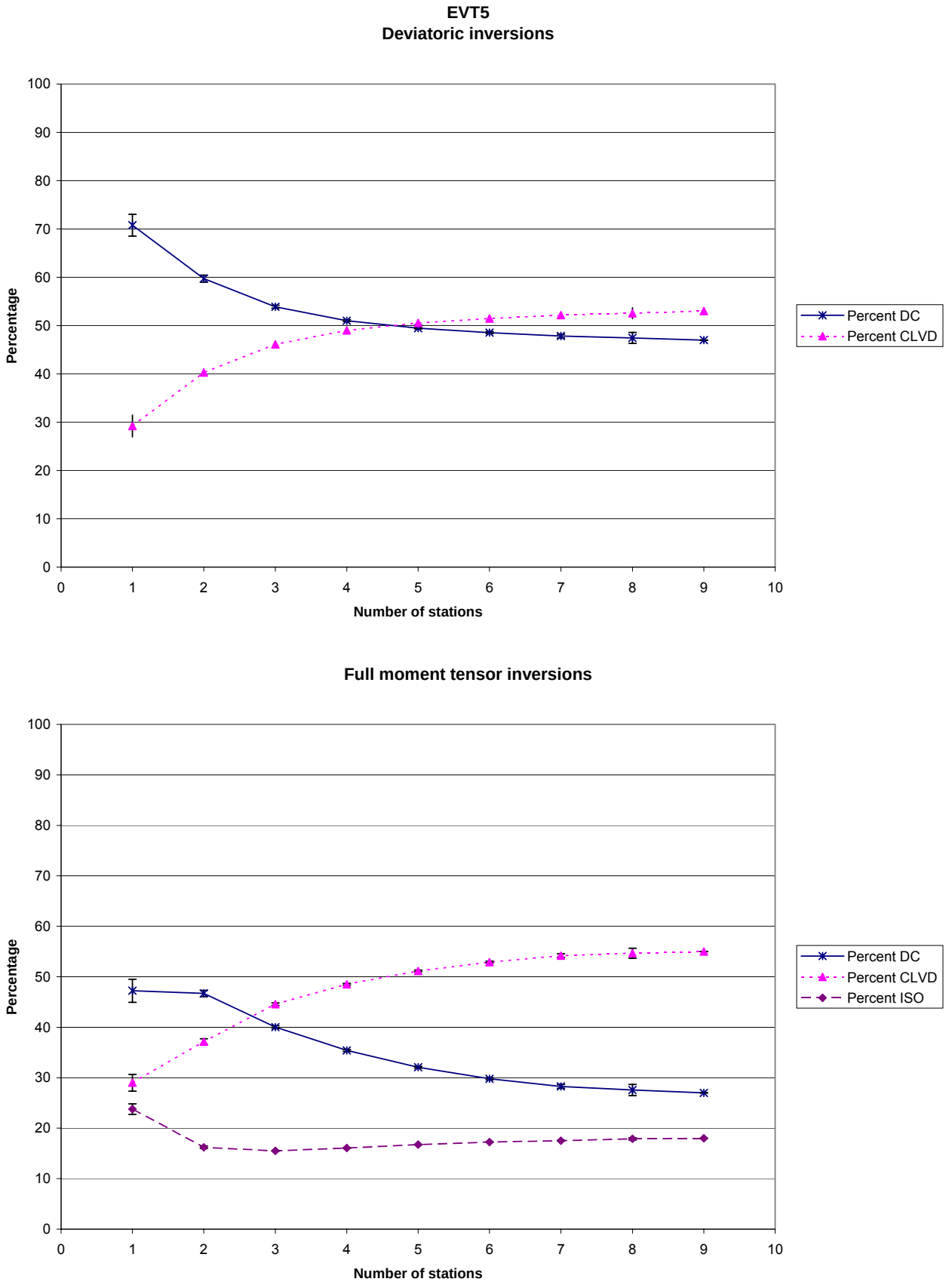
EVT5
Deviatoric inversions
Percentage
Number of stations
Percent DC
Percent CLVD
Full moment tensor inversions
Percentage
Number of stations
Percent DC
Percent CLVD
Percent ISO

Figure 121

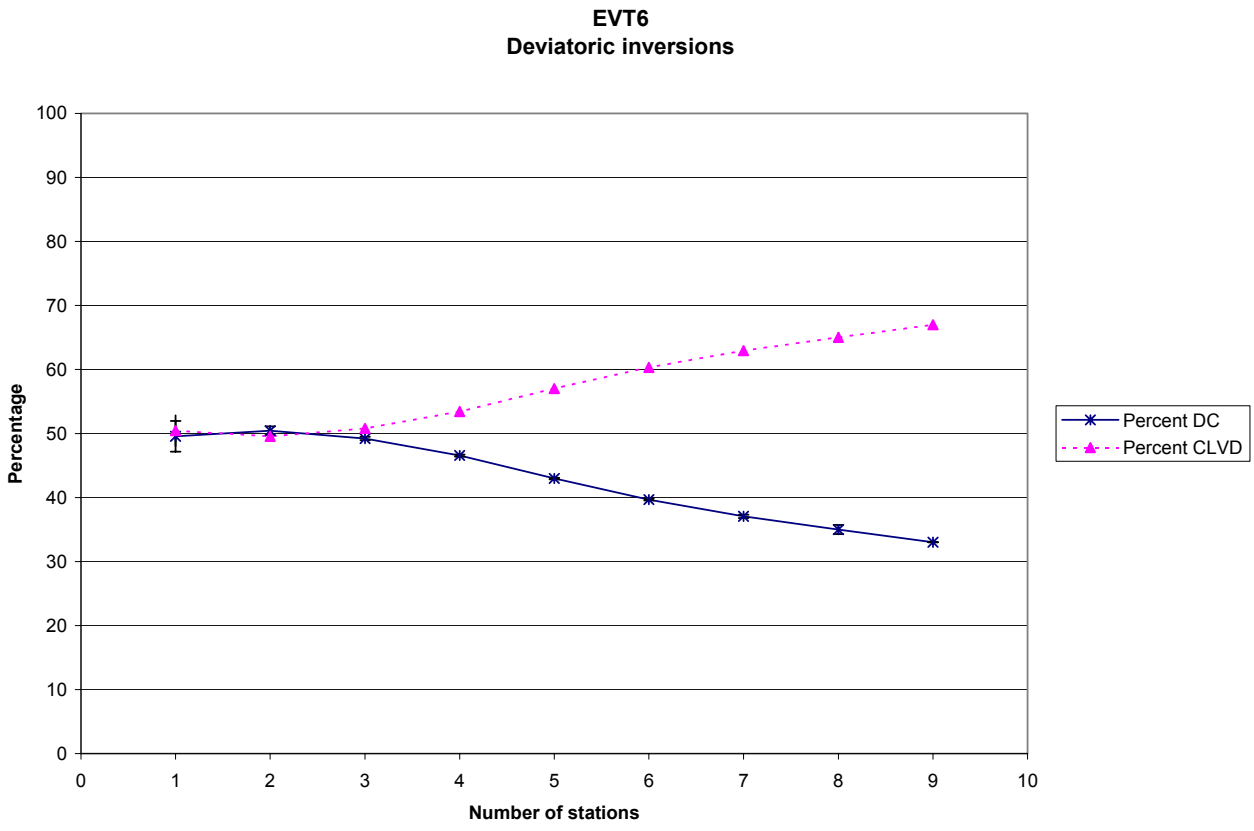
EVT6
Deviatoric inversions
Percentage
Number of stations
Percent DC
Percent CLVD

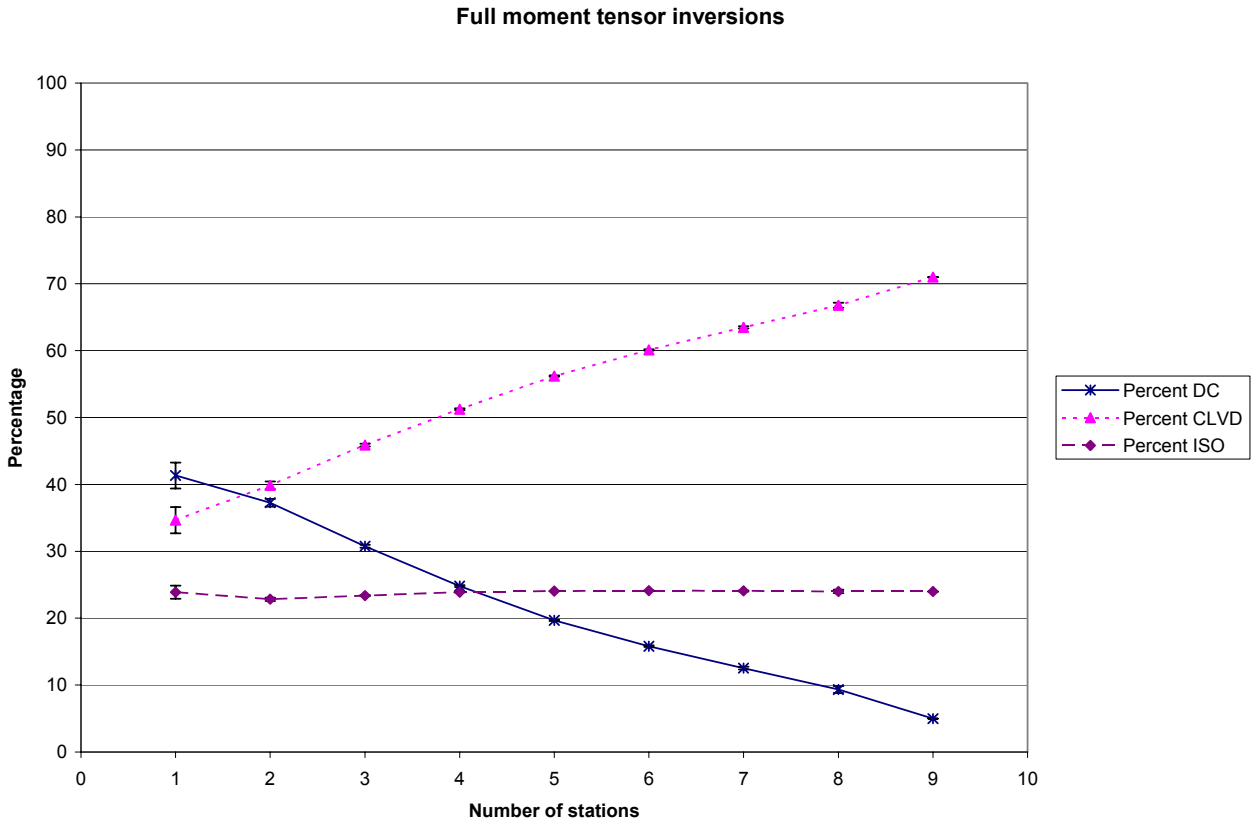
Full moment tensor inversions
Percentage
Number of stations
Percent DC
Percent CLVD
Percent ISO

Figure 122

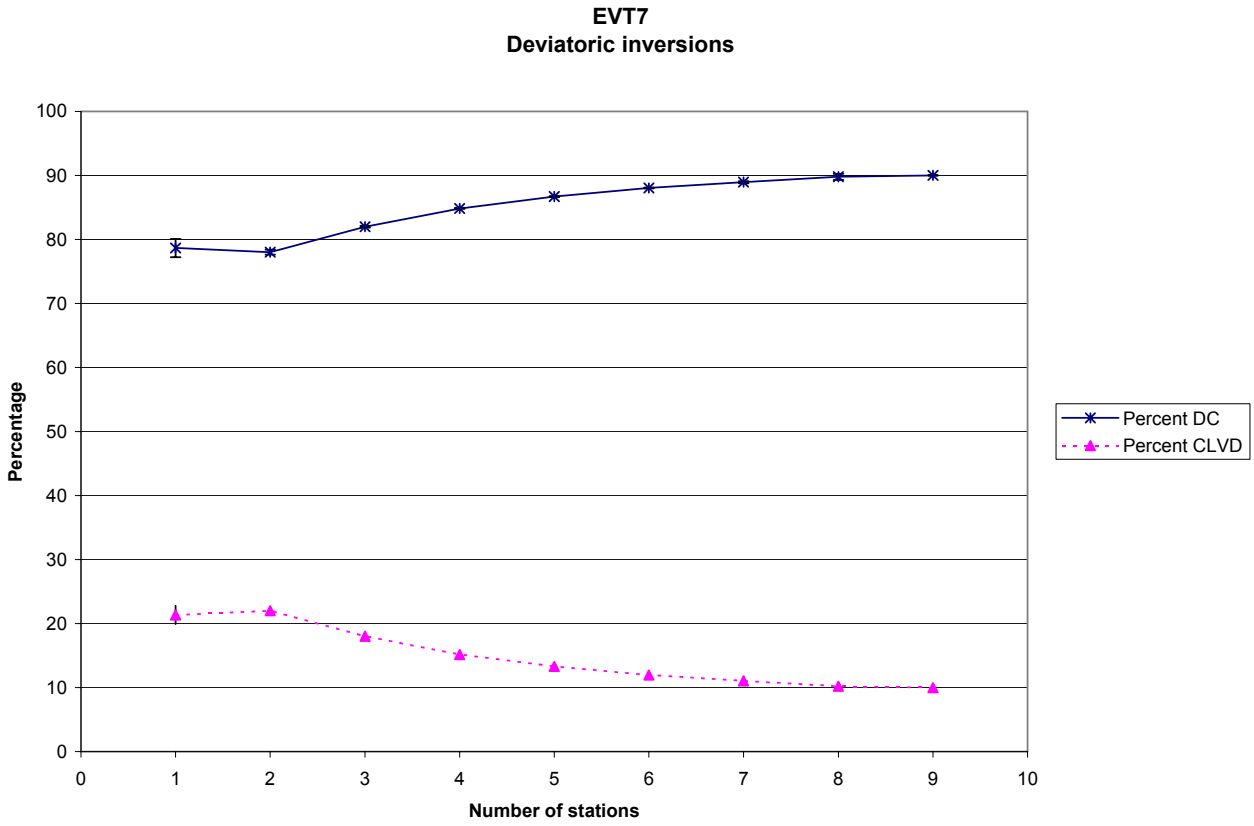
EVT7
Deviatoric inversions
Percentage
Number of stations
Percent DC
Percent CLVD

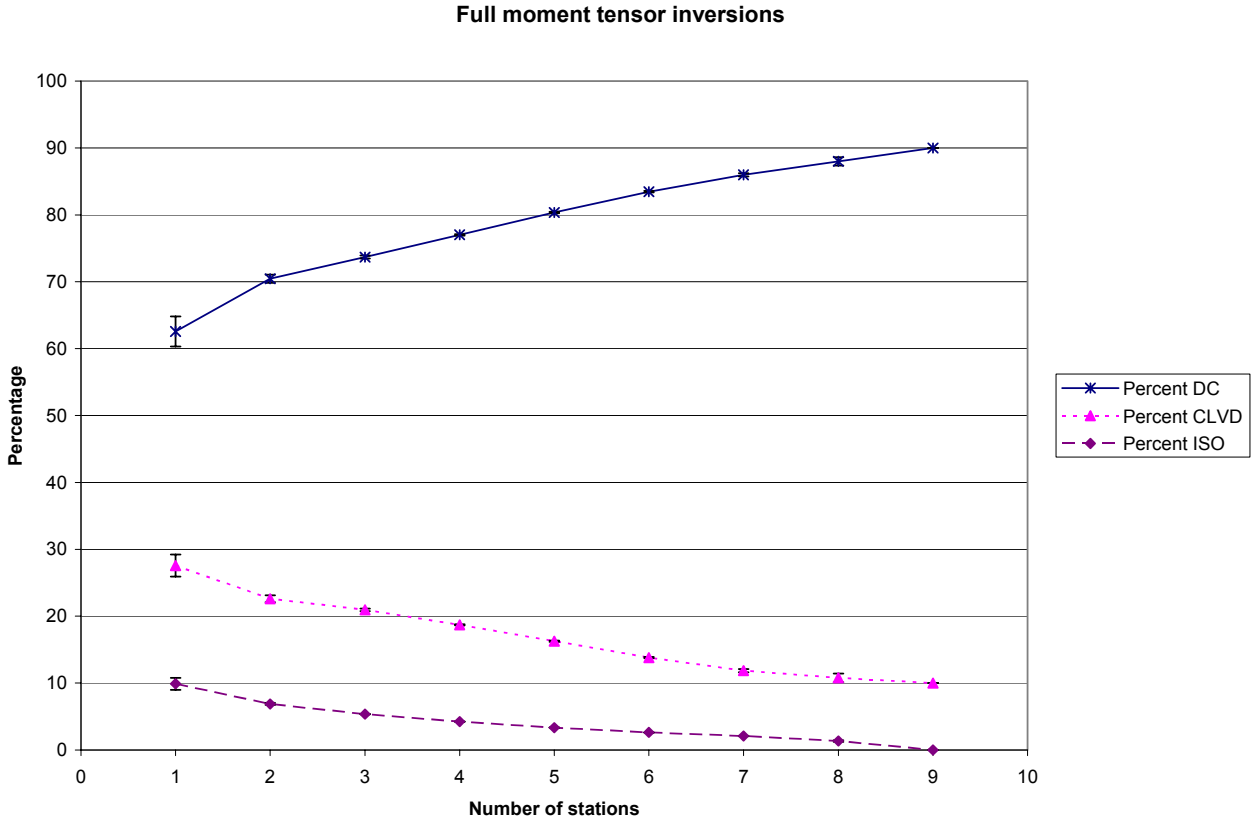
Full moment tensor inversions
Percentage
Number of stations
Percent DC
Percent CLVD
Percent ISO

Figure 123

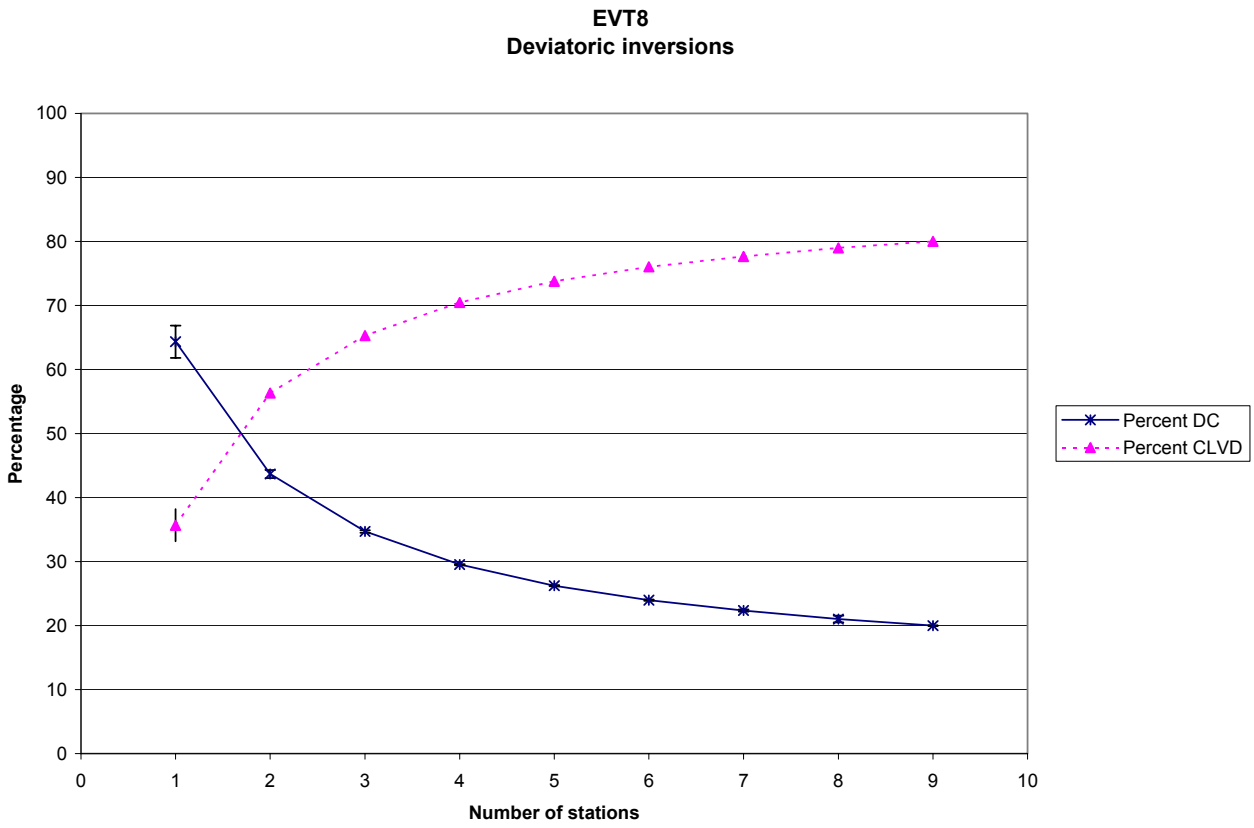
EVT8
Deviatoric inversions
Percentage
Number of stations
Percent DC
Percent CLVD
0
10
20
30
40
50
60
70
80
90
100
0
1
2
3
4
5
6
7
8
9
10

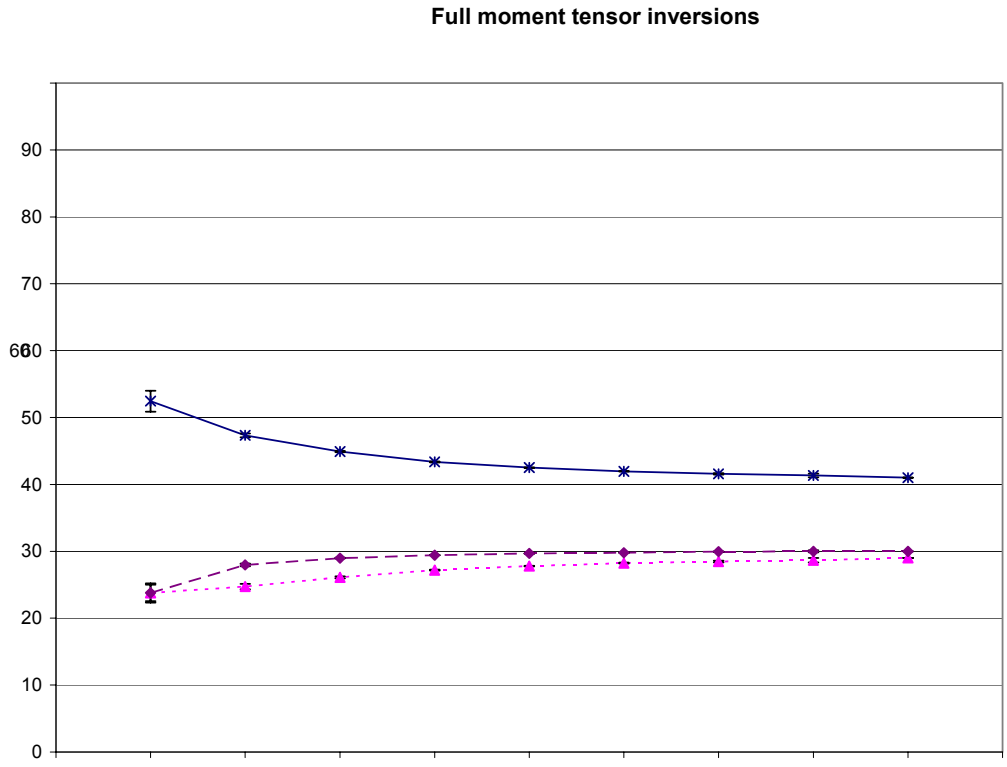
Full moment tensor inversions
0
10
20
30
40
50
60
70
80
90

Figure 124

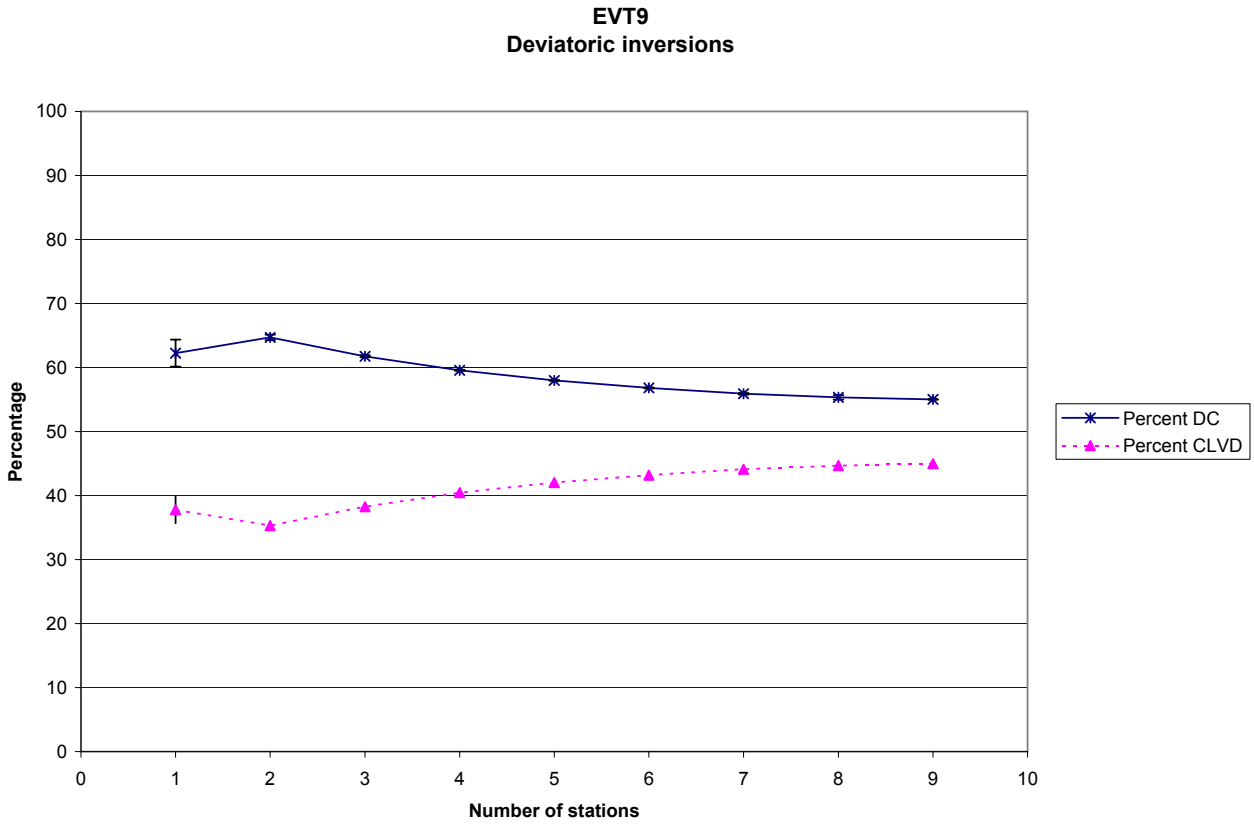
EVT9
Deviatoric inversions
Percentage
Number of stations
Percent DC
Percent CLVD

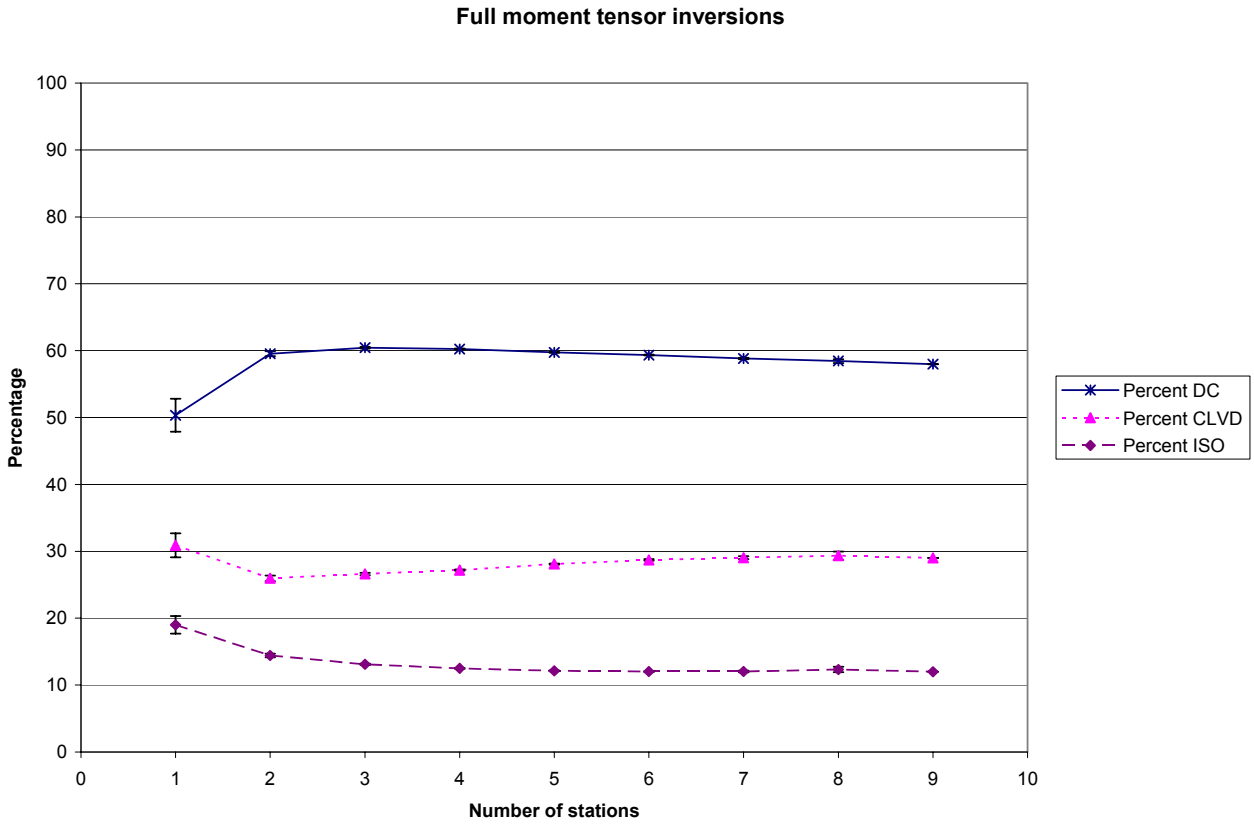
Full moment tensor inversions
Percentage
Number of stations
Percent DC
Percent CLVD
Percent ISO

Figure 125

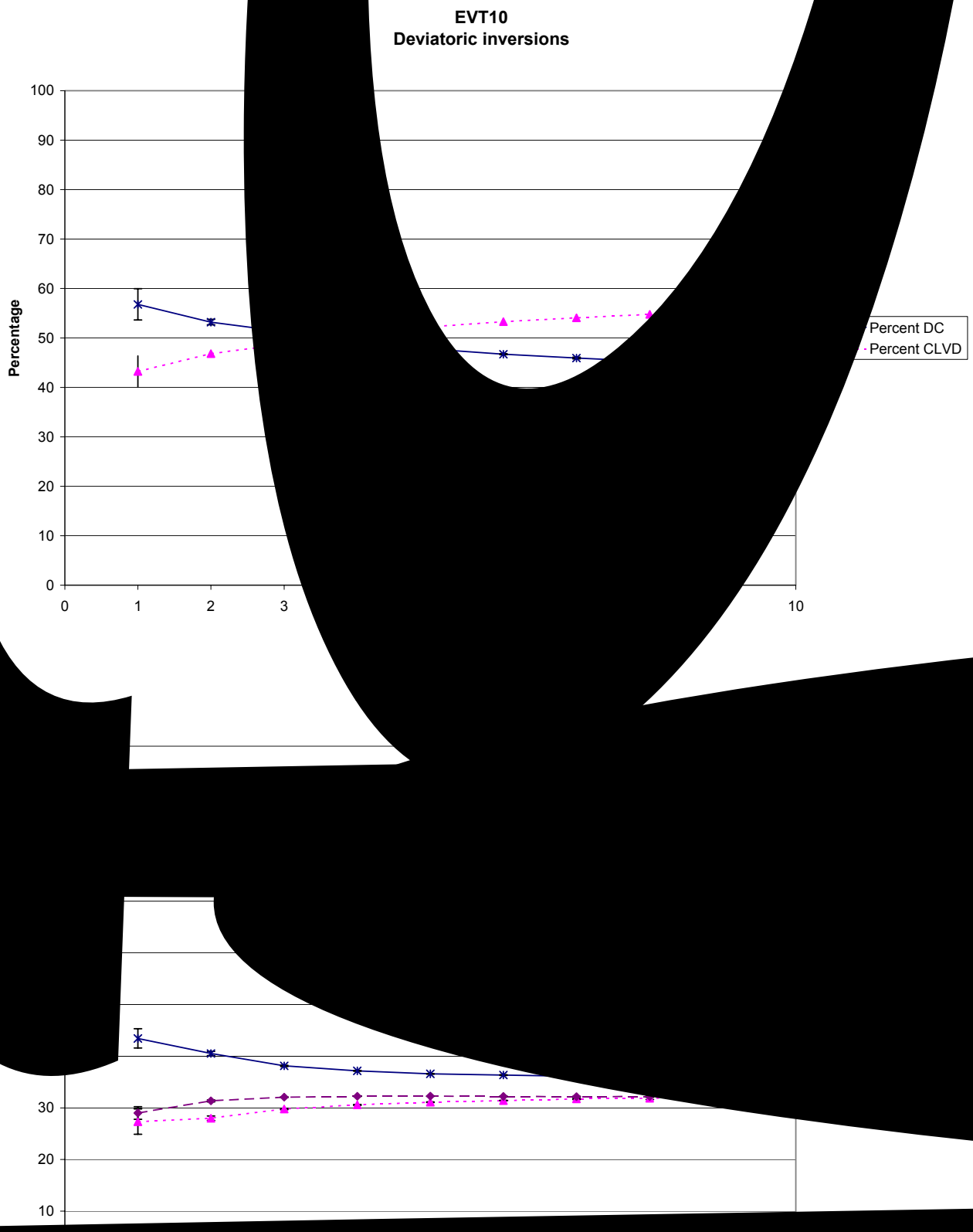
EVT10
Deviatoric inversions
Percentage
100
90
80
70
60
50
40
30
20
10
0
0
1
2
3
10
Percent DC
Percent CLVD

Figure 126

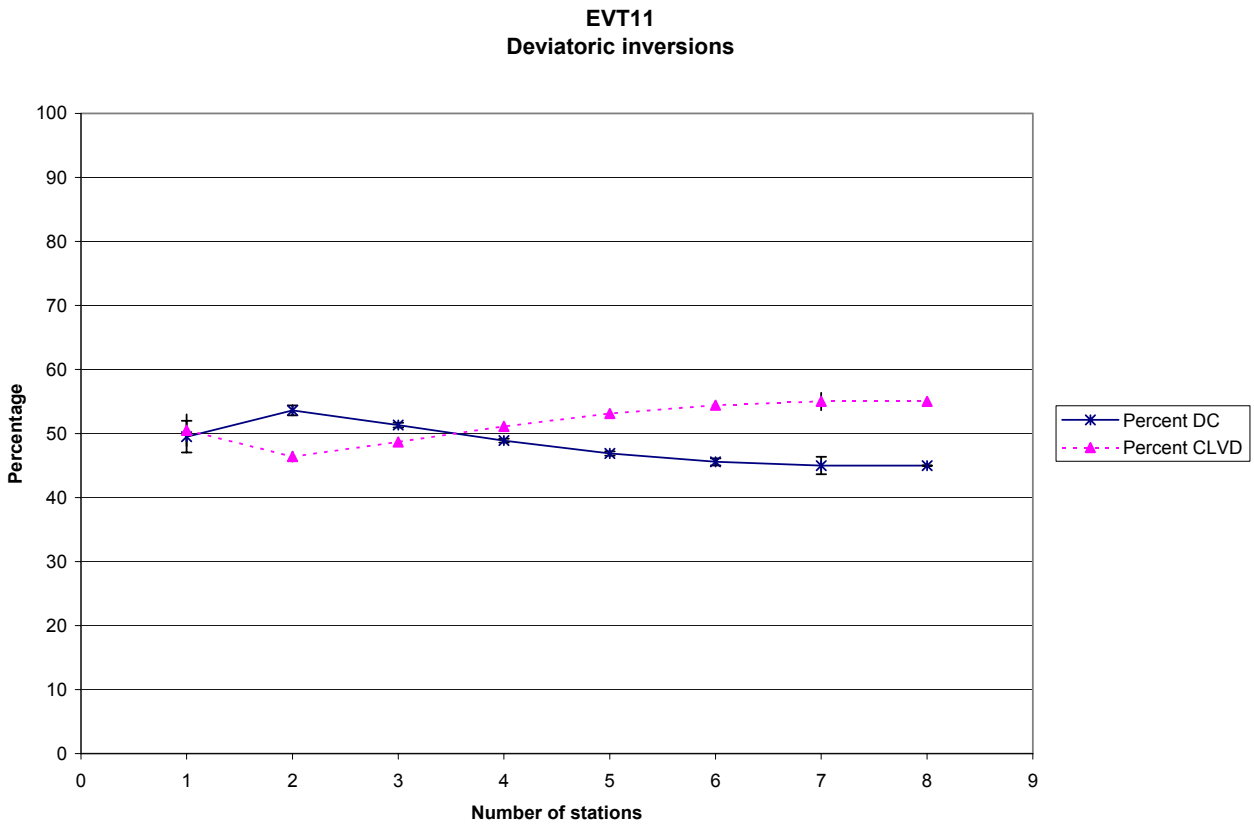
EVT11
Deviatoric inversions
Percentage
Number of stations
Percent DC
Percent CLVD

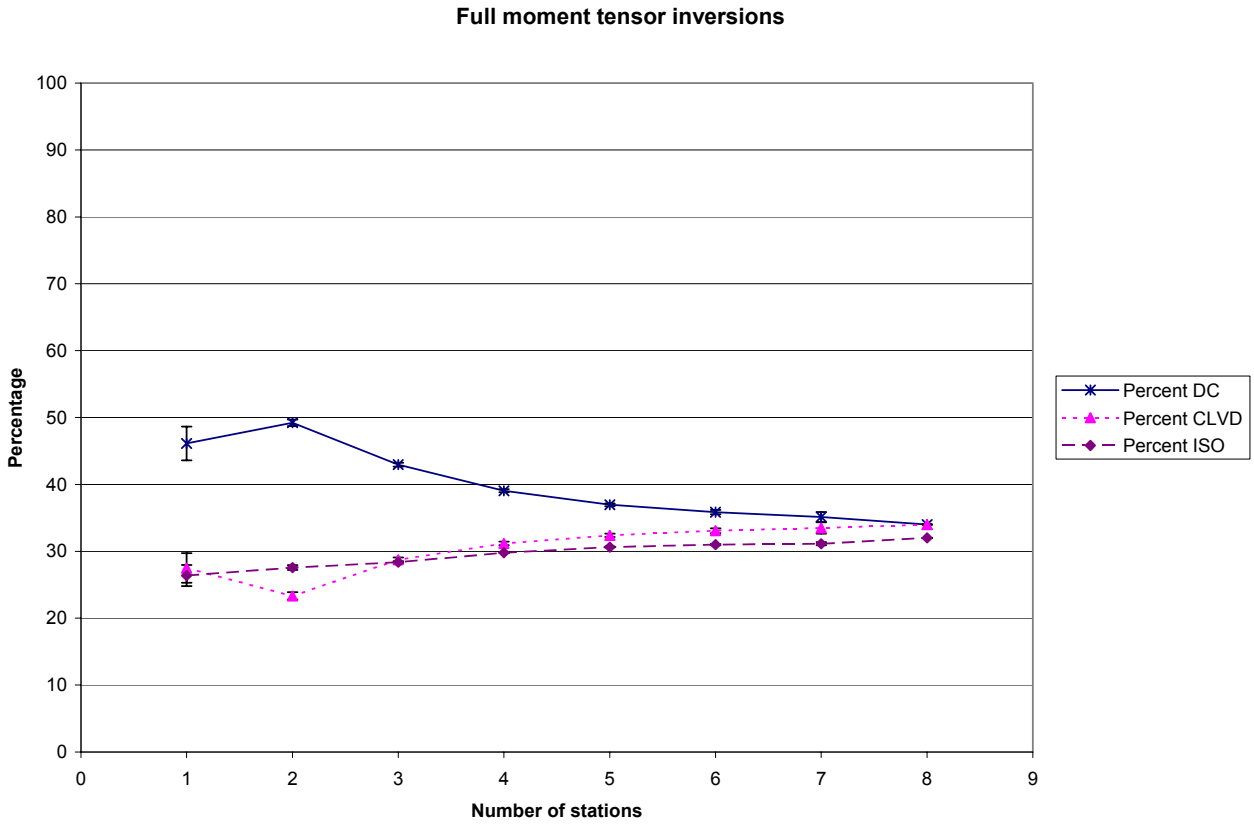
Full moment tensor inversions
Percentage
Number of stations
Percent DC
Percent CLVD
Percent ISO

Figure 127

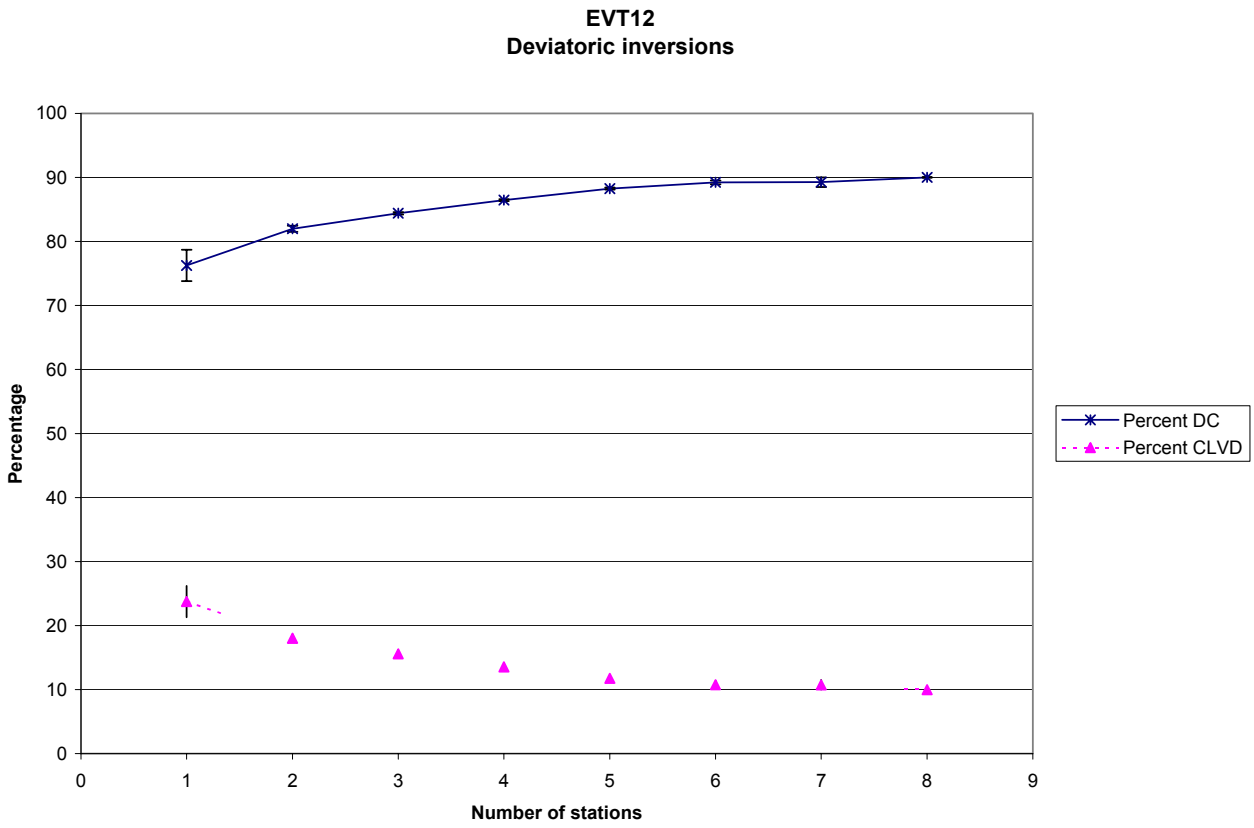
EVT12
Deviatoric inversions
Percentage
Number of stations
Percent DC
Percent CLVD

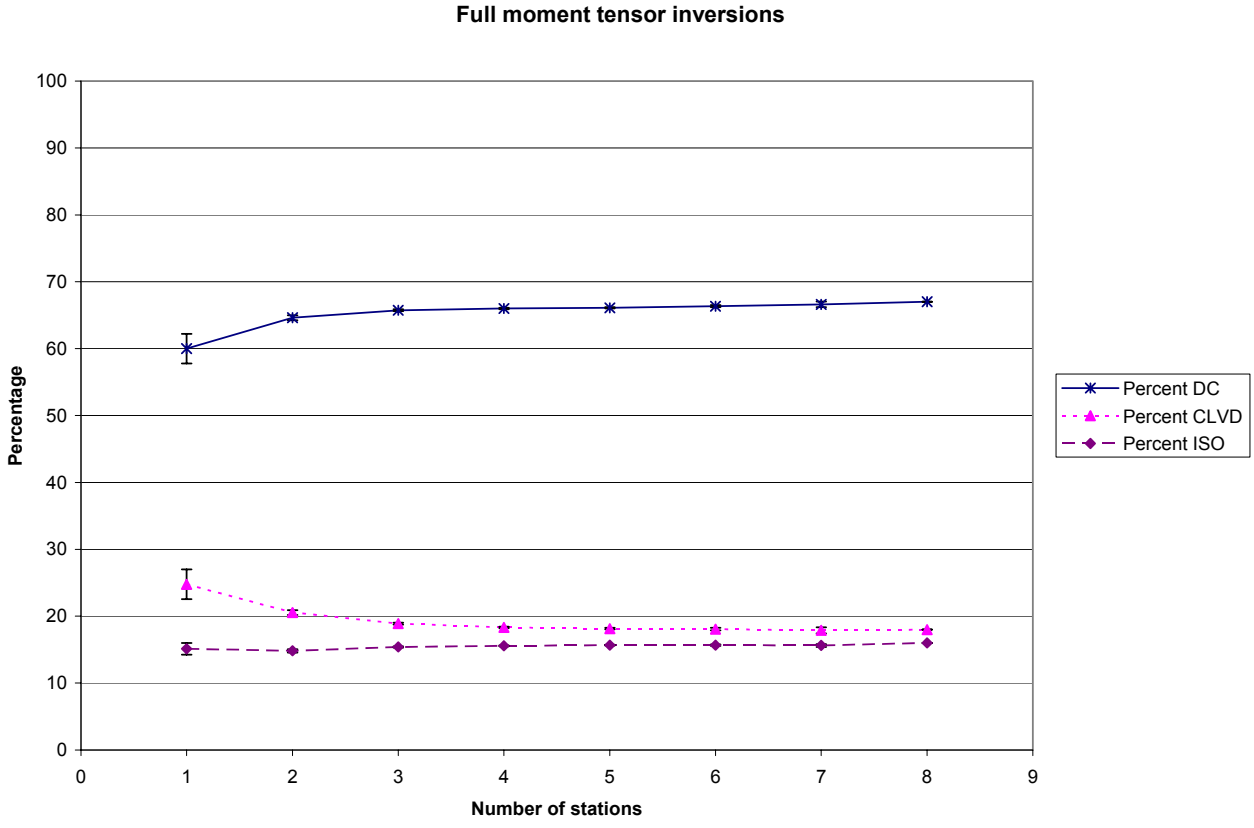
Full moment tensor inversions
Percentage
Number of stations
Percent DC
Percent CLVD
Percent ISO

Figure 128

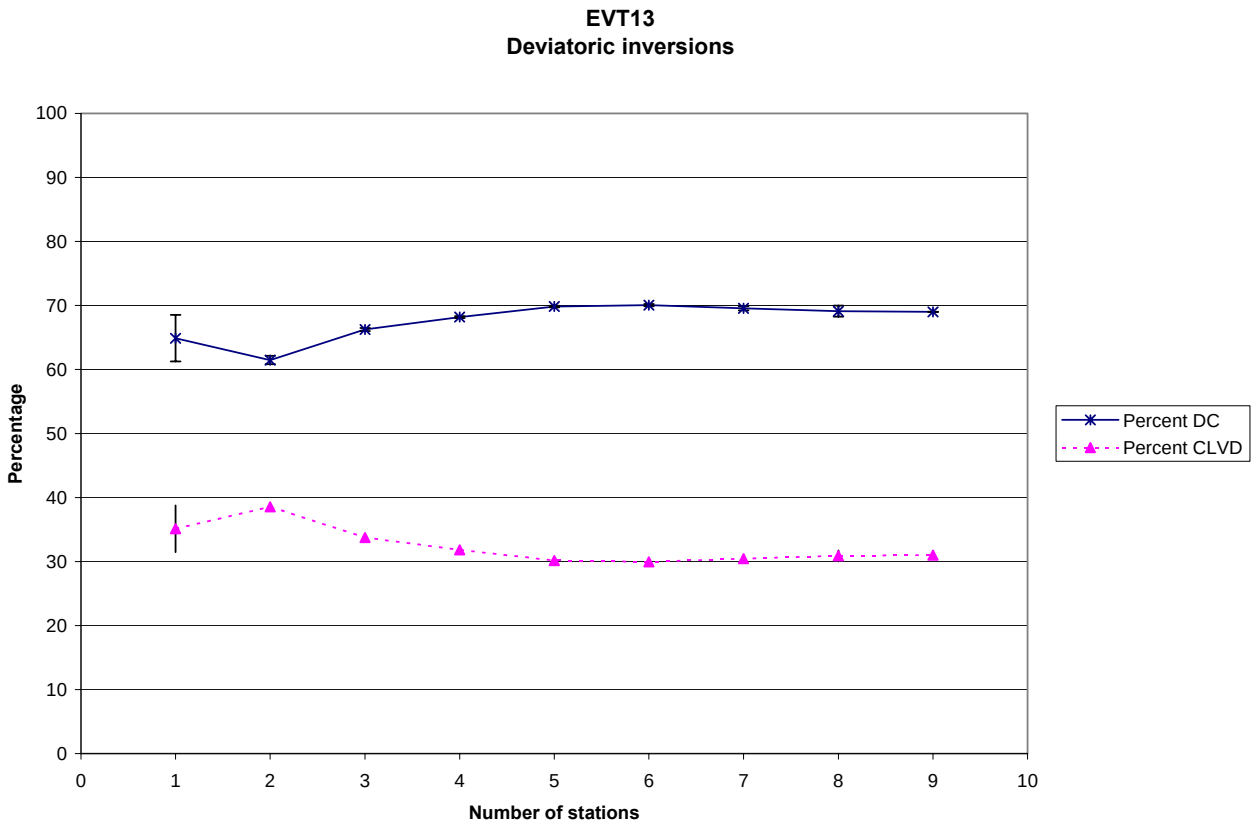
EVT13
Deviatoric inversions
Percentage
Number of stations
Percent DC
Percent CLVD

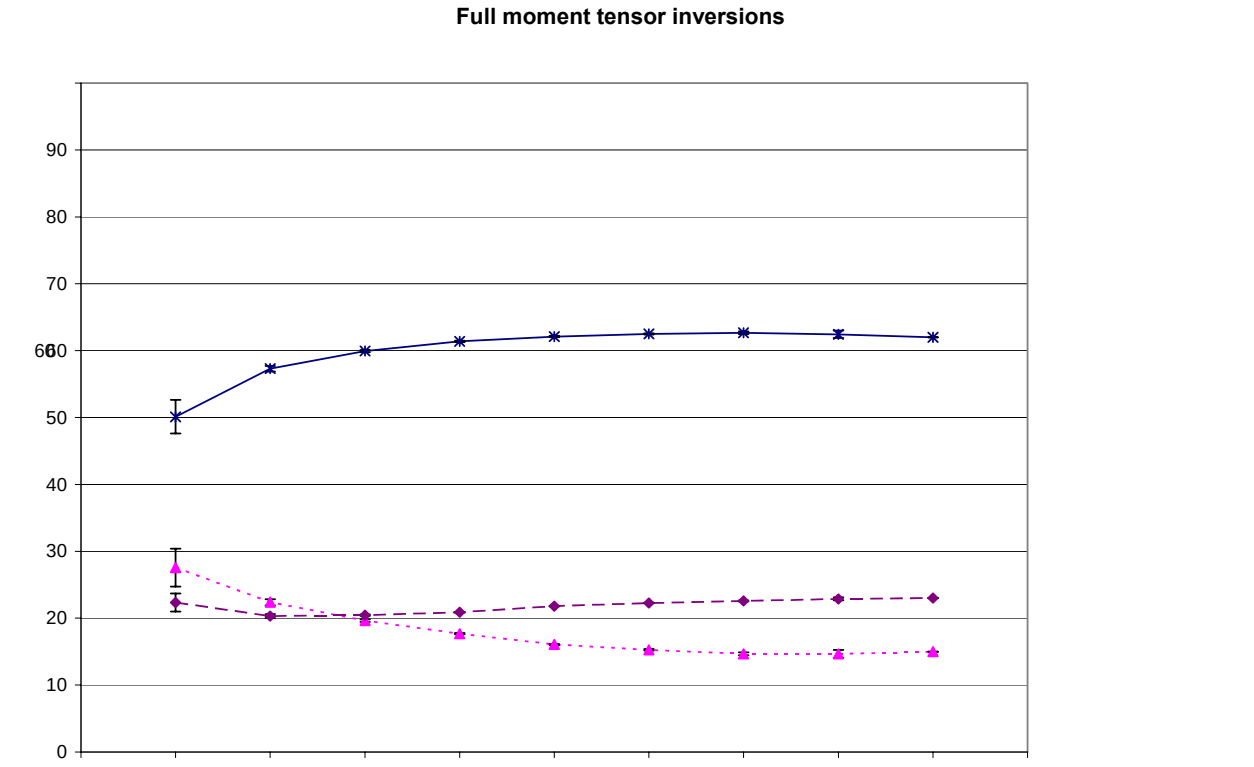
Full moment tensor inversions

Figure 129

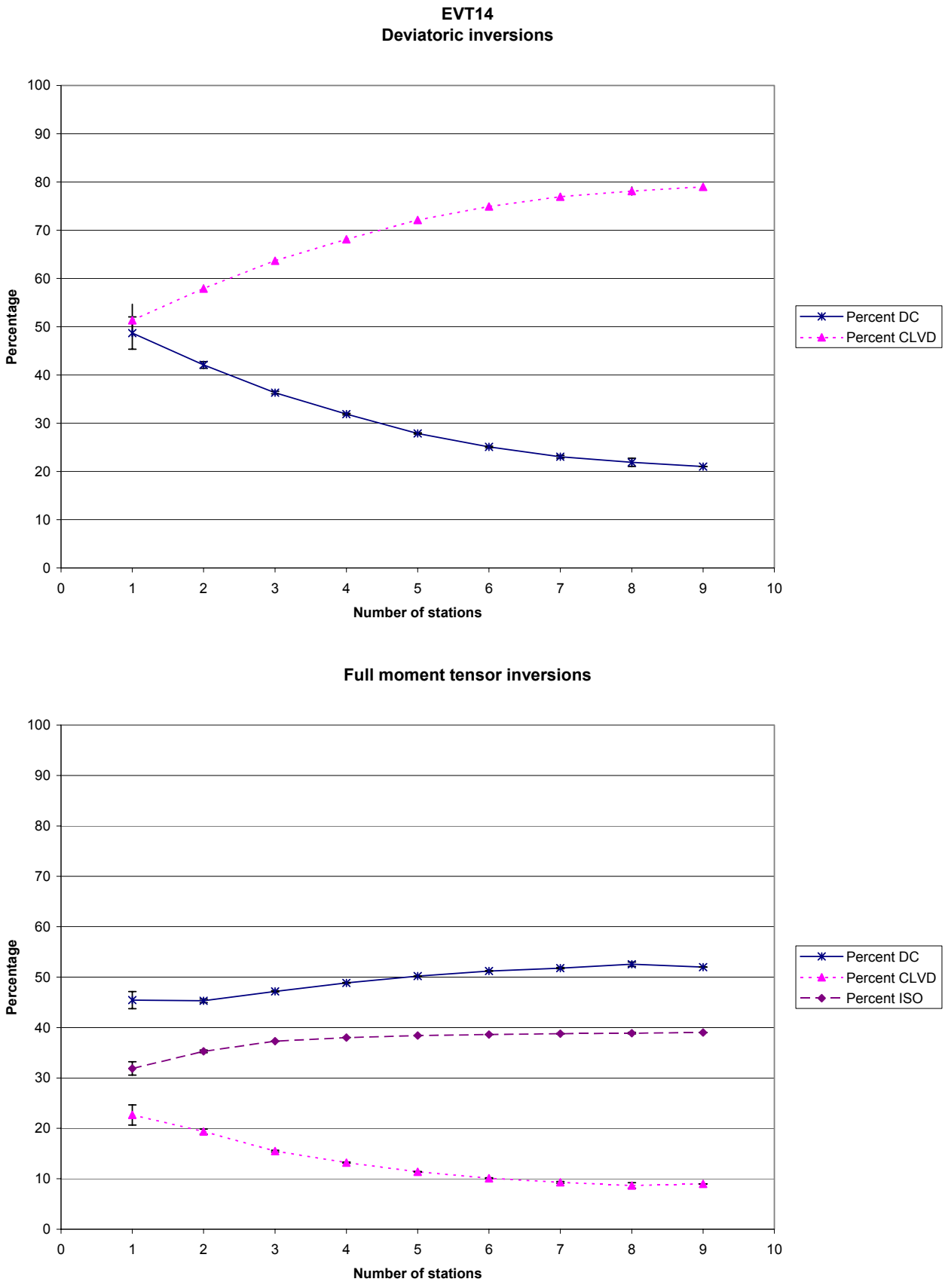
EVT14
Deviatoric inversions
Percentage
Number of stations
Percent DC
Percent CLVD
Full moment tensor inversions
Percentage
Number of stations
Percent DC
Percent CLVD
Percent ISO

Figure 130

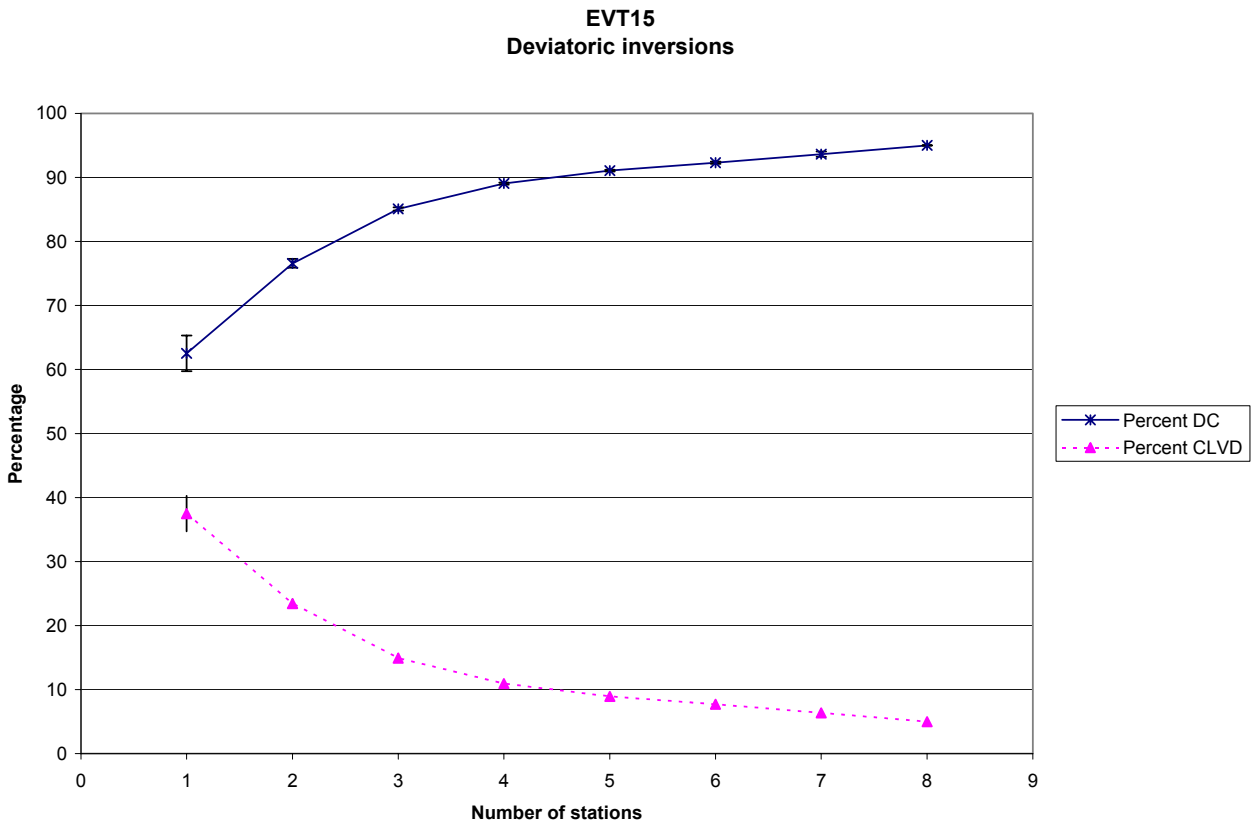
EVT15
Deviatoric inversions
Percentage
Number of stations
Percent DC
Percent CLVD

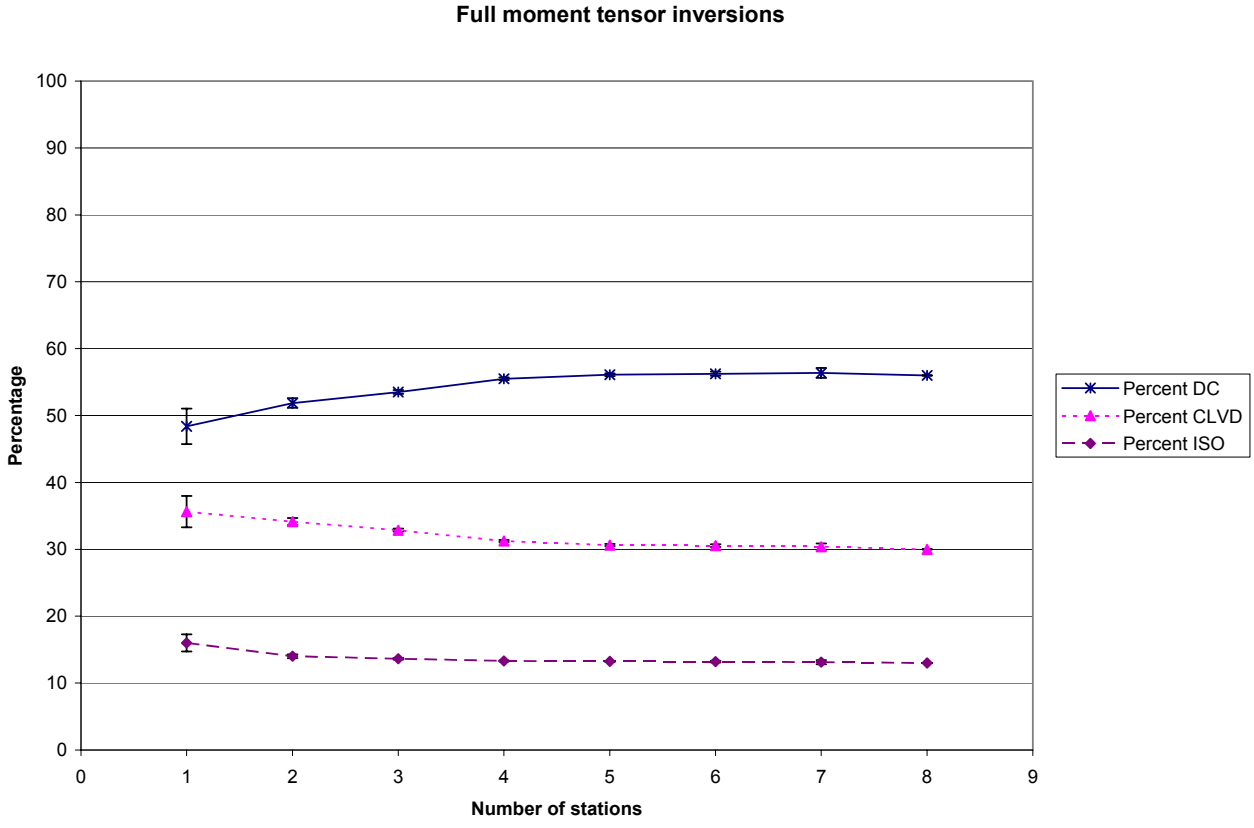
Full moment tensor inversions
Percentage
Number of stations
Percent DC
Percent CLVD
Percent ISO

Figure 131

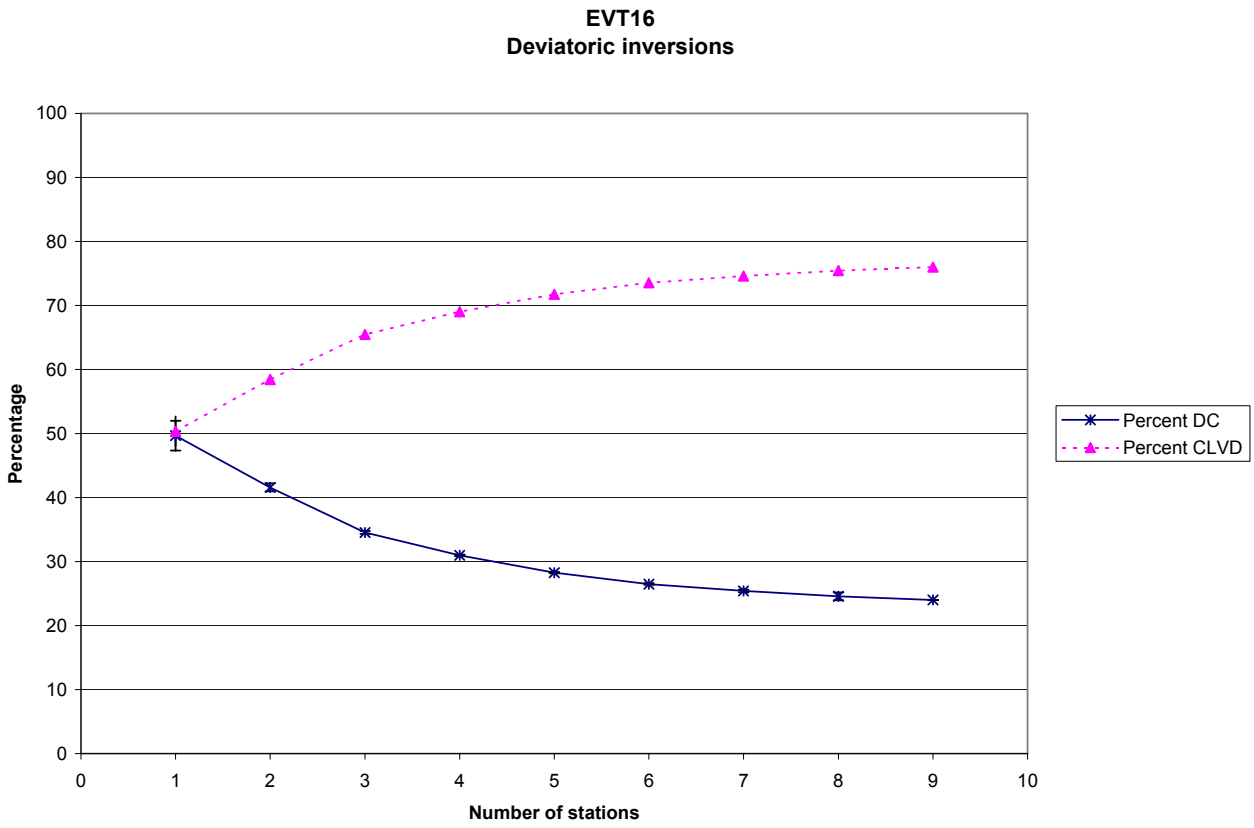
EVT16
Deviatoric inversions
Percentage
Number of stations
Percent DC
Percent CLVD

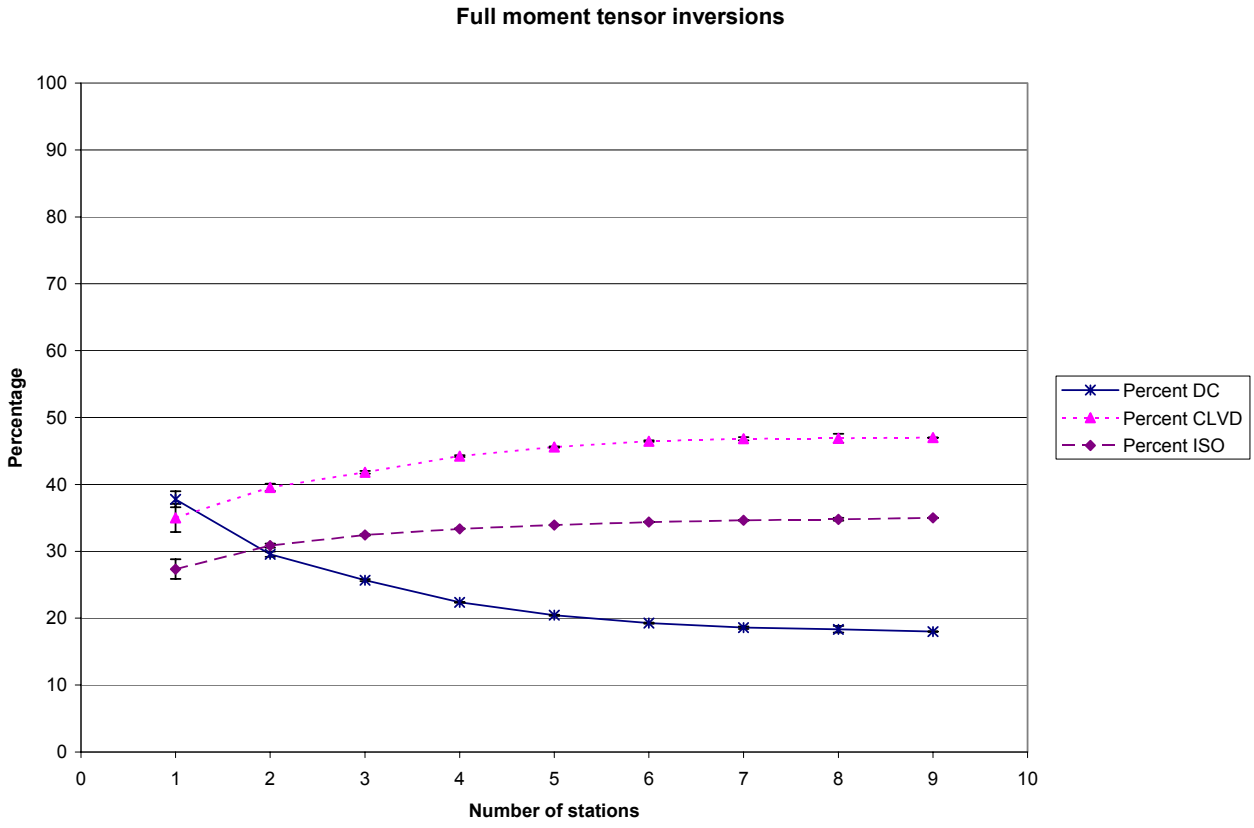
Full moment tensor inversions
Percentage
Number of stations
Percent DC
Percent CLVD
Percent ISO

Figure 132

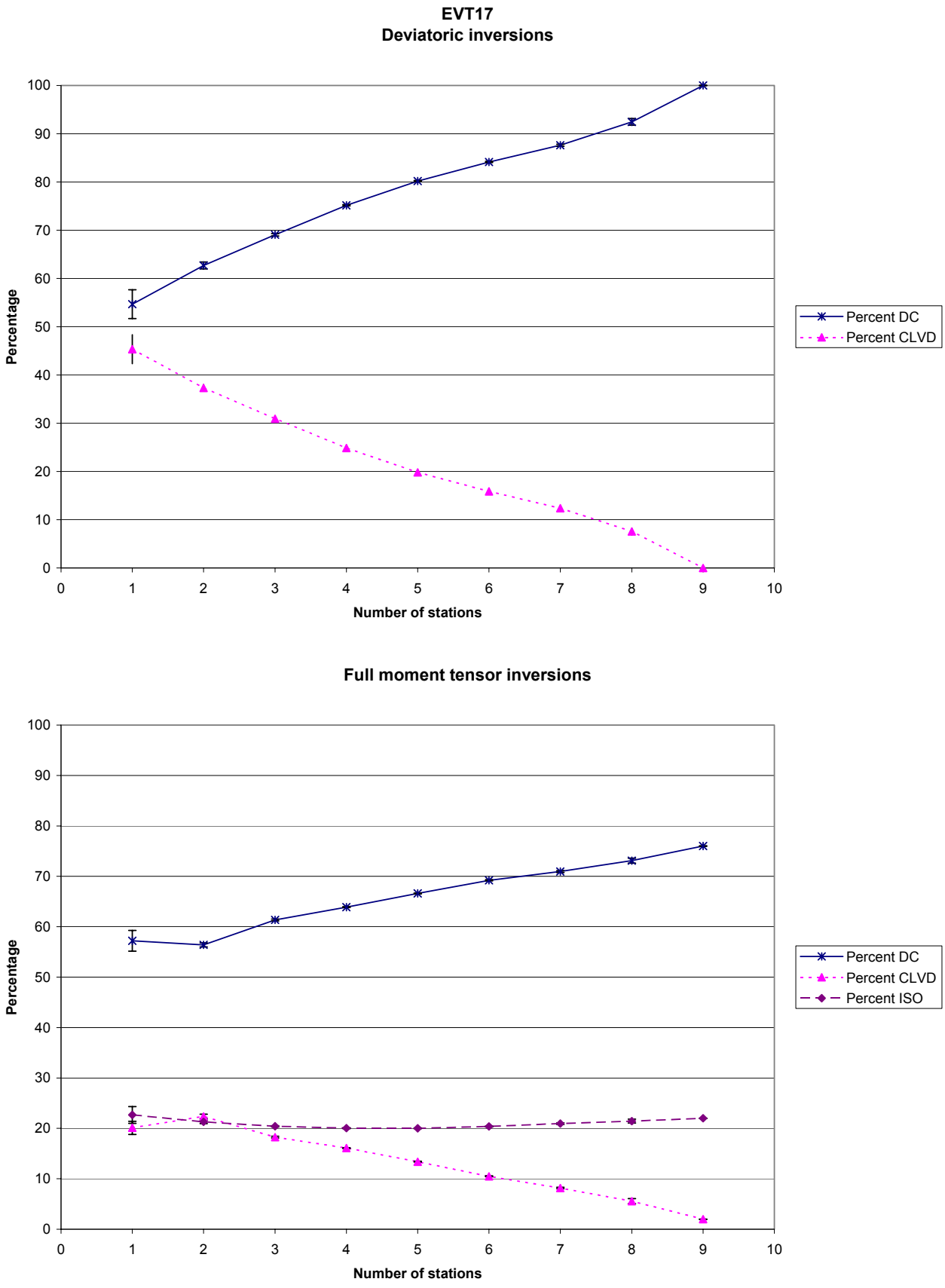
EVT17
Deviatoric inversions
Percentage
Number of stations
Percent DC
Percent CLVD
Full moment tensor inversions
Percentage
Number of stations
Percent DC
Percent CLVD
Percent ISO

Figure 133

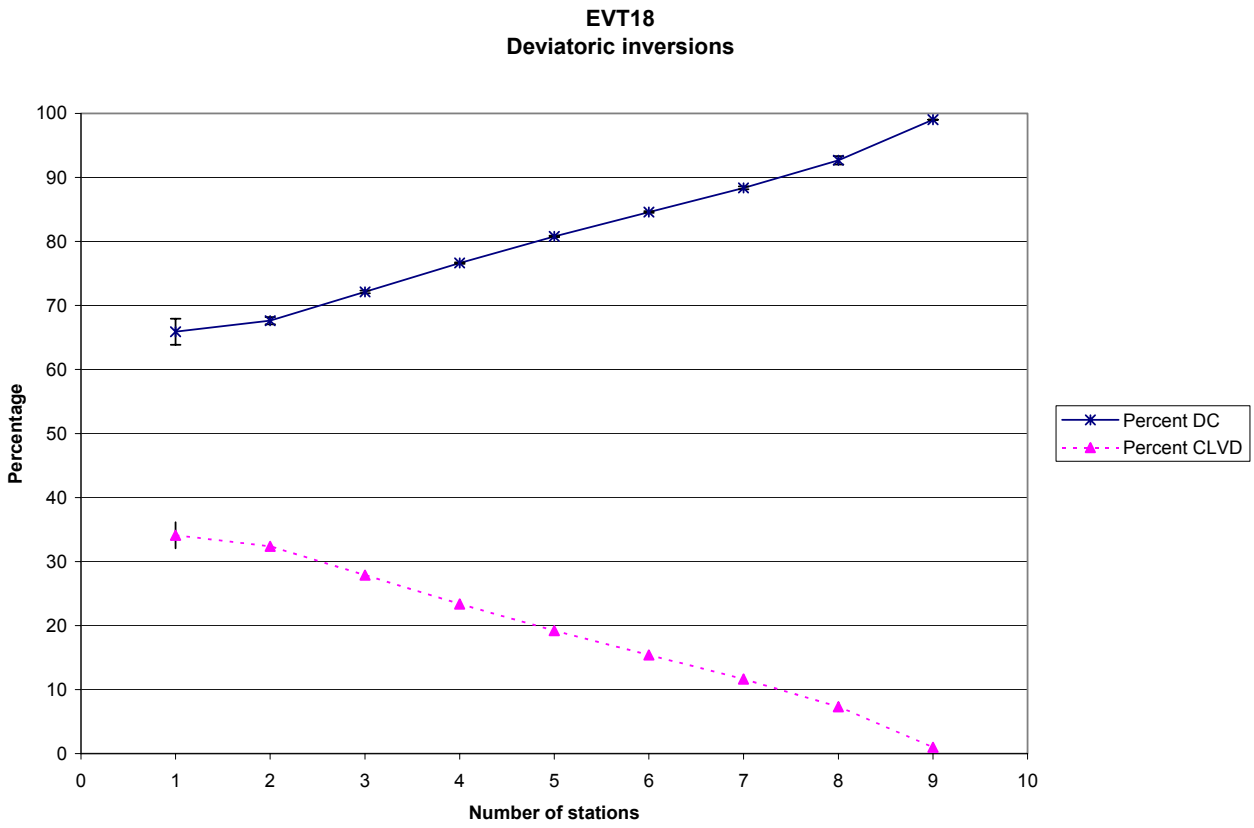
EVT18
Deviatoric inversions
Percentage
Number of stations
Percent DC
Percent CLVD

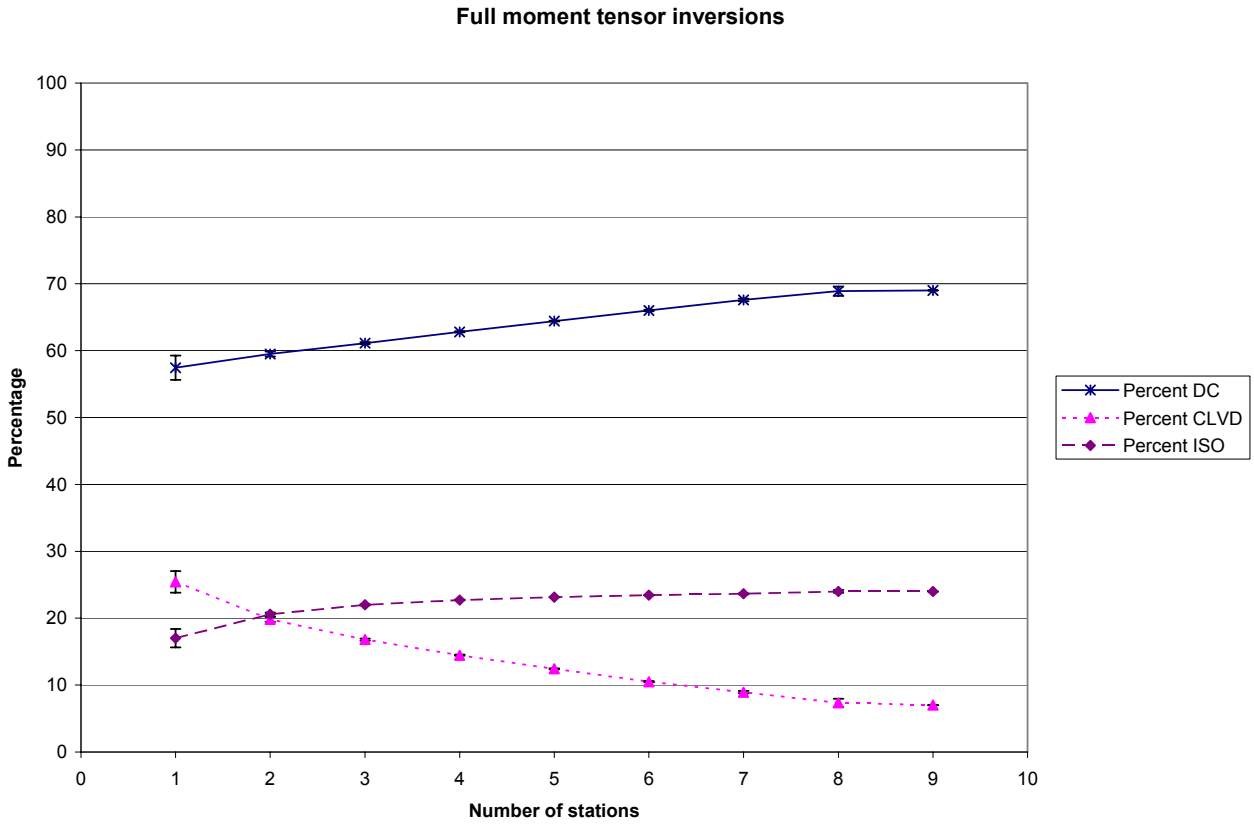
Full moment tensor inversions
Percentage
Number of stations
Percent DC
Percent CLVD
Percent ISO

Figure 134

EVT1

T-axes from deviatoric inversions

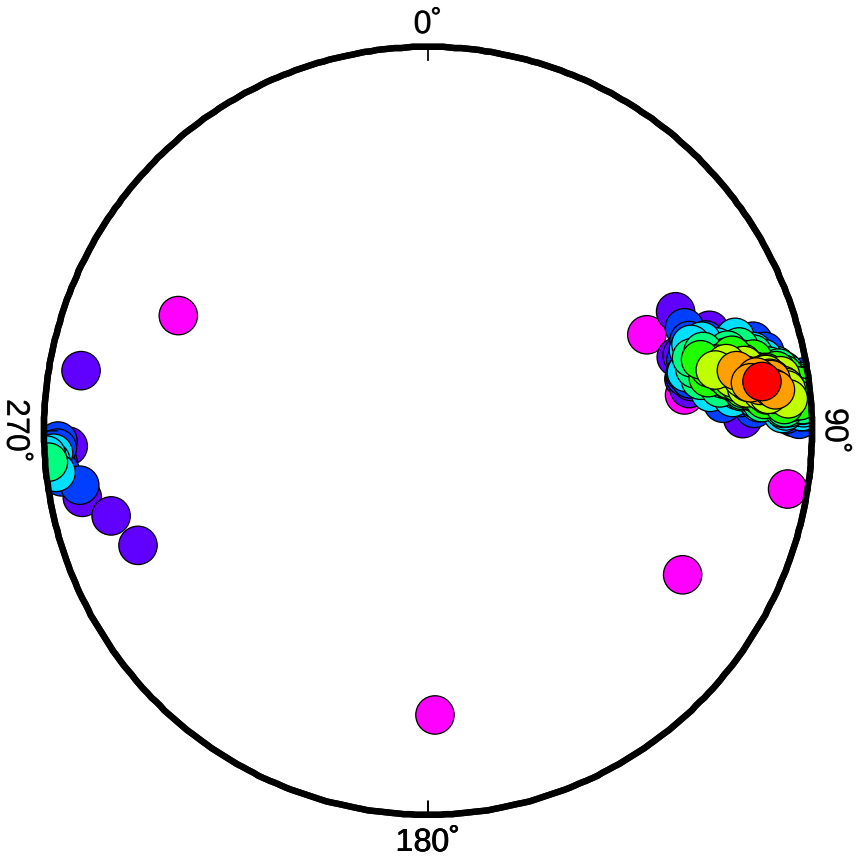

T-axes from full moment tensor inversions

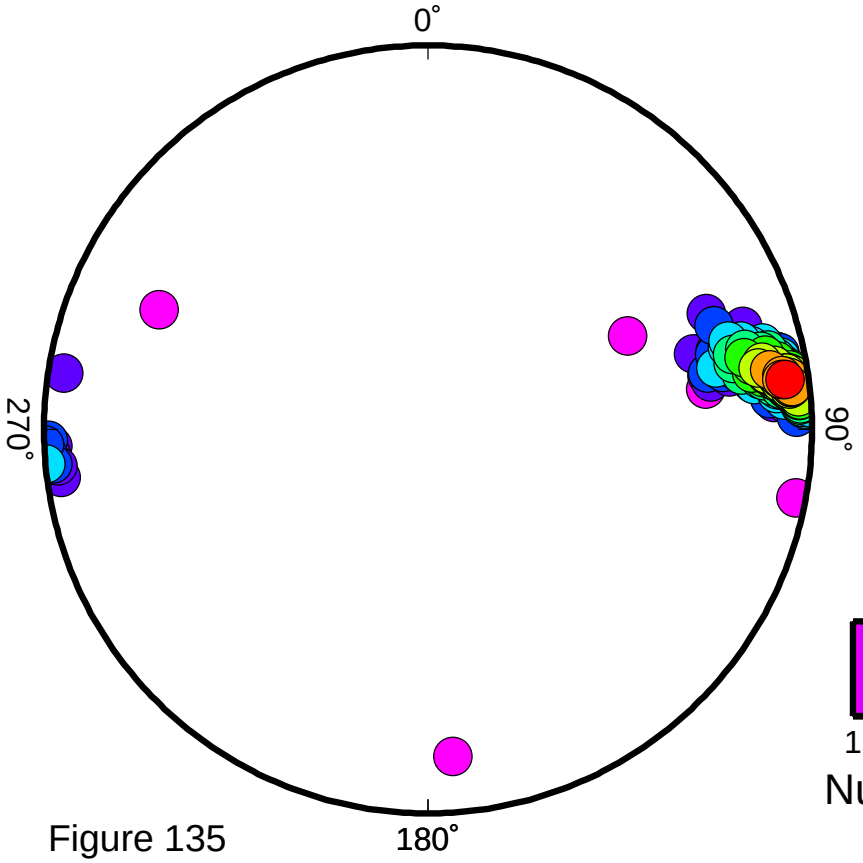

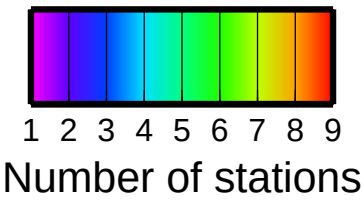

Figure 135

EVT2

T-axes from deviatoric inversions

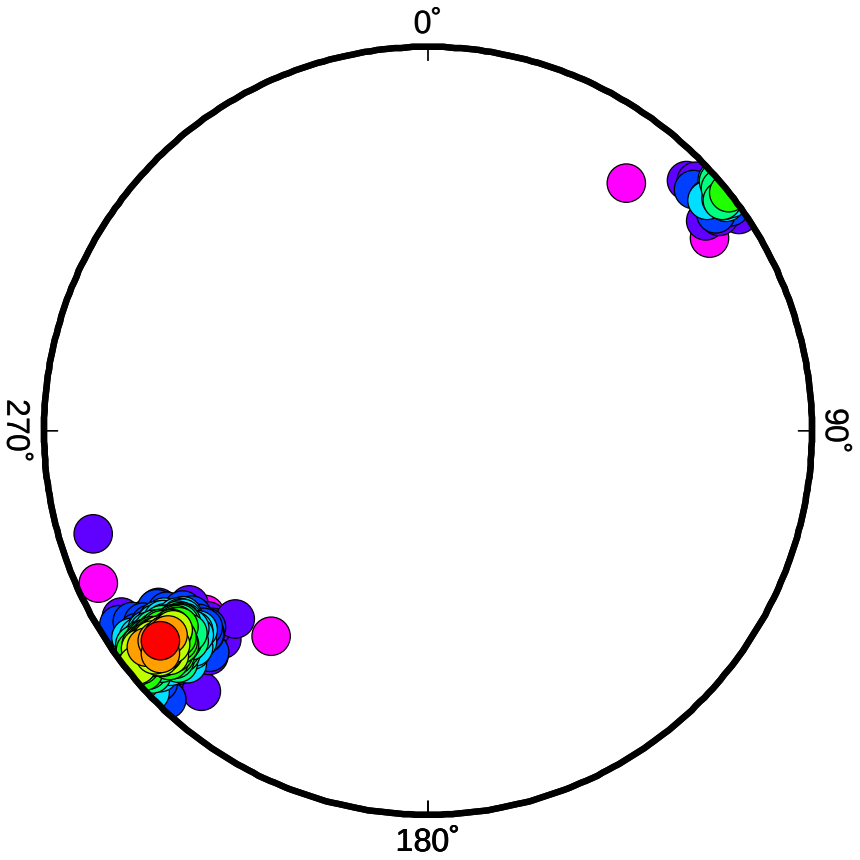

T-axes from full moment tensor inversions

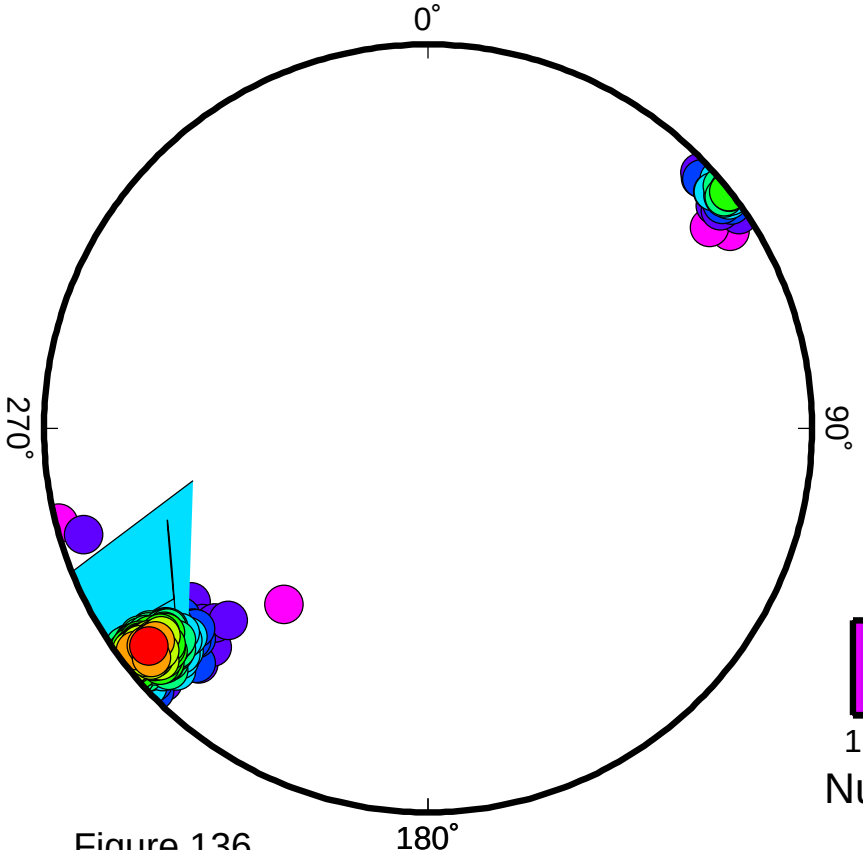

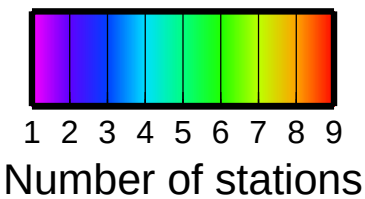

Figure 136

EVT3

T-axes from deviatoric inversions

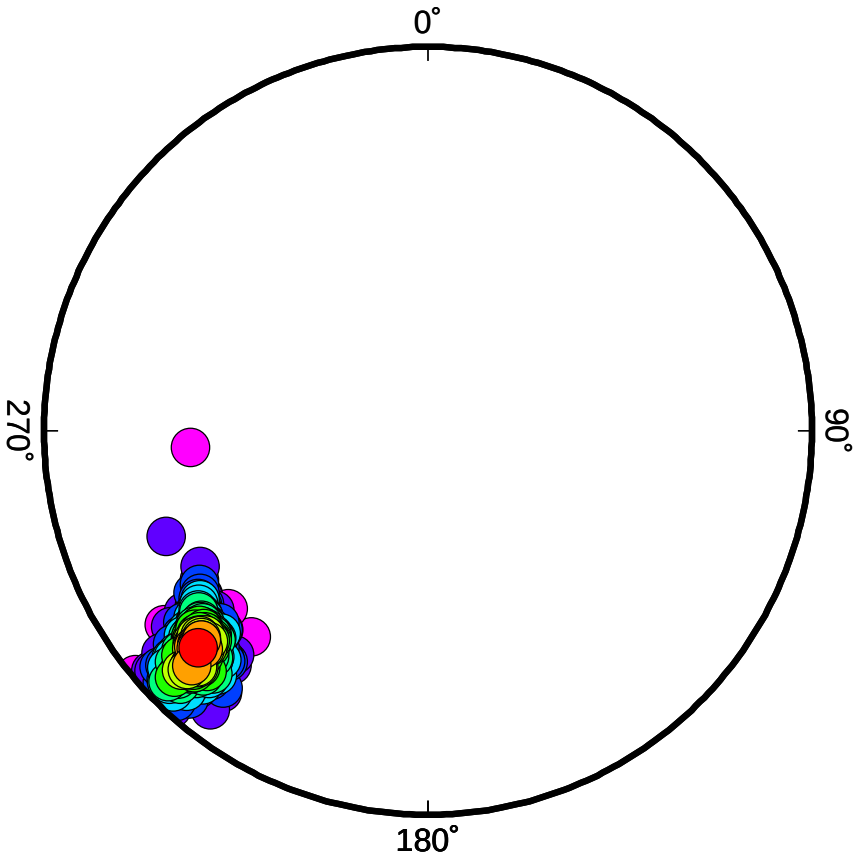

T-axes from full moment tensor inversions

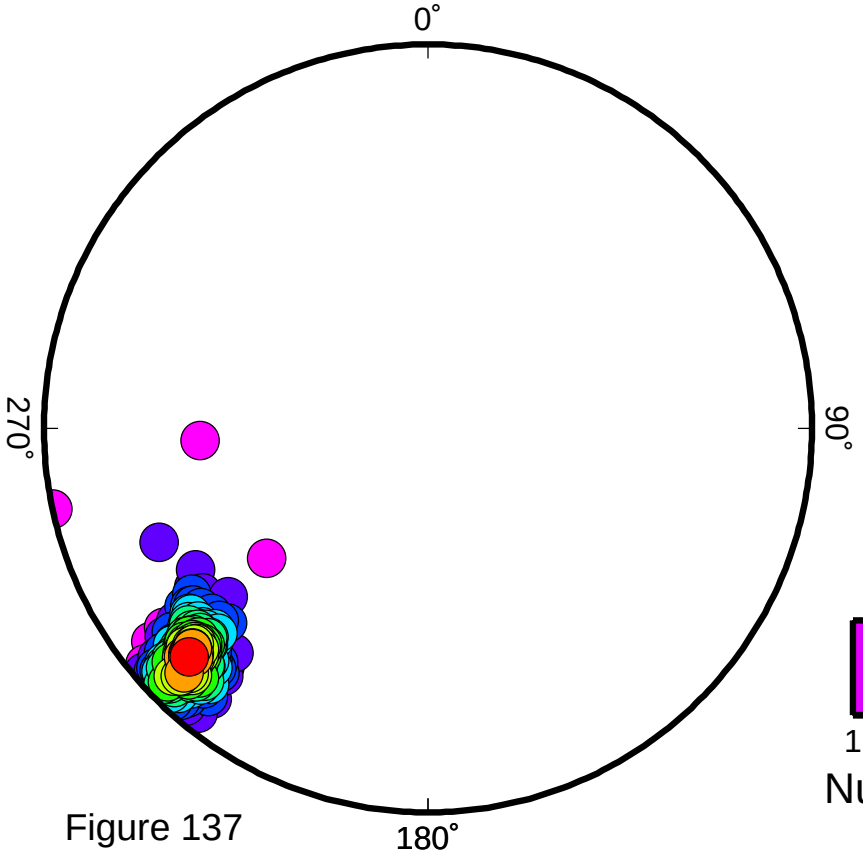

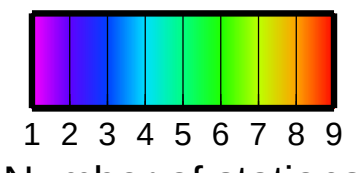

Figure 137

EVT4

T-axes from deviatoric inversions

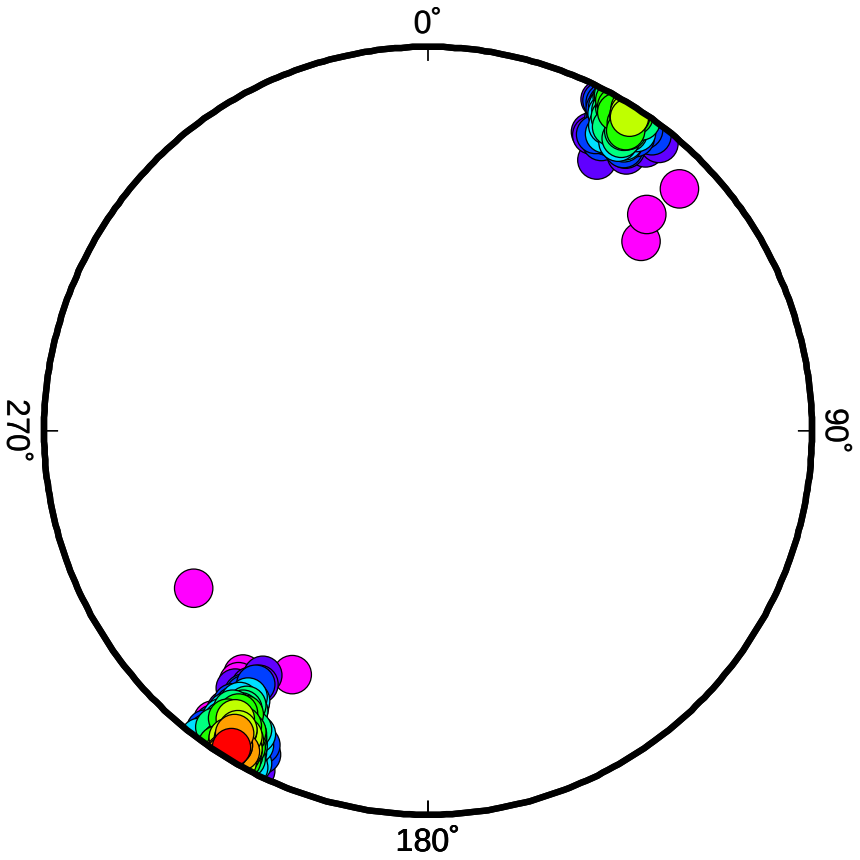

T-axes from full moment tensor inversions

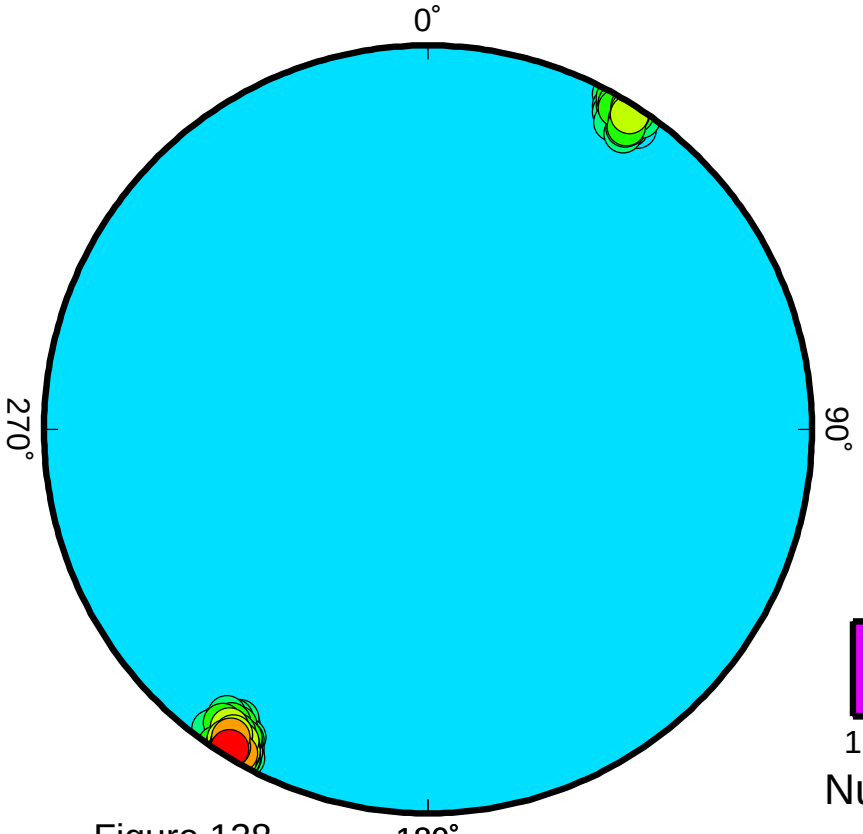

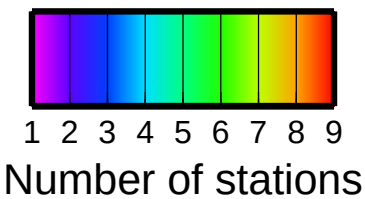

Figure 138

EVT5

T-axes from deviatoric inversions

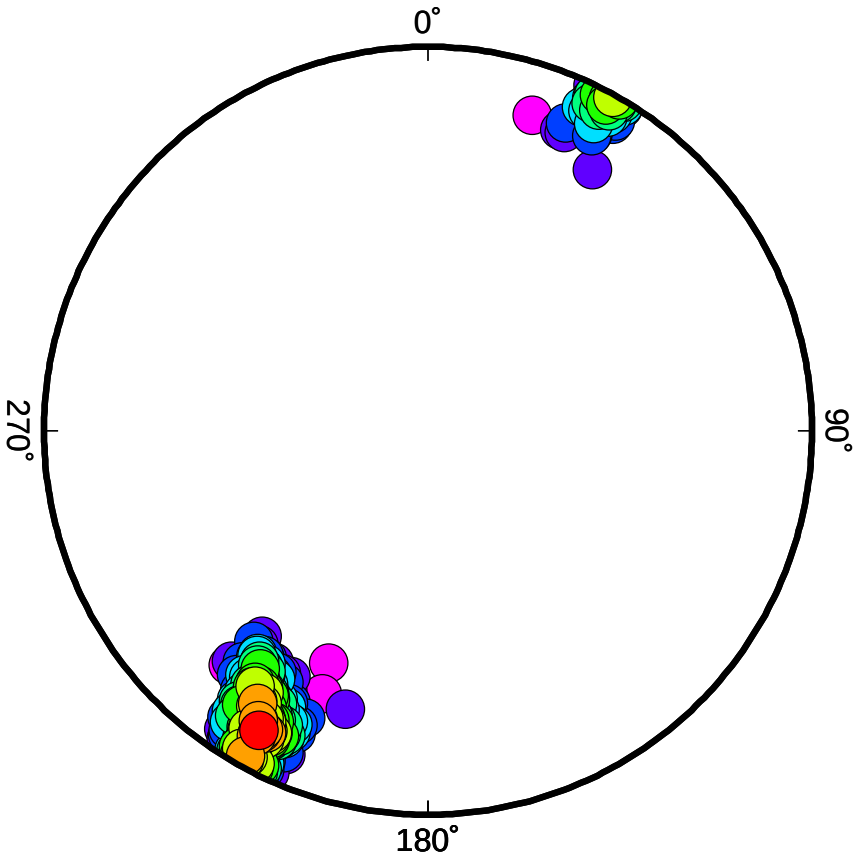

T-axes from full moment tensor inversions

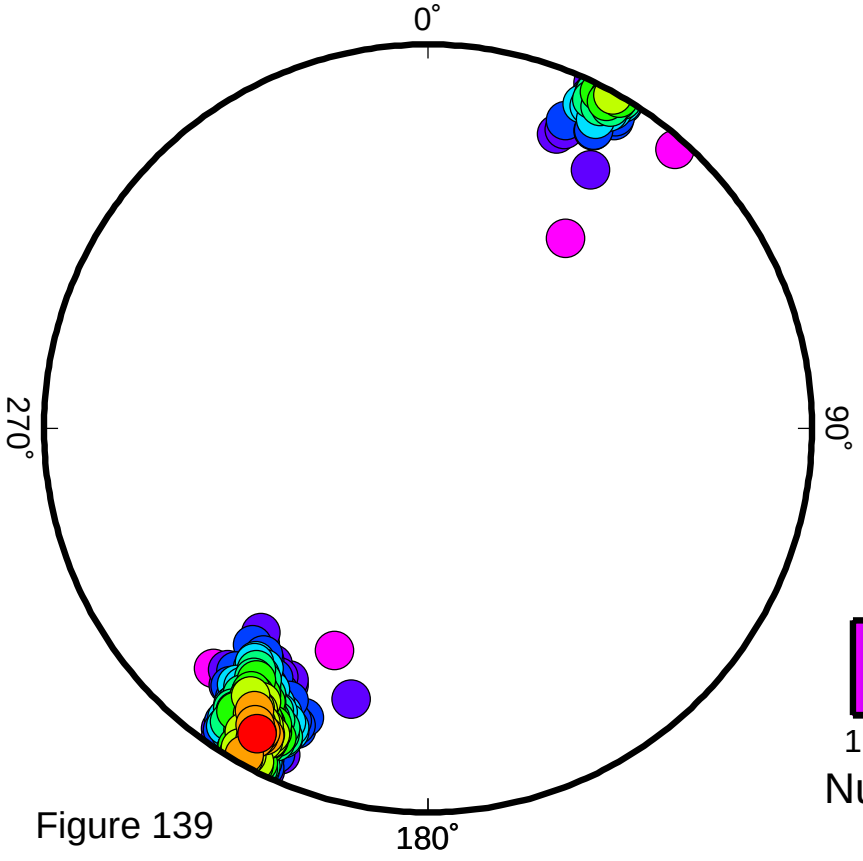

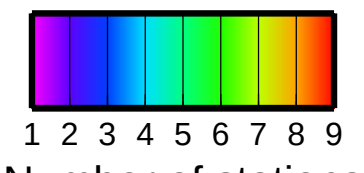

Figure 139

EVT6

T-axes from deviatoric inversions

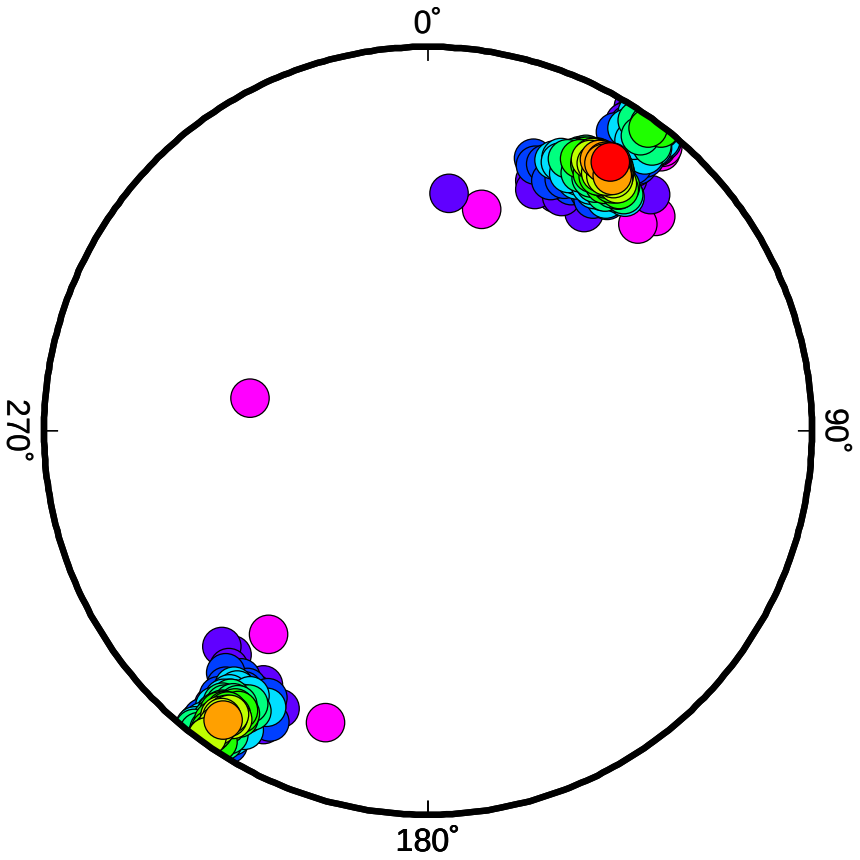

T-axes from full moment tensor inversions

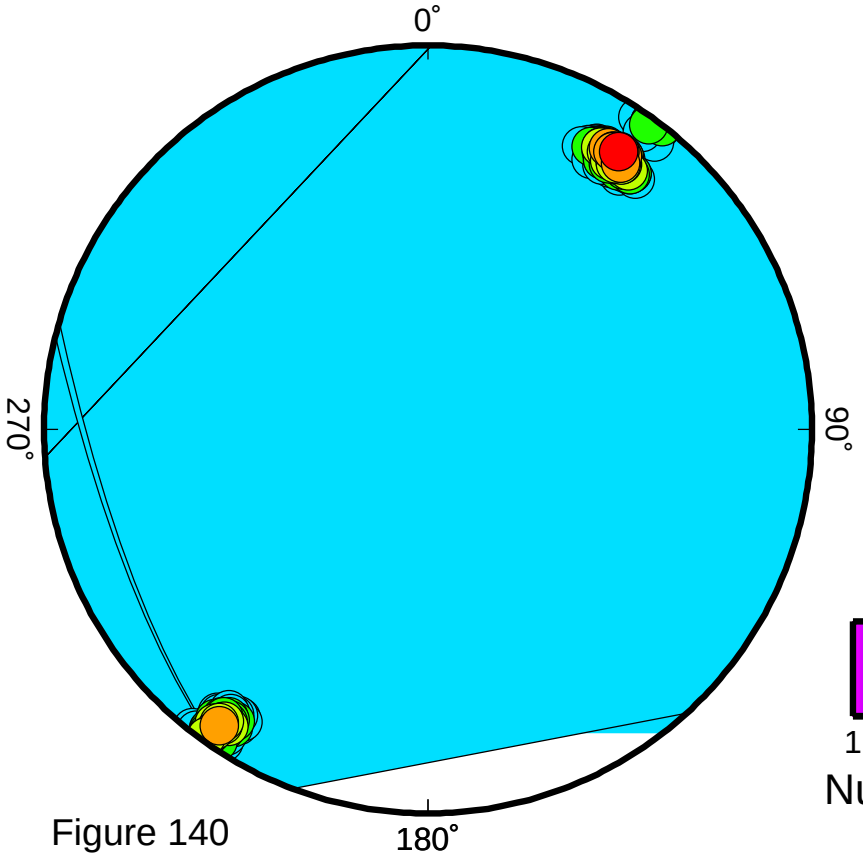

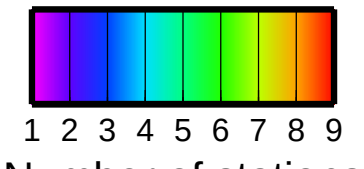

Figure 140

EVT7

T-axes from deviatoric inversions

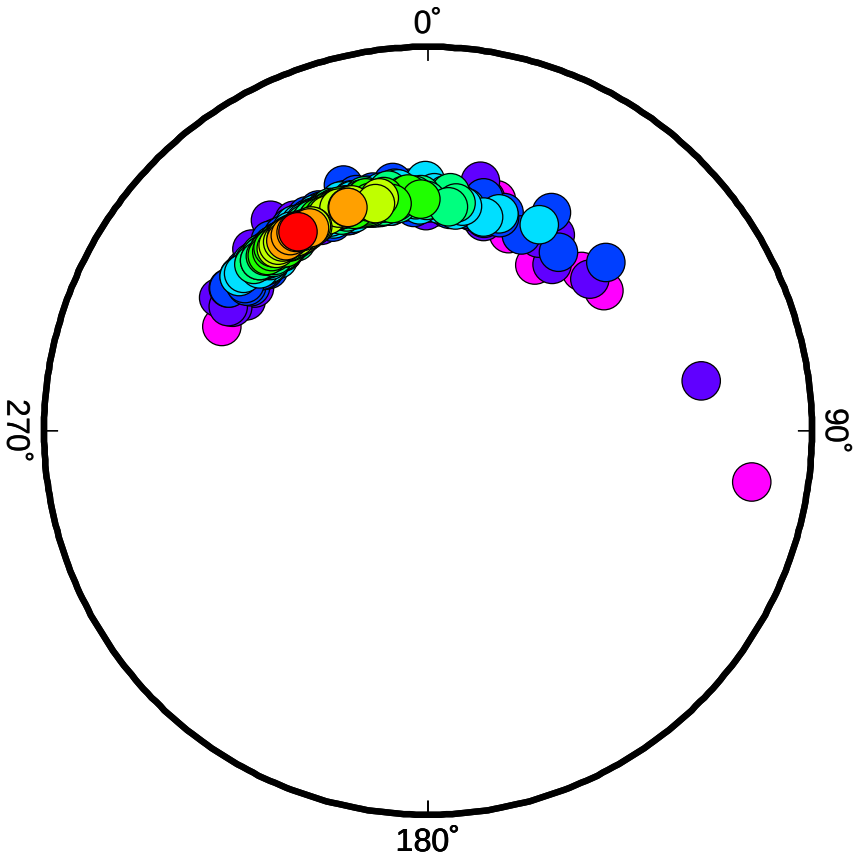

T-axes from full moment tensor inversions

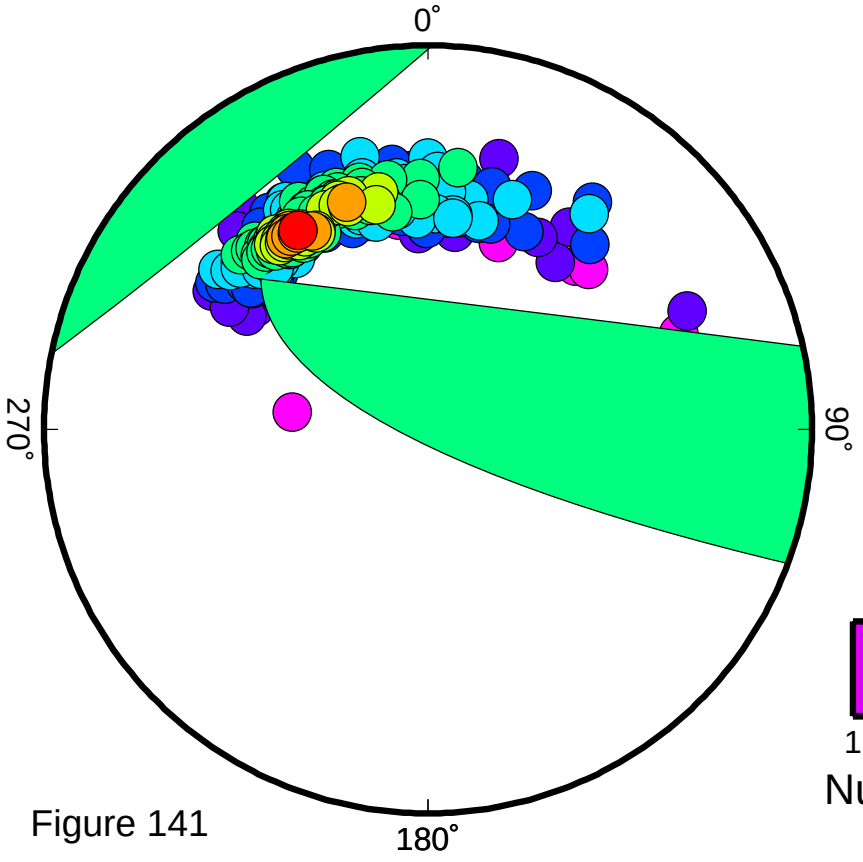

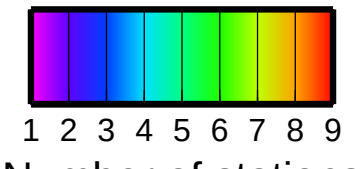

Figure 141

EVT8

T-axes from deviatoric inversions

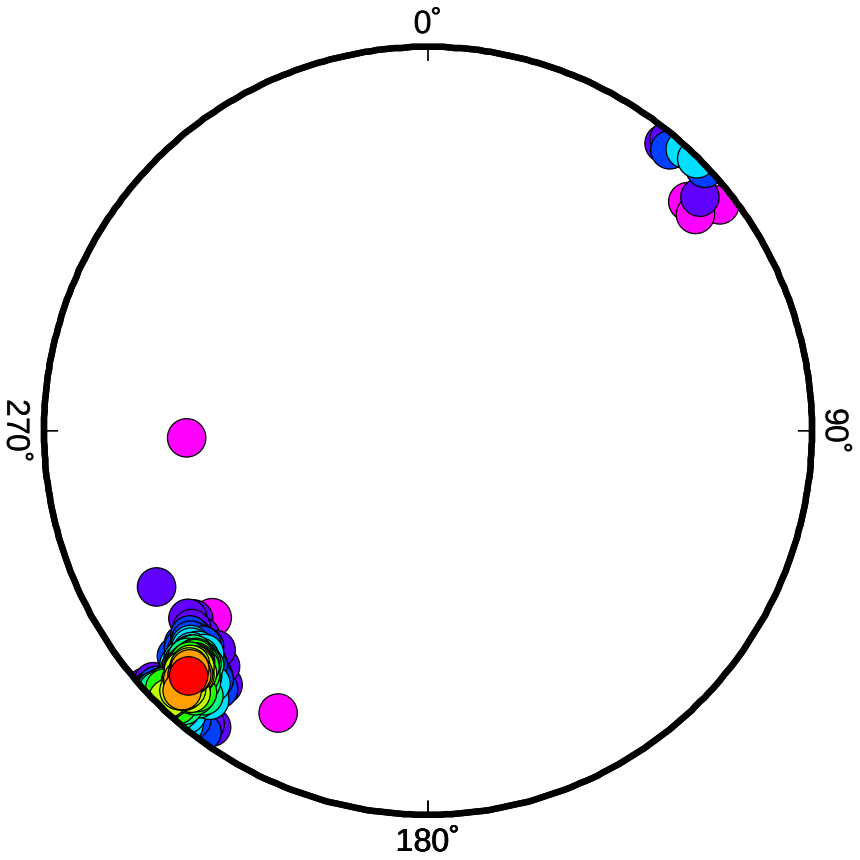

T-axes from full moment tensor inversions

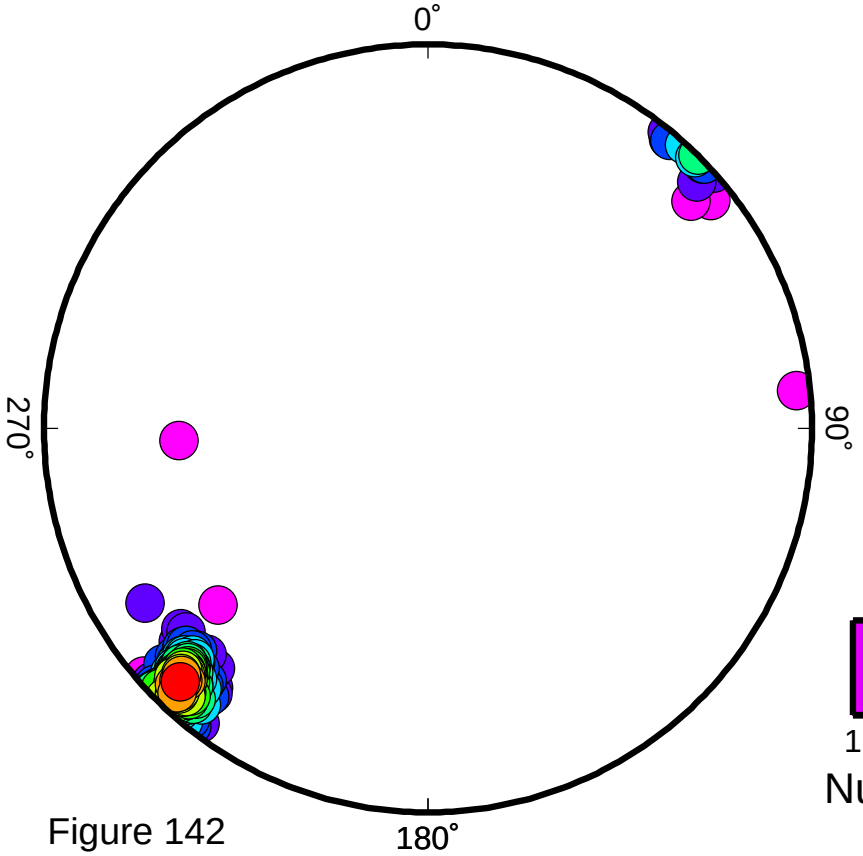

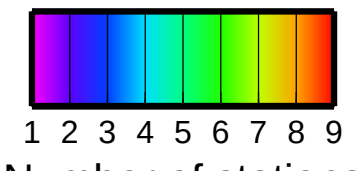

Figure 142

EVT9

T-axes from deviatoric inversions

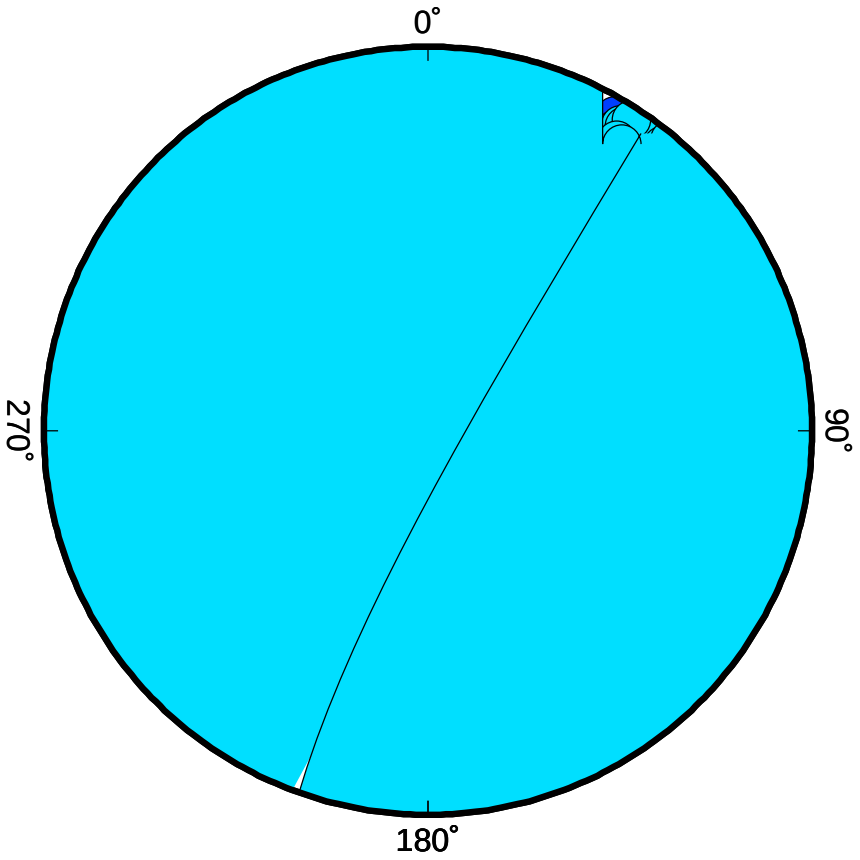

T-axes from full moment tensor inversions

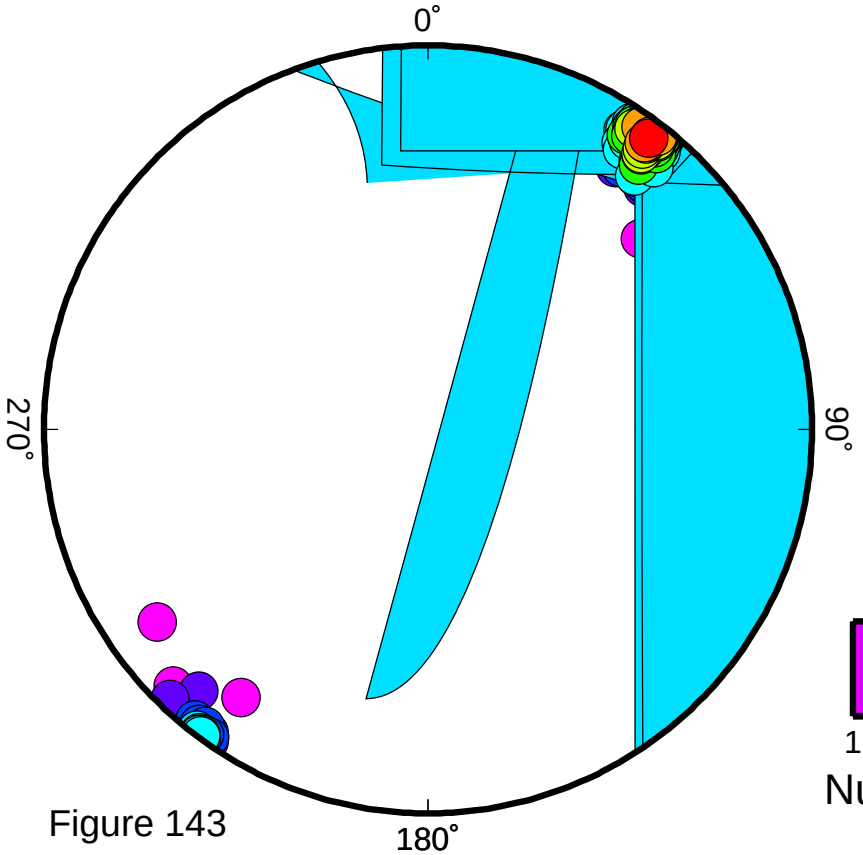

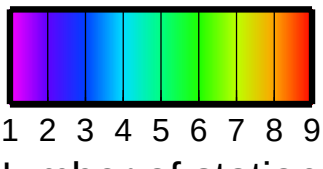

Figure 143

EVT10

T-axes from deviatoric inversions

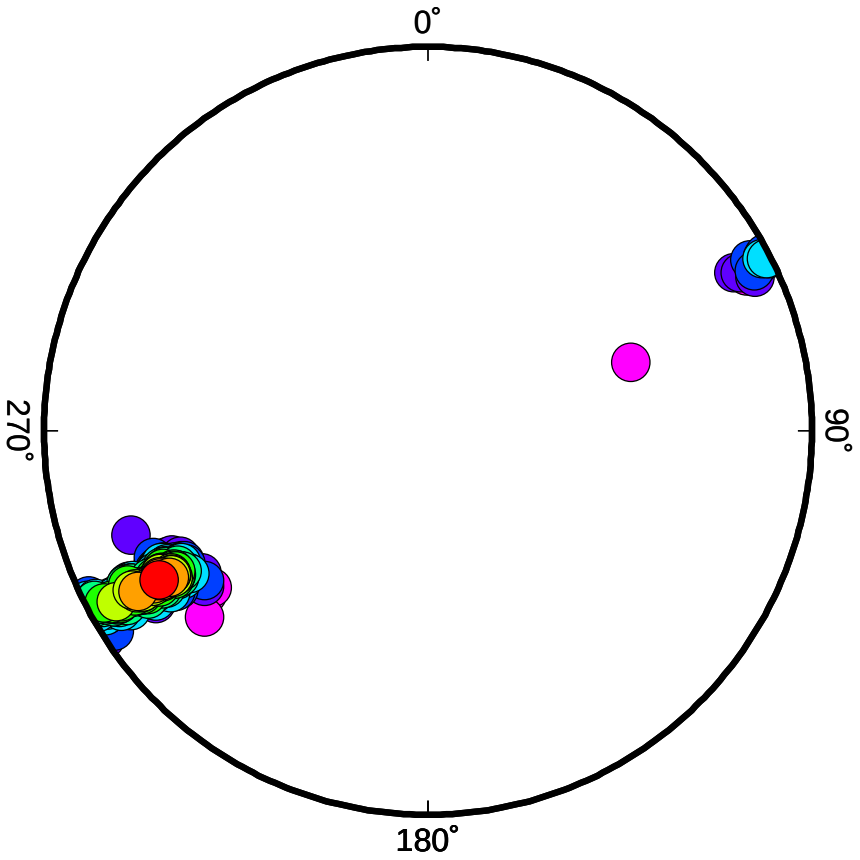

T-axes from full moment tensor inversions

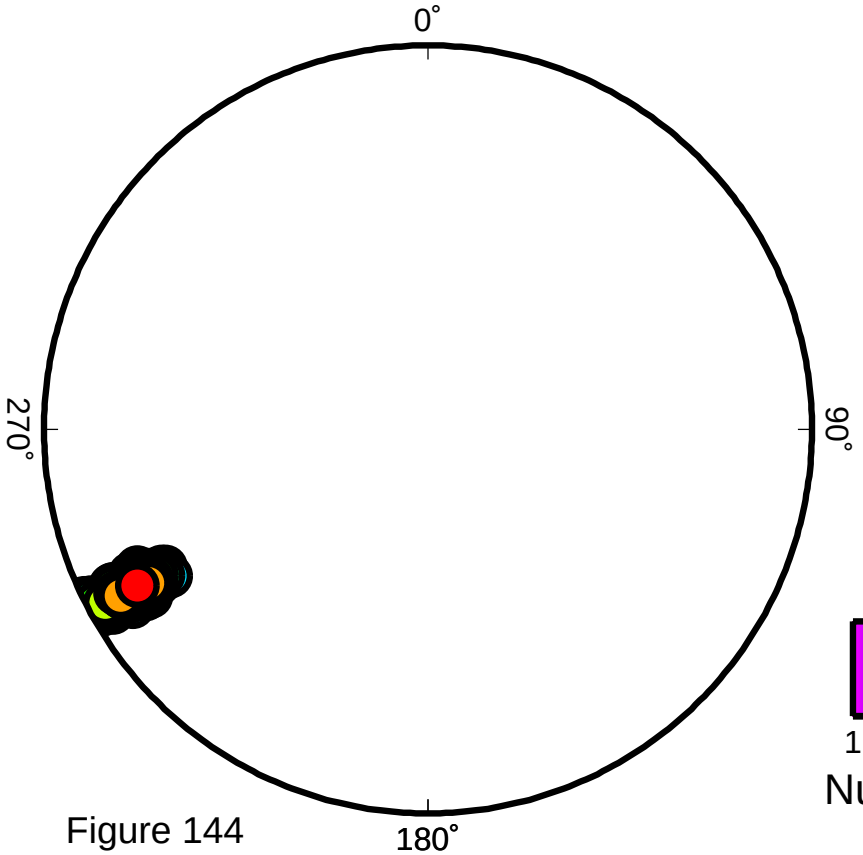

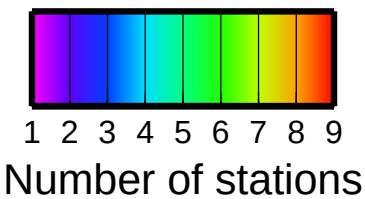

Figure 144

EVT11

T-axes from deviatoric inversions

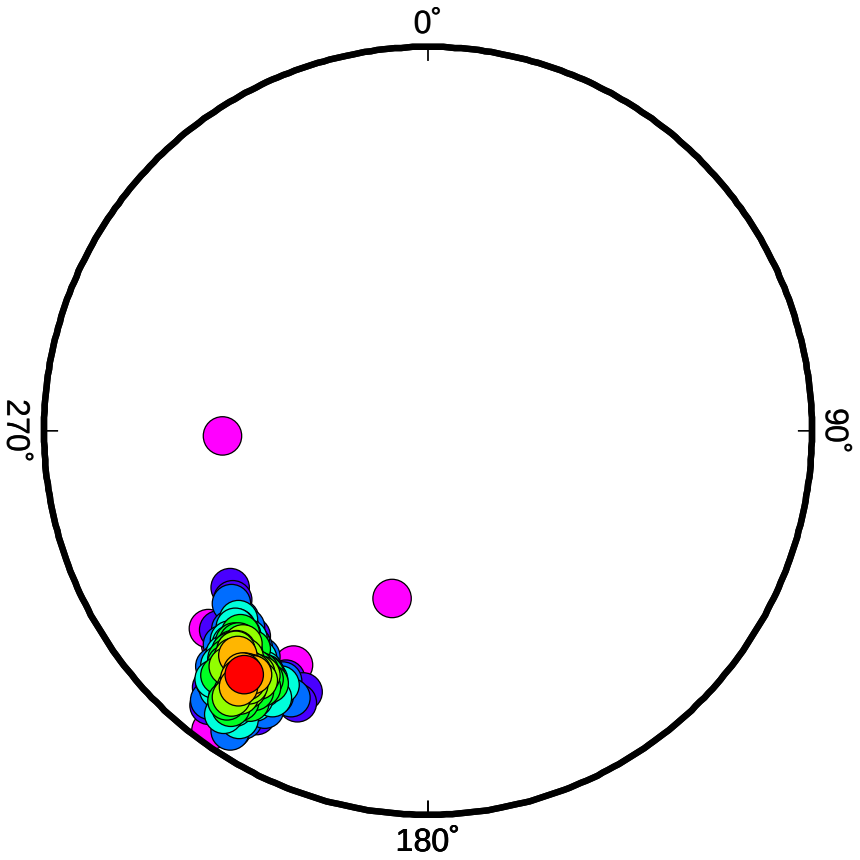

T-axes from full moment tensor inversions

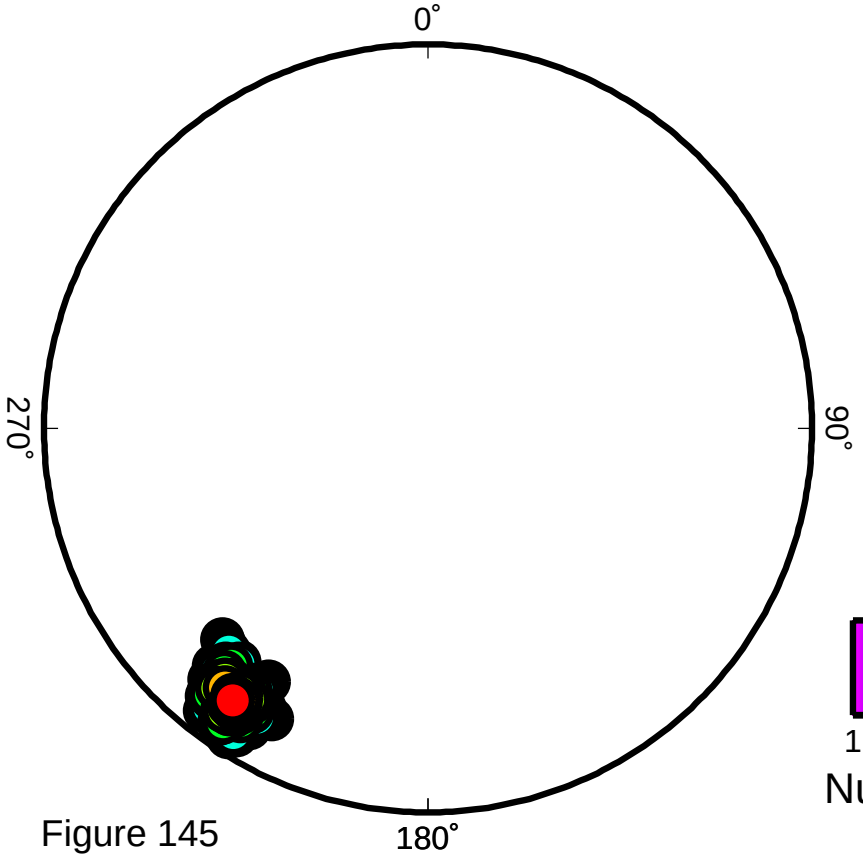

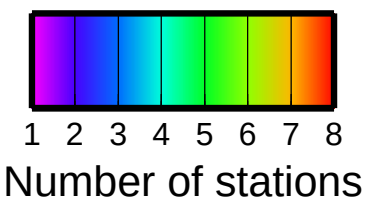

Figure 145

EVT12

T-axes from deviatoric inversions

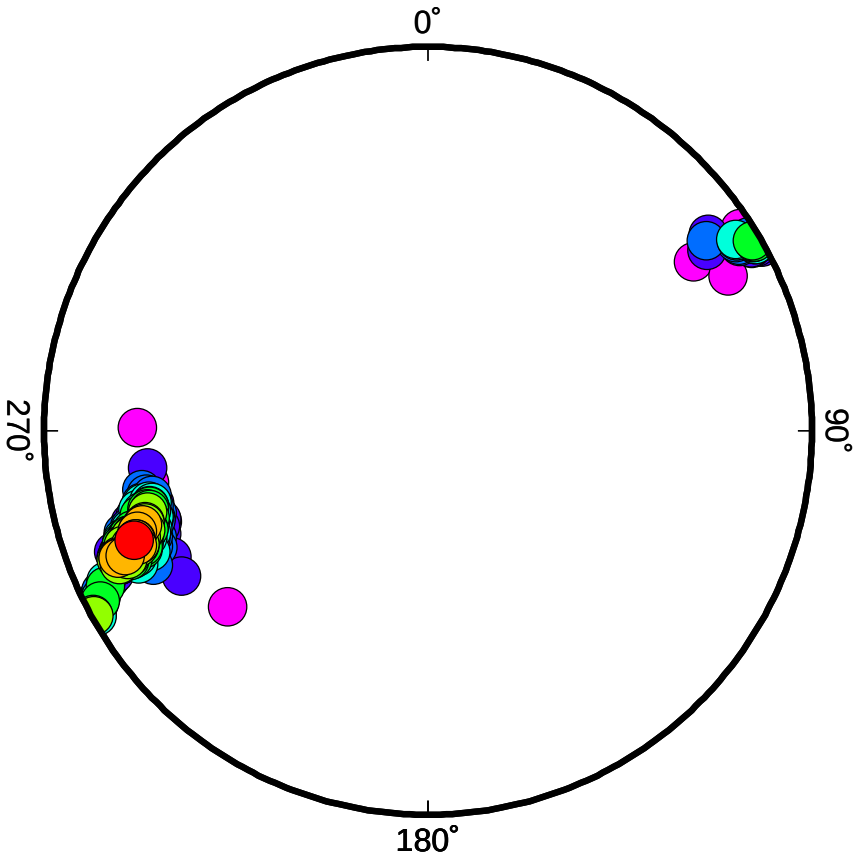

T-axes from full moment tensor inversions

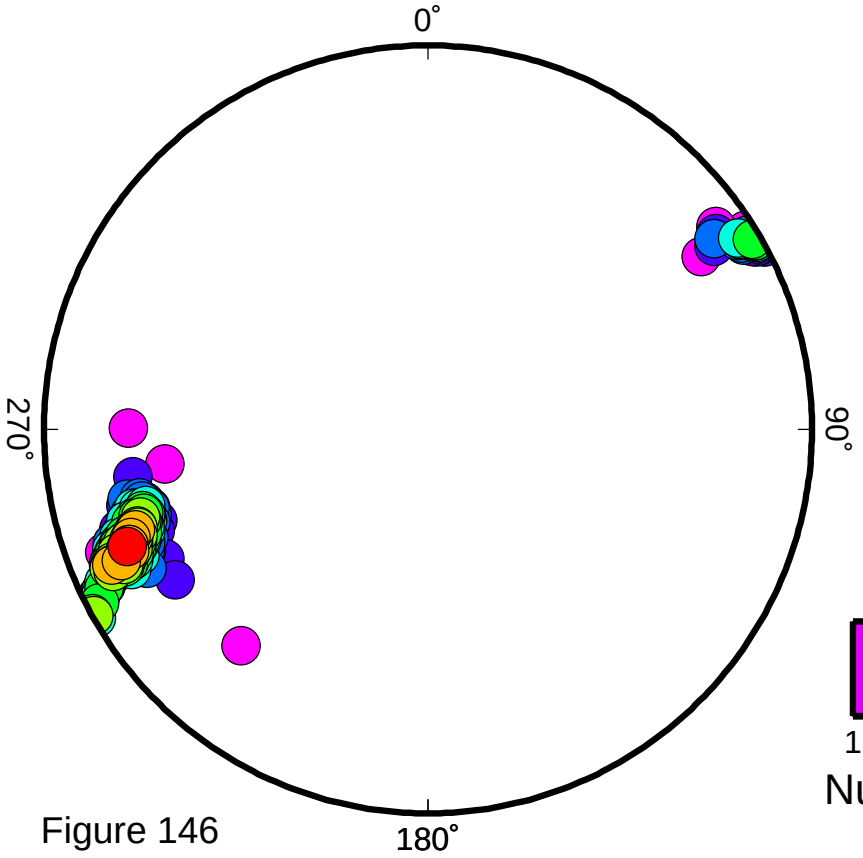

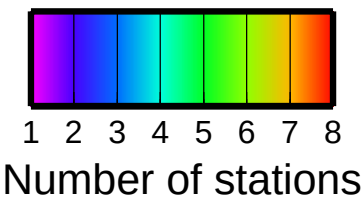

Figure 146

EVT13

T-axes from deviatoric inversions

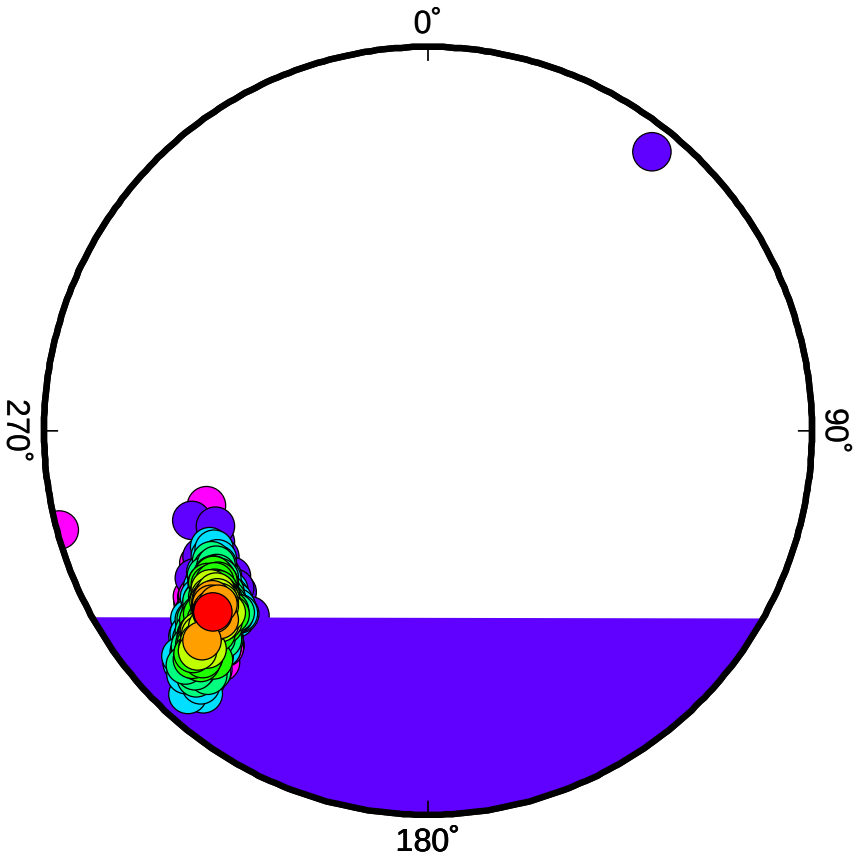

T-axes from full moment tensor inversions

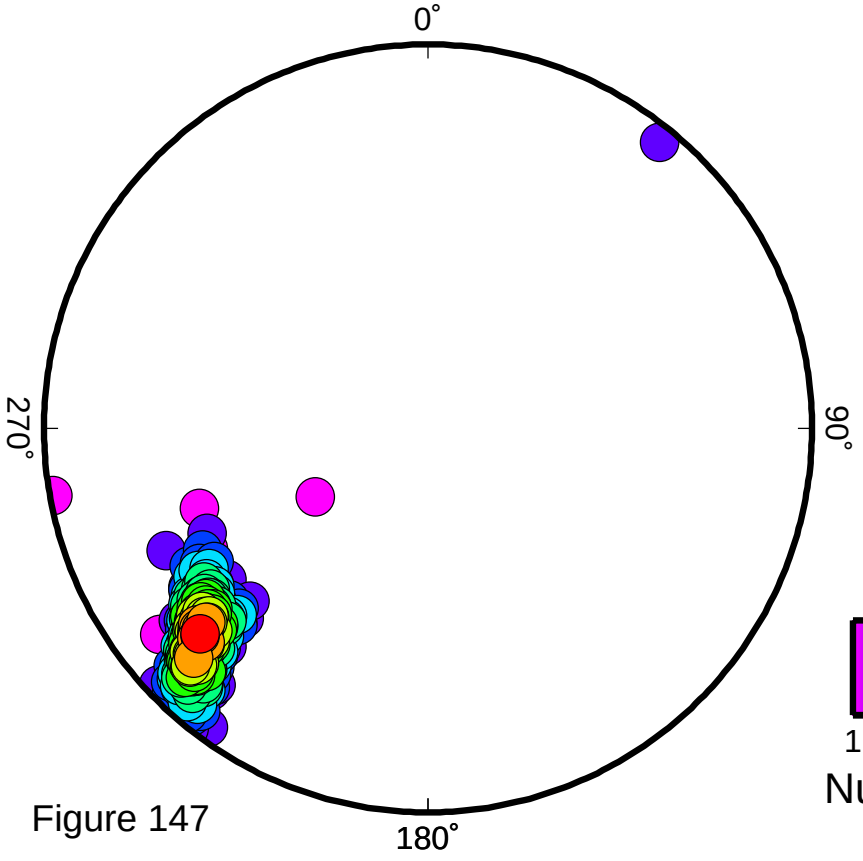

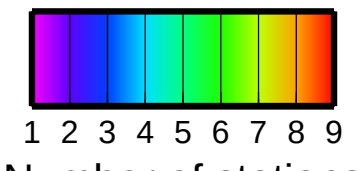

Figure 147

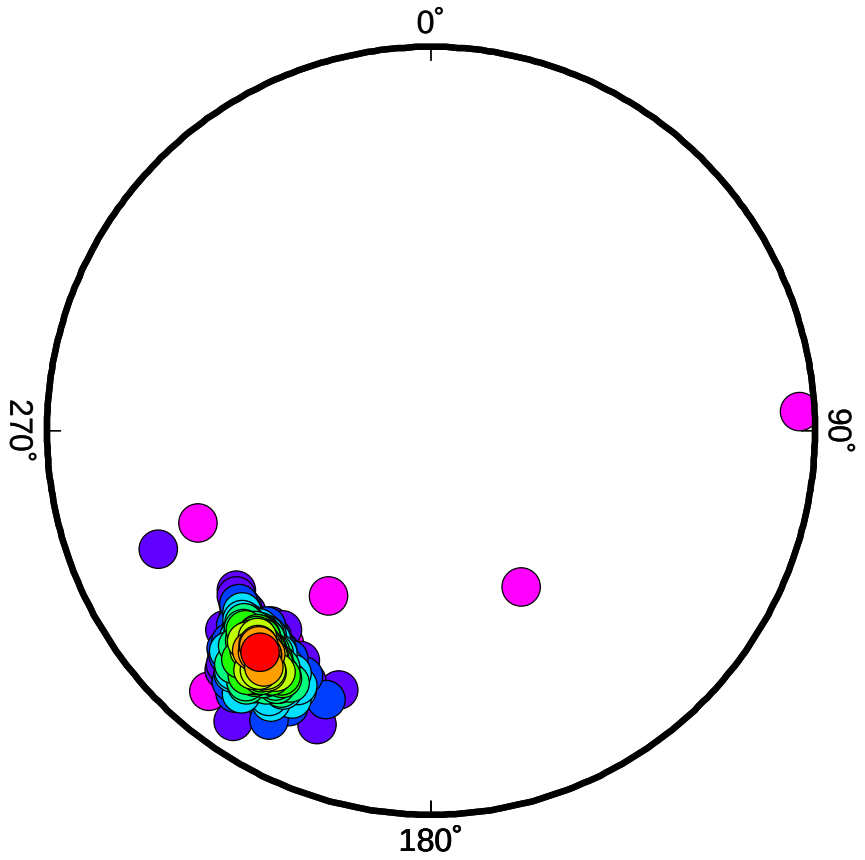

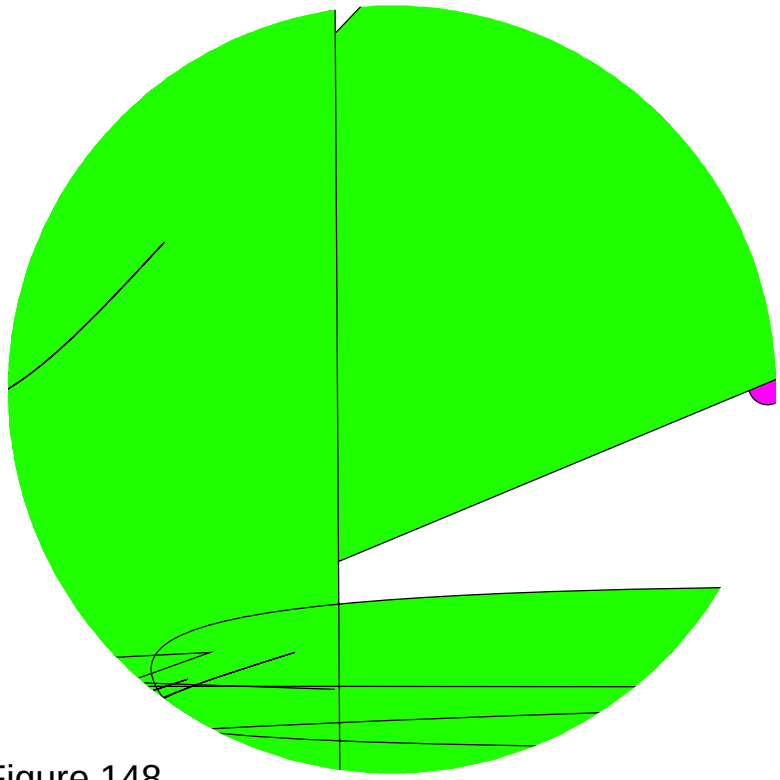

Figure 148

EVT15

T-axes from deviatoric inversions

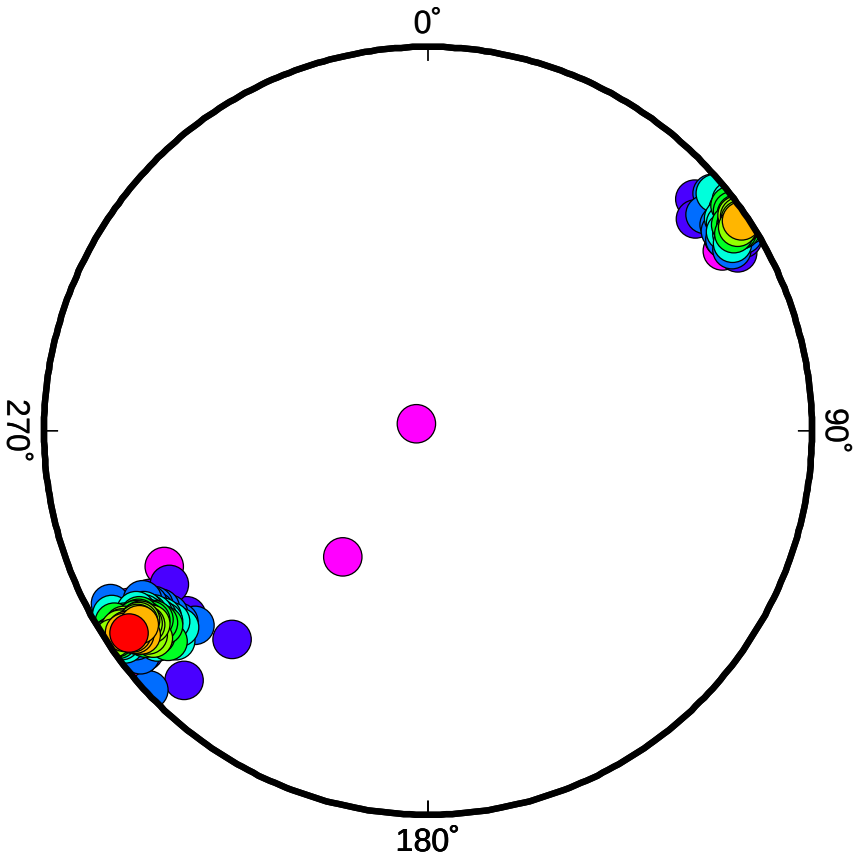

T-axes from full moment tensor inversions

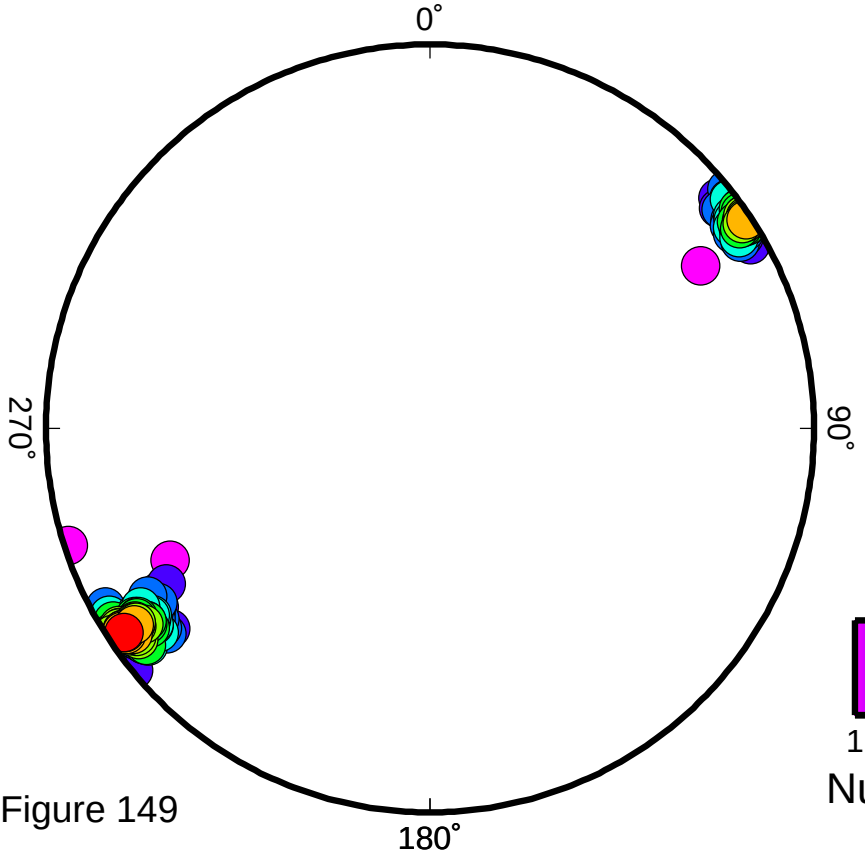

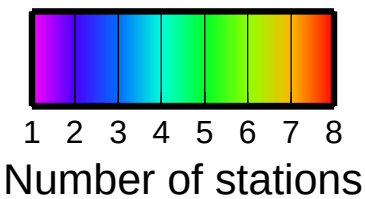

Figure 149

EVT16

T-axes from deviatoric inversions

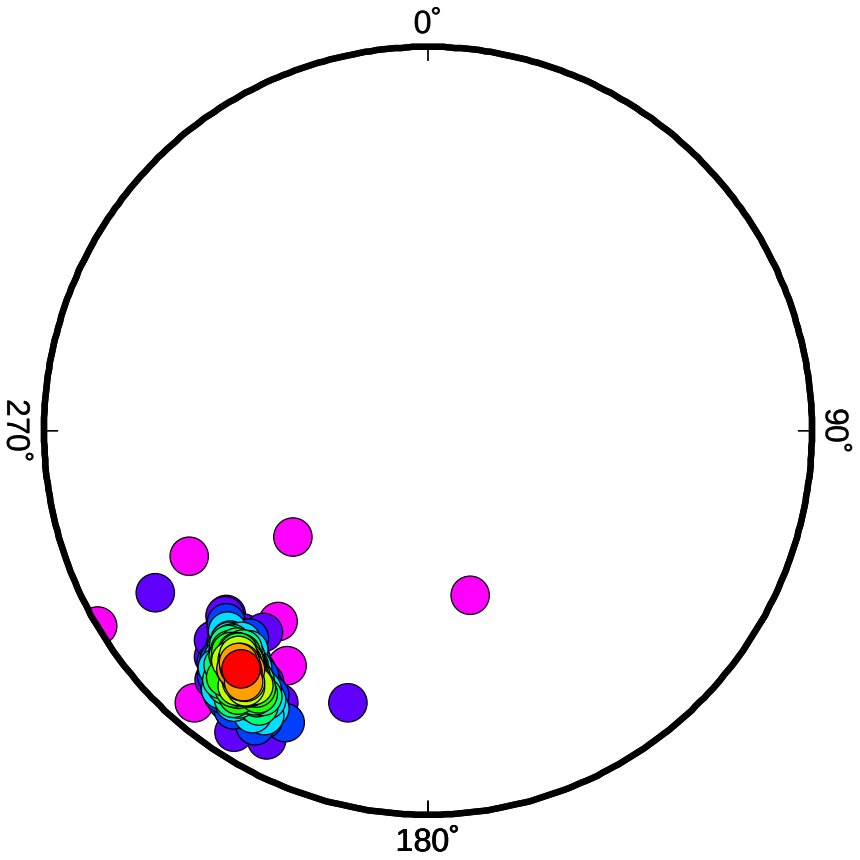

T-axes from full moment tensor inversions

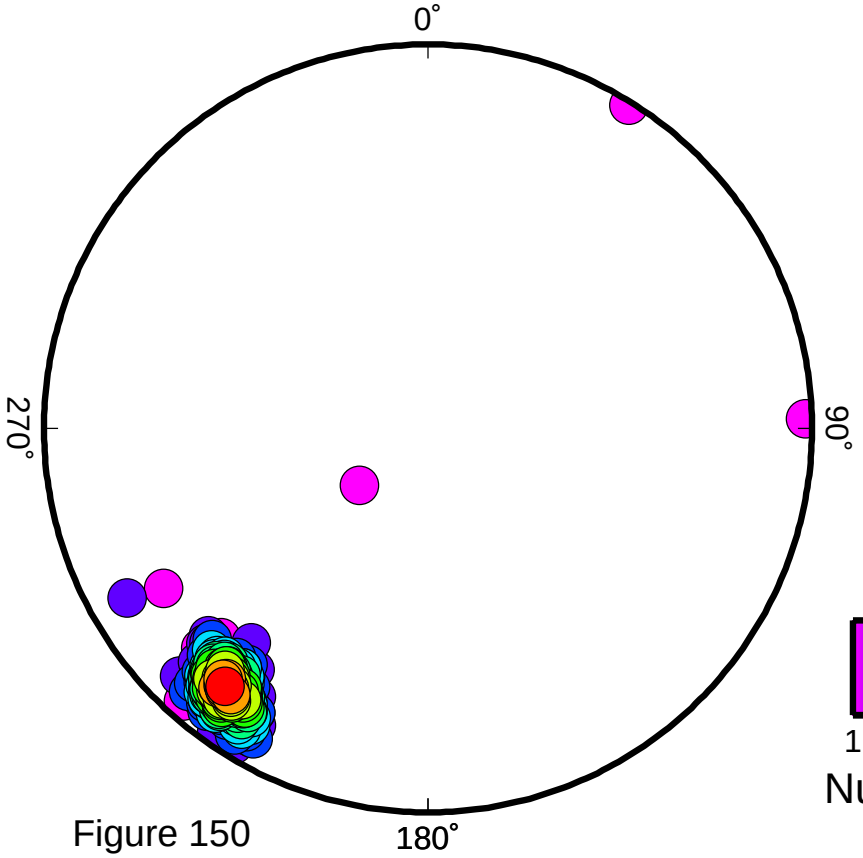

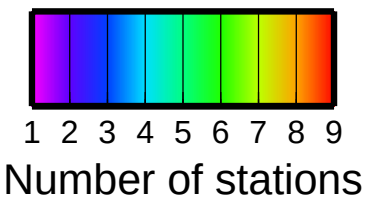

Figure 150

EVT17

T-axes from deviatoric inversions

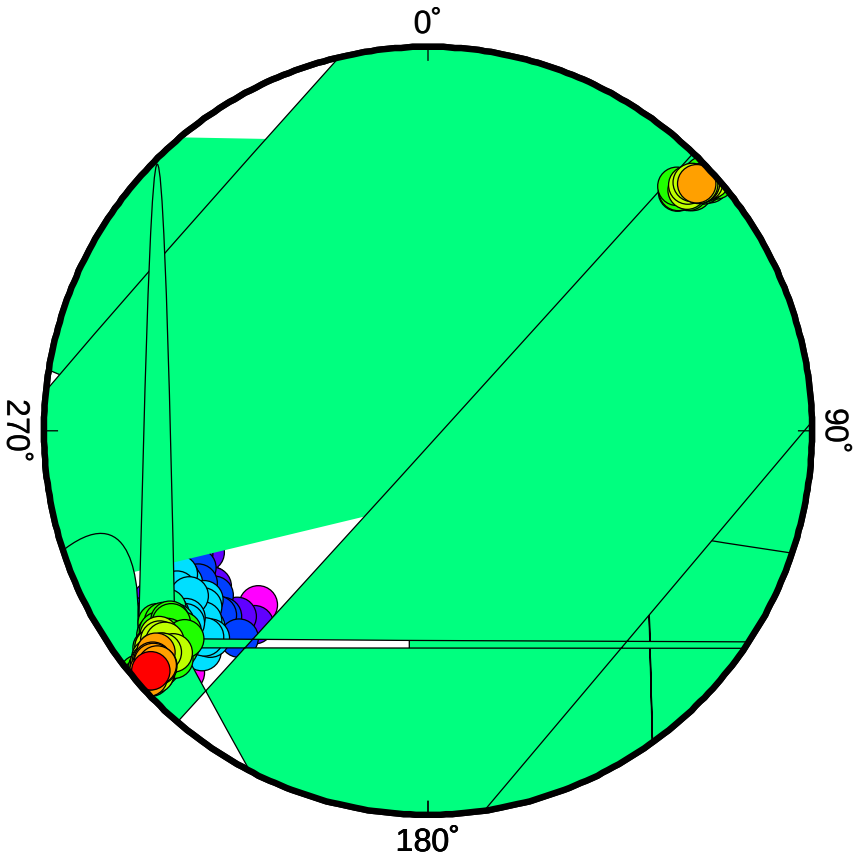

T-axes from full moment tensor inversions

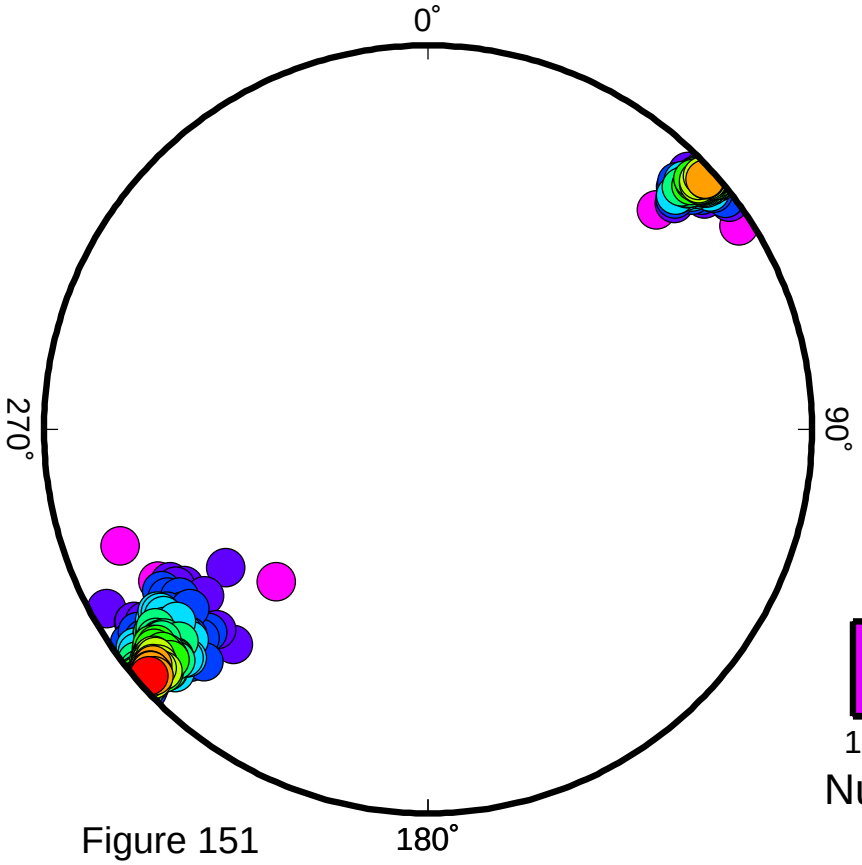

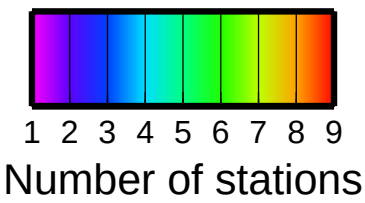

Figure 151

EVT18

T-axes from deviatoric inversions

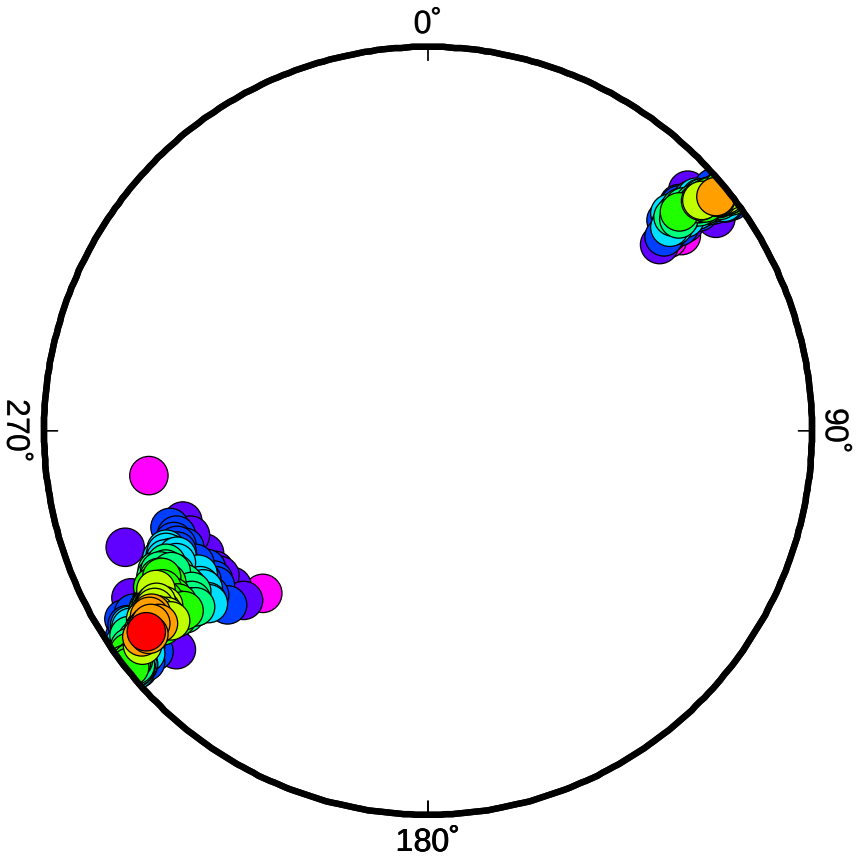

T-axes from full moment tensor inversions

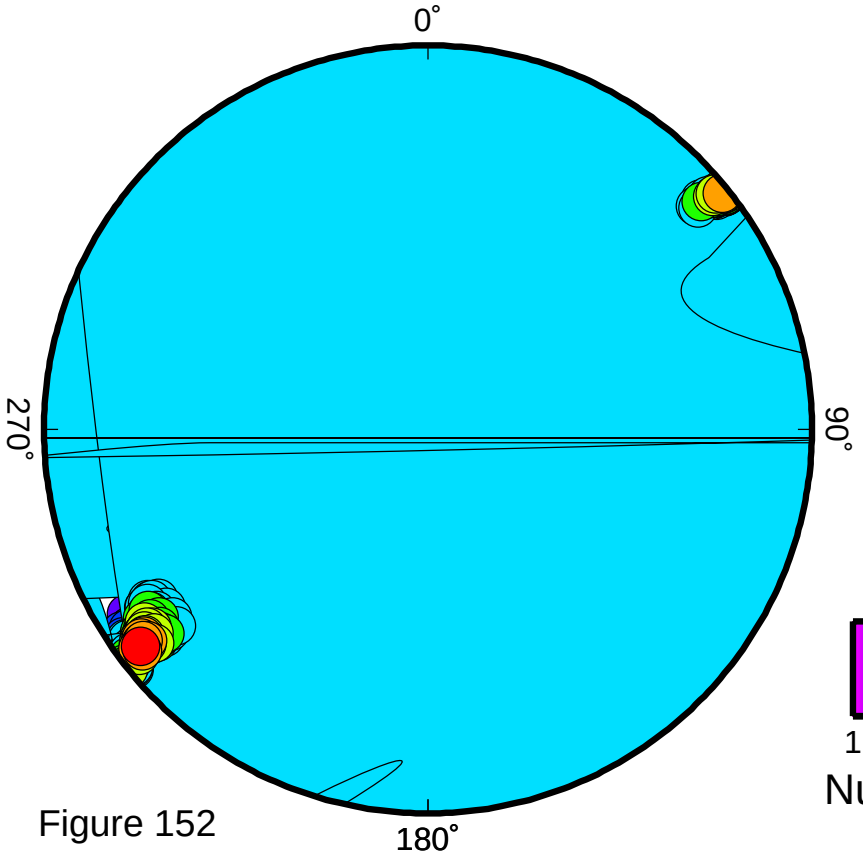

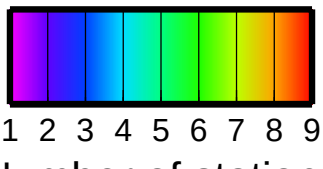

Figure 152

EVT1

T-axes from deviatoric inversions

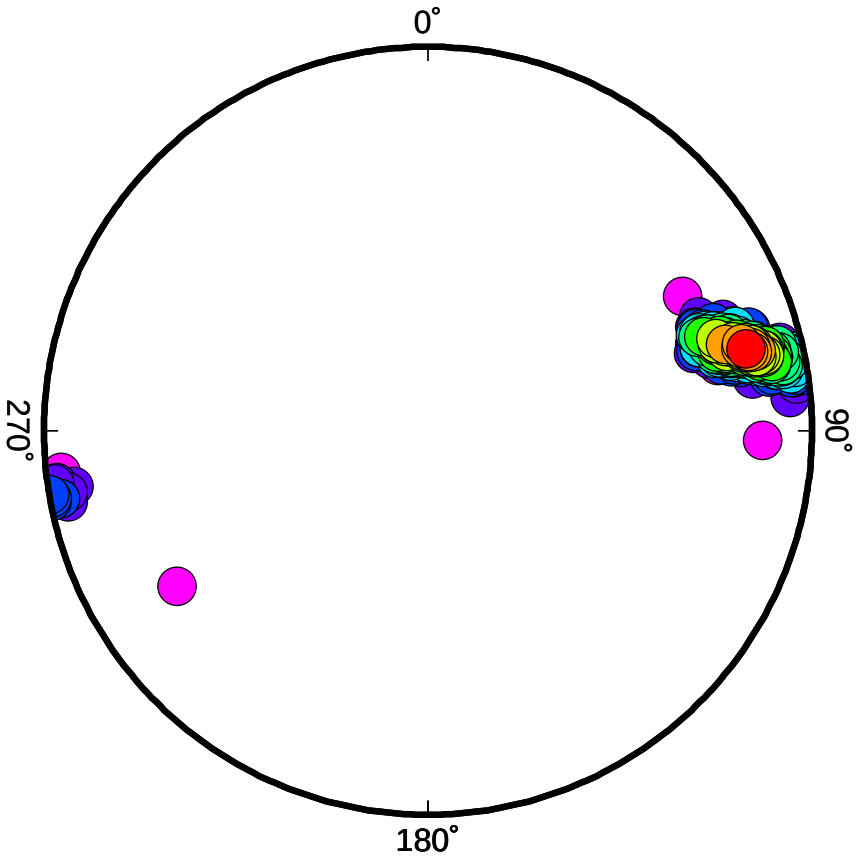

T-axes from full moment tensor inversions

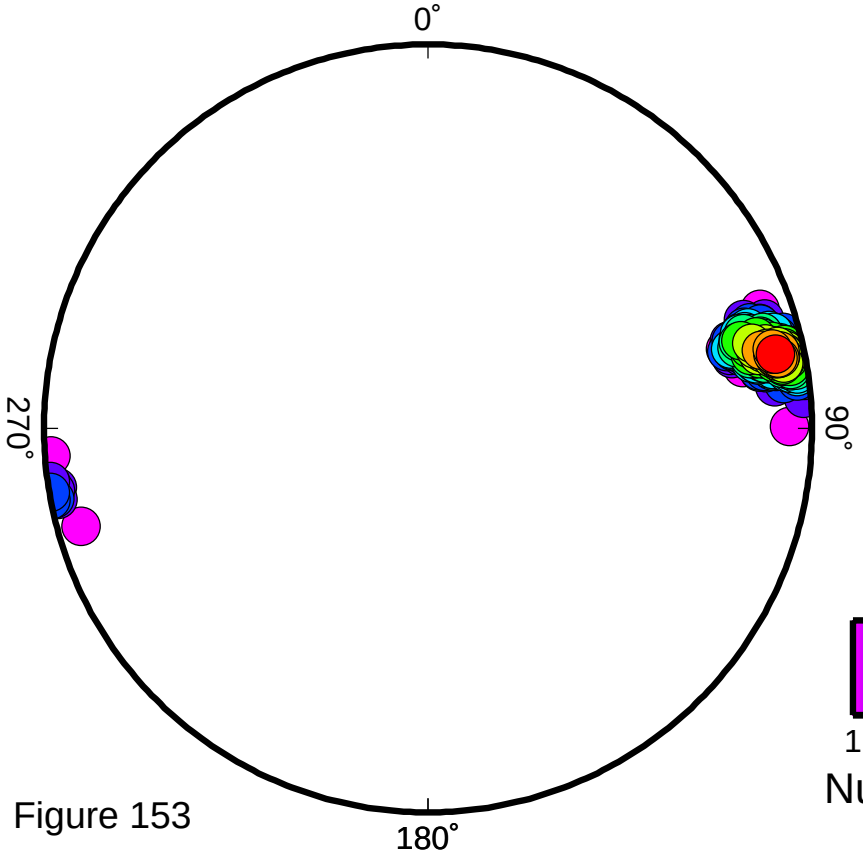

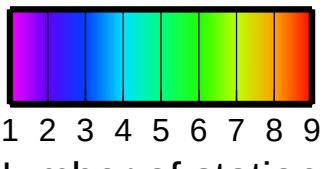

Figure 153

EVT2

T-axes from deviatoric inversions

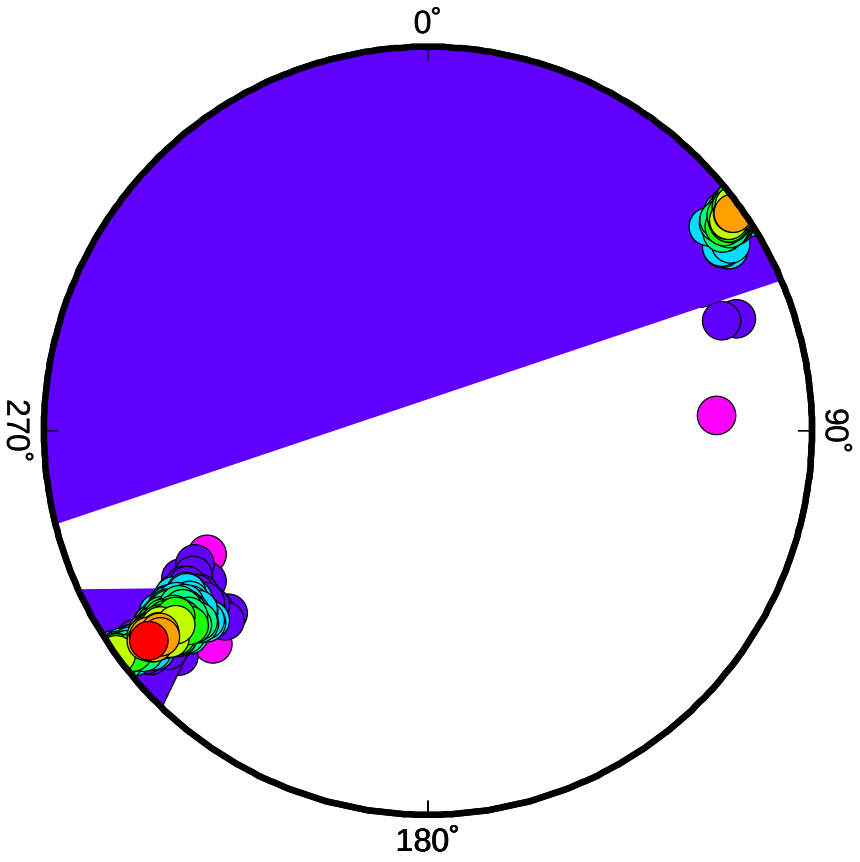

T-axes from full moment tensor inversions

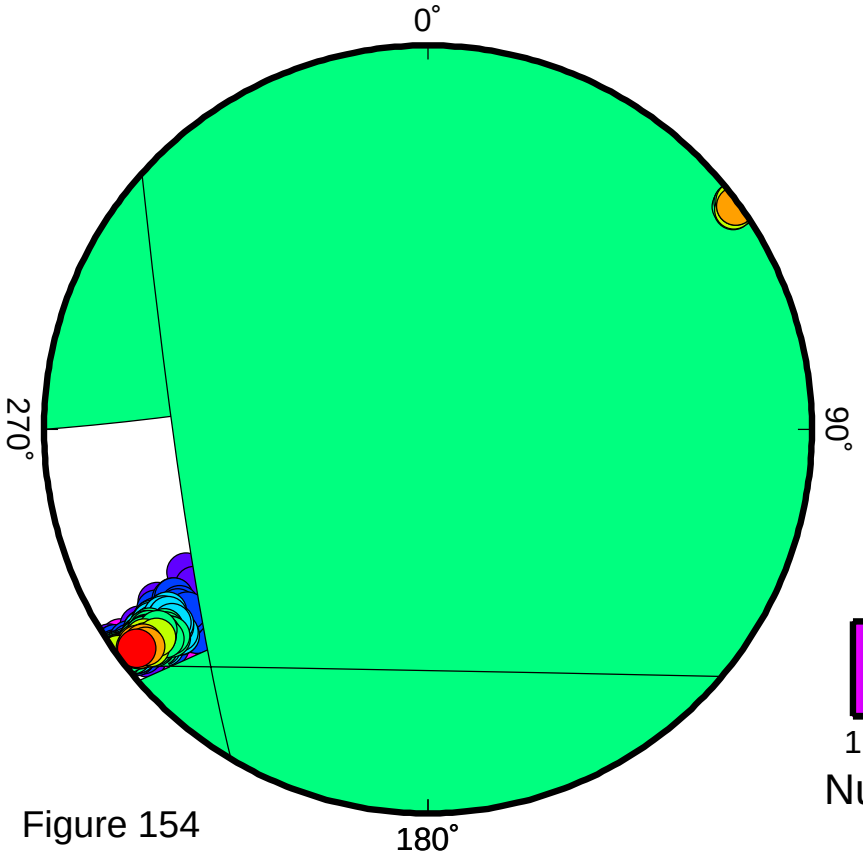

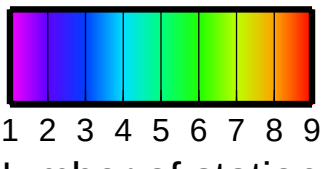

Figure 154

EVT3

T-axes from deviatoric inversions

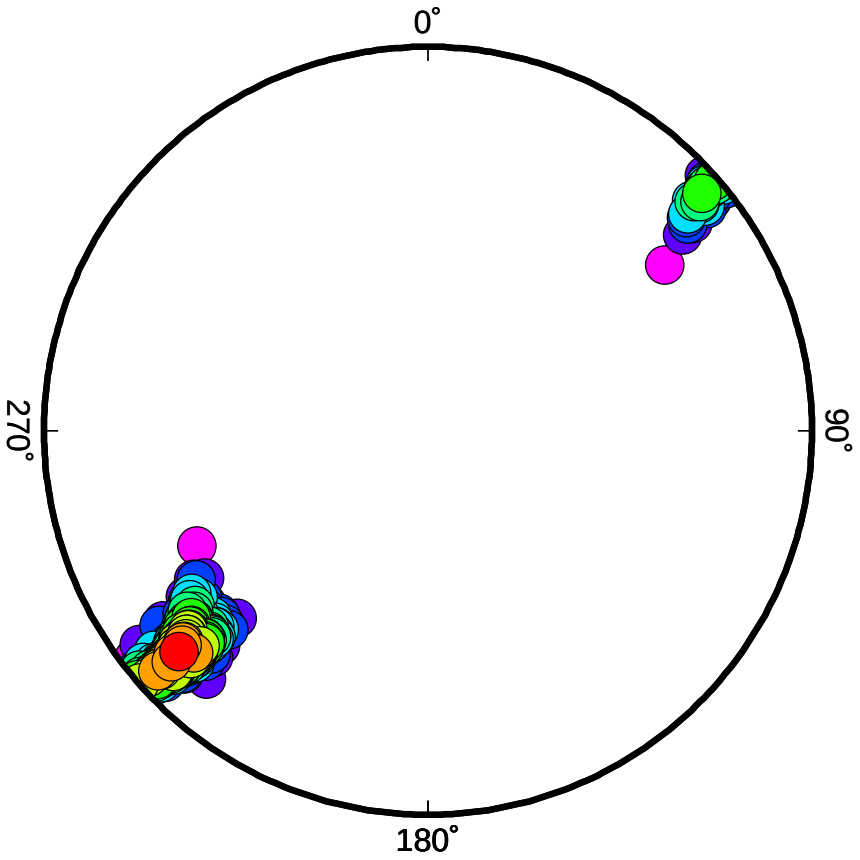

T-axes from full moment tensor inversions

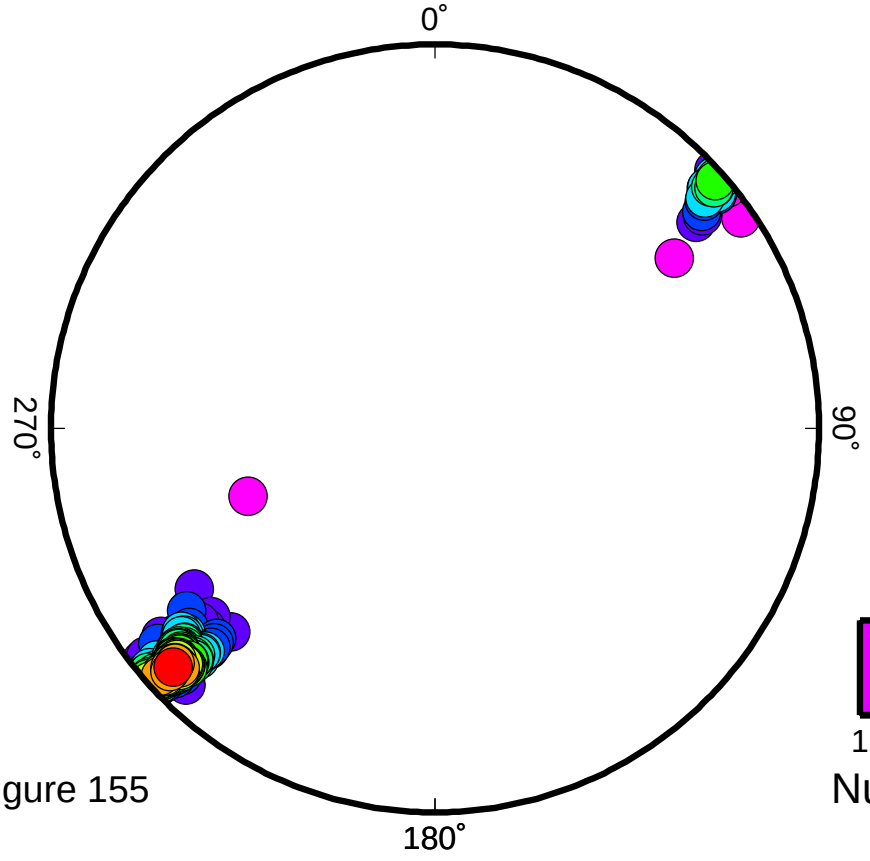

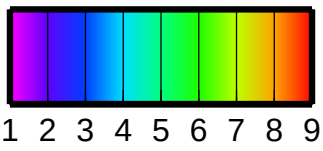

Number of stations

Figure 155

EVT4

T-axes from deviatoric inversions

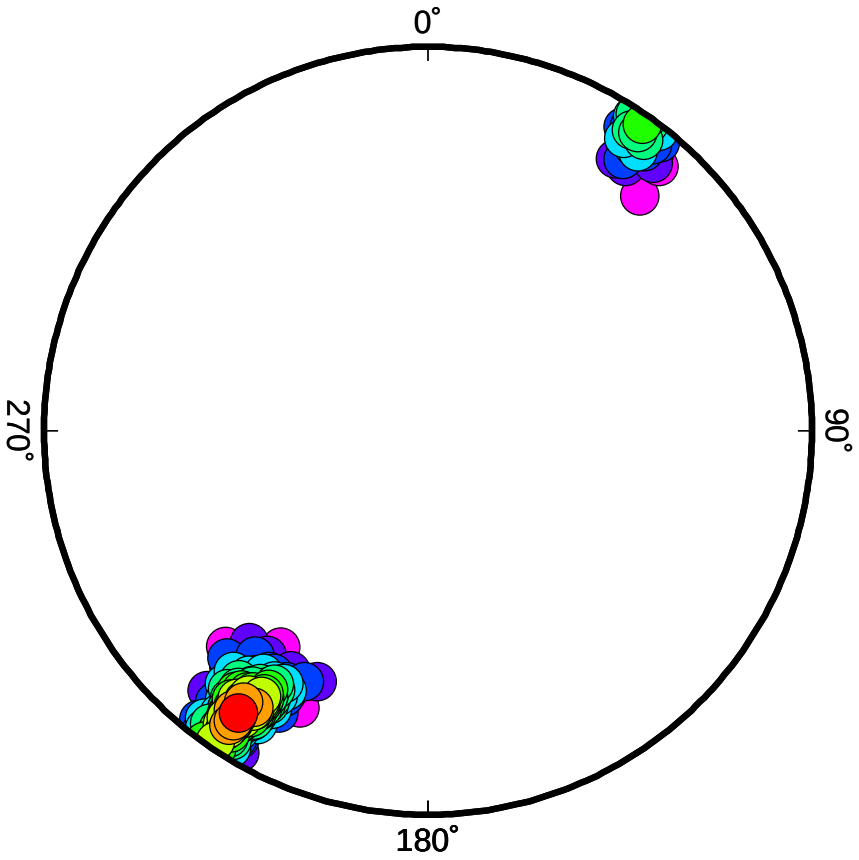

T-axes from full moment tensor inversions

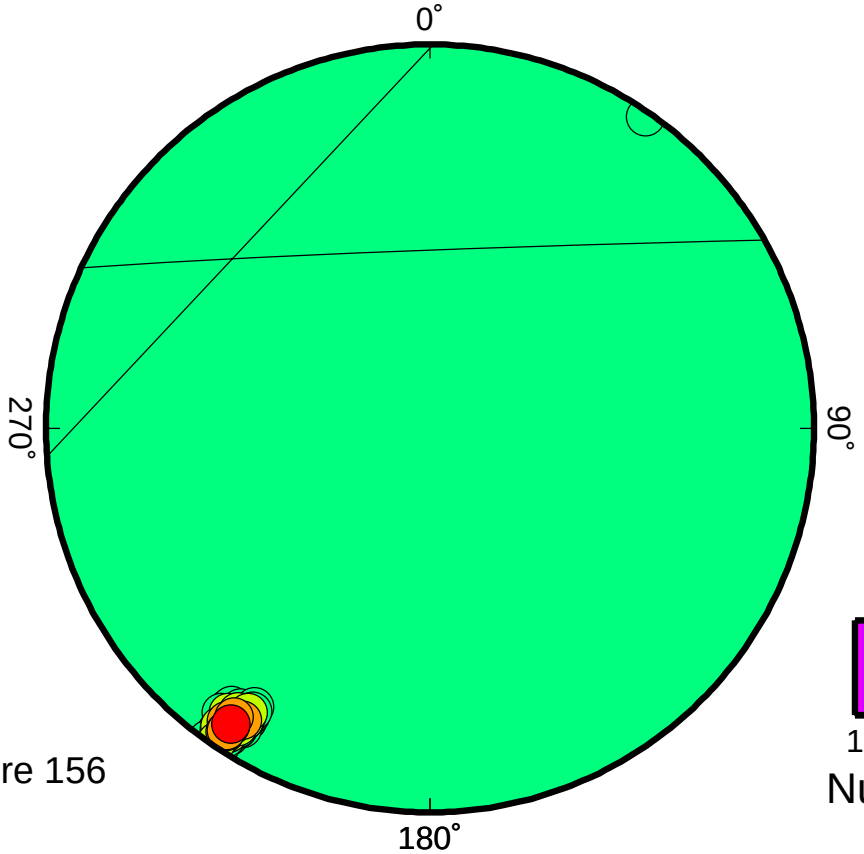

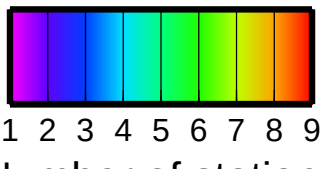

Figure 156

EVT5

T-axes from deviatoric inversions

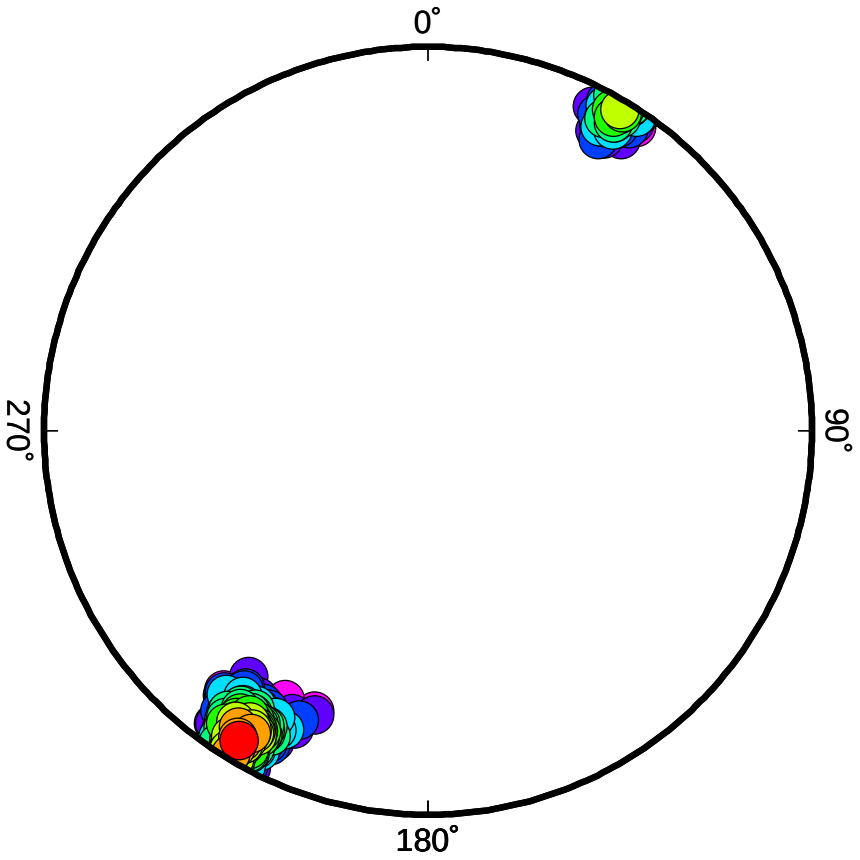

T-axes from full moment tensor inversions

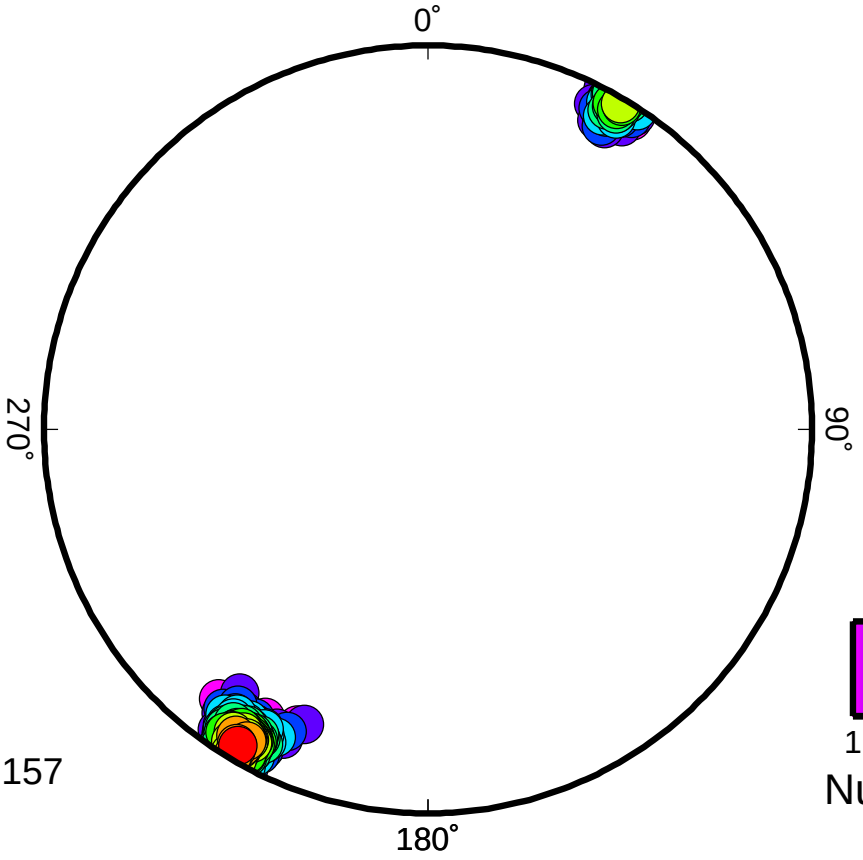

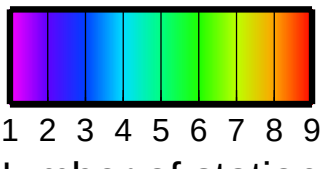

Figure 157

EVT6

T-axes from deviatoric inversions

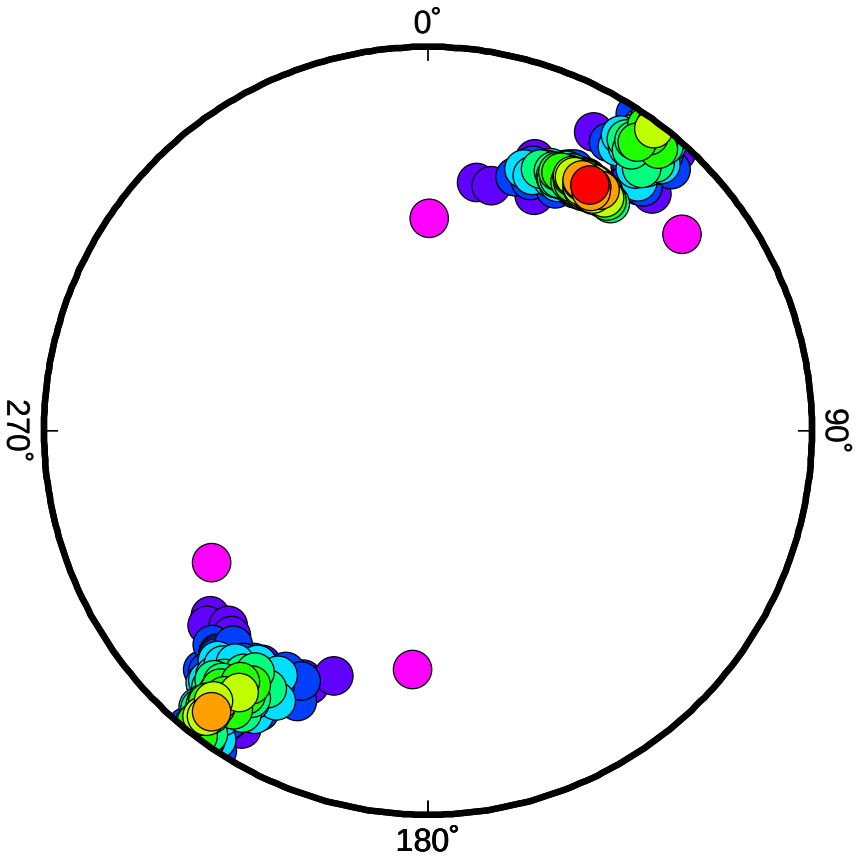

T-axes from full moment tensor inversions

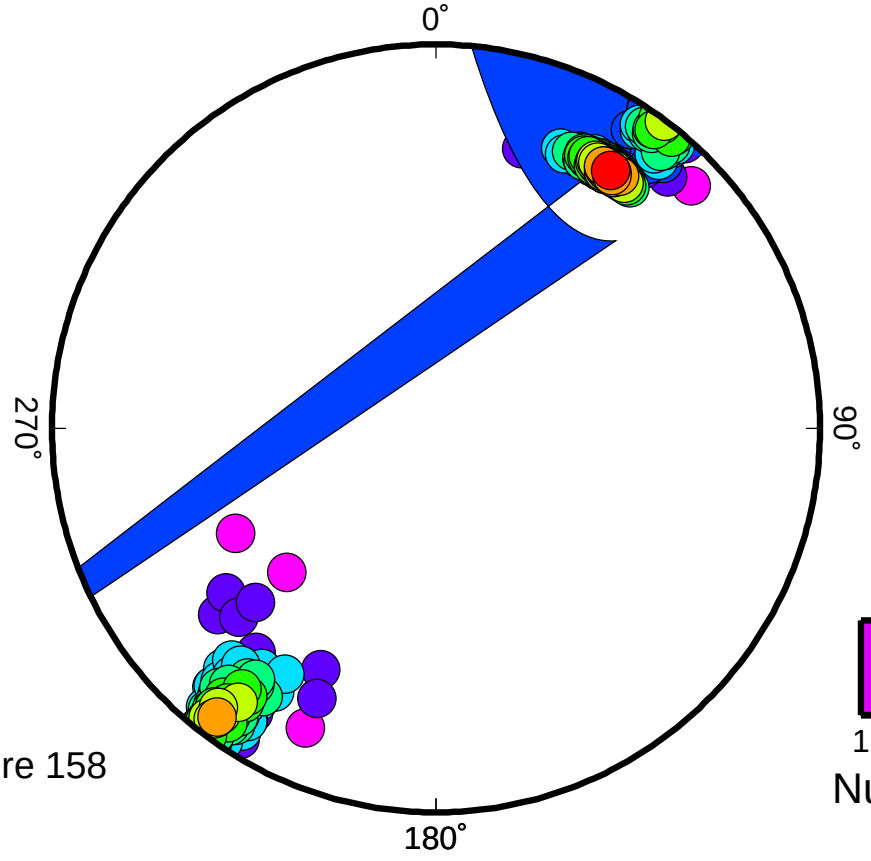

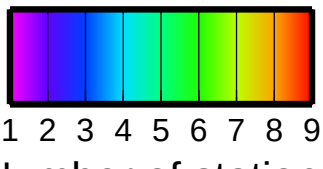

Figure 158

EVT7

T-axes from deviatoric inversions

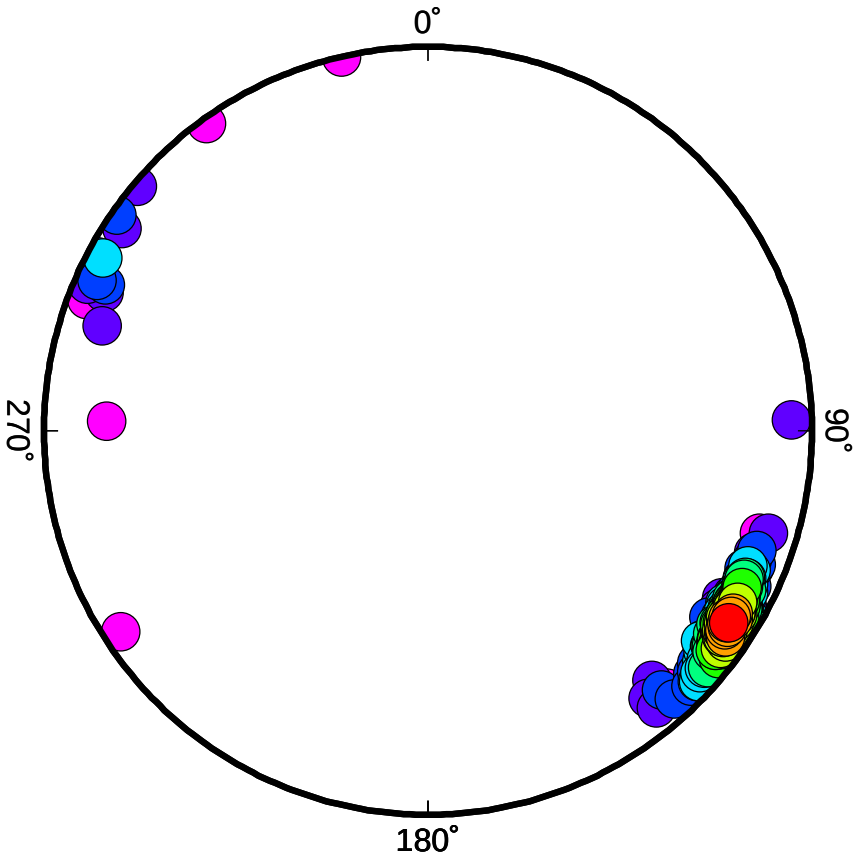

T-axes from full moment tensor inversions

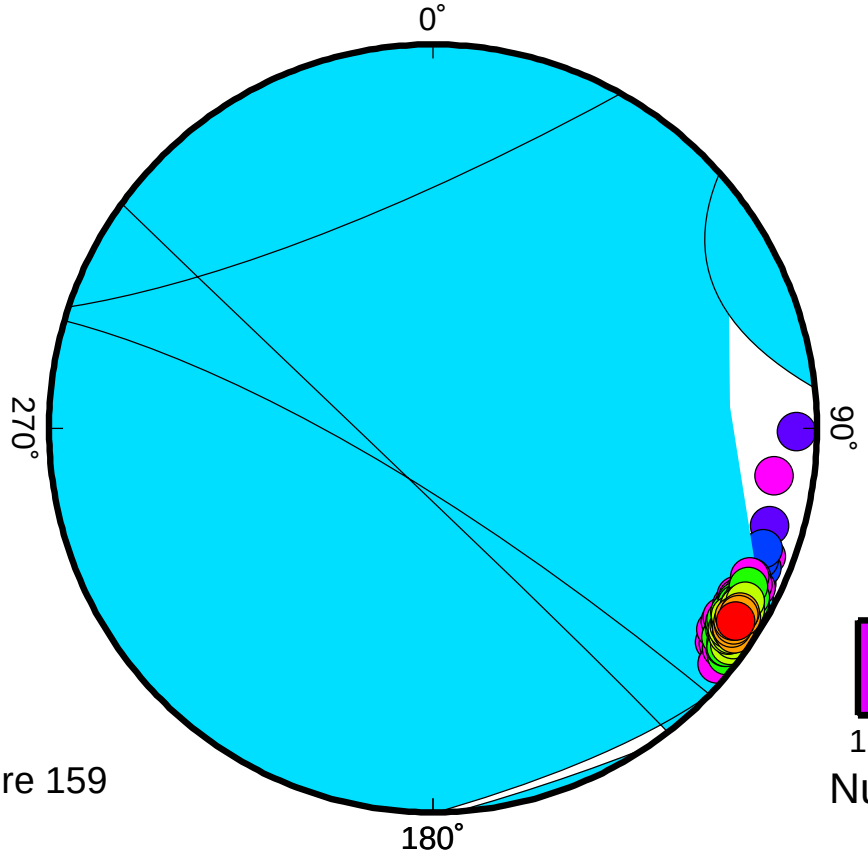

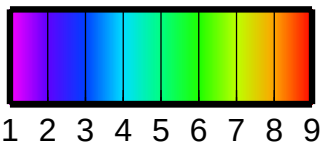

Figure 159

EVT8

T-axes from deviatoric inversions

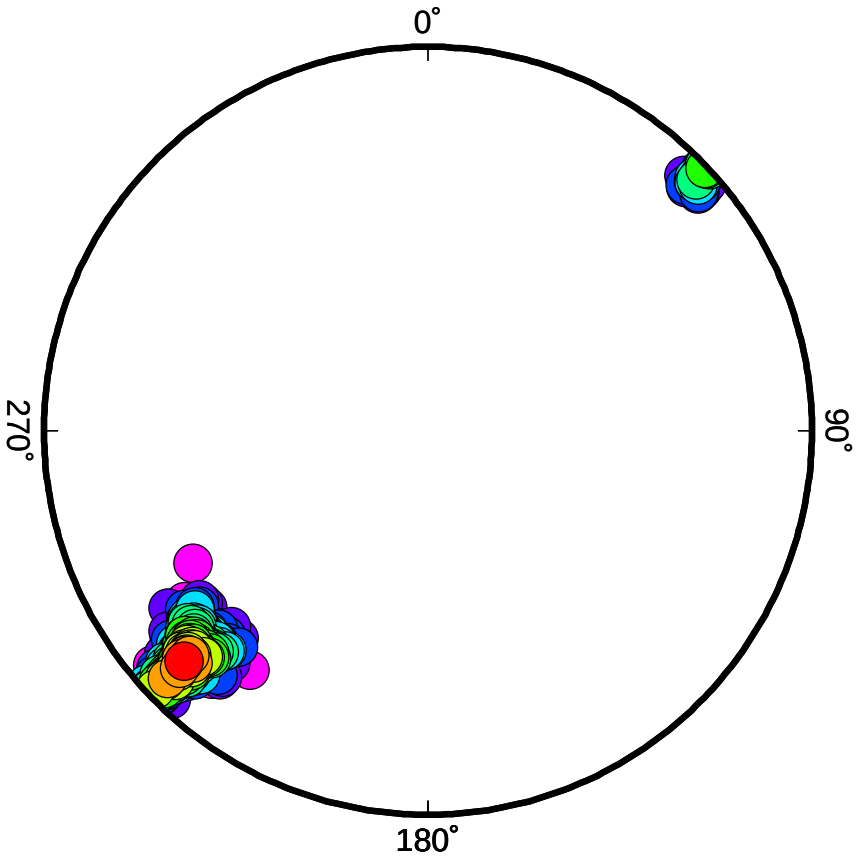

T-axes from full moment tensor inversions

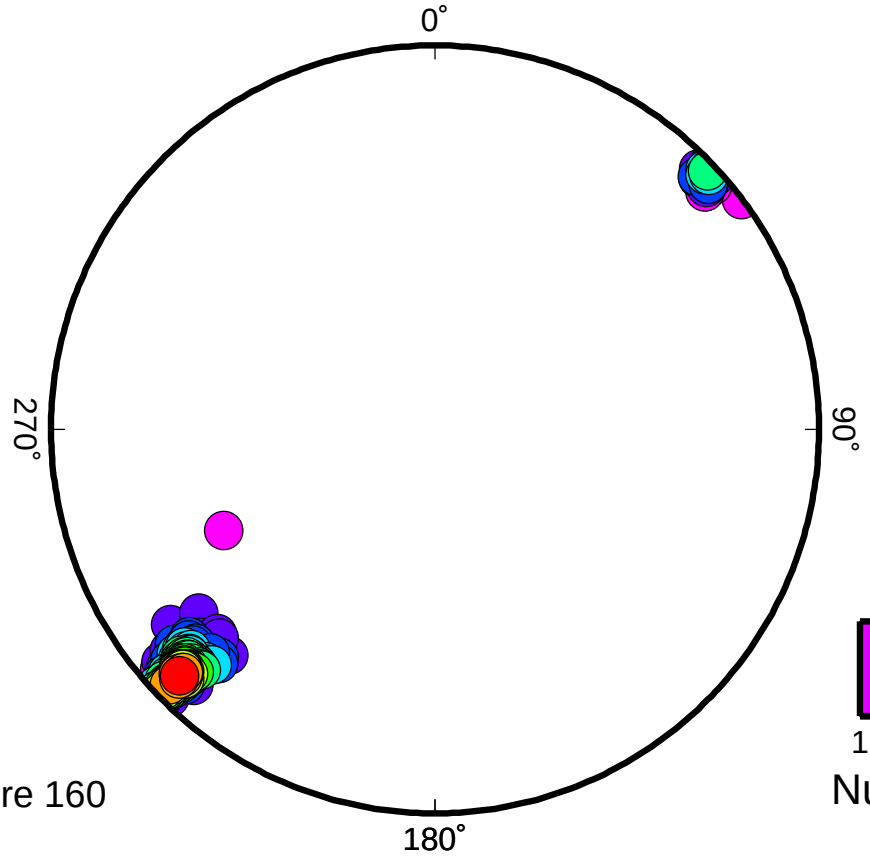

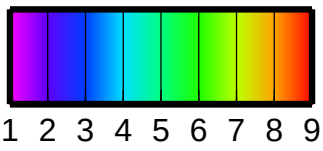

Number of stations

Figure 160

EVT9

T-axes from deviatoric inversions

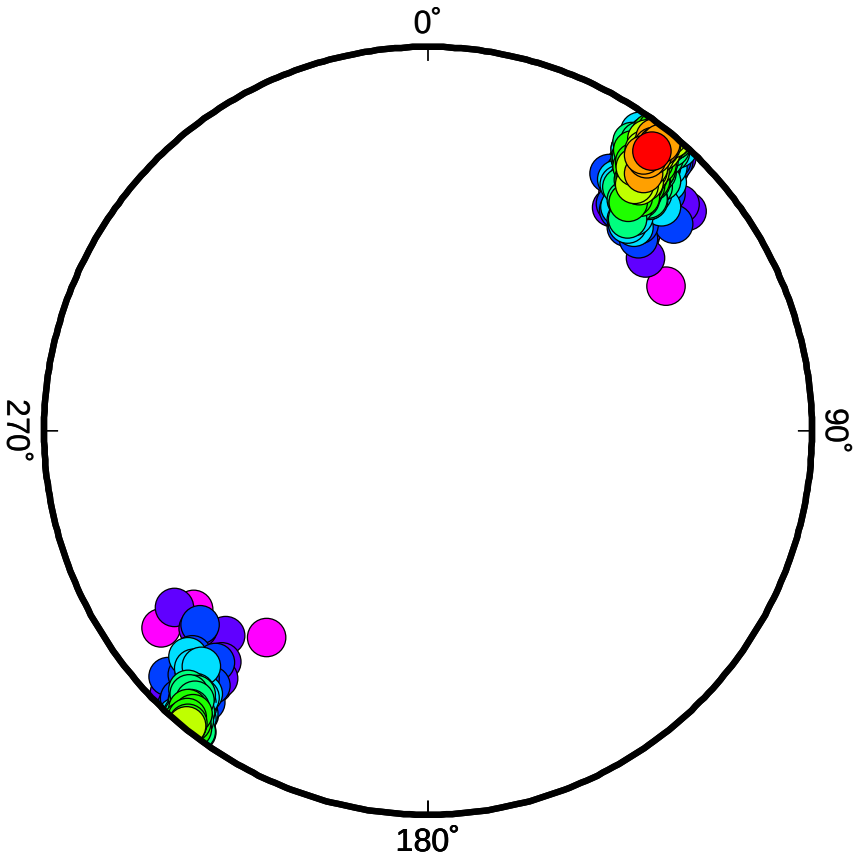

T-axes from full moment tensor inversions

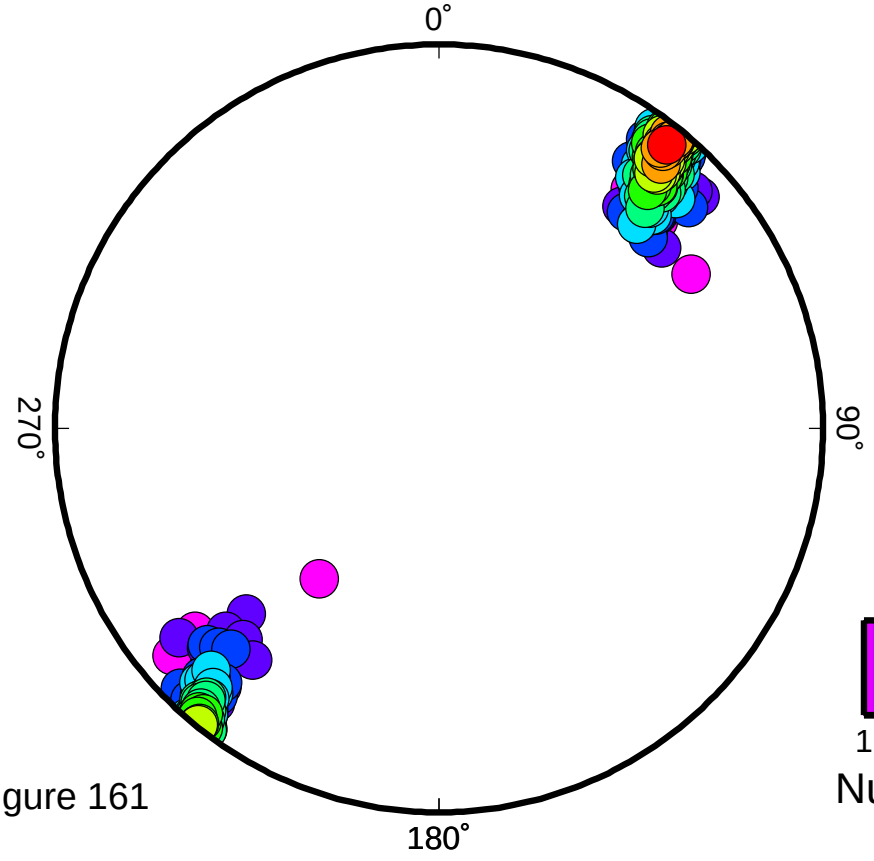

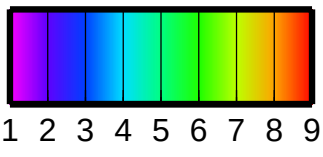

Number of stations

Figure 161

EVT10

T-axes from deviatoric inversions

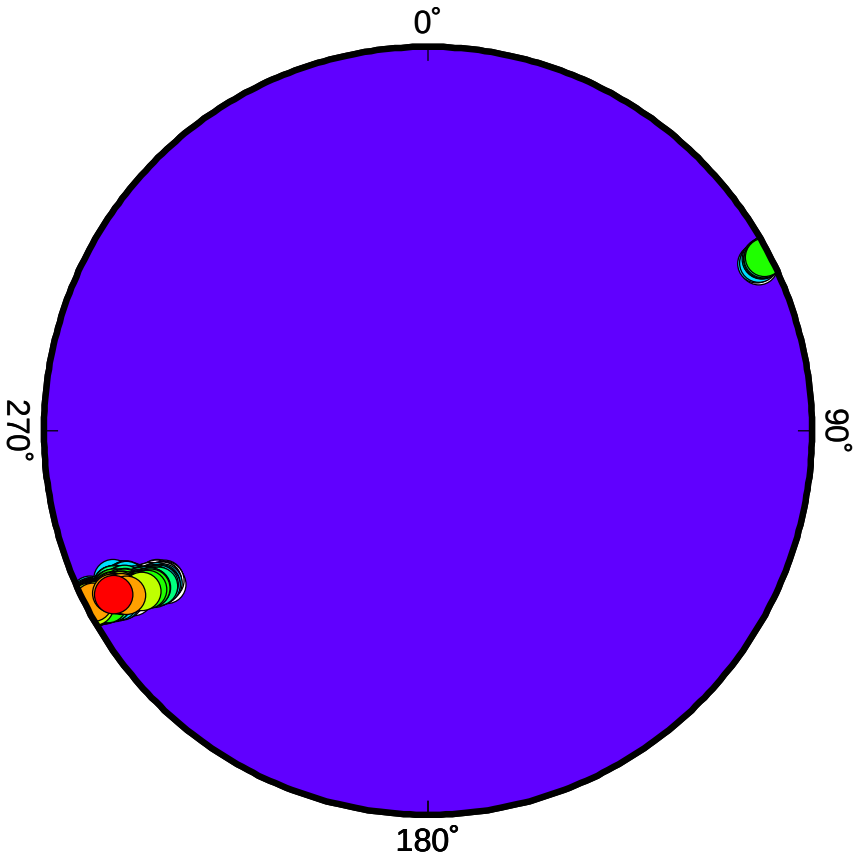

T-axes from full moment tensor inversions

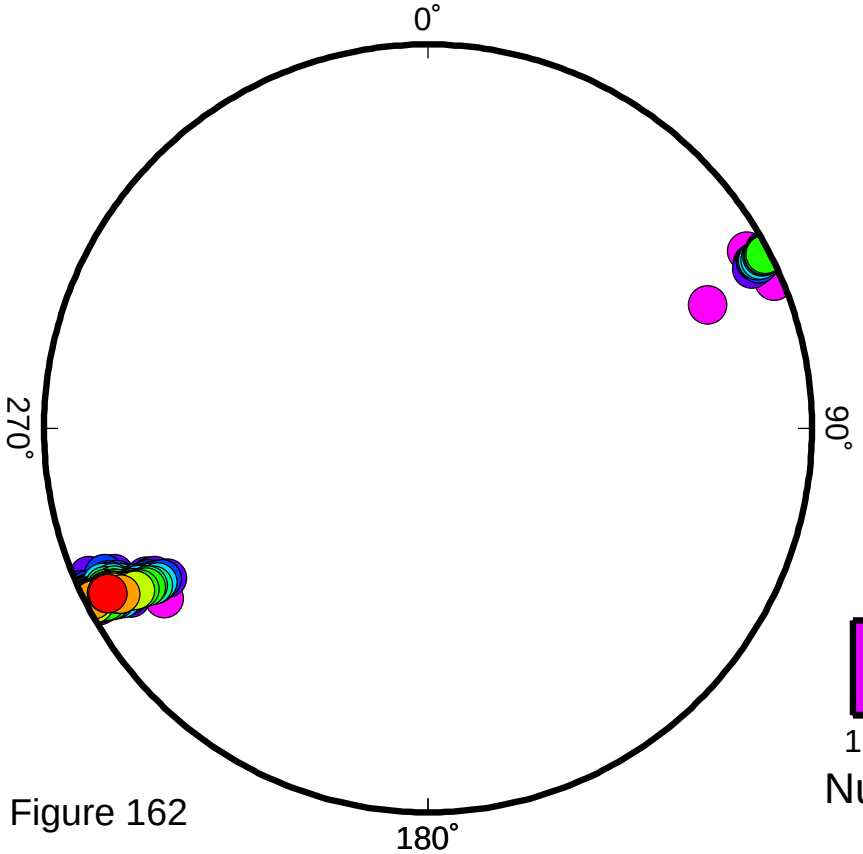

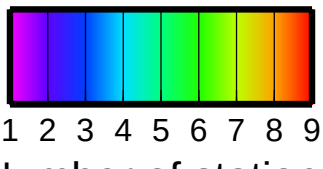

Figure 162

EVT11

T-axes from deviatoric inversions

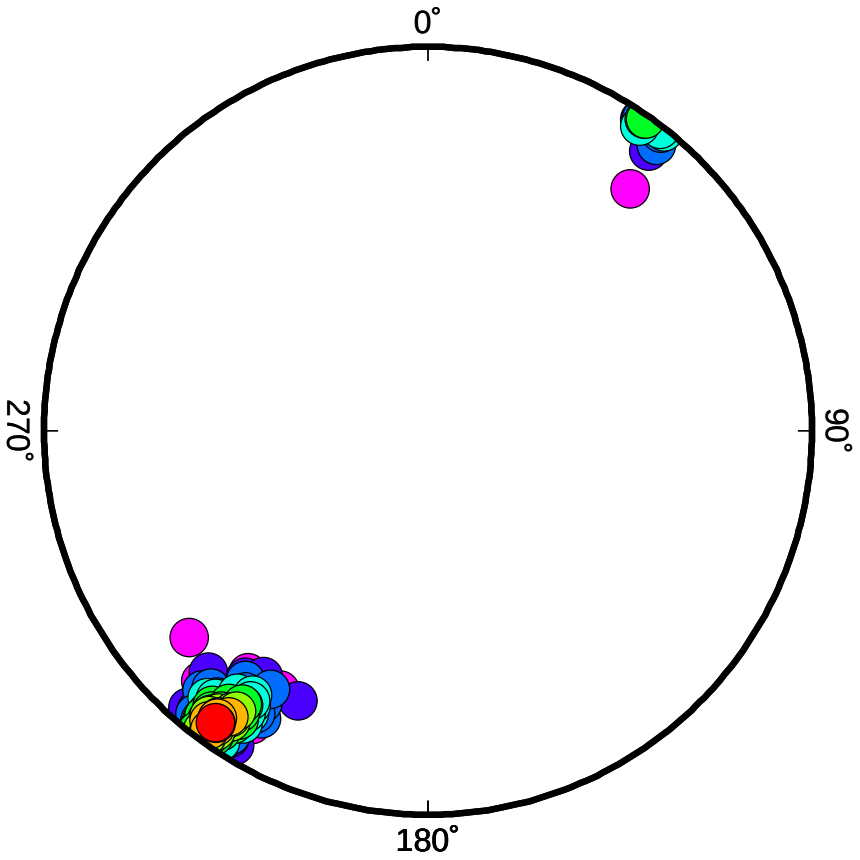

T-axes from full moment tensor inversions

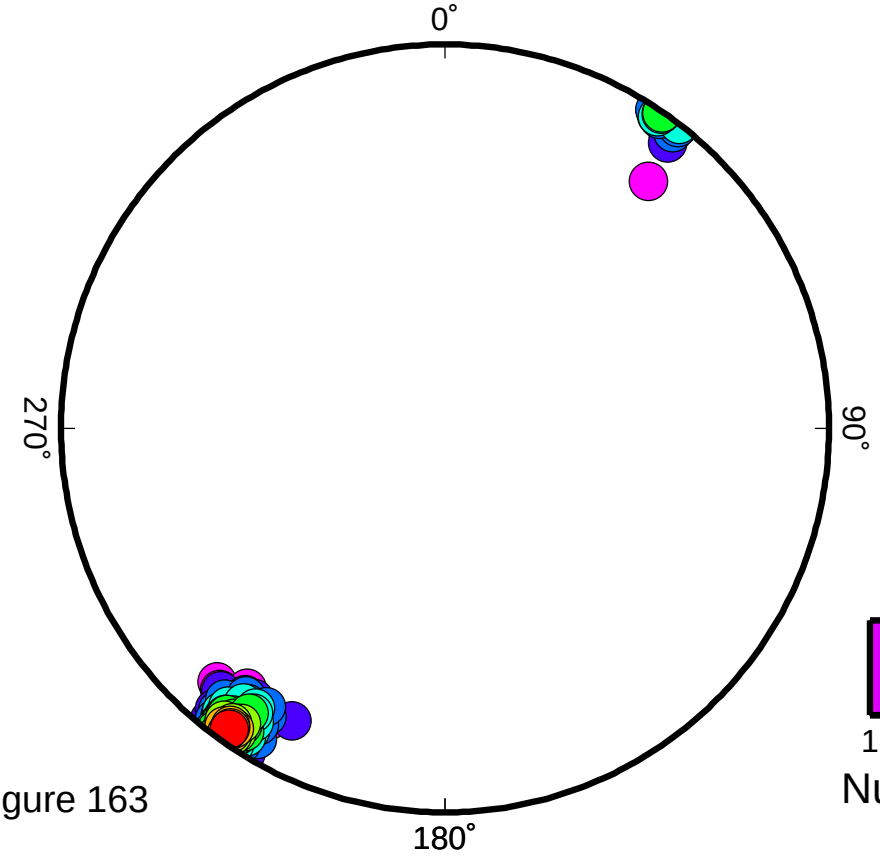

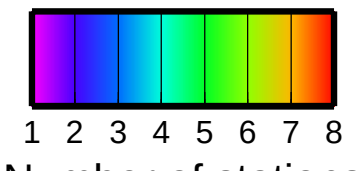

Figure 163

EVT12

T-axes from deviatoric inversions

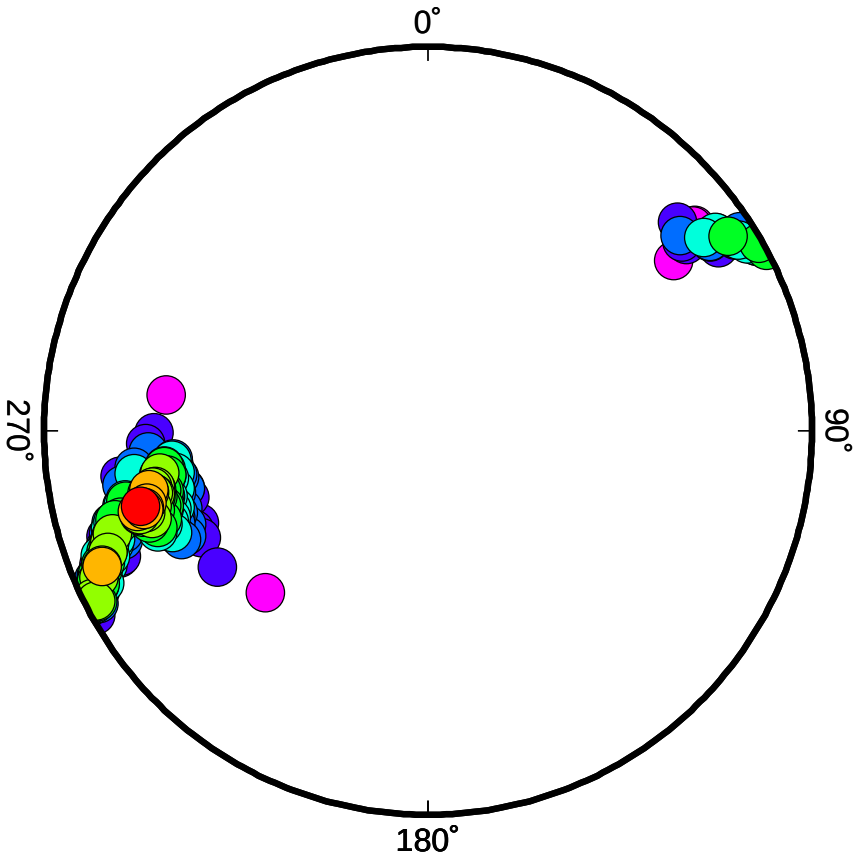

T-axes from full moment tensor inversions

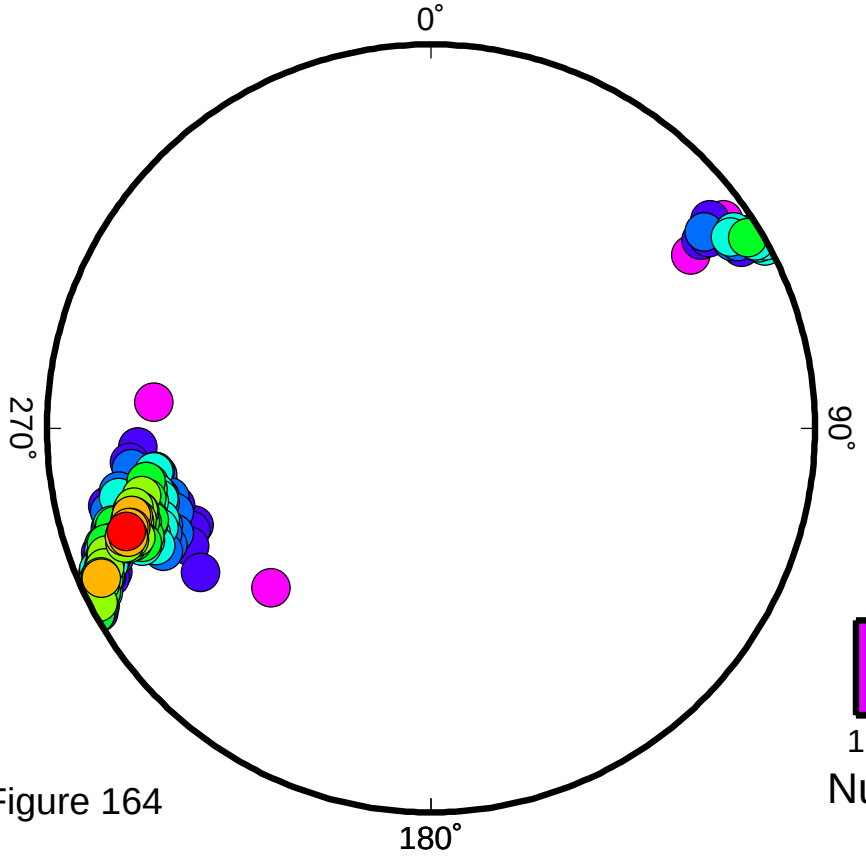

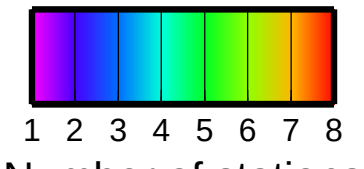

Figure 164

EVT13

T-axes from deviatoric inversions

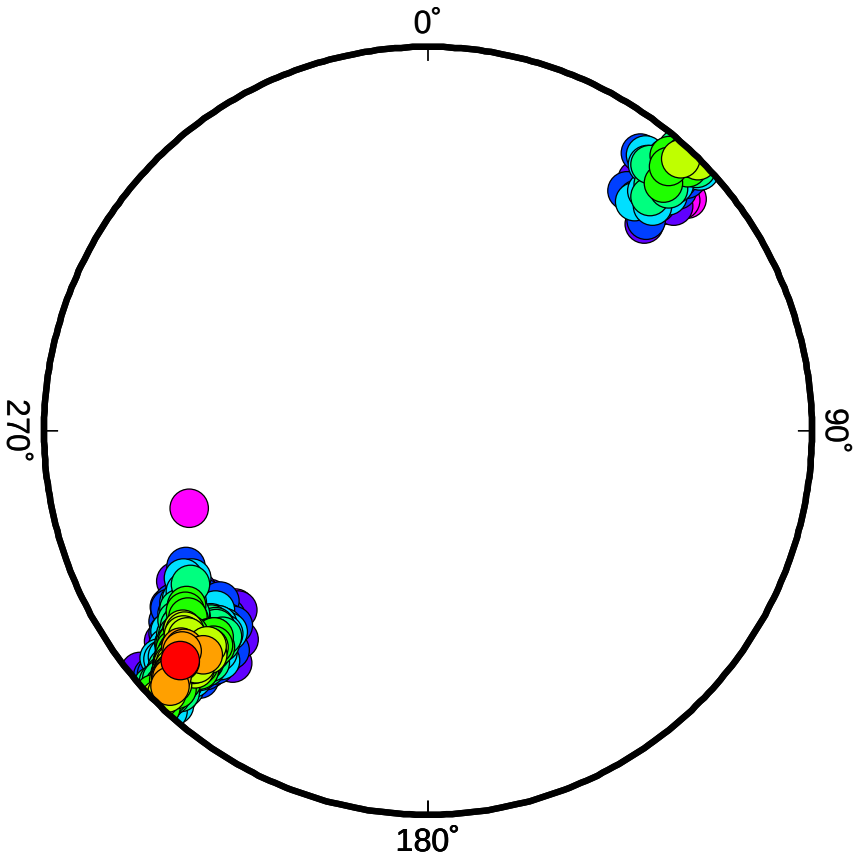

T-axes from full moment tensor inversions

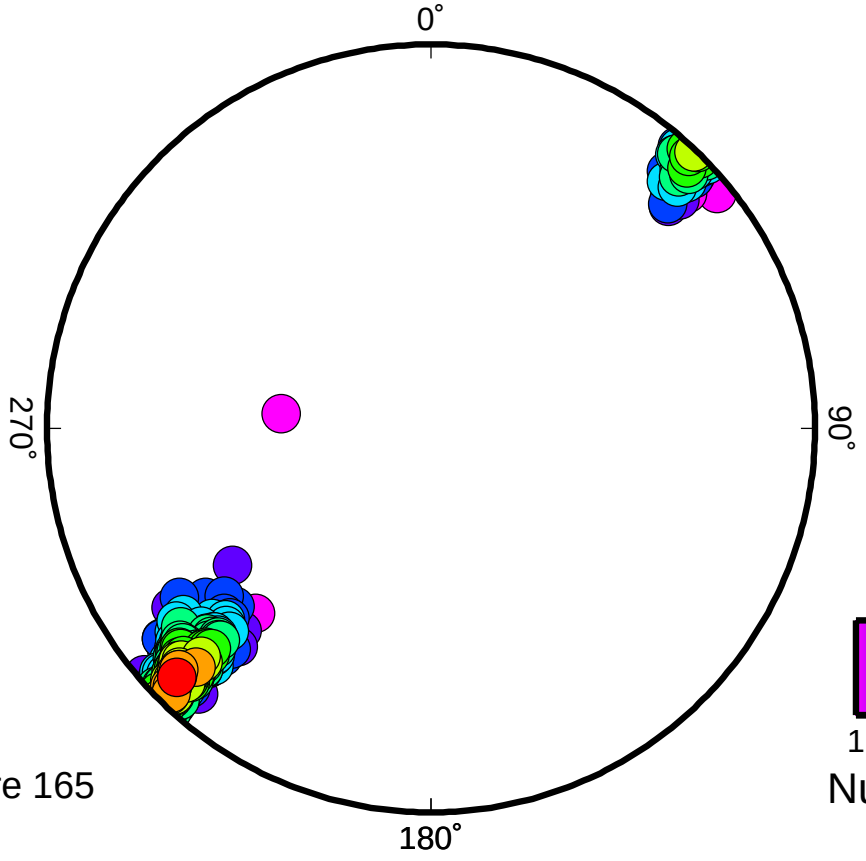

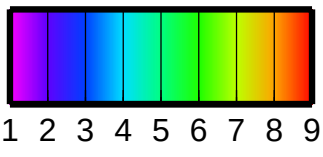

Number of stations

Figure 165

EVT14

T-axes from deviatoric inversions

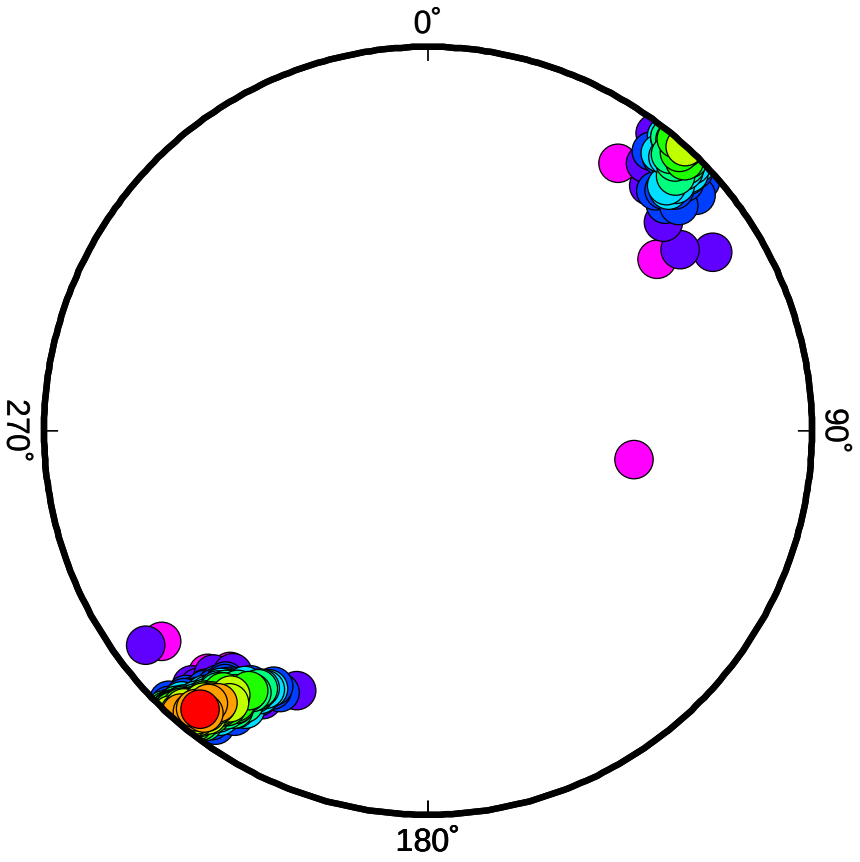

T-axes from full moment tensor inversions

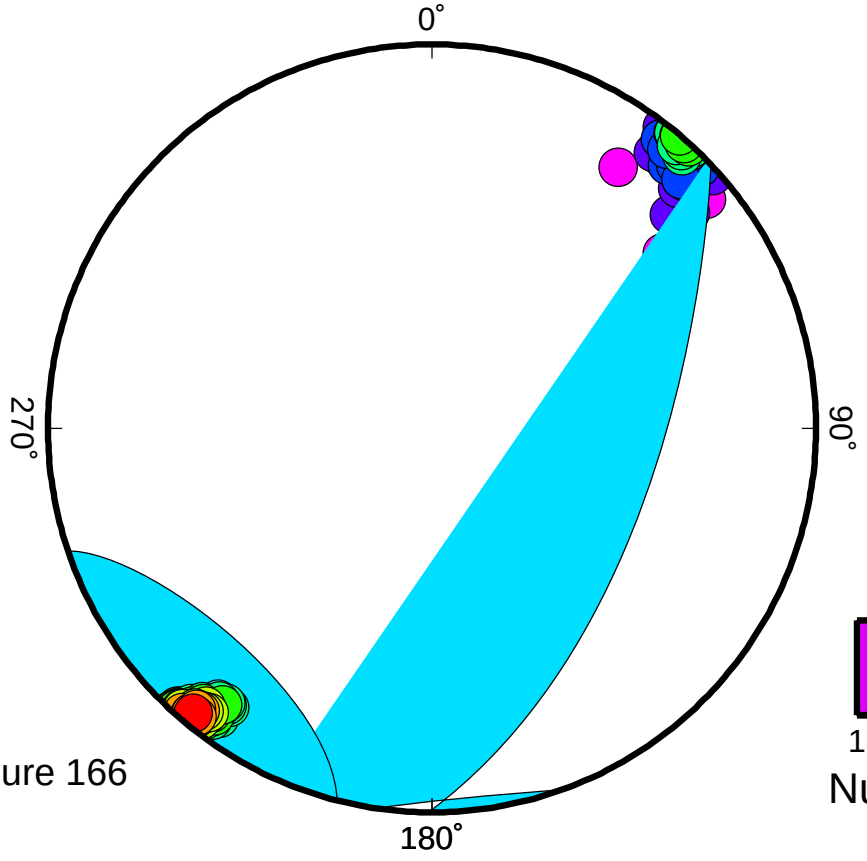

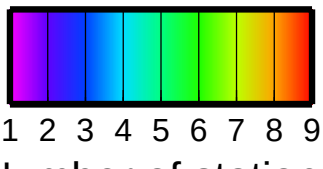

Figure 166

EVT15

T-axes from deviatoric inversions

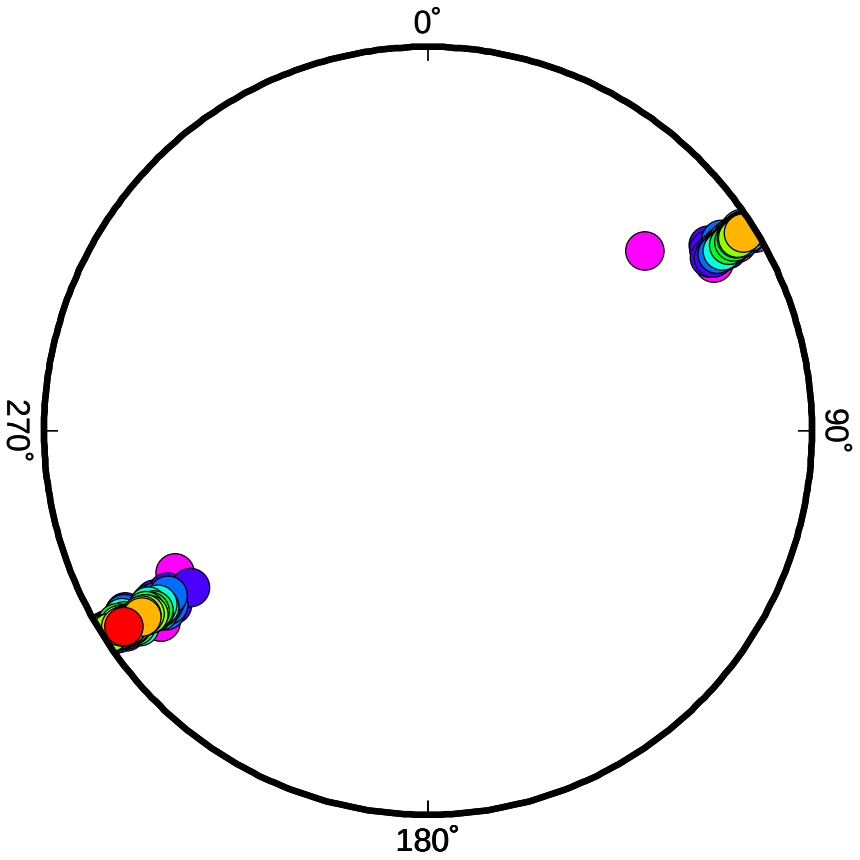

T-axes from full moment tensor inversions

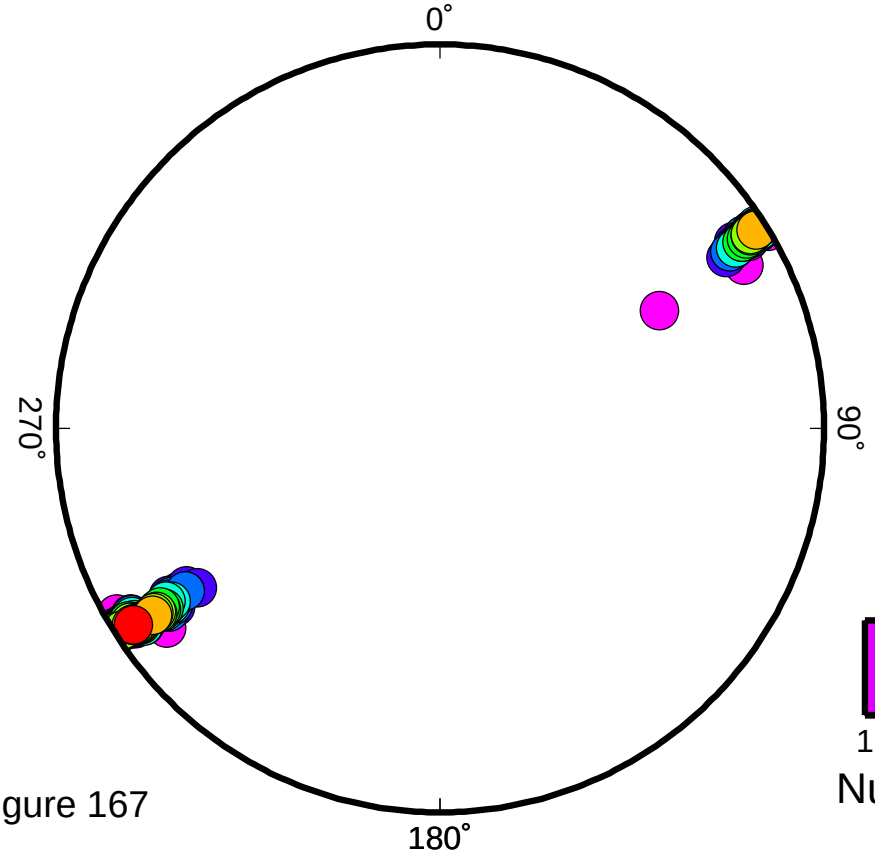

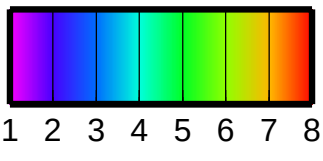

Figure 167

EVT16

T-axes from deviatoric inversions

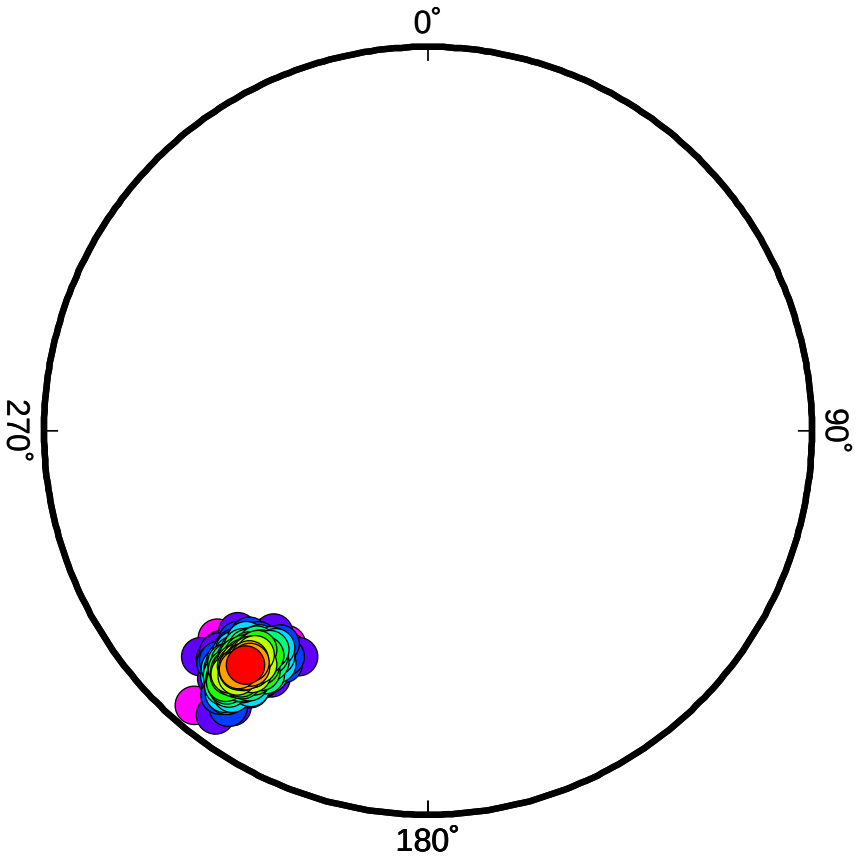

T-axes from full moment tensor inversions

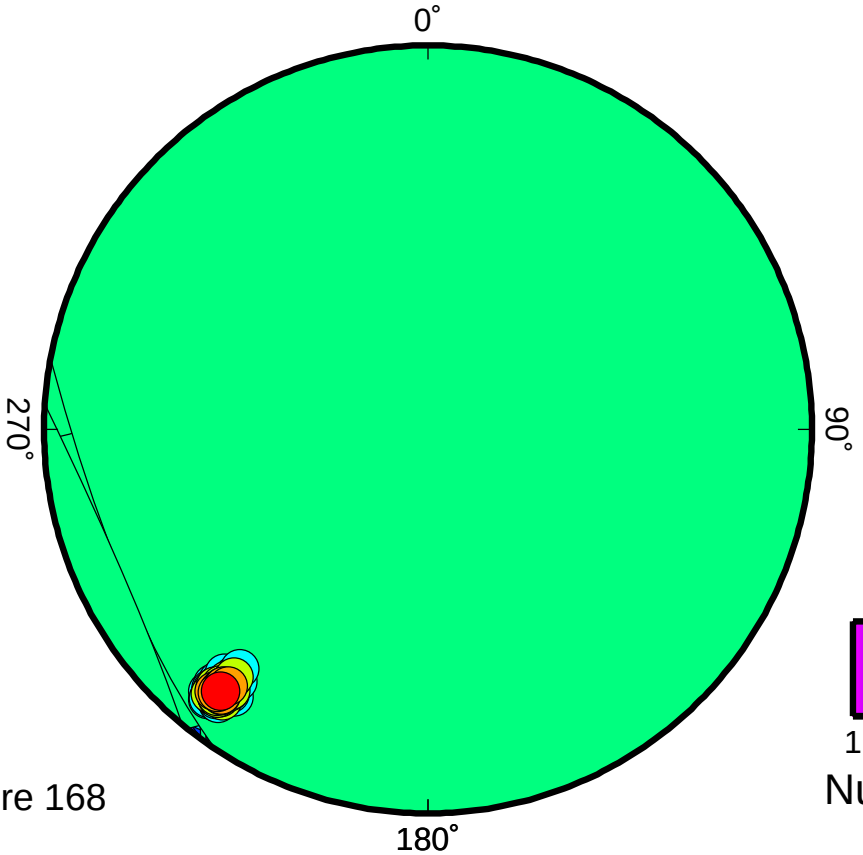

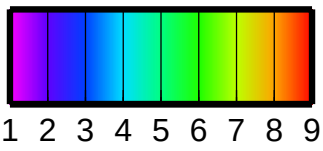

Figure 168

EVT17

T-axes from deviatoric inversions

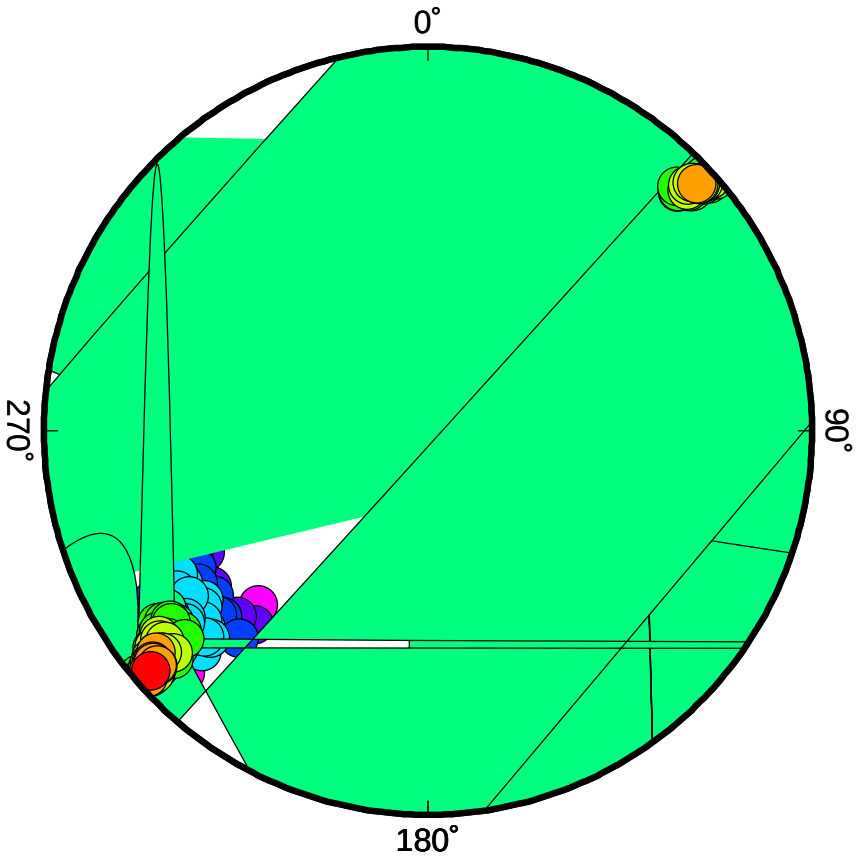

T-axes from full moment tensor inversions

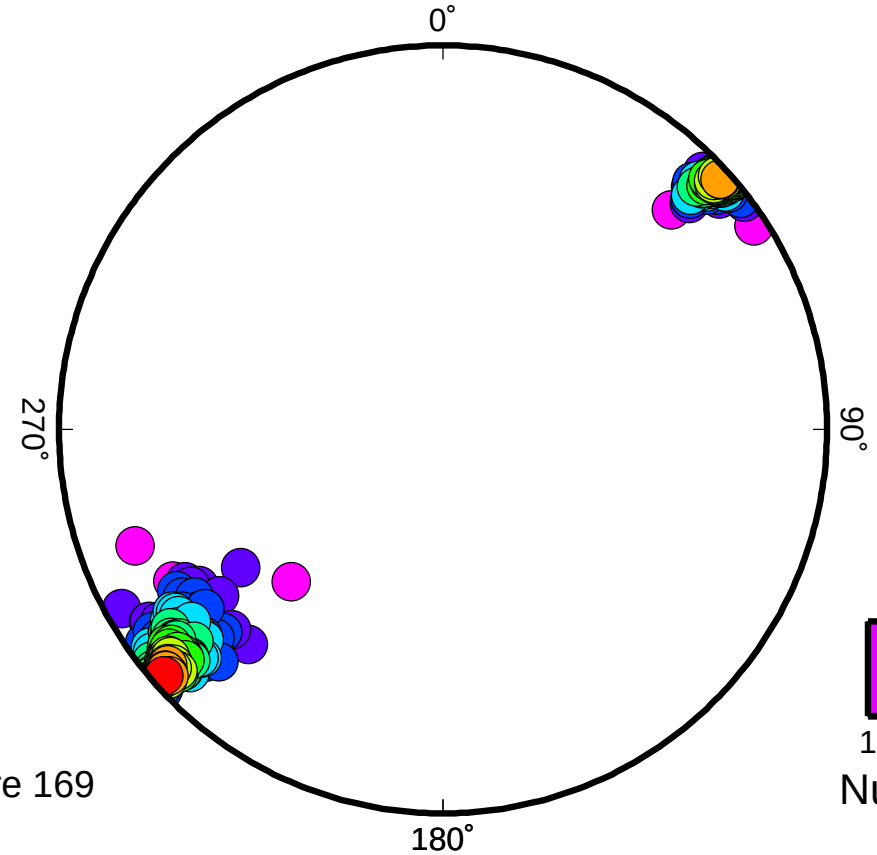

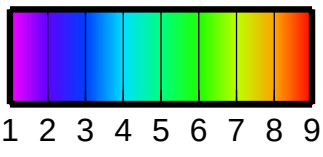

Figure 169

EVT18

T-axes from deviatoric inversions

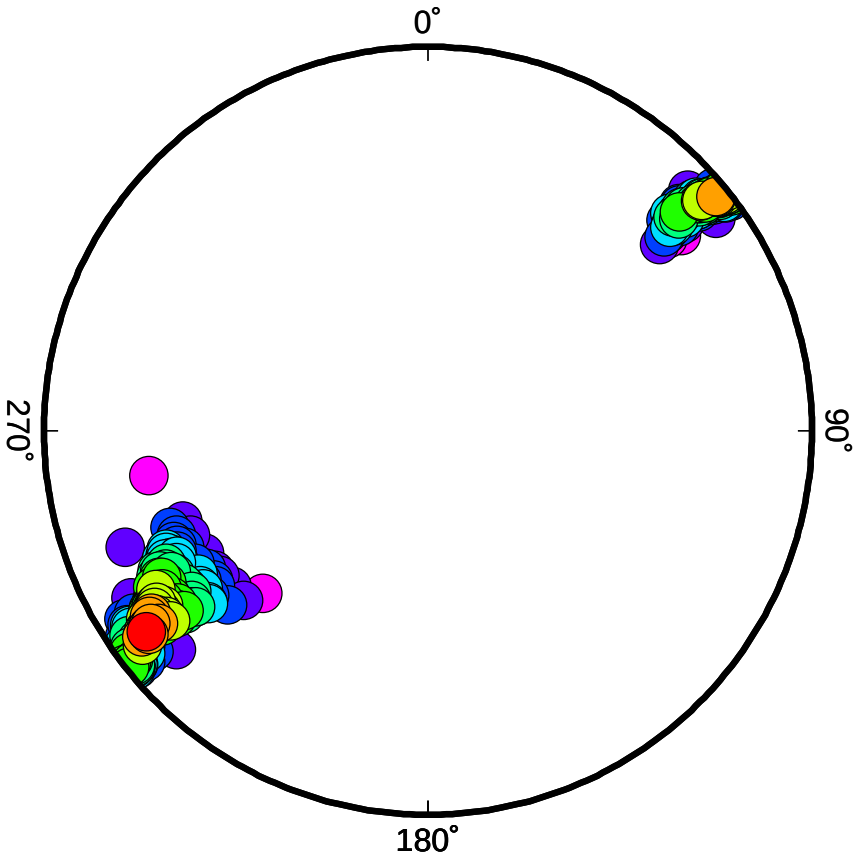

T-axes from full moment tensor inversions

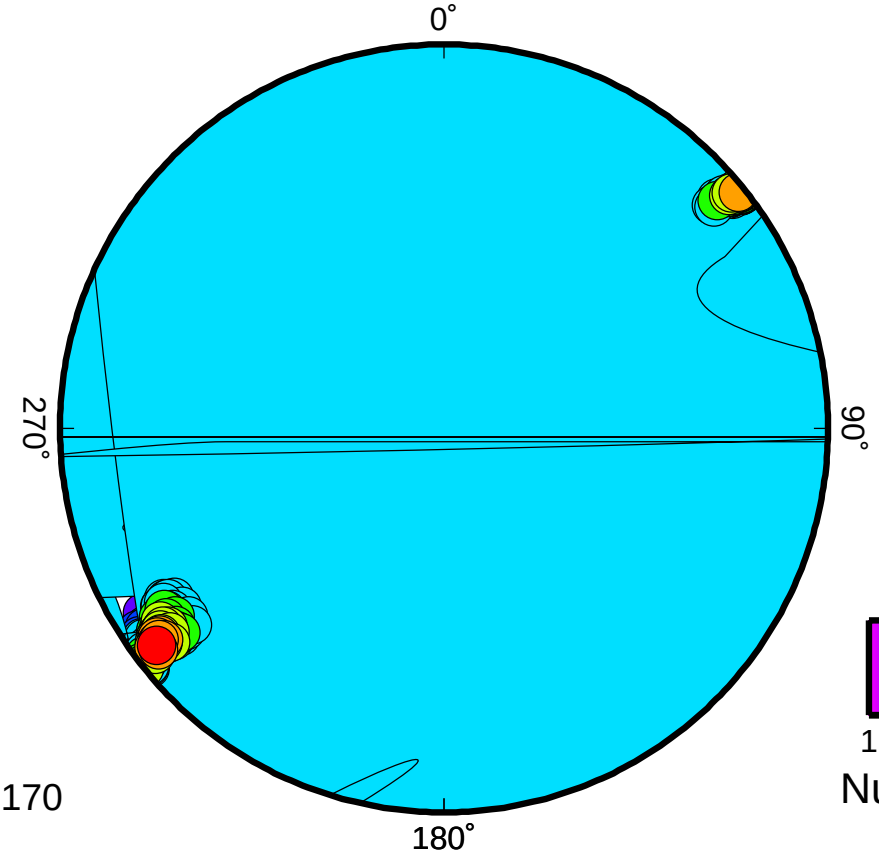

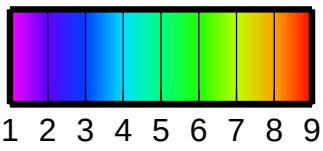

Number of stations

Figure 170

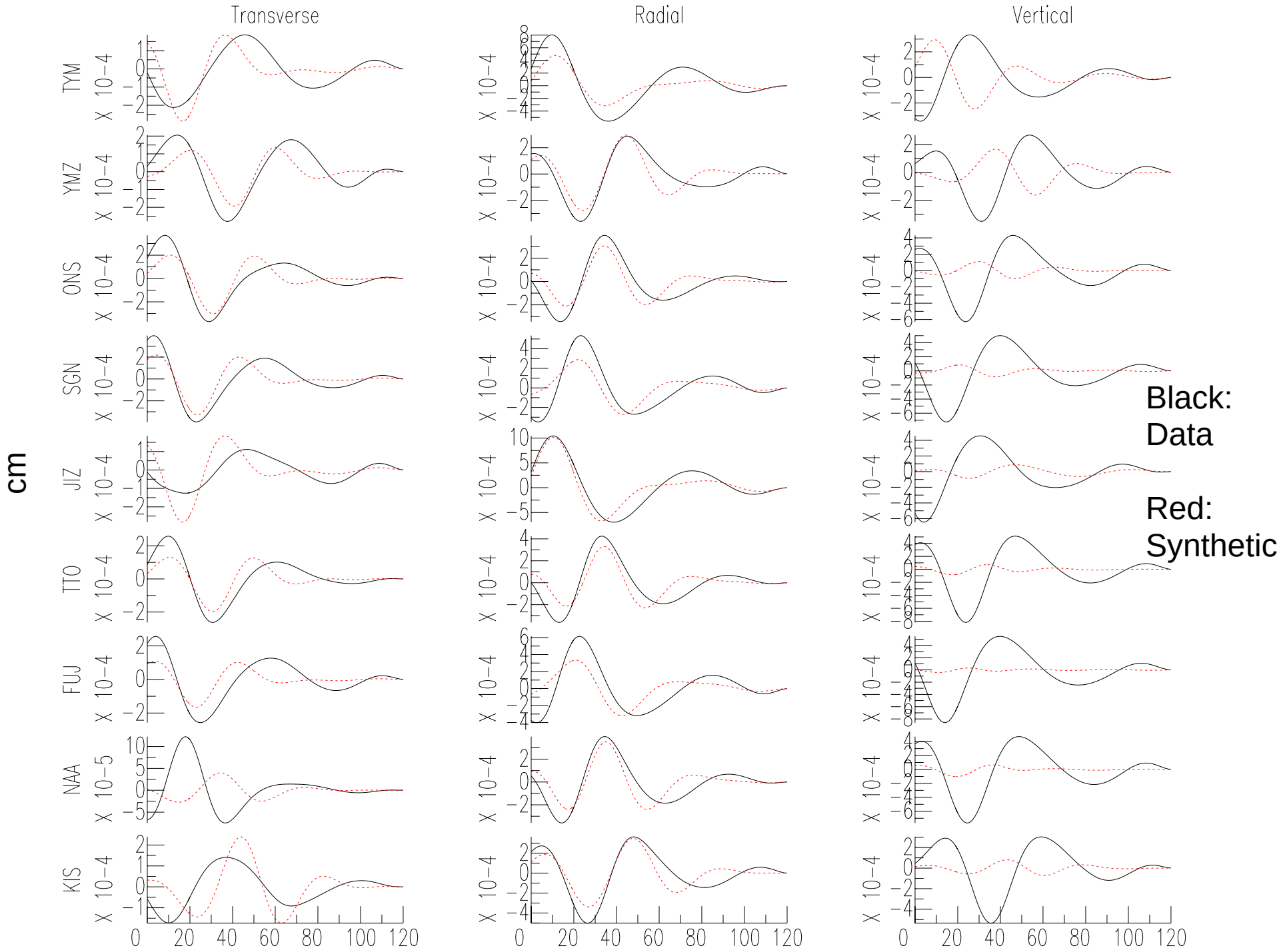
Transverse
Radial
Vertical
TYM
YMZ
ONS
SGN
JIZ
TTO
FUJ
NAA
KIS
X 10-4
X 10-5
cm
Black:
Data
Red:
Synthetic
0 20 40 60 80 100 120
Seconds

Figure 171

Results of moment tensor inversions for EVT7 in 0.01 to 0.033 Hz passband

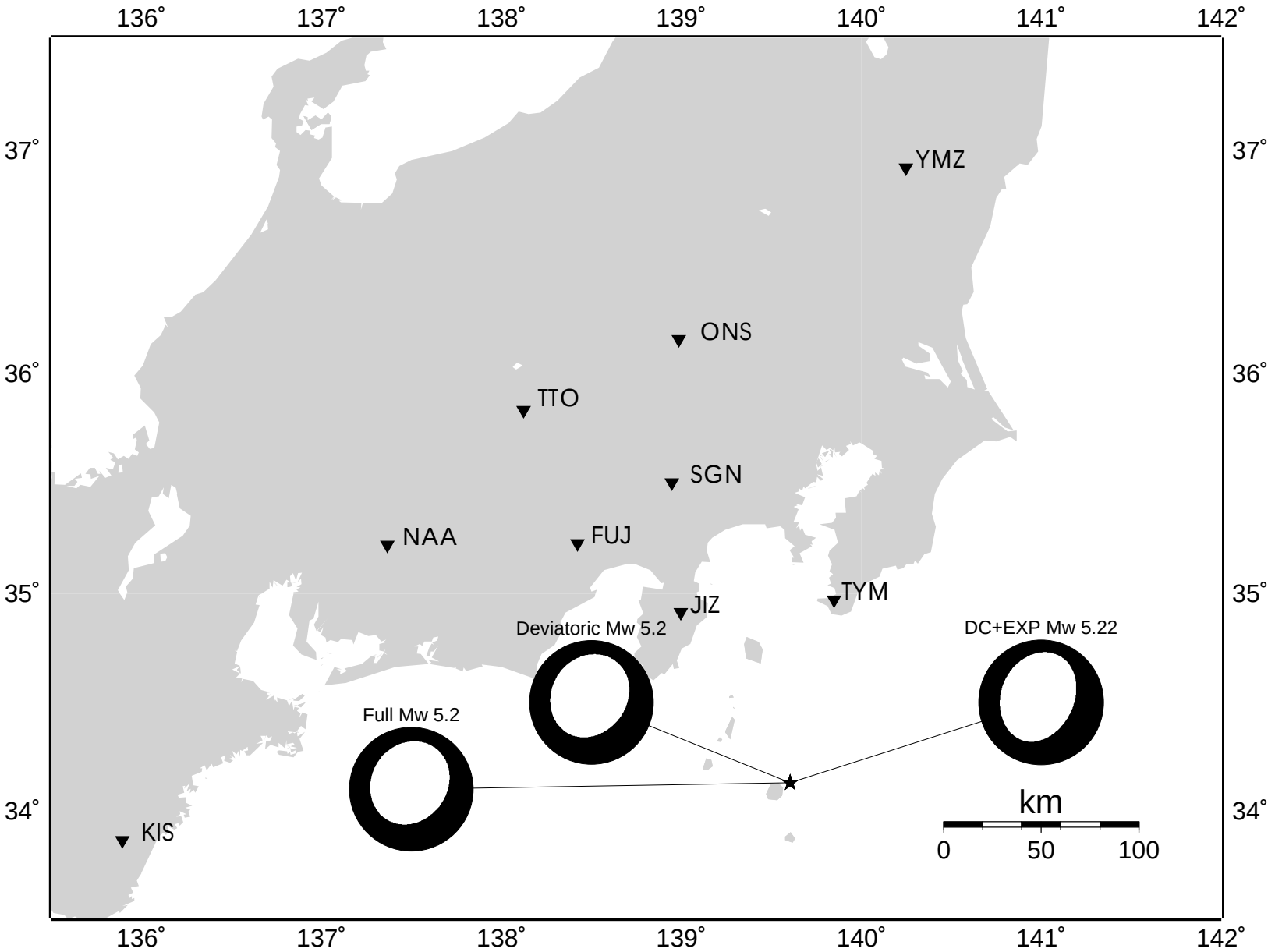

Figure 172

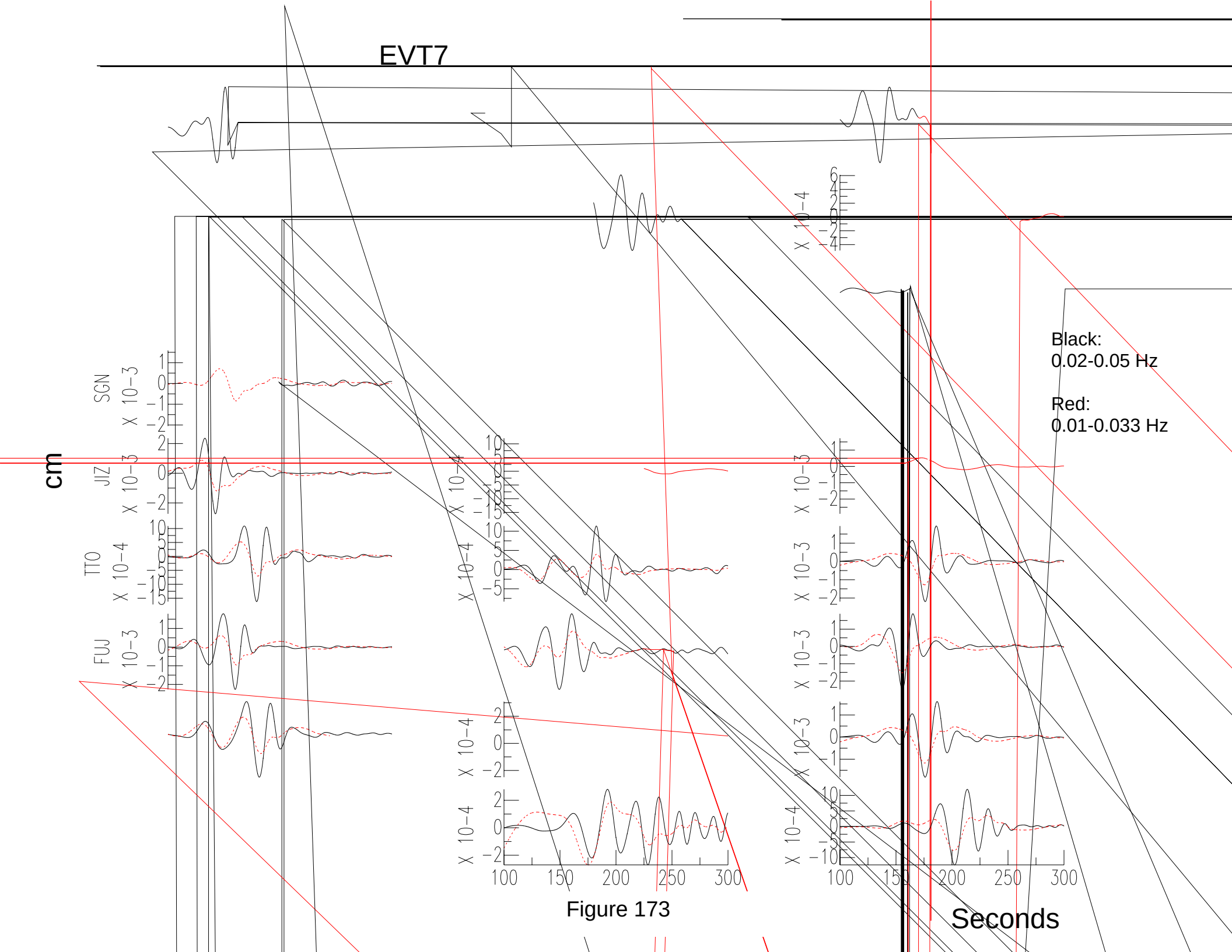
EVT7
cm
SGN
JIZ
TTO
FUJ
X 10-3
X 10-4
Black:
0.02-0.05 Hz
Red:
0.01-0.033 Hz
100
150
200
250
300
Seconds

Figure 173

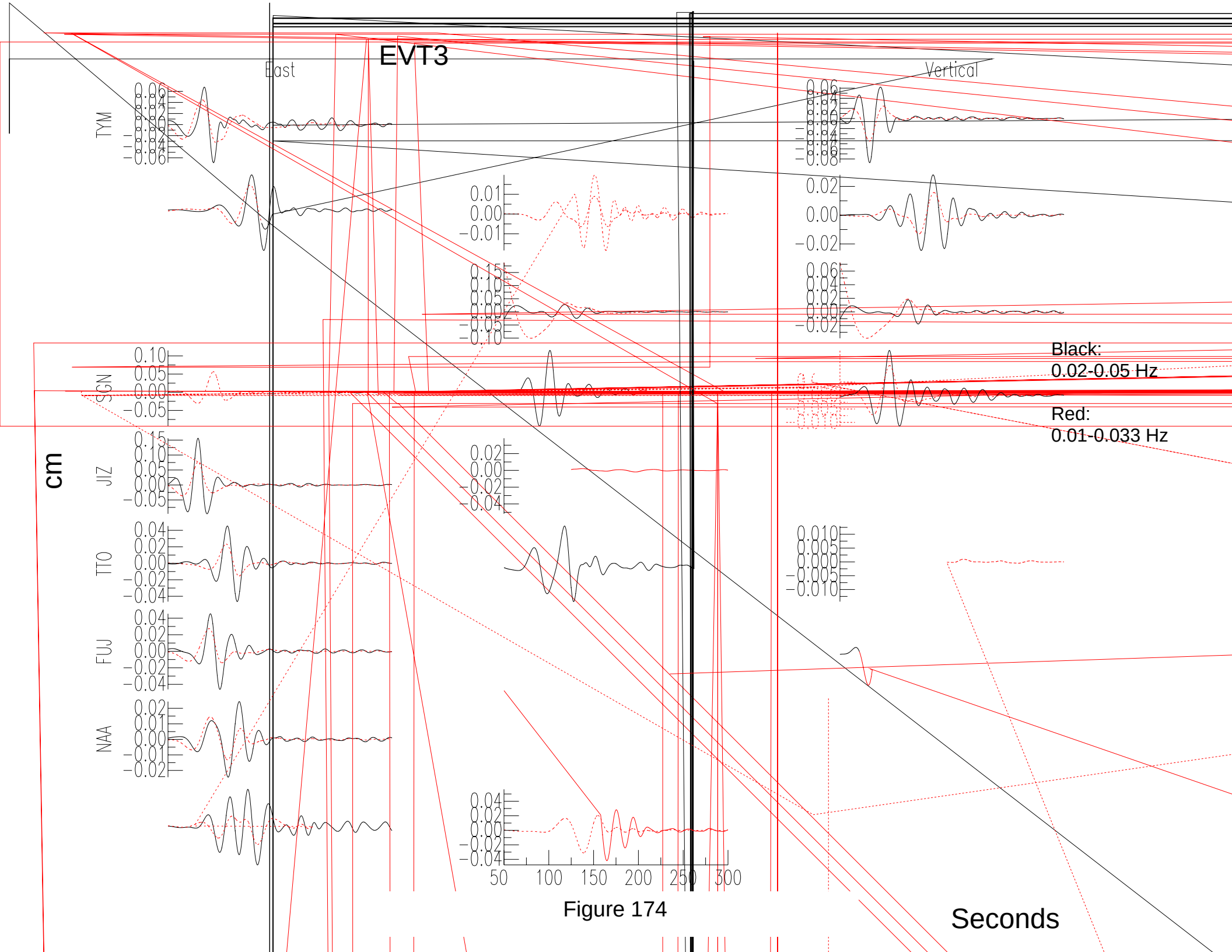
EVT3
East
Vertical
TYM
SGN
JIZ
TTO
FUJ
NAA
cm
Black:
0.02-0.05 Hz
Red:
0.01-0.033 Hz
50
100
150
200
250
300
Seconds

Figure 174

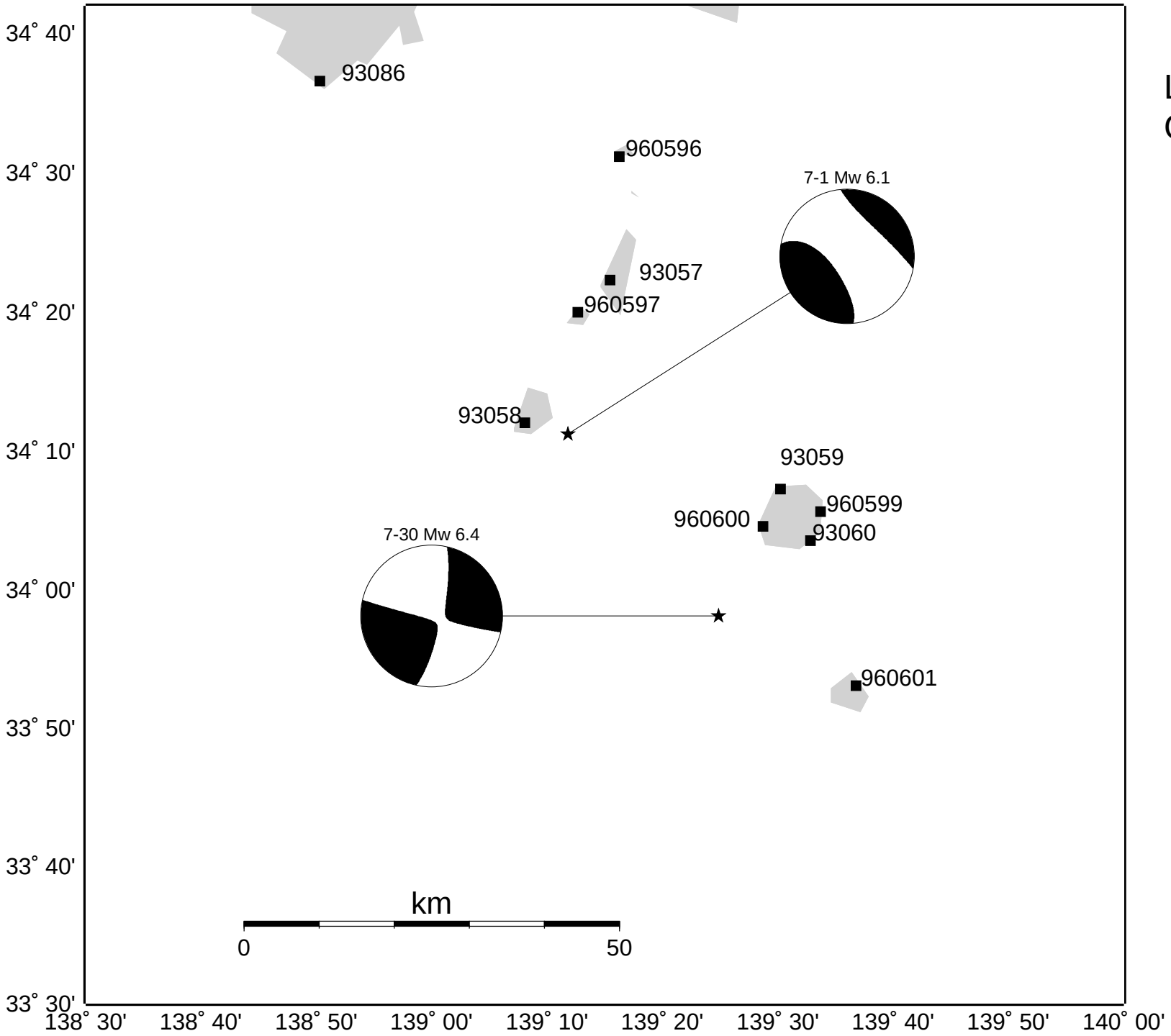

Locations of GPS stations

Figure 175

Results of inversions of GPS data for EVT15 Model 1. The three faults in the inversion, the dike, magma chamber, and earthquake fault are shown by red boxes where the double line is the down-dip edge of the fault. The black arrows are the observed horizontal displacements and the clear arrows are the predicted displacements. Similarly, the black bars are the observed vertical displacements and the yellow bars are the predicted displacements. Circles denote the locations of earthquakes occurring in the 24 hours after the event of interest, the epicenter of which is marked with a star.

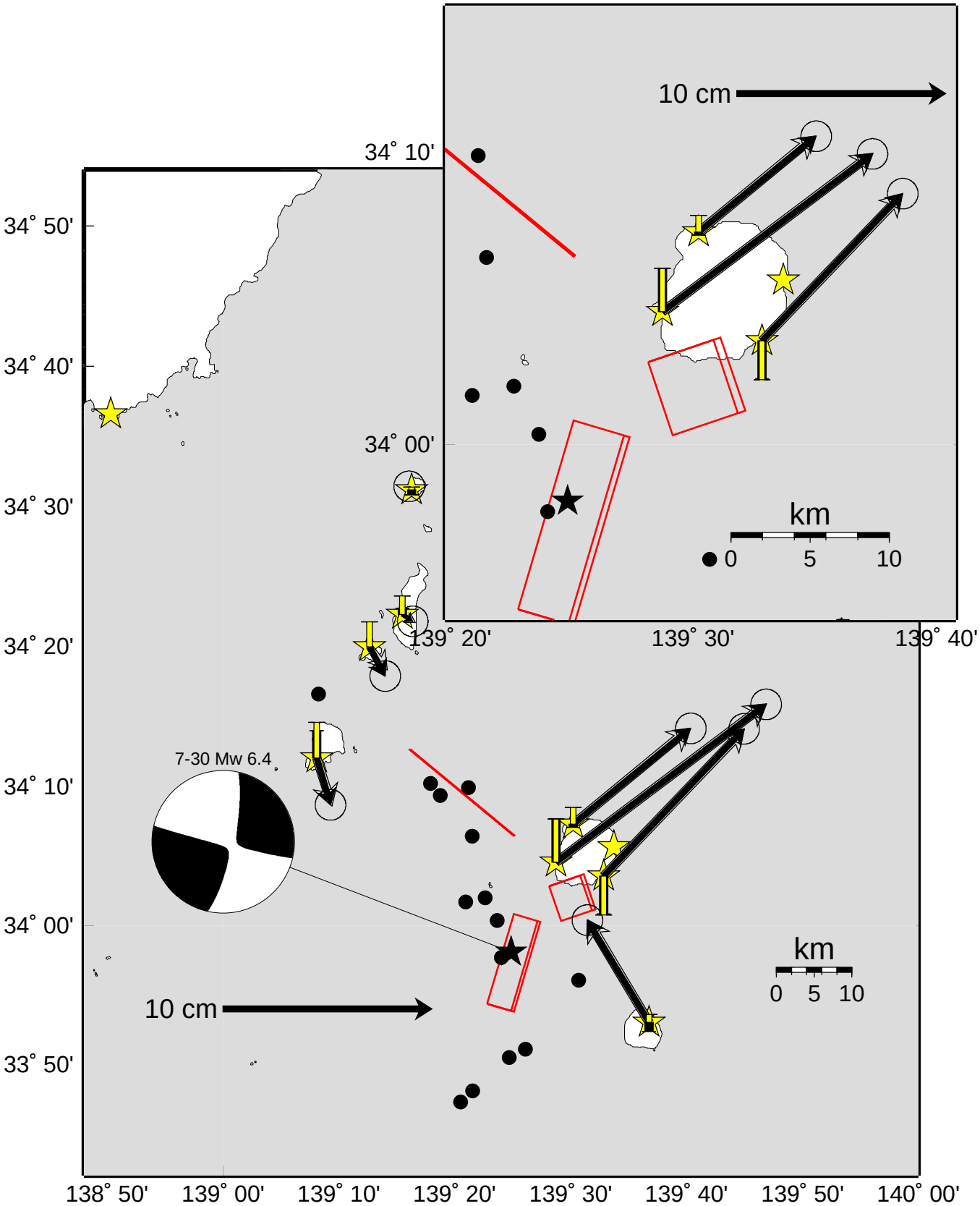

Figure 176

GMT 2003 May 10 16:27:43

Same as Figure 176 for EVT15 Model 2.

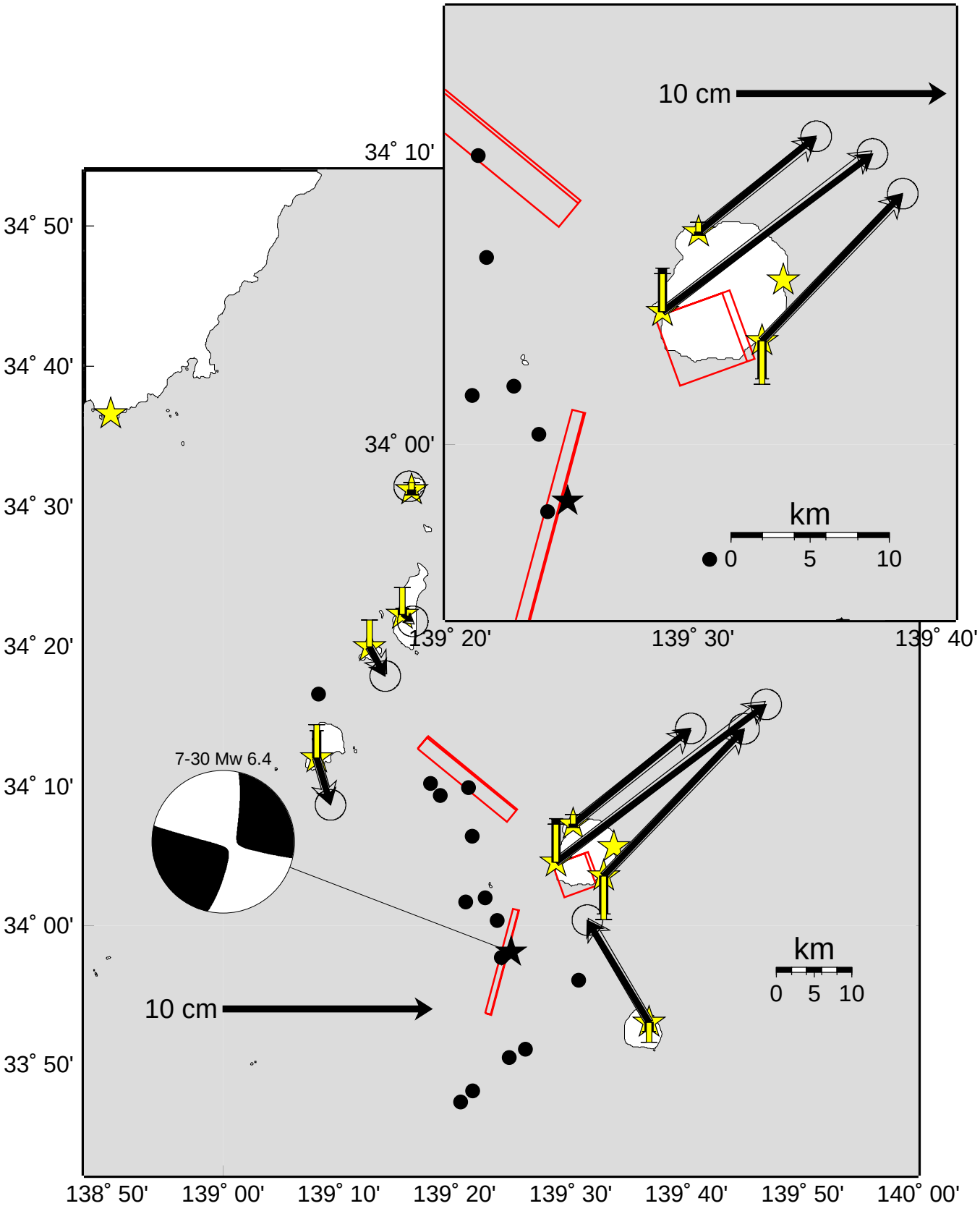

Figure 177

GMT 2003 May 10 16:29:28

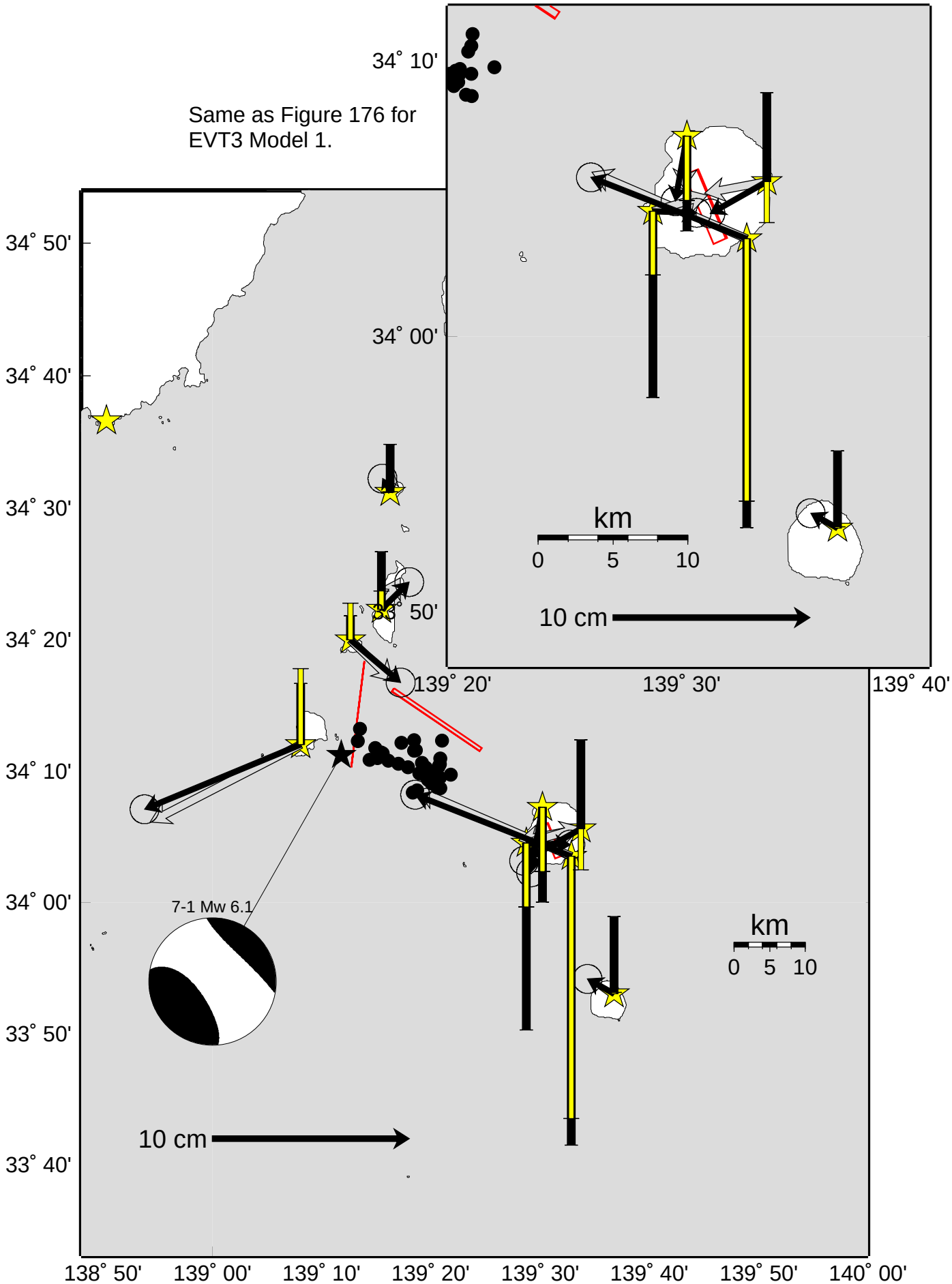

Figure 178

GMT 2003 May 9 20:42:05

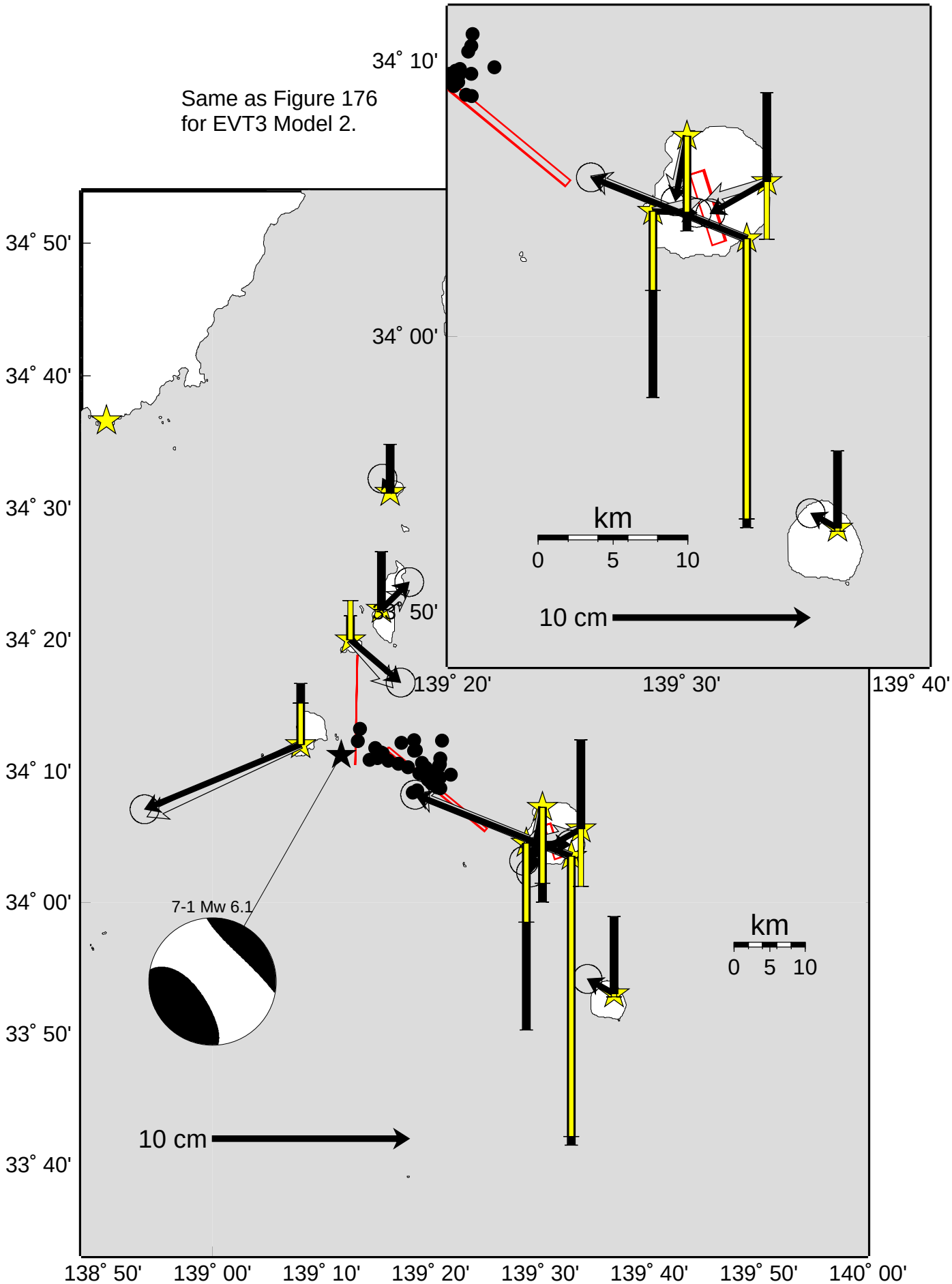

Figure 179

GMT 2003 May 9 20:44:28

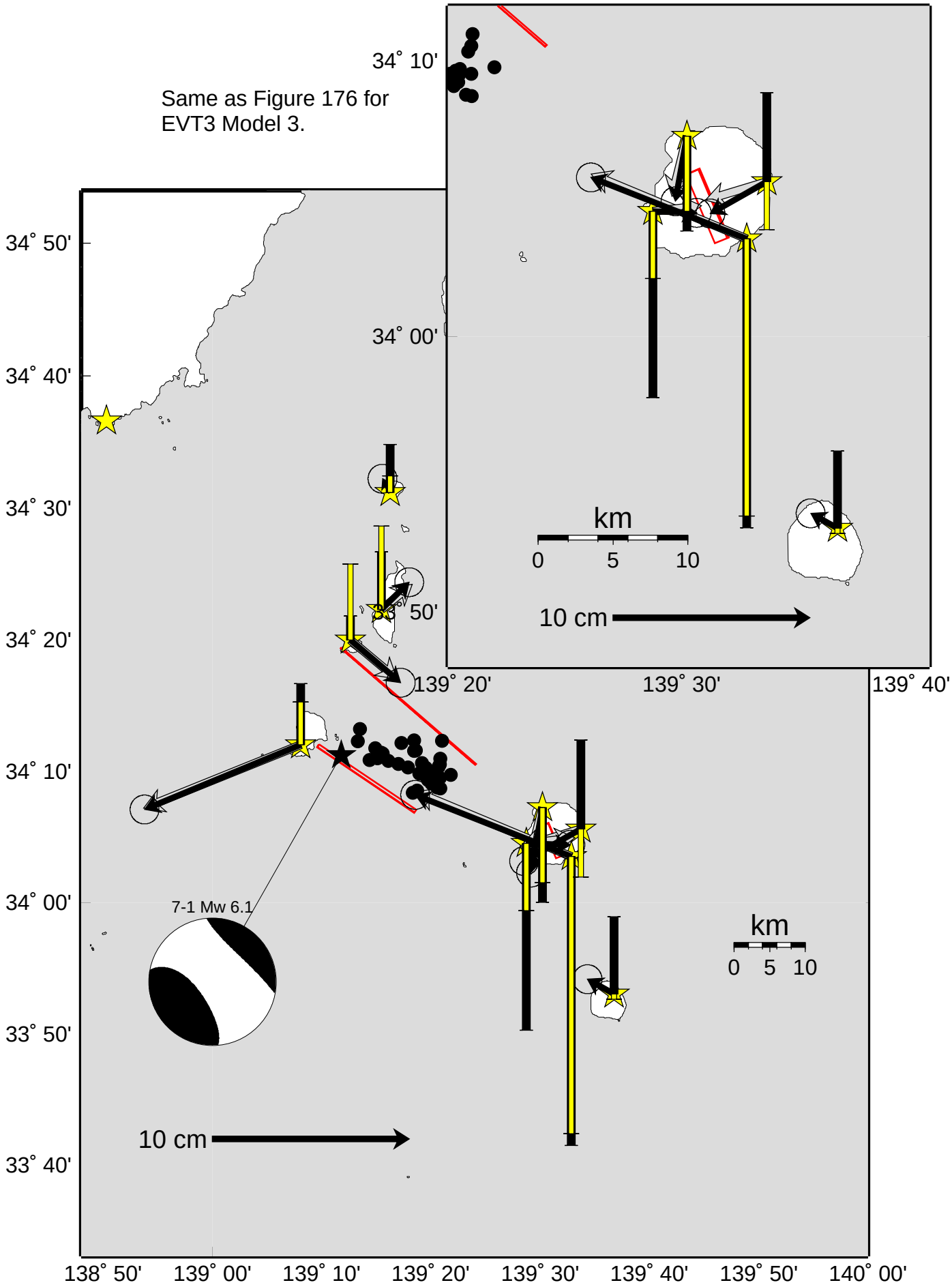

Figure 180

GMT 2003 May 10 19:00:51

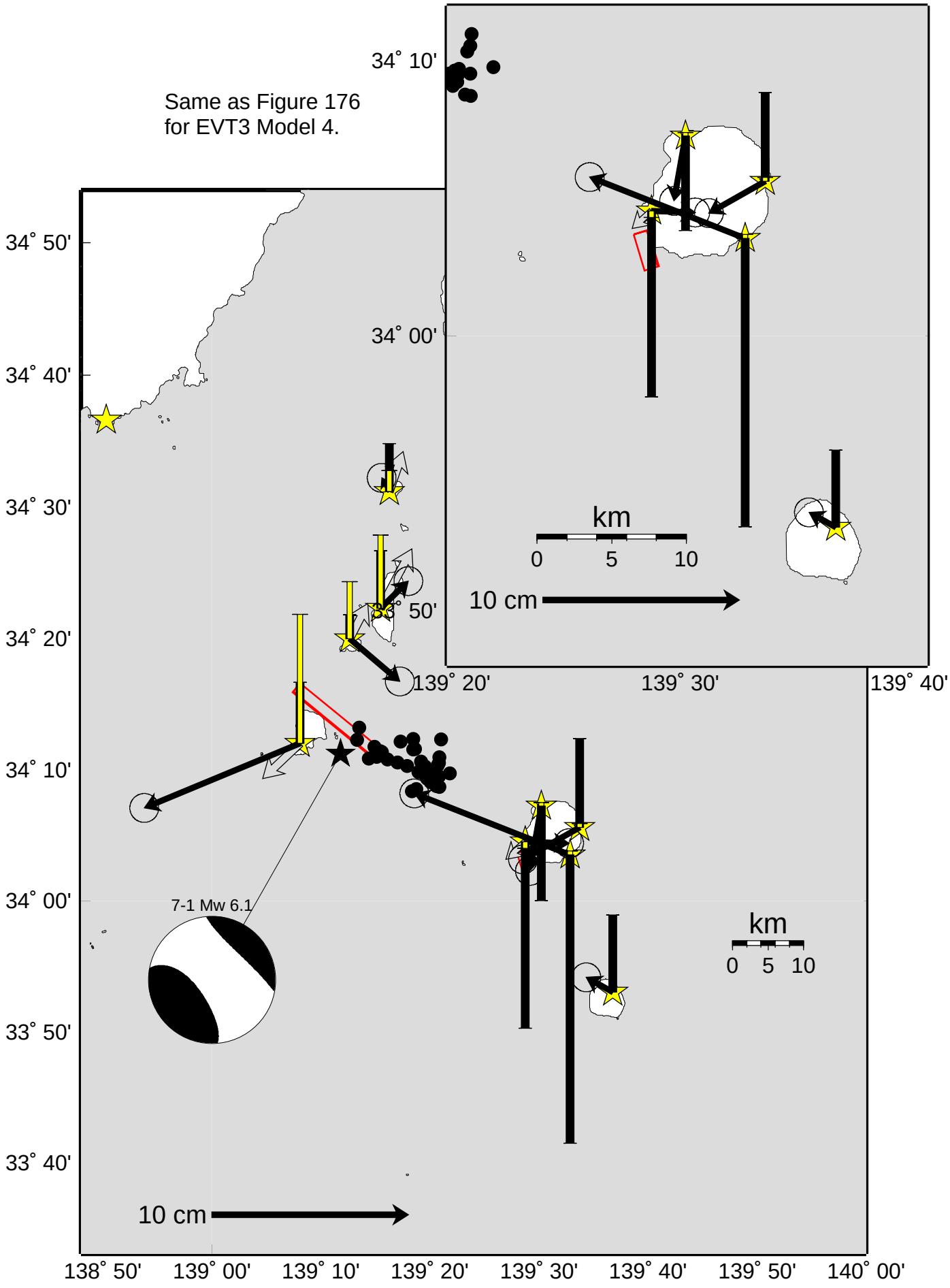

Figure 181

GMT 2003 May 13 17:12:29